Persistence and tensile strength of incipient rock discontinuities

Junlong Shang

Submitted in accordance with the requirements for the degree of
Doctor of Philosophy

The University of Leeds

School of Earth and Environment

July 2016

The candidate confirms that the work submitted is his own and that appropriate credit has been given where reference has been made to the work of others.

Acknowledgements

I would like to thank my supervisors Dr Jared West and Professor Steve Hencher for their time, encouragement and valuable supervision. Thanks to Dr Jared West for his continuous support, patience on the reviewing of my writing works as well as financial support (partially) in the experiments. I also learned a lot from his positive attitudes towards family, life and work, I believe, to some extent, those are more important than knowledge. Special thanks must give to Prof Steve Hencher for his valuable supervision in the thesis topic selection, very valuable discussion and the finance seeking for my visit in Hong Kong. The very detailed and constructive feedback of my work from Prof Hencher is greatly appreciated.

I am grateful to Dry Rigg Quarry manager Michael Cardus, Blackhill Quarry manager Craig Morrell for their permissions of work in the sites and valuable discussions in the quarries.

Thanks would also go to Julian Tyson (CH2MHILL, HK) for this support and arrangement during my visit in Hong Kong in 2014. I also want to thank Roy Hung at Geotechnical Engineering Office (The Government of the HK SAR) for accompany me visiting the Anderson Road Quarry in Hong Kong. Thanks Riccardo Amici for arranging my visit of MTR construction (Admiralty Section), Hong Kong I would also like to thank Yun Cheung Chan as well as his wife for their kindly welcome and discussion of my PhD project.

Sincere thanks must go to Kirk Handley for his constructive assistance with laboratory work and field experiments. I would also thank a gentle man Mark Hall for this patient instruction of driving in the England, which make it more convenient for my field experiments.

I would also like to thank all my colleagues at the University of Leeds for their assistance and support, especially Mohammed Aliyu, Giacomo Medici and John Martin.

Finally and mostly, my deepest thanks go to my families for their enormous love and support which made me who I am today! This thesis will be a dedication to all of family members. Thank you all.

Abstract

Rock discontinuities are fundamentally important to most rock engineering projects but predicting or measuring their properties such as roughness, aperture, shape and extent (persistence) are fraught with difficulty. So far the solution of how to measure or predict persistence is poorly researched partly because the concept of how to investigate the extent of rock discontinuities within a rock mass seems intractable, by any economical methods. In the majority of engineering applications it is a fairly widespread practice to follow a conventional approach, assuming a 100% persistence value. However that is certainly incorrect even if usually a conservative assumption.

This project is a small step towards resolving this issue. A series of laboratory and field research activities were carried out to investigate incipient nature of rock discontinuities and the extent of rock bridges.

Uniaxial tensile strength of incipient discontinuities was quantified in the laboratory using cylindrical rock samples. The tested samples included incipient joints, mineral veins and bedding. It has been confirmed that such visible yet incipient features can have high tensile strength, approaching that of the parent rock. Factors contributing to the tensile strength of incipient rock discontinuities have been investigated. It is concluded that the degree of incipiency of rock discontinuities is an important factor that should be differentiated as part of the process of rock mass classification to inform more realistic engineering design and that this might best be done with reference to the tensile strength relative to that of the parent rock. An original methodology has been developed in the laboratory using expansive chemical splitters in drillholes, to quantify the tensile strength of large-scale incipient rock joints. In these tests, smaller tensile strengths were obtained, which probably was the result of localised stress concentration, low pressurization rate and unavoidable variations of expansive tensile force arising from the chemical splitter.

A technique ‘Forensic Excavation of Incipient Rock Discontinuities (FEIRD)’ was established and employed to investigate areal extent and incipient nature of discontinuities in the field. Large rock blocks, containing incipient features, were split using similar expansive grout techniques as developed in the laboratory. Test results were interpreted and discussed with respect to fracture mechanics, fractographic features (such as hackle and rib marks), as well as geological conditions affecting the incipiency of the tested discontinuities including degree and extent of weathering and mineralisation.

One common observation from the tests conducted is that breakage of non-persistent sections of incipient rock joints (rock bridges) leads to the development of rough surfaces over those freshly broken areas, and this may have implications for rock fracture development more generally. Despite rock bridge failure (say as part of rock slope mass movement), the freshly formed surfaces might be expected to have relatively high strength compared to the pre-existing persistent sections. An important conclusion from this research is that areal extent of open rock discontinuities (persistence) can be investigated realistically using the FEIRD technique. It has been found that estimates of persistence from trace mapping on rock exposures can be wildly inaccurate and it is concluded that field studies using FEIRD techniques (perhaps at a larger scale than used for this research to date) can be used to understand and quantify better the true nature of rock mass fracture network connectivity and extent that are important parameters for many rock engineering endeavours.

Table of Contents

List of Tables

List of Figures

List of Abbreviations

ADVDPC, Advanced Pressure/Volume Controller

AE, Acoustic emission

BB, Barton-Bandis

BCM, Boundary collocation method

BEM, Boundary element method

BGS, British Geological Survey

Bi, Biotite

BQ, Blackhill Quarry

BSD, Block size distribution

C, Calcite

CB, Chevron bend specimen

CCNBD, Cracked chevron notched Brazilian disc

Cl, Clay

CVF, Complex variable function

D, Dolomite

DEM, Distinct element method

DFN, Discrete fracture network

DRQ, Dry Rigg Quarry

DSM, Digital surface model

$ETF_{(t)}$, The total expansive tensile force (kN) perpendicular to the splitting plane from chemical splitter

F, Feldspar ($KAlSi_3O_8$)

F_i, Resisting force (kN) of rock material / incipient joint at the point of fracture initiation.

F_{LC}, Measured force (kN) using load cell

F_{LCA}, Measured force (kN) using load cell A

F_{LCB}, Measured force (kN) using load cell B

F_m, Maximum resisting force (kN) of rock material / incipient joint at sample failure

F_{PR}, Measured force (kN) using PR

F_r, Resisting force (kN) of intact rock material / incipient joint to be split

FDM, Finite difference method

$F_{D(t)}$, Applied radial froce (kN) from chemical splitter

FEIRD, Forensic excavation of incipient rock discontinuities

FEM, Finite element method

FIE, Fredholm integral equation

FT, Fracture toughness

GSI, Geological strength index

HAL, Hencher Associates Limited

IM, Integral methods

ISRM, International Society for Rock Mechanics

JCS, Joint wall compressive strength

JRC, Joint roughness coefficient

LC, Load cell

LEFM, Liner elastic fracture mechanics

LVDT, Linear variable differential transformer

MC, Mohr-Coulomb

MTR, Mass transit railway

NDT, Non-destructive testing

P, Pyrite

PFC, Particle flow code

PPE, Personal protective equipment

PR, Proving ring

Q, Quartz

RB, Rock bridge

RMR, Rock mass rating

RQD, Rock quality designation

RVE, Representative volume element

SCB, Semi-circular bend

SM, Safety margin

SR, Short rod specimen

SS, Scanline sampling

SU, Strength underestimation

TDP, Terrestrial digital photogeammetry

TLS, Terrestrial laser scanner

UCS, Uniaxial compressive strength

UDEC, Universal distinct element code

UTS, Uniaxial tensile strength

WS, Windows sampling

XRD, X-ray power diffraction

3DEC, Three dimensional distinct element code

Chapter 1
Introduction

1.1 Research background

Rock discontinuities are of primary importance to strength, deformability and permeability of rock masses and overall stability of rock engineering projects. Characterisation of discontinuity properties, such as orientation, spacing, roughness and persistence (areal extent), is the first step to understand the overall behaviour of rock masses. It has been nearly four decades since awareness of the importance of discontinuity persistence on rock engineering (Barton 1975 and Cruden 1977). Significant efforts have been made to consider persistence during the measurement of discontinuities (e.g. Barton 1975, Priest and Hudson 1981 and Latham et al. 2006) and in the assessment of rock mass stability (e.g. Einstein et al. 1983 and Pariseau et al. 2008). However these endeavours are still a matter of engineering judgment as no constructive or standard methods have been proposed to quantify real persistence. International Society for Rock Mechanics (ISRM 1978a) proposed the concept of termination index, with an aim to incorporate the non-persistent nature of discontinuity into rock engineering but failed to give a precise guidance on how to quantify persistence.

It is extremely difficult to quantify discontinuity properties especially real persistence due to the three dimensional nature of rock discontinuities within rock masses. Currently, in rock engineering and modelling, trace length of discontinuities obtained from outcrop is used as an approximation of real persistence (e.g. Kim et al. 2007a, b and Umili et al. 2013); sometimes the persistence value of 100% is assumed for simplification purpose (e.g. Park 2005 and Jiang et al. 2015). All these approximation and assumption are ‘geological guesswork’.

1.2 Aims and structure of thesis

This research will be a small step towards the problematic issue described above. The following questions are answered in this work, which are:

(1) How to quantify the incipiency of a geological discontinuity? What are the factors governing discontinuity incipiency?

(2) What is the relationship between the incipiency of a geological discontinuity and its persistence?

(3) Is that possible to measure tensile strength of small and large scale incipient rock discontinuities in the laboratory?

(4) Is that possible to quantify the persistence of a discontinuity, or at least on a conceptual level?

The thesis comprises a further six chapters. A review of discontinuity persistence with regard to its definition, implications and quantification is discussed in Chapter 2. Tensile strength of incipient rock discontinuities is measured in Chapter 3 and a method to quantify the incipiency of discontinuities is presented. Chapter 4 presents a possible approach to quantify tensile strength of large-scale incipient rock discontinuity. A new forensic technique is proposed and described in Chapter 5 to quantify real persistence. A synthesis of the main findings of this thesis is present in Chapter 6. Summary, conclusions and the scope of future work are presented in Chapter 7.

Chapter 2
Literature Review

2.1 Introduction

The focus of this chapter is to review current knowledge of discontinuity persistence. Its implications for rock engineering and the state-of-the-art methodologies and techniques to quantify real persistence or its approximation are discussed in following text. The rest of this chapter are organized as follows. In section 2, definitions of incipient discontinuities, persistence and surface features of discontinuities is presented. Stresses (mode I and mode II) around fracture tips which control discontinuity propagation and development are discussed in section 3. In section 4, the mechanical properties including tensile and shear strength of single incipient discontinuities are discussed, in which the actions of incipiency (persistence) are emphasised. Rock masses containing multiple incipient discontinuities are the focus in section 5, volume and size of rock blocks within rock masses as well as its strength and stability are discussed. In section 6, current methodologies for measuring or estimating discontinuity persistence are reviewed. A summary is presented in section 7.

2.2 Definitions

2.1.1 Incipient and mechanical rock discontinuities

Rock discontinuity is normally recognised as a general term to describe any weak mechanical breaks including most joints, weak bedding planes, weakness zones and faults within rock masses (ISRM 1978a). Hencher (2015a) commented the crudeness and misuse of the discontinuity definition in engineering practice. He argued that this definition does not allow for stronger incipient traces, however, all these traces are normally visualised as ISRM defined discontinuities by academics as well as practitioners and are recorded during discontinuity logging in the outcrop regardless of strength (Hencher and Knipe 2007 and Hencher 2014, 2015a). This common practice tends to underestimate strength of rock masses, while overestimating permeability; which therefore can considerably increase expenditure on rock support system and also influence reliable prediction of water, oil and gas extraction. It is practically and theoretically important to differentiate the degree of incipiency of discontinuities.

Incipient (or integral) rock discontinuities retain considerable tensile strength as a result of partial development due to the varying stress conditions or due to secondary mineralization or cementation processes. This conception is illustrated by Figures 2.1 and 2.2, in which near-vertical incipient rock discontinuities were partially developed. These incipient rock discontinuities will develop as a response to weathering, mechanical breakage, stress variation or precipitation into mechanical (open) discontinuities which have zero tensile strength (see Figure 2.3). Figure 2.4 presents the different developing stages of incipient joints on faces cut by diamond wire saw. Sets of joints can be seen as linear traces stained with iron oxides, cutting the granite. These joints were evidently formed from brittle fracture propagation at a late stage during cooling/emplacement of the granite as can be interpreted from cross-cutting relationships and the geometrical association of some joints with mineral differentiation (as at 1 in an area washed off with water). Note that some of the joints are poorly defined and terminate (as visible features) as at 2. The joint pattern is a ‘blueprint’ that, given time, would propagate as interconnecting true, mechanical discontinuities in the sense defined by ISRM. Note at 3 that one of the shallowly dipping joints (not-sheeting), has an open aperture locally, allowing seepage of groundwater.

Figure 2.1 Partially developed joint which is incipient, Horton-in-Ribbesdale, Yorkshire, England.

Figure 2.2 A set of near vertical incipient joints at Blackhill Quarry, West Yorkshire, UK. Note that rock materials are weathered predominately along joint traces, person for scale.

Figure 2.3 Section of rock core, andesitic tuff, Island Road, Hong Kong. Incipient and mechanical rock discontinuities can be noticed. Relative tensile strength, i.e. high, moderate and weak strength relative to the strength of the parent rock, were suggested by Hencher (2014) to differentiate these discontinuities. After Hencher (2014).

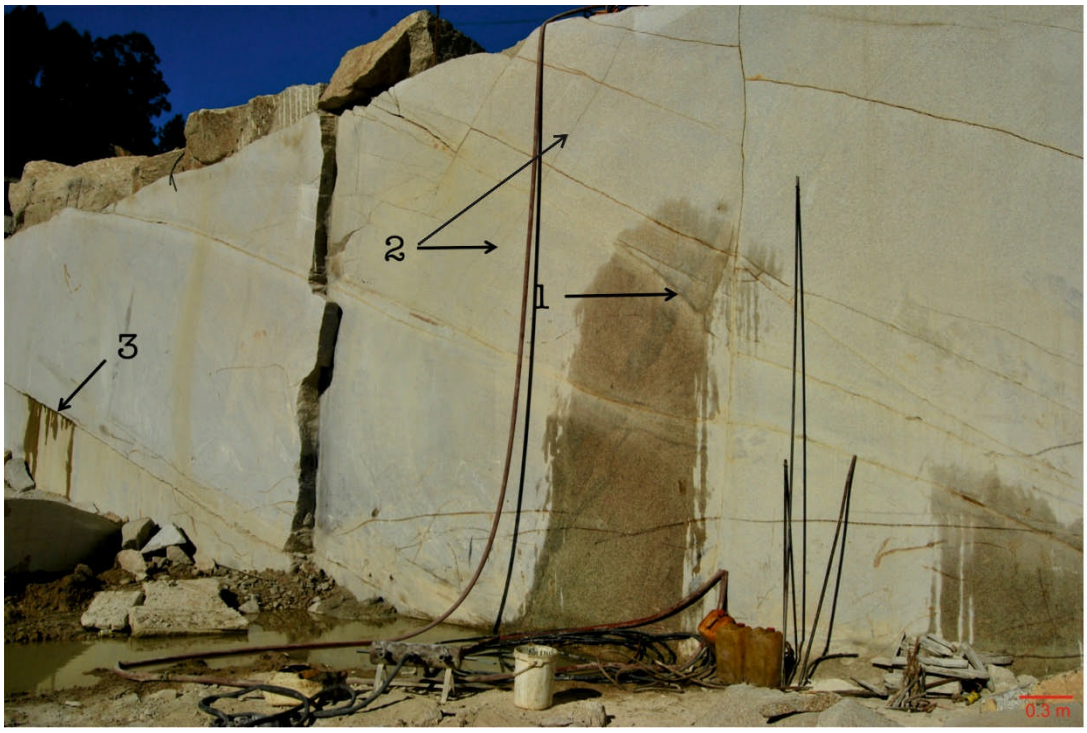

Figure 2.4 Face cut by diamond wire saw in dimension stone quarry near Tui, Galicia, Spain. Joint 1 and 2 are in earlier incipient stages (which are always poorly defined by current standards). Joint 3 is in later incipient stage and it has a persistent area partially, allowing seepage of fluid. For more details see text. Image courtesy of Steve Hencher.

2.1.2 Rock bridges and discontinuity persistence

In jointed rock masses, rock bridges exist because of the incipient (non-persistent) nature of discontinuities. A rock bridge is defined as the small intact/strong rock material separating coplanar and non-coplanar discontinuities (Kim et al. 2007b, c). In this review, only coplanar discontinuities along with the intervening rock bridges are considered so as to follow the definition of persistence proposed by ISRM (1978a) and Einstein et al. (1983).

Discontinuity persistence is areal extent of a rock discontinuity. Until now there have been several different definitions of this parameter. Jennings's mechanical model (Jennings 1970), as illustrated by Figure 2.5a, firstly incorporated joint persistence (estimation) into rock engineering.

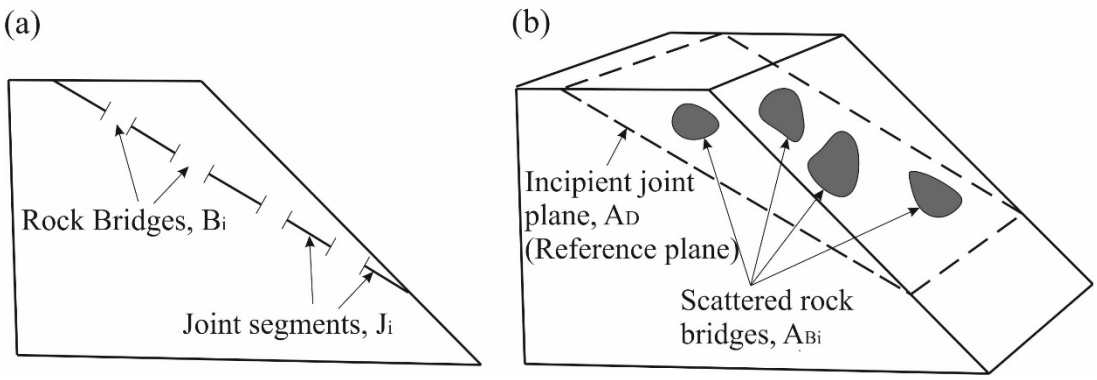

Figure 2.5 Definitions of rock discontinuity persistence. **a** Linear extent definition (approximation of persistence) and **b** Areal extent of discontinuity (real persistence)

In his model, joint persistence *K* was defined as a linear ratio of sum of joint segments $\sum J_i$ and the total length of coplanar given line $\sum (J_i + B_i)$:

$$K = \sum J_i / \sum (J_i + B_i) \tag{2-1}$$

This two-dimensional definition is an estimation of real persistence but has been widely accepted and employed in experimental, analytical and numerical studies for its straightforward meaning and easily obtainable nature (e.g. Lajtai 1969a, b, Zhang et al. 2006, Prudencio and Van Sint Jan. 2007, Ghazvinian et al. 2012, Bahaaddini et al. 2013, Kim et al. 2013a, Shang et al. 2013 and Jiang et al. 2015). Jennings's model deals only with two-dimensional coplanar incipient joints; it cannot be extended to three dimensions. ISRM (1978a) suggested a three dimensional discontinuity persistence which was defined as the fraction of continuous discontinuity area which can be expressed by the following equation (see Figure 2.5b):

$$K = \sum \left(A_D - A_{Bi} \right) / A_D \tag{2-2}$$

where $\sum A_{Bi}$ is the total area of scattered rock bridges, A_D is the reference area (termed as weakness plane by Lajtai (1969b)) including rock bridges and continuous discontinuity segments.

This three dimensional persistence definition can be treated as an extension of Jennings's model on the assumption that discontinuity generates along the predefined weakness plane. It enhances the application of three dimensional stability analyses which takes into account the effects of incipient discontinuity into rock engineering. For example in a recent work presented by Viviana et al. (2015) effects of the spatially distributed rock bridges along a main sliding plane were investigated. To author's knowledge, ISRM (1978a) defined

discontinuity persistence applies to various scales from small scale on laboratory samples to large scale in field situations.

A limit of Equation (2-2) was proposed by Einstein et al. (1983) as a separate definition of three dimensional persistence. It means persistence can approach zero when A_D approaches infinity; this scale-dependent nature has been pointed out by Lu and Latham (1999).

The above traditional definitions mainly focus on the geometrical behaviour of single incipient discontinuity and ignore its mechanical behaviour like stress distribution and concentration around joint tips as stated by Kevin (1980) and Wasantha et al. (2014). There have been some studies trying to consider the mechanical influence on degree of discontinuity persistence. A publication by Wasantha et al. (2014) is an example in which a new parameter was proposed to define joint persistence considering stress distributions around joint tips.

The above persistence definitions imply that discontinuities and intervening rock bridges are coplanar. When dealing with randomly generated rock discontinuities, probabilistic approaches have been developed to describe persistence. The general approaches of these methods are:

(1) Assume a measurable distribution of discontinuity trace length (an estimation of persistence), types of discontinuity, sampling bias and corresponding corrections (will describe in section 2.6.1) are normally described;

(2) Statistical methodologies combining field observations with the above are employed to estimate the distribution of parameters in the proposed equation;

(3) Artificially generated or natural data are then used to illustrate and validate the complete distribution equation.

2.1.3 Surface features of rock discontinuity

Joint surface morphology or topography is normally decorated by some textures such as hackle (feather) and rib markings that depict the joint initiation, orientation and propagation (Pollard and Aydin, 1988). A discipline named “fractography” was developed to investigate this topic (Ameen 1995), in which fractography features including surface patterns directly observed on exposed joint surface and fracture traces observed on a free surface were defined. Figure 2.6 shows the classic feather (hackle) and rib markings on surface of a discontinuity. Figure 2.7 shows conchoidal feather and rib markings formed by impacting with hammer.

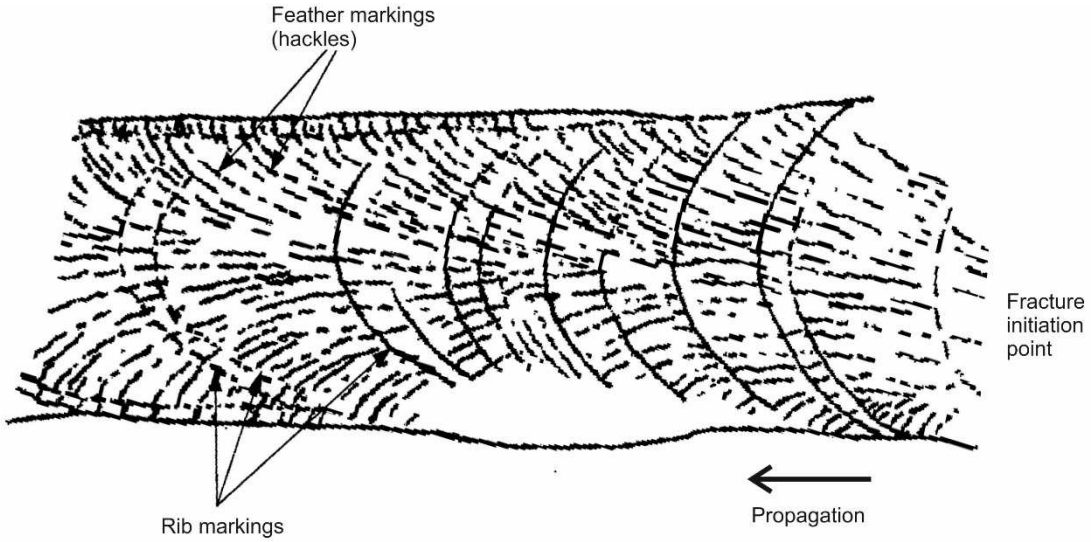

Figure 2.6 Diagram showing the classic feather and rib markings on a fracture surface radiating from a point formed geologically. Modified from Zhang and Einstein (2010).

Figure 2.7 Fractography features on fracture surfaces broken by impact with hammer. Conchoidal feather and rib markings radiating from points of impact in micritic limestone cobble. Foot for scale. Photo courtesy of Steve Hencher (2015).

In following section, we will discuss stresses around fracture tips which control the incipiency of discontinuities.

2.3 Stress field in the vicinity of fracture tips

Rock discontinuities within rock material can close, open, slide or propagate under different loading conditions. In linear elastic fracture mechanics, all these discontinuities can be approximately treated as cracks and fractures defined by Kulander et al. (1990) as breaks in rock caused by stresses exceeding the rock's strength. Stress distributed around crack tips govern mechanical behaviour and failure patterns (Griffith 1921). Basically two crack patterns including wing cracks (tensile cracks) and secondary cracks (shear cracks) can be observed around pre-existing crack tips in rocks and rock-like materials under compression, as those simplified shown in Figure 2.8 (Ingraffea and Heuze 1980, Ingraffea 1980, Huang et al. 1990, Shen and Stephansson 1994 and Antonio 2000). Many publications are available on the topic of fracture initiation and propagation which will not be extensively discussed here as beyond the scope of this review. A review recently by Hoek (2014) is recommended to readers who are interested in this topic. In this section, the Mode-I and mode-II stress field in the vicinity of fracture tips is discussed which is the basis of fracture initiation, tensile and shear properties of incipient discontinuities.

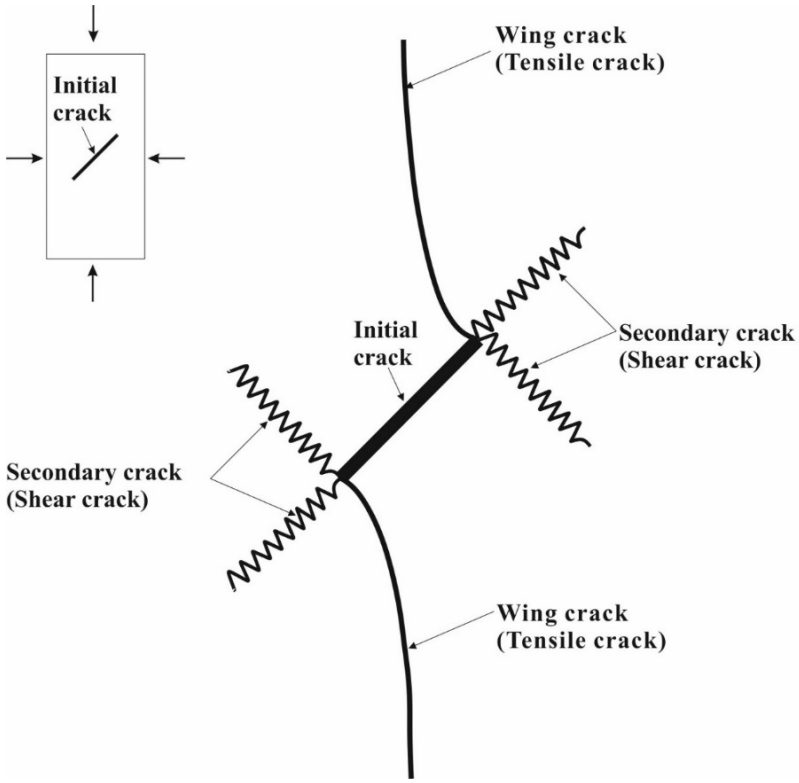

Figure 2.8 Simplified reduced tensile and shear crack patterns around pre-existing crack tips within a rock sample under compression, modified from Antonio (2000).

2.3.1 Stress modes near fracture tips

Griffith (1921) inferred that the stress concentration around the tips of open cracks leads to the failure of material when this concentration exceeds strength of material. This original assumption was then verified and extended to closed cracks by Murrell (1958), McClintock and Walsh (1962) and Brace (1964).

Irwin (1957) pointed out that the stress field around fracture tip can be grouped into three components, i.e. Mode I open fracture, Mode II shear fracture and Mode III tearing fracture, as shown in Figure 2.9. Considering the crack tip to be a two dimensional problem (in the *xz* - plane), the three stresses can be expressed as (Sun and Jin 2012)

$$\begin{aligned}
\sigma_{yy} &= \frac{K_I}{\sqrt{2\pi x}} + O\sqrt{x}, \qquad \sigma_{xy} = \sigma_{yz} = 0 \\
\sigma_{xy} &= \frac{K_{II}}{\sqrt{2\pi x}} + O\sqrt{x}, \qquad \sigma_{yy} = \sigma_{yz} = 0 \\
\sigma_{yz} &= \frac{K_{III}}{\sqrt{2\pi x}} + O\sqrt{x}, \qquad \sigma_{yy} = \sigma_{xy} = 0
\end{aligned} \tag{2-3}$$

where K_I , K_{II} and K_{III} are stress intensity factors (MPa●m$^{1/2}$) corresponding to Mode-I open fracture, Mode-II shear fracture and mode III tearing fracture. x (m) is the distance from existing fracture tip. The capital letter *O* (not a zero) is a symbolism used in mathematics to describe the asymptotic behaviour of functions.

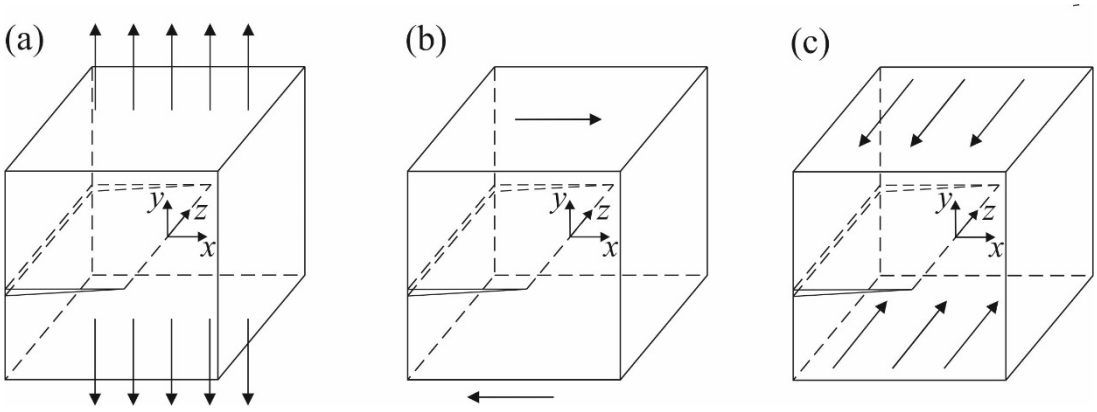

Figure 2.9 Schematic of one fracture tip within surrounding rock materials under different stress modes: (a) Mode I (Tension), (b) Mode II (In-plane shear) and (c) Mode III (Out-of-plane shear). Modified from Sun and Jin (2012).

It is well known that stress intensity factors (SIFs) describe the stress fields near fracture tips in rock materials under different loading conditions in the context of liner elastic fracture mechanics (LEFM). Whittaker et al. (1992) concluded that SIFs were able to be measured analytically (e.g. complex variable function (CVF), integral methods (IM)), experimentally (e.g. photo-elastic techniques, acoustic emission (AE) and some indirect measurements (such as ISRM-Suggested methods)) and numerically (e.g. finite element method (FEM), finite difference method (FDM), boundary element method (BEM), and boundary collocation method (BCM)). There have been hundreds of publications dealing with stress field near fracture tips. In the following section, main contributions towards mode I and mode II stress distributions were briefly reviewed.

2.3.2 Mode-I stress distribution near fracture tips

It has been shown that the CVF method proposed by Muskelishvili (1952) was a very marked and convenient method to deal with stresses around the two-dimensional crack problems in anisotropic media (Savin 1961 and Lekhnitskii 1963). Sih et al. (1965) derived the general equations for stresses near fracture tips in anisotropic bodies. The major contribution of their work was the extension of the application of CVF in isotropic bodies into anisotropic media in which the generalized Hooke's law was adopted. The general Mode I stress around crack tips in anisotropic media proposed by Sih et al. (1965) is

$$\begin{aligned}
\sigma_x &= \frac{K_I}{\sqrt{2r}}\,\mathrm{Re}\left[\frac{\mu_1\mu_2}{\mu_1-\mu_2}\left(\frac{\mu_2}{\sqrt{\cos\theta+\mu_2\sin\theta}}-\frac{\mu_1}{\sqrt{\cos\theta+\mu_1\sin\theta}}\right)\right]\\
\sigma_y &= \frac{K_I}{\sqrt{2r}}\,\mathrm{Re}\left[\frac{1}{\mu_1-\mu_2}\left(\frac{\mu_1}{\sqrt{\cos\theta+\mu_2\sin\theta}}-\frac{\mu_2}{\sqrt{\cos\theta+\mu_1\sin\theta}}\right)\right]\\
\tau_{xy} &= \frac{K_I}{\sqrt{2r}}\,\mathrm{Re}\left[\frac{\mu_1\mu_2}{\mu_1-\mu_2}\left(\frac{1}{\sqrt{\cos\theta+\mu_1\sin\theta}}-\frac{1}{\sqrt{\cos\theta+\mu_2\sin\theta}}\right)\right]
\end{aligned} \qquad (2\text{-}4)$$

where K_I is the Mode-I stress intensity factor (MPa●m$^{1/2}$); r and θ are in polar coordinates, r is the radial distance from the crack tip (m) and θ is the angle between the radius vector and the extension of the crack plane (°). μ_1 and μ_2 are dimensionless coefficients.

After Sih et al. (1965), investigations about the near-tip stresses in anisotropic materials have been undertaken by many researchers (e.g. Bogy 1972, Bowie

and Freese 1972, Barnett and Asaro 1974, Kuo and Bogy 1974, Tupholme 1974, Rathod 1979, Ting and Chou 1981, Hoenig 1982 and Piva and Viola 1988). An alternative complex variables approach considering the non-singular terms proposed by Caroloni et al. (2013) was employed to investigate the Mode I stress field at an inclined crack tips within an orthotropic medium under biaxial load.

Tweed and Das (1972) derived the solution of the Fredholm integral equation (FIE) which was used to express SIFs of a radial crack in an elastic disc. Following Tweed and Das (1975), modification and extension of solutions of FIE in the use of stress analysis have been investigated by some authors including Yarema (1979), Theotokoglou (1990) and Chen (1993). A comprehensive review regarding this topic was provided by Chen (1995) in which some proposals for formulating the FIE in the plane elasticity crack problem were emphasised.

Fracture toughness (FT), the ability of rock resisting fracturing and propagating of existing fracture, can be defined as the critical value of stress intensity factor, when a fracture propagates (Liu 1983 and Ke et al. 2008). Since the early 1970's, laboratory experimental techniques have been investigated to determine the static mode I FT, but mainly subjected to limited rock core-based geometrical configurations including chevron notched short rod (e.g. Barker 1977, 1983, Munz et al. 1980 and Ouchterlony 1988), Brazilian disk-based specimen (e.g. Fowell and Xu 1993, 1994, Xu and Fowell 1994, Iqbal and Mohanty 2006, Cigdem and Levent 2011and Sabri et al. 2016), radial cracked ring and its modification (e.g. Bradley 1971, Amir 1989, Levemt and Cigdem 2012), single edge cracked half disc specimen (e.g. Chong and Kuruppu 1984, Chong et al. 1987, Lim et al. 1994, Molenar et al. 2002, Obara et al. 2007 and Kataoka et al. 2015), and notched round bar (e.g. Swan 1980, Sun and Ouchterlony 1986 and Wang 1990).

Based on the earlier studies, International Society for Rock Mechanics (ISRM) developed three standard methods for the determination of mode I static FT (Ouchterlony 1988, Fowell 1995 and Kunruppu et al. 2014), in which four different core-based specimens were suggested, i.e. semi-circular bend (Figure 2.10), cracked chevron notched Brazilian disc (Figure 2.11), chevron bend specimen (Figure 2.12) and short rod specimen (Figure 2.13). The corresponding equations derived to calculate mode I static fracture toughness K_{IC} (MPa·m$^{1/2}$) are

$$
\begin{aligned}
K_{IC1} &= K_1 \frac{P_{max}\sqrt{\pi a}}{rt} \quad (for\ SCB) \\
K_{IC2} &= K_2 \frac{P_{max}}{B\sqrt{r}} \quad (for\ CCNBD) \\
K_{IC3} &= K_3 \frac{P_{max}}{D^{1.5}} \quad (for\ CB) \\
K_{IC4} &= \frac{24 P_{max}}{D^{1.5}} \quad (for\ SR)
\end{aligned}
\tag{2-5}
$$

where,

$$
\begin{aligned}
K_1 &= -1.297 + 9.516(d/2r) - (0.47 + 16.457 \times (d/2r)\ )\beta \\
&\quad + (1.071 + 34.401(d/2r)\ )\beta^2 \\
K_2 &= u \cdot e^{v \cdot a_1} \\
K_3 &= [1.835 + 7.15 a_0/D + 9.85(a_0/D)^2 \cdot S/D]
\end{aligned}
\tag{2-6}
$$

and $\beta = a/r$, K_1 is the non-dimensional stress intensity factors derived using finite element method while assuming plane-strain condition (Kunruppu et al. 2014). K_2 is the critical stress intensity factor value and geometrical dependent under linear elastic fracture mechanics, and u, v are geometrical constants (Fowell 1995). K_3 also is dimensionless (Ouchterlony 1988). Notations in Equations (2-5) and (2-6) are defined in Figures 2.10 - 2.13.

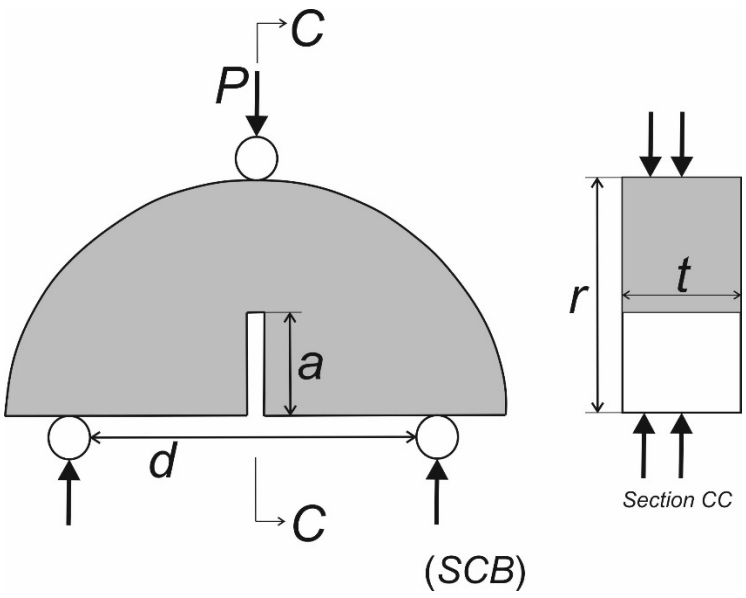

Figure 2.10 Semi-circular bend method (SCB) to determine mode I static fracture roughness: geometrical and loading configurations. (*r* radius of the specimen, *t* thickness, *a* notch length, d distance between support rollers, *P* monotonically increasing load, after and modified from Kunruppu et al. 2014).

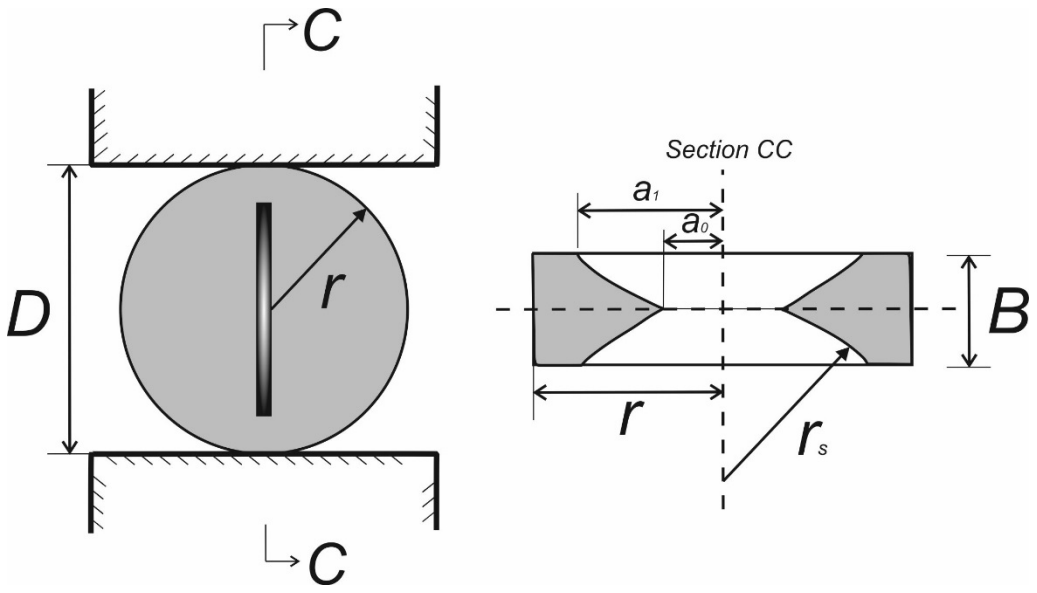

Figure 2.11 Cracked chevron notched Brazilian disc method (CCNBD) to determine mode I static fracture roughness: geometrical and loading configurations. (*r* radius of disc, *B* thickness of disc, *D* diameter of disc, r_s radius of saw, a_0 initial half-length of chevron notch, a_1 final half-length of chevron notch, after and modified from Fowell 1995).

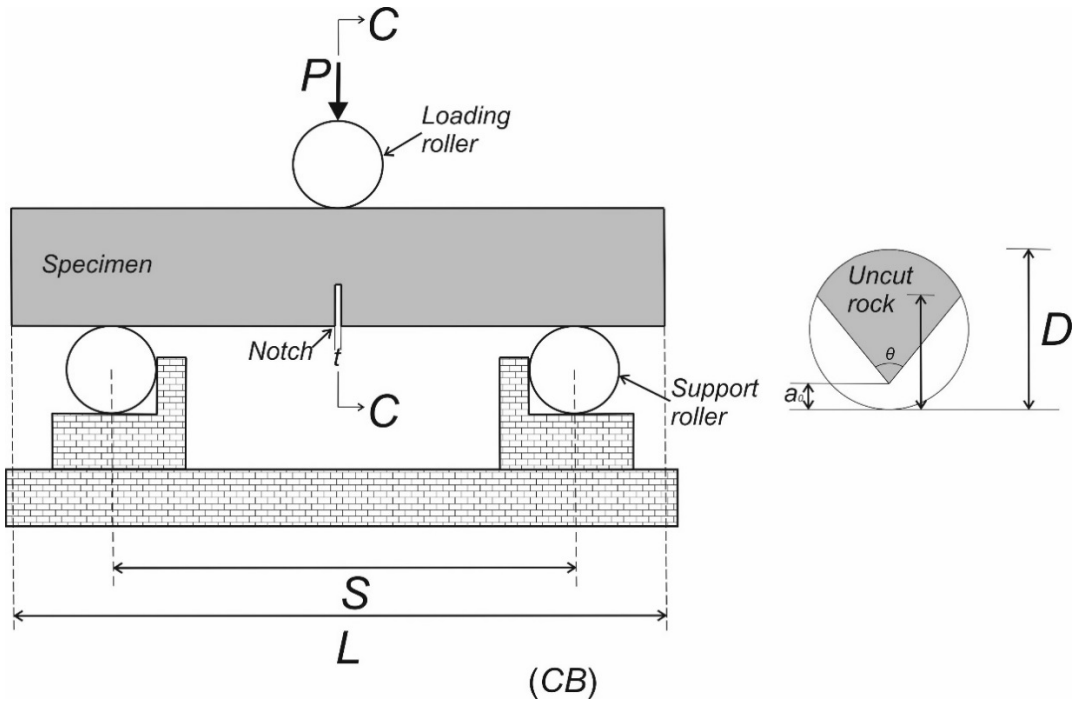

Figure 2.12 Chevron bend specimen method (CB) to determine mode I static fracture roughness: geometrical and loading configurations. (*L* length of chevron bend specimen, *S* distance between support rollers, a_0 distance of chevron tip from specimen surface, *a* length of crack, *D* diameter of chevron bend specimen, *θ* chevron angle, *t* width of notch, after and modified from Ouchterlony 1988).

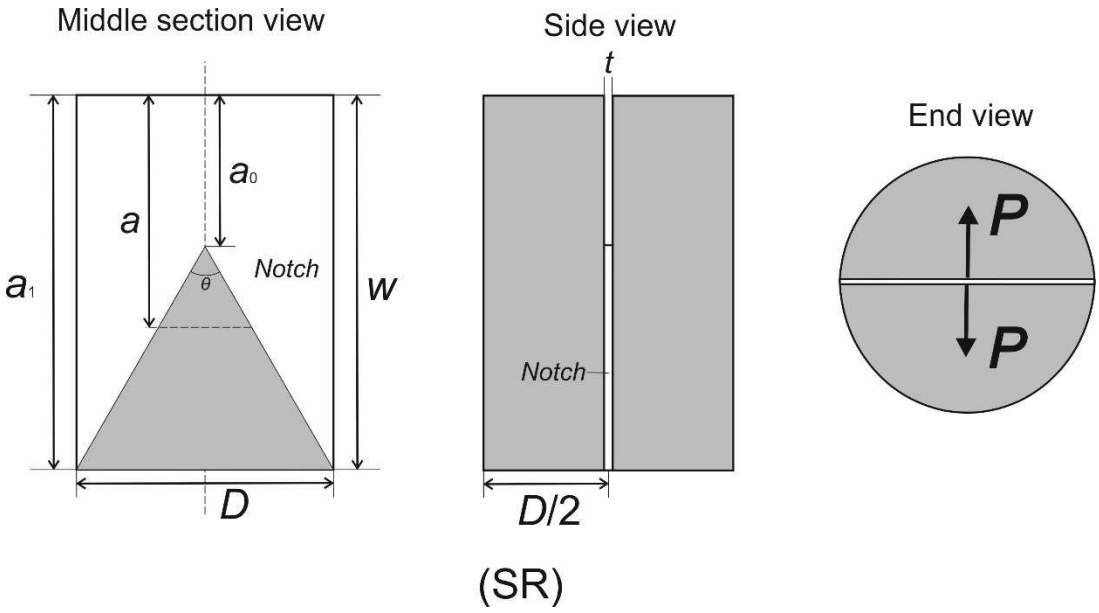

Figure 2.13 Short rod specimen method (SR) to determine mode I static fracture roughness: geometrical and loading configurations. (*D* diameter of short rod specimen, *W* length of specimen, *θ* chevron angle, a_0 chevron tip distance from loaded end, *a* crack length, a_1 maximum depth of chevron flanks, *t* notch width, *P* monotonically increasing load, after and modified from Ouchterlony 1988).

Note that determination of the geometrical parameters for the specimens is a key factor in obtaining accurate fracture toughness. Numerical modelling approaches including boundary element method and finite element method have been used to calibrate stress intensity factor (e.g. Chen 1990, Xu and Fowell 1994, Wang et al. 2003 and Dai et al. 2015).

Analytical and experimental solutions in the determination of mode I fracture toughness are often limited to regular geometrical specimens and simple boundary conditions, and for irregular and complicated cases numerical solutions are normally needed. Since 1970s, numerical solutions have been used to investigate Mode I fracture intensity but with a focus on fractures in materials including composite and adhesive joints (Muraakami 1976). Until 1986, a pioneer work by Thiercelin and Roegiers (1986) was reported in which modelling technique was firstly employed to investigate fracture toughness problem in rock. In their study, the modified ring (MR) test was proposed to determine Mode-I FT for soft and heterogeneous rocks and displacement discontinuity modelling was used to compute Mode I stress intensity factor. It was found that toughness was independent of the flat loading surface length. This geometrical effects of MR on toughness were then investigated using

finite element method (FEM) (e.g. Thiercelin 1987, Thiercelin et al. 1986, Thiercelin 1989, Fischer et al. 1996 and Levent and Cigdem 2012)

Distinct element method (DEM) pioneered by Cundall (1971) was used in the study of Mode-I stress intensity factor (Potyondy and Cundall 2004). In the numerical model, rock is represented by a dense packing of spherical particles that are bonded together at the contact points, and the physical mechanisms for failure of contact points under loading are illustrated by Figure 2.14. In the work reported by Potyondy and Cundall (2004), a cubic packing of unit-thickness (t =1) disks of radius R was bonded together and subjected to an extension strain. Program PFC2D was used to produce patterns of bonded-particles which are similar to the fracture initiation and propagation in rocks. The Mode-I FT K_{IC} was given by equation:

$$K_{IC} = \sigma_t / \sqrt{\pi R} \tag{2-7}$$

where σ_t is the contact-bond tensile strength (in force units, MPa), R is disk radius (m).

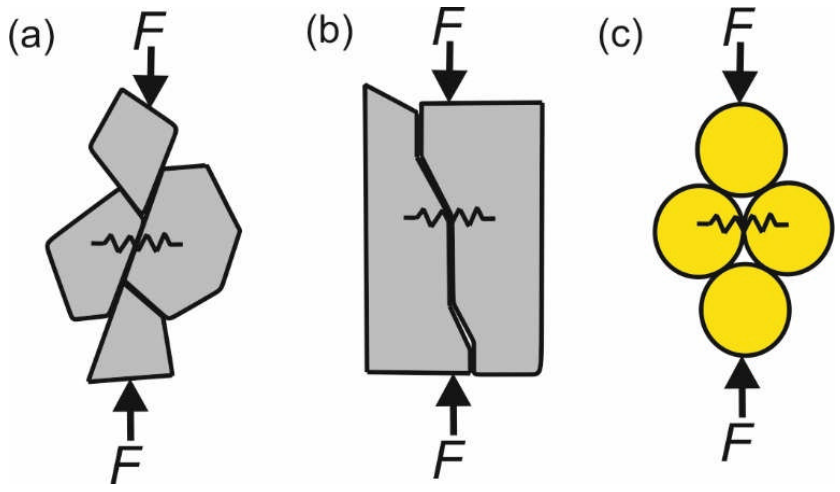

Figure 2.14 a and **b** Physical models for compression induced tensile fracture, and **c** Idealization of the bonded circular particles in PFC program. After Potyondy and Cundall (2004).

Moon et al. (2007) developed a more general approach to investigate rock fracture mechanics problems using DEM. Two approaches, energy balance method and collocation method, were employed to measure Mode-I FT. The results of both methods agree well with Yarema formula (Yarema and Krestin 1966).

2.3.3 Mode-II stress distribution near fracture tips

In contrast to Mode-I stress, Mode-II stress analysis is scarce and still no standards are proposed to measure mode-II fracture toughness. Even though there have been many laboratory test methods to measure Mode-II FT, and the core-based specimens used for measuring Mode-I FT also are employed but in those tests inclined cracks were produced relative to loading direction (e.g. Ayatollahi and Aliha 2006, Takahiro et al. 2014 and Masoud and Sistaninia 2015). Semi-circular bend (SCB) and Brazilian disc (BD) specimens were employed by Masoud and Sistaninia (2015) to measure the Mode-II FT. Compressive loading *P* was employed on these samples containing appropriate inclined cracks. Four different sizes of SCB samples (R=30 mm, 50 mm 70 mm and 100 mm respectively) were manufactured to investigate the scale effect on the Mode-II FT. It was found that the average mode-II fracture FT values for these four different-size samples were 0.53, 0.73, 0.77, and 0.90 MPa●m$^{1/2}$ which indicated that Mode-II fracture significantly depended on the specimen size. A saturation value exists (1.2 MPa●m $^{1/2}$) when sample size increased to 200 mm in diameter. Rao et al. (2003) proposed a shear-box test approach to measure Mode-II FT in which cubic granite, marble and sandstone samples containing two different notches (single and double) were used. Figures 2.15a, b schematically show the two samples with two kinds of notches under loading.

The acoustic emission technique was employed to detect the fracture initiation and energy release. Mode-II FT for the single-width sample and double-width sample can be calculated by

$$K_{IIs} = \frac{Q_e}{B\sqrt{W}} F_s\left(\frac{a}{W}\right)$$
$$K_{IId} = \frac{Q_e}{B\sqrt{W}} \sqrt{\pi a} F_d\left(\frac{2a}{W}\right) \quad (2\text{-}8)$$

where W and B are the sample width and thickness, respectively. Q_e is the effective shear load, a is the notch width. $F_s\left(\frac{a}{W}\right)$ and $F_d\left(\frac{2a}{W}\right)$ are sample shape factors that can be calculated by

$$F_s\left(\frac{a}{W}\right) = \frac{2.138 - 5.2(a/W) + 6.674(a/W)^2 - 3.331(a/W)^3}{\sqrt{1 - a/W}} \quad (2\text{-}9)$$

$$F_\sigma\left(\frac{2a}{W}\right) = 1.780 + 3.095\left(\frac{2a}{W}\right) - 10.559\left(\frac{2a}{W}\right) + 8.167\left(\frac{2a}{W}\right)^3 \qquad (2\text{-}10)$$

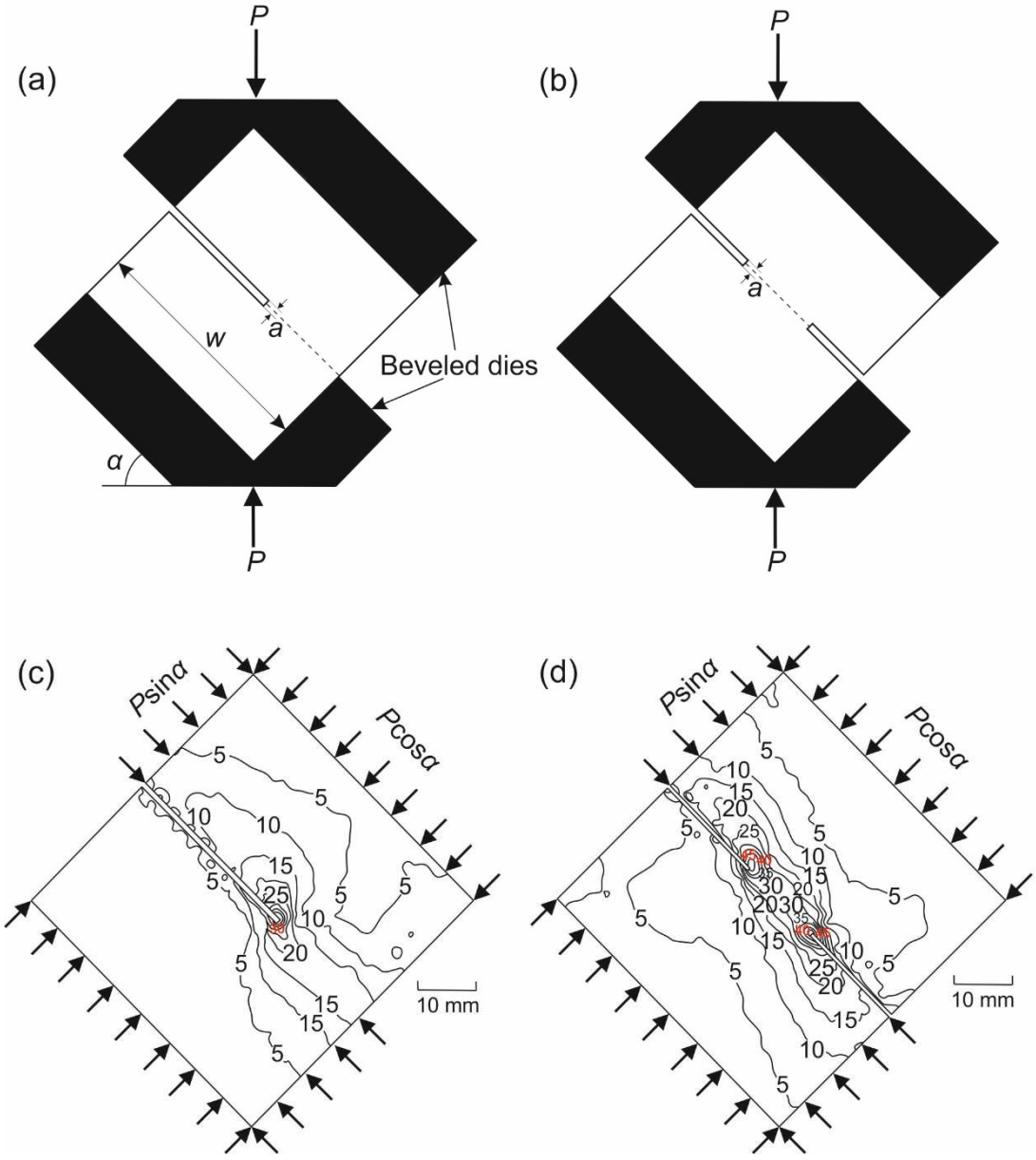

Figure 2.15 State of load of single-notched sample (**a**) and double-notched sample (**b**). Shear stress (MPa) trajectories from finite element analysis of a single-notched sample (**c**) and a double-notched sample (**d**). Modified from Rao et al. (2006).

Stress distributions of single-width and double-width samples under shearing were investigated using finite element method. Figures 2.15c, d show two examples of stress trajectories. It can be seen that shear stress was smaller in upper and lower areas for both samples and reached the peak strengths at the notch tips. Peak shear stresses around tips of the double notches (45 MPa) were larger than that around the tip of single notch (30 MPa).

In addition to the laboratory experiments, there have been several analytical solutions for assessing the Mode-II failure including the maximum tangential

stress (MTS) criterion (Erdogan and Sih 1963), the maximum energy release rate criteria (Hussain et al. 1974) and the minimum strain energy density criterion (Sih 1973).

Relations between Mode-I and Mode-II fracture toughness as well as mechanical properties of various rocks have been investigated using experimental and analytical solutions. Previous study results showed that the ratio of Mode-II FT and Mode-I FT (K_{II}/K_I) normally lies between 0.45 and 2.2 (Ayatollahi and Aliha 2006). Lim et al. (1994) reviewed the experimental and theoretical K_{II}/K_I, tensile strength and Poisson's ratio of various rock types. It was found that no clear relation can be found between K_{II}/K_I ratio and Poisson's ratio from the data. Empirical relation between Mode-I FT and tensile strength of rock also have been examined by many researchers. Zhang (2002) summarized previous studies on this topic, and the relationship is replotted in Figure 2.16, from which liner relationship can be obtained.

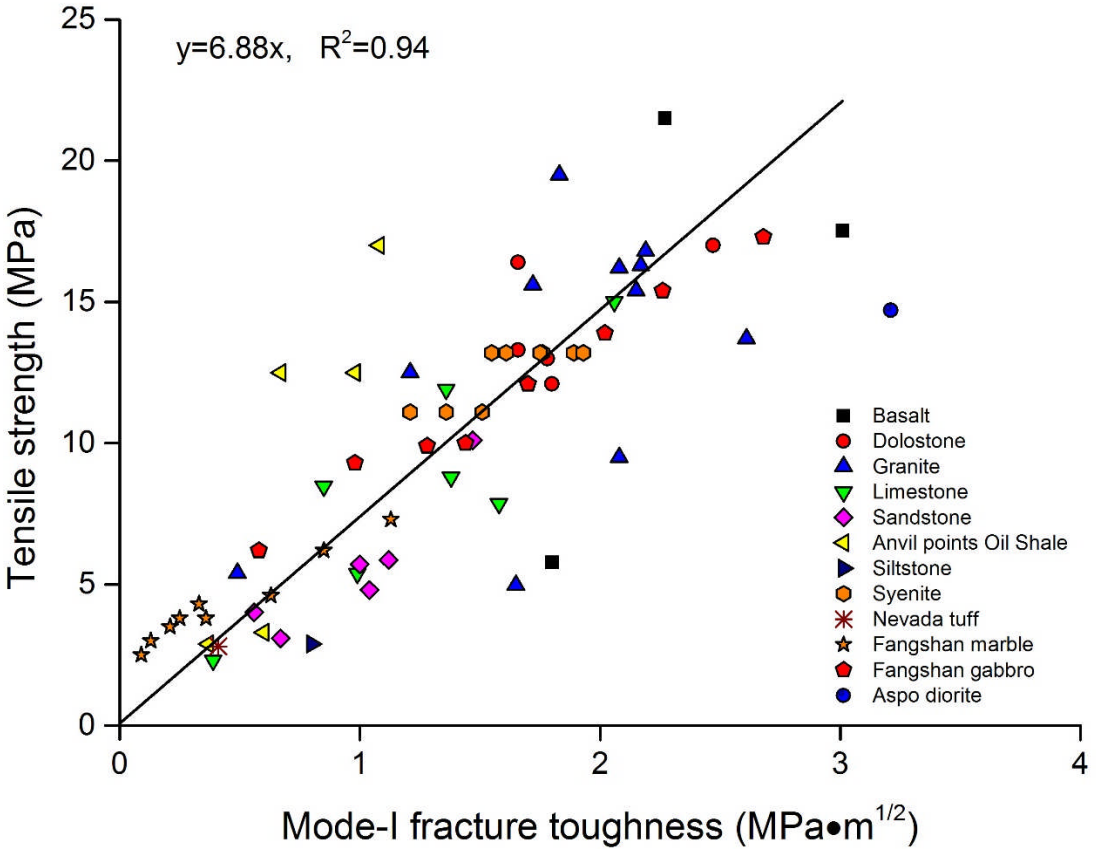

Figure 2.16 Empirical relationship between Mode-I FT and tensile strength of various rocks. Modified from Zhang (2002). Raw date from Whittaker et al. (1992), Zhang et al. (1998), Khan and Al-Shayea (2000), Yu (2001) and Norlund et al. (1999).

2.3.4 Summary

Stresses around fracture tips (Figure 2.8) control the initiation and propagation of fractures within rock masses under loading (Griffith, 1921), therefore govern the incipiency of geological discontinuities. Mode I and Mode II stresses (Figures 2.9a, b) proposed by Irwin (1957) in the vicinity of fractures and their quantitative descriptions were discussed earlier in this section. Before leaving this topic, a brief summary of what learned from the discussion are as follows:

(1) Stresses around fracture tips were grouped into three categories including Mode I (opening), Mode II (shearing) and Mode III (tearing) (see Figure 2.9). Stress intensity factor was employed to describe these three stresses which can be quantified analytically, experimentally and numerically. Fracture toughness, the ability of rock resisting fracturing, was defined as the critical value of stress intensity factor when a fracture propagates.

(2) There have been several standards proposed by ISRM to quantify Mode I static fracture toughness experimentally. Four-core based samples were used in the suggested methods, as shown in Figures 2.10-2.13. Fracture toughness K_{IC} can be calculated by Eqs. 2-5 and 2-6. Semi-circular bend (SCB) sample and crack chevron notched Brazilian disc (CCNBD) are suggested for the quantification of Mode I fracture toughness due to easier sample preparation.

(3) Quantification of the Mode II fracture toughness however is scare and still no standards are proposed. In the limited available publications about this topic, core-based samples also were employed with inclined pre-existing notches (see one example shown Figure 2.15).

(4) Numerical analysis plays an important role in the quantification of the Mode I and Mode II fracture toughness of irregular samples, but the calibration of established numerical models is vital for a reliable result.

(5) Ratio of Mode II and Mode I fracture toughness normally lies between 0.45 and 2.2, depending on lithology.

(6) An Empirical linear relationship between Mode I fracture toughness and tensile strength of rocks was established, as shown in Figure 2.16. The relation is important in understating the mechanical failure of rock due to stress concentration around fracture tips.

In section 2.4 and 2.5, we discuss engineering implications of rock joint persistence including its mechanical properties and influence on rock block size and mass stability.

2.4 Mechanical properties of incipient rock discontinuities

Tensile or shear failure of incipient fractures is often the ‘final straw’ leading to instability of rock masses. Mechanical properties including tensile (Mode I opening) and shear (Mode II shearing) strength of incipient rock discontinuities that significantly depend on the incipiency of discontinuities are discussed in this section.

2.4.1 Tensile strength of incipient rock discontinuities

In exposures and tunnel roofs, many overhanging and threatening rock blocks or slabs only remain in place because of the strength of incipient discontinuities (see Figure 2.17). Despite its obvious importance, it has to be acknowledged that degree of incipiency is extremely difficult to assess, predict or quantify which is probably why it has been largely ignored in the literature. Nevertheless there have been some attempts to define and quantify its importance. For example, Cravero and Iabichino (2004) discussed the flexural failure of a gneissic slab from a quarry face, which had been apparently stable for at least 15 years prior to failing. It was concluded that instability involved tensile failure of a single slab initiated by water pressure or seismic loading. Paronuzzi and Serafini (2009) assessed the stress state of a collapsed overhanging rock slab previously connected to the rock mass by an incipient joint (see Figure 2.18). The area of rock bridge revealed after collapse was 2.82 m^2 and a value of tensile strength for this area σ_t = 5.19 MPa was derived from 3D numerical analysis.

Figure 2.17 Slope with daylighting rock slabs threatening highway in central Taiwan. The incipient nature of the discontinuities contributes tensile and shear strength and allows temporary stability.

Although the importance of incipiency of discontinuities is well understood, and measurement of tensile strength of incipient rock discontinuities is the first step towards this topic. To date, however, there have been no publications available to investigate the tensile strength of incipient rock discontinuities. The lack of investigations into the measurement of tensile strength of incipient rock discontinuities probably can be attributed to two reasons: (1) Insufficient understanding of the engineering issues arising from the conservative assumption of 100% persistence or over-simplistic of discontinuity persistence. (2) Lack of ideas to reflect discontinuity persistence (incipiency) in a practical way.

Figure 2.18 General view of a collapsed overhanging limestone slab located at northern part of Cellina Valley gorge on January 26th, 1999. A rock bridge (red-hatched area) was exposed after failure. The average tensile strength of this rock bridge was calculated as 5.19 MPa on back-analysis by Paronuzzi and Serafini (2009).

2.4.2 Shear strength of incipient rock discontinuities

A large amount of investigations have been undertaken to measure shear strength of discontinuities, but mostly focusing on mechanical (open) discontinuities which have zero true cohesion. Generally, mechanical rock discontinuities can be regarded as a special state or simplest case of incipient discontinuities when fully developed. The work reported by Lajtai (1969) is a pioneer in the investigation of shear properties of a single incipient rock joint (termed as plane of weakness in his study) under direct shear loading. It was shown that shear strength of incipient rock joints was determined by three components including fundamental shear strength (true cohesion from rock bridges), internal friction in solid bridges (after rock bridges are mobilized) and friction from the persistent joint along the separated parts of the incipient joint plane. Relative shear strength contributions from these three factors were experimentally investigated. Three types of plaster samples were moulded (Dimension: 152 mm × 76 mm × 76 mm). For the type 1 samples, joint persistence was 100% to examine the pure joint friction. In the type 2 samples, joint friction from the persistent sections was eliminated completely by leaving the joints open with approximately 0.2 mm width notches. The type 3 shear block samples contained tight interlocking joints separated by bridges. In type

1 samples, joint persistence *K* were 100%; in type 2 and type 3 sample preparation processes, joint persistence *K* were set to be a constant value of 50%. The test results were reproduced in Figure 2.19 and the diagrams of tested samples were also included. Experimental data have been fitted to the analytical derived curves (for procedures see section 2 of Lajtai (1969)) and four zones were defined based on the available data, i.e. zone of tensile normal stress (area left to the $\sigma_n = 0$ axis when normal stress below zero), zone of primary strength (area immediately to the right of the $\sigma_n = 0$ axis), transitional zone from primary to ultimate strength at intermediate values of normal stresses and zone of ultimate strength at higher values of normal stresses. It was also concluded that the minimum resistance (R_{min}) to shear along incipient rock joint is a function of tensile strength σ_t of rock bridges in the form of

$$R_{min} = (1-K)A[\sigma_t(\sigma_t - \frac{\sigma_n}{1-K}) \ ]^{\frac{1}{2}} \qquad (2\text{-}11)$$

where *K* is joint persistence, *A* is longitudinal cross-sectional area of shear sample (m^2).

The existence of intact rock bridges significantly increased the shear strength of single incipient rock discontinuity as they produced a strength reserve and need to be mobilised firstly prior to failure can occur and sliding along the incipient joint plane (Jennings 1970 and Stimpson 1978).

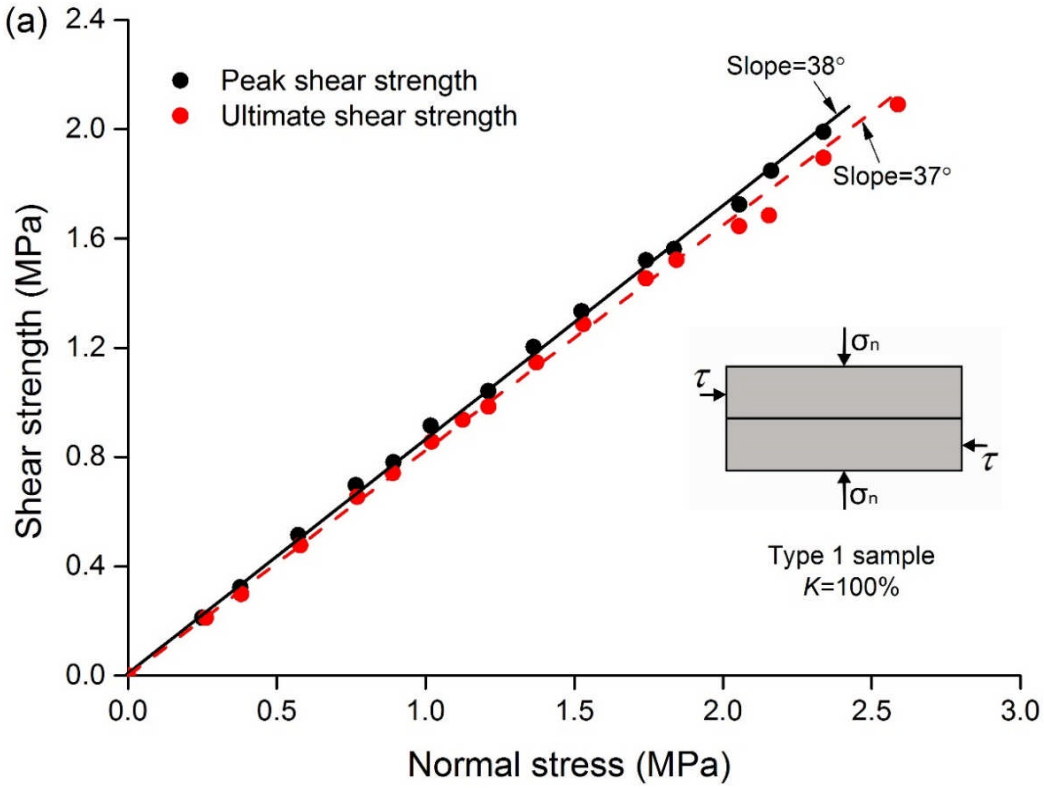
(a)
Peak shear strength
Ultimate shear strength
Slope=38°
Slope=37°
σn
τ
τ
σn
Type 1 sample
K=100%
Shear strength (MPa)
Normal stress (MPa)
0.0
0.4
0.8
1.2
1.6
2.0
2.4
0.0
0.5
1.0
1.5
2.0
2.5
3.0

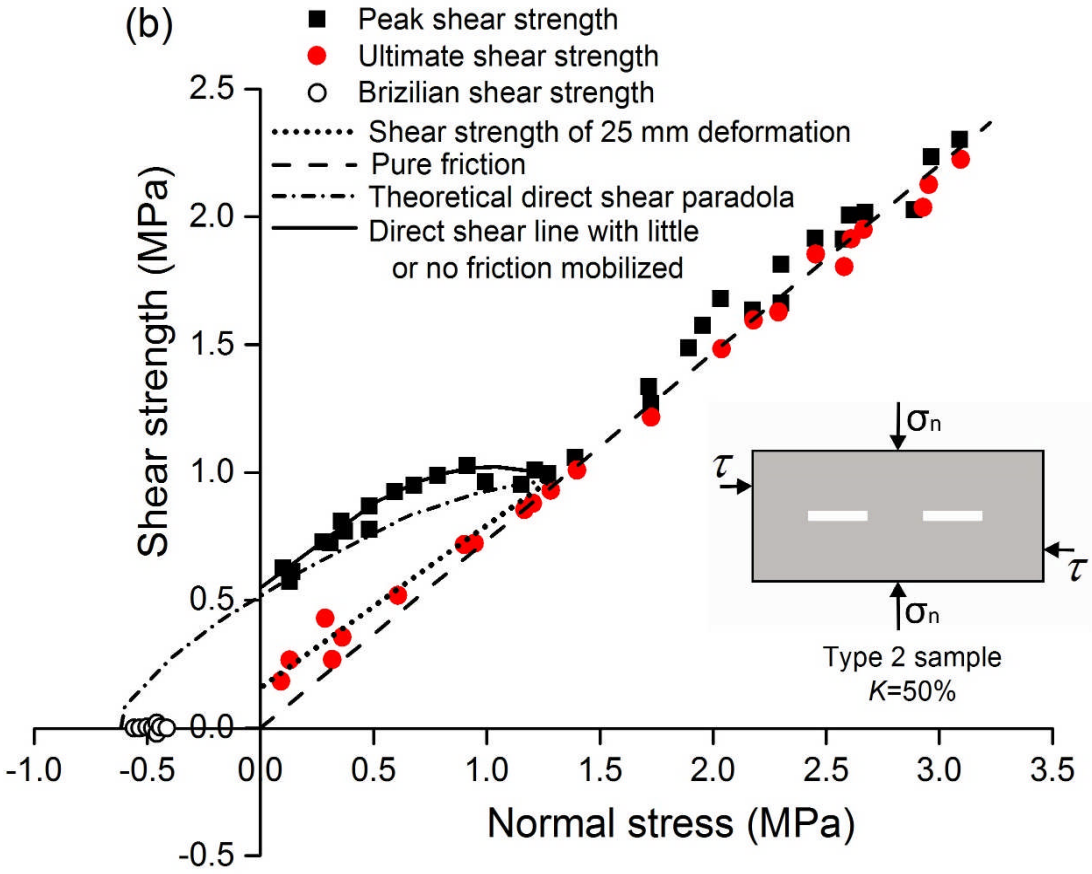
(b)
Peak shear strength
Ultimate shear strength
Brizilian shear strength
Shear strength of 25 mm deformation
Pure friction
Theoretical direct shear paradola
Direct shear line with little
or no friction mobilized
σn
τ
τ
σn
Type 2 sample
K=50%
Shear strength (MPa)
Normal stress (MPa)
-0.5
0.0
0.5
1.0
1.5
2.0
2.5
-1.0
-0.5
0.0
0.5
1.0
1.5
2.0
2.5
3.0
3.5

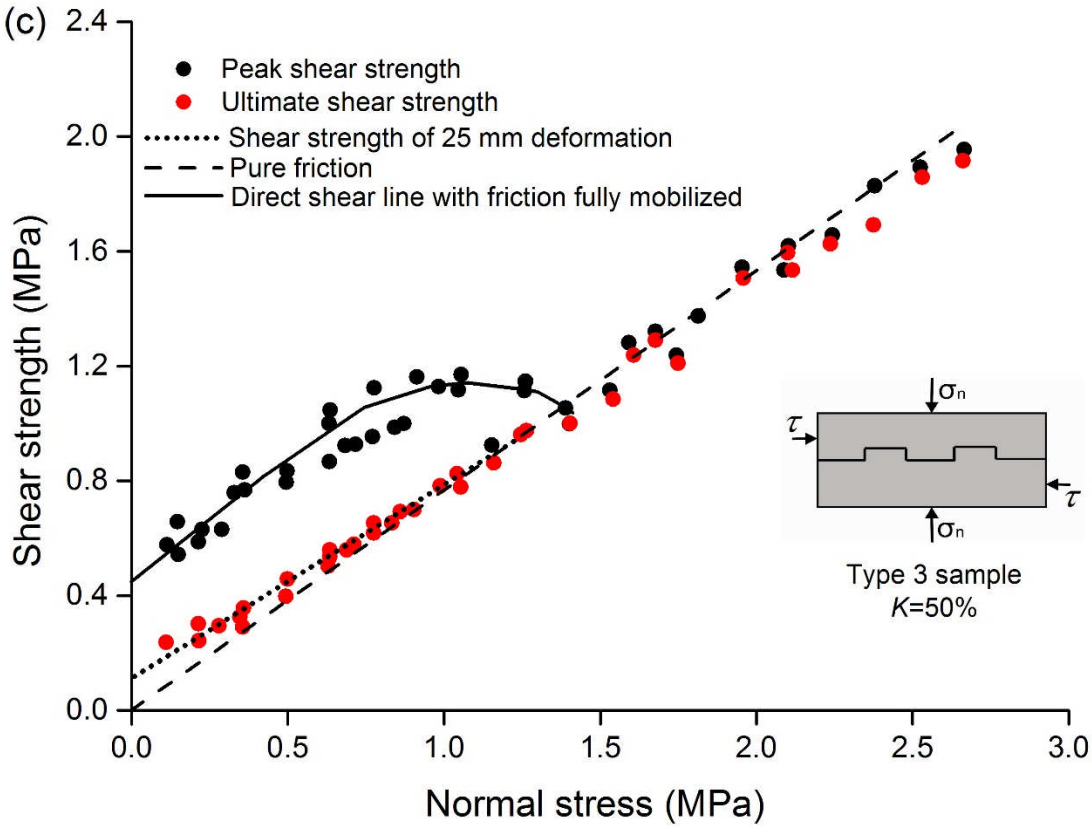

Figure 2.19 **a** Pure frictional resistance from type 1 sample containing a fully persistent joint (K=100%), Notice that friction angle for ultimate shear strength was slightly lower than that of peak shear strength; Experimental results from direct tension shear tests on type 2 sample containing incipient joint (K=50%) (**b**) and type 3 sample containing tight interlocking joints (**c**) .

It is however rare to see the shear testing on natural incipient rock joint as it is near impossible to secure groups of natural rock samples containing incipient rock discontinuities of identical strength characteristics. An example of a natural rock bridge under direct shear loading reported by Hencher (1984) showed the strength contribution from natural rock bridge (light area in Figure 2.20). It was found that the cohesive contribution from the light area was 750 kPa, measured during the direct shear testing.

Based on the Mohr-Coulomb (MC) failure criterion, an equivalent shear strength calculation method of unfilled and unweathered incipient rock joints was proposed in which strength contributions from rock bridges and persistent joint areas were linearly combined (Lajtai 1969 and Harrison and Hudson 2000). It can be expressed by the following equation:

$$\tau = c_i + \sigma \tan \varphi_i = [K \cdot c_p + (1-K) \cdot c_B] + \sigma [K \cdot \tan \varphi_p + (1-K) \tan \varphi_B] \quad (2\text{-}12)$$

where τ and σ are shear strength of incipient rock joints and given normal stress, c_i and φ_i are the equivalent cohesion and internal friction angle of incipient rock joints, c_p and φ_p are the cohesion and internal friction angle of persistent joint, c_B and φ_B are the cohesion and internal friction angle of intact rock bridges. *K* is the joint persistence.

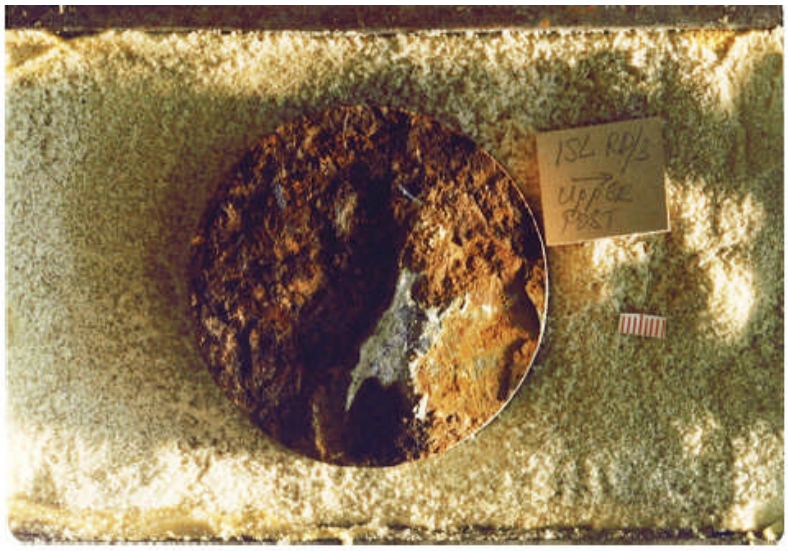

Figure 2.20 Intact rock bridge (light area) revealed after direct shearing. Shear strength contribution from this bridge area was found to be 750 kPa. After Hencher (1984)

Lajtai (1969) commented that the equation (2-12) tends to overestimate the shear strength of incipient rock discontinuity as it assumes that rock bridges and friction of persistent joint areas are mobilized simultaneously, that is at the same deformation. In addition, MC criterion is only applicable to the smooth joint surface or rough joint under lower normal stress level, thus equation (2-12) has limited applications. For rough joint plane under higher level normal stress, shear strength is a bi-linear function of the given normal stress (Patton 1966) because of the shearing failure of asperities and suppression of any expansion (Barton, 1973). Barton-Bandis (BB) failure criterion was suggested to describe this non-linear behaviour by the following equation (Barton, 1976)

$$\tau = \sigma \tan [JRC \log_{10}(\frac{JCS}{\sigma}) + \varphi_b] \quad (2\text{-}13)$$

where *JRC* is the joint roughness coefficient, *JCS* is the joint wall compressive strength, and φ_b is the basic friction angle of a smooth and planar discontinuity.

An extension of equivalent shear strength calculation method based on the BB criterion under biaxial stress state was investigated by Halakatevakis and Sofianos (2010). In this mathematical model, stress acting on rock specimen containing a single joint was divided into shear and normal stress components on the joint plane. Any increase in normal stress due to the dilation of joint during shearing was assumed to be negligible. The extended equivalent shear strength of incipient joints can be expressed by

$$\tau = [\ (\sigma_1 + \sigma_3) + (\sigma_1 - \sigma_3)\cos 2\alpha] \cdot \tan[JRC \cdot \log\ (\frac{2JCS}{(\sigma_1 + \sigma_3) + (\sigma_1 - \sigma_3)\cos 2\alpha}) + \varphi] \quad (2\text{-}14)$$

where σ_1 and σ_3 are major and minor principle stresses, α is the joint angle relative to normal loading axis.

Zhang et al. (2006) numerically investigated the shear strength of incipient rock joints. Shear strength of planar incipient joints within rock were measured under direct shear test. Figure 2.21 reproduced the relationship between shear force and displacement of incipient rock joints with different geometrical parameters. A numerical rock sample containing a horizontal incipient joint was also included.

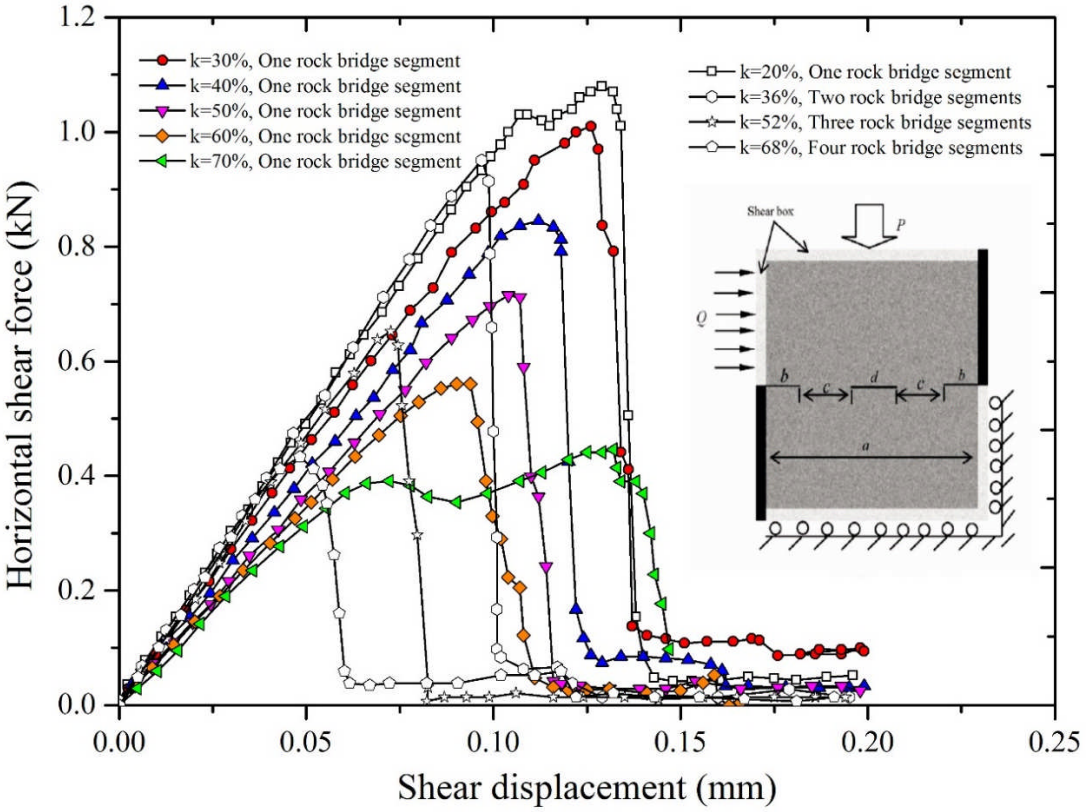

Figure 2.21 Relationship between shear displacement and horizontal shear force for various numerical models containing incipient rock joint with different geometrical parameters. Adapted from Zhang et al. (2006).

It can be seen from Figure 2.21 that shear strength rose to a clear peak and then reduced suddenly to a very low residual strength. This brittle failure phenomenon can be related to the failure of intact rock bridges and the ideally generated smooth joint in the numerical modelling. That is to say, unlike the rock bridge segments under direct shear, the saw-cut joint surfaces have relatively low friction. Figure 2.22 presents the relation between peak shear load and persistence based on the raw data from Zhang (2006). It is found that shear strength of incipient rock joints increased linearly with the persistence and independent of number of notched joints.

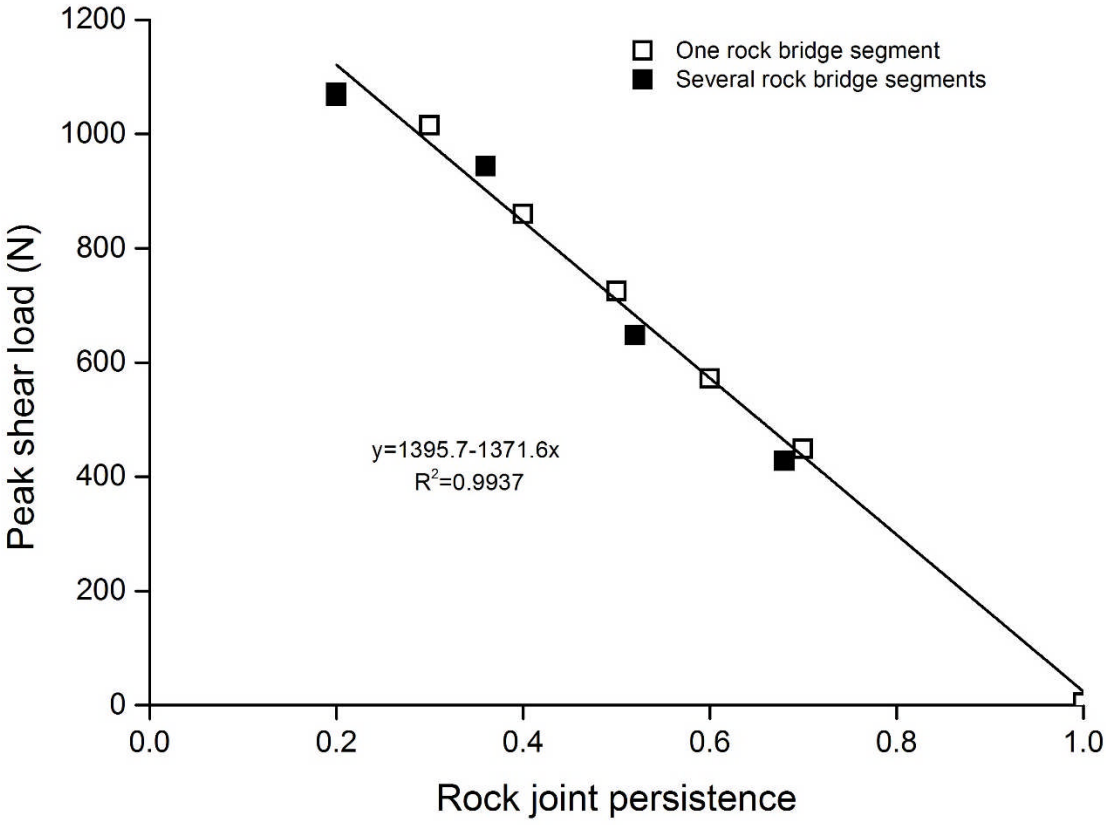

Figure 2.22 Linear relation between rock joint persistence (areal persistence) and peak shear load. Raw data of numerical studies from Zhang (2006).

The paper reported by Ghazvinian et al. (2007) was an example of the effects of persistence and rock bridge geometries on the shear strength of incipient rock joints in the laboratory. Forty five three dimensional incipient rock joints within cubic rock-like specimens (dimension: 150 mm × 150 mm × 150 mm) were prepared and tested under direct shear strength considering three different normal stresses (333 kPa, 555 kPa and 777 kPa). Rock bridge areas vared from 4500 mm^2, 6300 mm^2 and 9000 mm^2, distributed separately within specimens in five different geometries (see Table 2.1). Main testing results are replotted in Figure 2.23.

Table 2.1 Geometrical specifications of modelled rock bridges. After Ghazvinian et al. (2007)

Rock bridge area (mm^2)	**Joint persistence**	**Rock bridge dimensions (a X b) (mm X mm)**	**Rock bridge geometries**
4500	0.4	G1 (300 x1500), G2(500 x 900), G3(600 x 750), G4(1000 x 450), G5(1500 x 300)	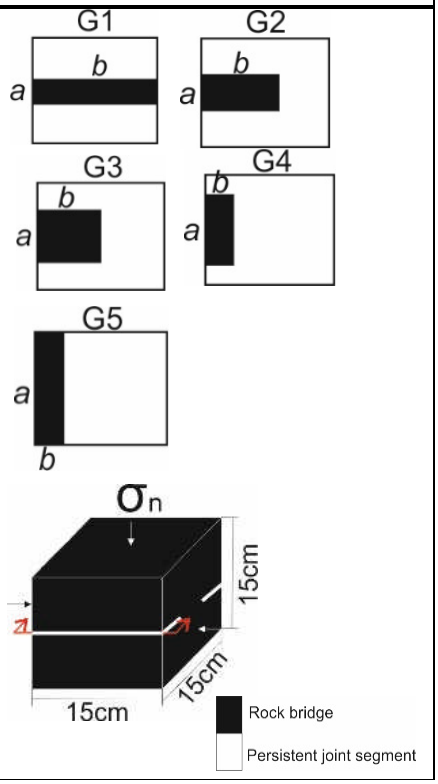
6300	0.28	G1 (420 x 1500), G2(700 x 900), G3(8.40 x 750), G4(1400 x 450), G5(1500 x 420)	
9000	0.2	G1 (300 x 1500), G2(500 x 900), G3(600 x 750), G4(1000 x 450), G5(1500 x 300)	

It was found that peak shear strength varied slightly with five different rock bridge geometries under the same discontinuity persistence. Incipient rock joints with G5 rock bridge geometries gave highest shear strength values for all the situations, while shear strength of incipient rock joints containing G1 rock bridges were the smallest. The different stress distributions around joint tips (because of the different rock bridge geometries) may result in this phenomenon, however more in-depth investigation towards this phenomenon is worthy to be emphasised.

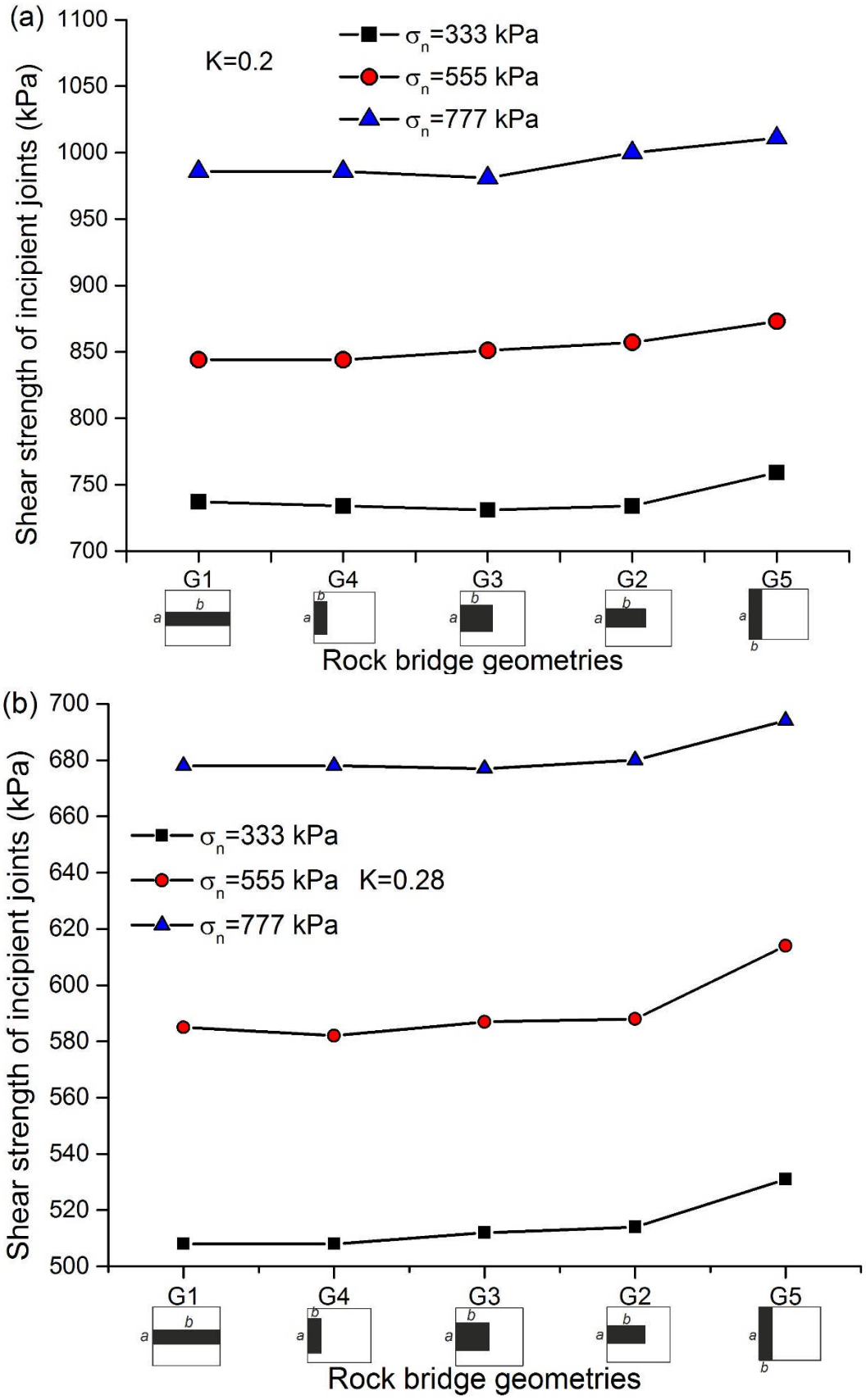
(a)
K=0.2
σn=333 kPa
σn=555 kPa
σn=777 kPa
Shear strength of incipient joints (kPa)
1100
1050
1000
950
900
850
800
750
700
G1
G4
G3
G2
G5
Rock bridge geometries
(b)
K=0.28
σn=333 kPa
σn=555 kPa
σn=777 kPa
Shear strength of incipient joints (kPa)
700
680
660
640
620
600
580
560
540
520
500
G1
G4
G3
G2
G5
Rock bridge geometries

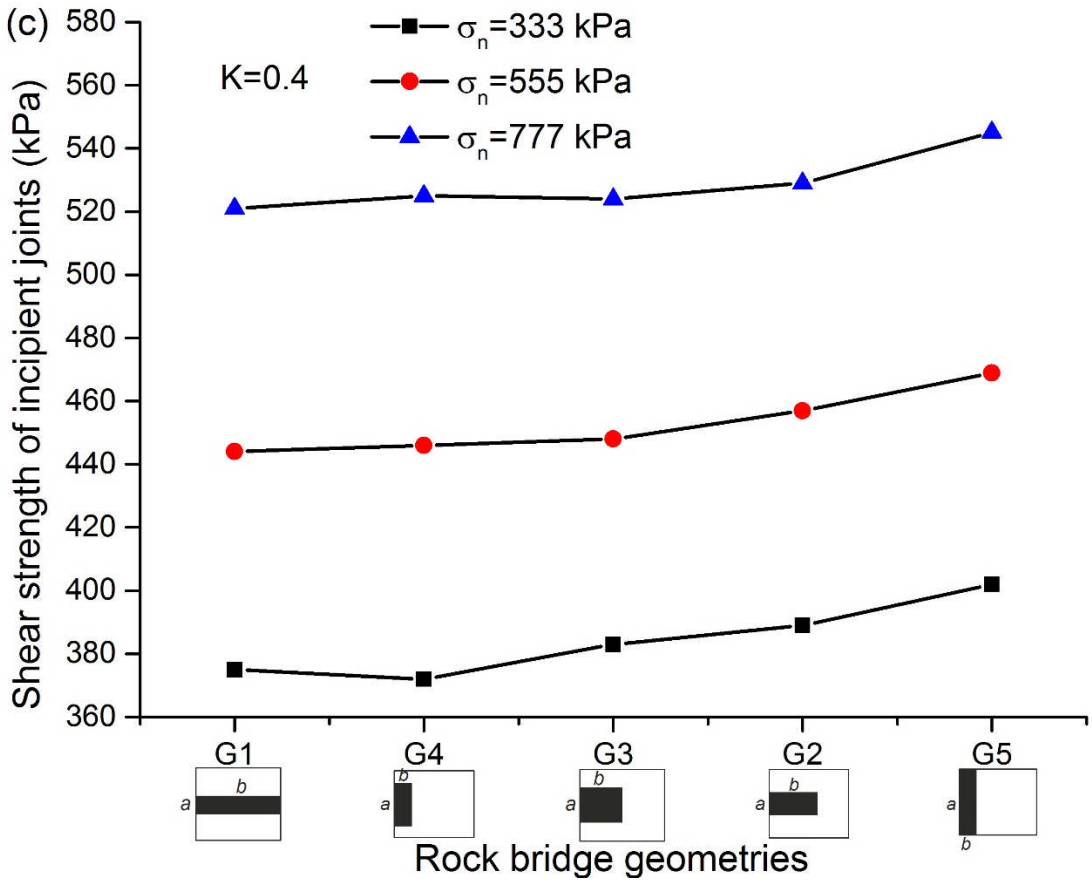

Figure 2.23 Shear strength of incipient rock joints against rock bridge geometries. **a** Joint persistence *K* is 0.2; **b** Joint persistence *K* is 0.28 and **c** Joint persistence *K* is 0.4. Replotted from Ghazvinian (2007).

Particle flow code 2D (PFC 2D) was adopted to simulate the shear behaviour of incipient rock joints within rock-like materials (Ghazvinian et al. 2012) but the main findings are essentially similar to those by Zhang et al. (2006) and Ghazvinian et al. (2007).

Hencher and Richards (2015) extensively reviewed the shearing test of rock discontinuities at laboratory scale and proposed an approach to assessing shear strength of rock discontinuity at project scale in the light of laboratory and analytical results. They pointed out that shear strength of incipient rock discontinuities is contributed to factors including local rock bridges, roughness at a relatively large-scale in the field and smaller asperity at a scale of core samples in the laboratory, but essentially agree with the findings by Lajtai (1969).

2.5 Implications of discontinuity persistence for rock mass strength and stability

Incipient rock discontinuities often have a controlling influence on rock mass strength and stability in rock engineering projects as well as on other properties such as deformability and hydraulic conductivity. The effects of incipient joints in various contexts on rock mass strength and stability are explored in the following sections

2.5.1 Block size and volume for rock masses with incipient discontinuities

Intersection of rock discontinuities within a rock mass leads to individual rock blocks (Maukdib 1994). Block size and volume are among the important factors in rock mass behaviour and classification (Barton 1990 and Goodman 1993). Assessing rock block size and volume has long been appreciated by lots of methods which can be roughly categorized into three groups such as index evaluation (e.g. ISRM 1978 and Sen et al. 1992), image-based measurement (e.g. Panek 1981 and Maerz 1996), and model dissection (e.g. Goodman and Shi 1985).

Generally rock block size and volume are determined by discontinuity geometrical parameters such as discontinuity spacing, discontinuity orientation, number of discontinuity sets and discontinuity persistence. Considering the scope of this review, publications accounting for discontinuity persistence were reviewed and the influence of discontinuity persistence to the rock block size and volume are discussed in this section.

For the rock masses containing several fully-persistent rock joint sets, the rock block volume within a representative rock mass can be empirically calculated by (Cai et al. 2004 and Palmstrom 2005)

$$V_p = \frac{S_1 \cdot S_2 \cdot S_3 \cdots S_i}{\sin\alpha_1 \cdot \sin\alpha_2 \cdot \sin\alpha_3 \cdots \sin\alpha_i} \tag{2-15}$$

where S_i and α_i are joint spacing and angle of inclination for each joint set, respectively.

Rock bridges along incipient rock joint planes lead to irregular rock block shapes and larger rock block size. In this case an equivalent spacing S_i' for incipient rock joint is defined as (Cai and Horri 1992)

$$S_i' = \frac{S_i}{\sqrt[3]{K_i}} \tag{2-16}$$

where K_i is joint persistence for each joint set.

Thus the equivalent rock block volume can be expressed by the following equation:

$$V_p^{'} = \frac{S_1 \cdot S_2 \cdot S_3 \cdots S_i}{\sqrt[3]{K_1 \cdot K_2 \cdot K_3 \cdots K_i} \times \sin\alpha_1 \cdot \sin\alpha_2 \cdot \sin\alpha_3 \cdots \sin\alpha_i} \qquad (2\text{-}17)$$

Probability analysis techniques are adopted to investigate rock block size and volume distributions considering every incipient rock discontinuity within rock masses rather than solely emphasis on representative ones by the aforementioned analytical solution.

Wang et al. (1991) presented an algorithm to predict block size distribution based on the real data collected from quarry. Although the difference between two block size distributions determined from incipient discontinuities as well as fully persistent discontinuities was presented, the algorithm they provided failed to consider the influence of incipiency on block size. Intersection probabilities of incipient discontinuities, related to occurrence probabilities of rock blocks that comprise the rock mass, was investigated by Mauldon (1996). Analytical solution was found concerning the probabilities of intersection of incipient discontinuities within a jointed rock mass. This solution has potential to be implemented into numerical modelling.

Wang et al. (2003) proposed another new algorithm accounting for persistence (linear extent) to predict size distribution of ore blocks after blasting in block caving. A synthetic database of field discontinuities measured in shafts and other underground engineering structures was established by using Monte Carlo Simulation. This algorithm was able to pick discontinuities from the database to form polyhedral blocks. It was found that ore fragmentation varied significantly when discontinuity persistence varies from 0.6 to 1.0. The work by Rogers et al. (2007) also demonstrated that in situ 2D and 3D fragmentation (block size and volume) of rock blocks were critically sensitive to the discontinuity intensity and persistence (expressed as fracture size). Kim et al. (2007) statistically examined how the rock bridge distributions (represented by the combination of joint orientation, spacing and persistence) affected the block size distribution by orthogonal arrays and experimental design. UDEC code (Itasca 2004b) and 3DEC code (Itasca 2004a) were employed in the parametric analysis to find the correlation of each parameter to the rock block size. The relations between discontinuity persistence and rock block size (including 294 cases examined by UDEC) as well as volume (including 144 cases examined by 3DEC) are reproduced in Figure 2.24. In

Figure 2.24a, groups 1 to 3 represents all simulation cases that the standard deviation of angle between each joint set is 5° and the standards deviation of spacing and trace length are 10, 20 and 30% of the mean values, respectively; groups 4 to 6 refer to all remaining cases that the standard deviations of the angle between each joint set is 10° and standard deviations of joint spacing and trace length are 10, 20 and 30% of the mean values, respectively. In Figure 2.24b, S represents simulation cases that the standard deviations of joint spacing and angle are 30% of the mean value. S is shown as 0, 10, 20 and 30%.

General trends can be seen from Figure 2.24 that the normalized rock block size (Figure 2.24a) as well as normalized rock block volume (Figure 2.24b) moves towards 1 when discontinuity persistence approaches 1. The regression equations for scattered dots in Figures 2.24a, b have been obtained

$$\frac{A_b}{A_0} = 1.03\,(K_A)^{-0.9} \quad (R^2 = 0.961, \text{Normalized block size vs. persistence}) \quad (2\text{-}18a)$$

$$\frac{V_b}{V_0} = 1.03\,(K_V)^{-1.0} \quad (R^2 = 0.829, \text{Normalized block volume vs. persistence}) \quad (2\text{-}18b)$$

where A_0 is the calculated block size considering joint spacing, joint angle, and 100% persistence, V_0 is the calculated block volume considering joint spacing, joint angle, and 100% persistence; A_b and V_b are equivalent rock block size and volume, respectively; K_A and K_V are joint persistence which are calculated by equations: $\sqrt{K_1 K_2}$ and $\sqrt[3]{K_1 K_2 K_3}$, respectively. Note that two joint sets were consider in UDEC model (Figure 2.24a) and three joint sets were involved in 3DEC model (Figure 2.24b). The analysis results by 3DEC regarding the relation of persistence and rock block volume agreed well with Cai et al. (2004).

Longoni et al. (2012) analysed the geometrical features of rock discontinuities including spacing, persistence in rock masses (sedimentary Triassic rocks including limestones, marls and dolomites) based on the data collected during surface and subsurface investigations. Three dimensional distinct element code was applied to generate rock mass structures. In their model, persistence was considered as the probability that any discontinuity cuts a block (through which rock block volume was correlated with persistence). The relationship between persistence and block volume found in this study, which

is essentially similar to that presented by Wang et al. (1991), was reproduced in Figure 2.25.

The full line depicts the volume distribution under conservative persistence (100%), while the dashed line depicts the volume distribution from the real persistence calculated from ground penetrating radar (GPR). It clearly demonstrates how discontinuity persistence changes the block size distribution, particularly for larger sizes.

A new technique based on Monte Carlo Simulations was proposed by Elmouttie and Poropat (2012) to estimate in situ rock block size distribution (BSD) in a jointed rock mass. More specific geometrical properties of discontinuities (represented as either polygons or triangulated surfaces) were used as input parameters. Discontinuity persistence was modelled realistically by utilizing a discrete fracture network (DFN). Three discontinuity persistence values (60%, 80% and 100%) were selected in the simulation. It was found that BSD is sensitive to persistence, especially when K=60%, rock blocks as large as 20 m were obtained which is not agree with the result (no block is larger than 4.5 m was predicted) presented by Wang et al. (2003). FrackMan code was used by Palleske et al. (2014) to examine the influence of discontinuity persistence (termed as fracture size in this study) to the mean block size determination for a given rock masses.

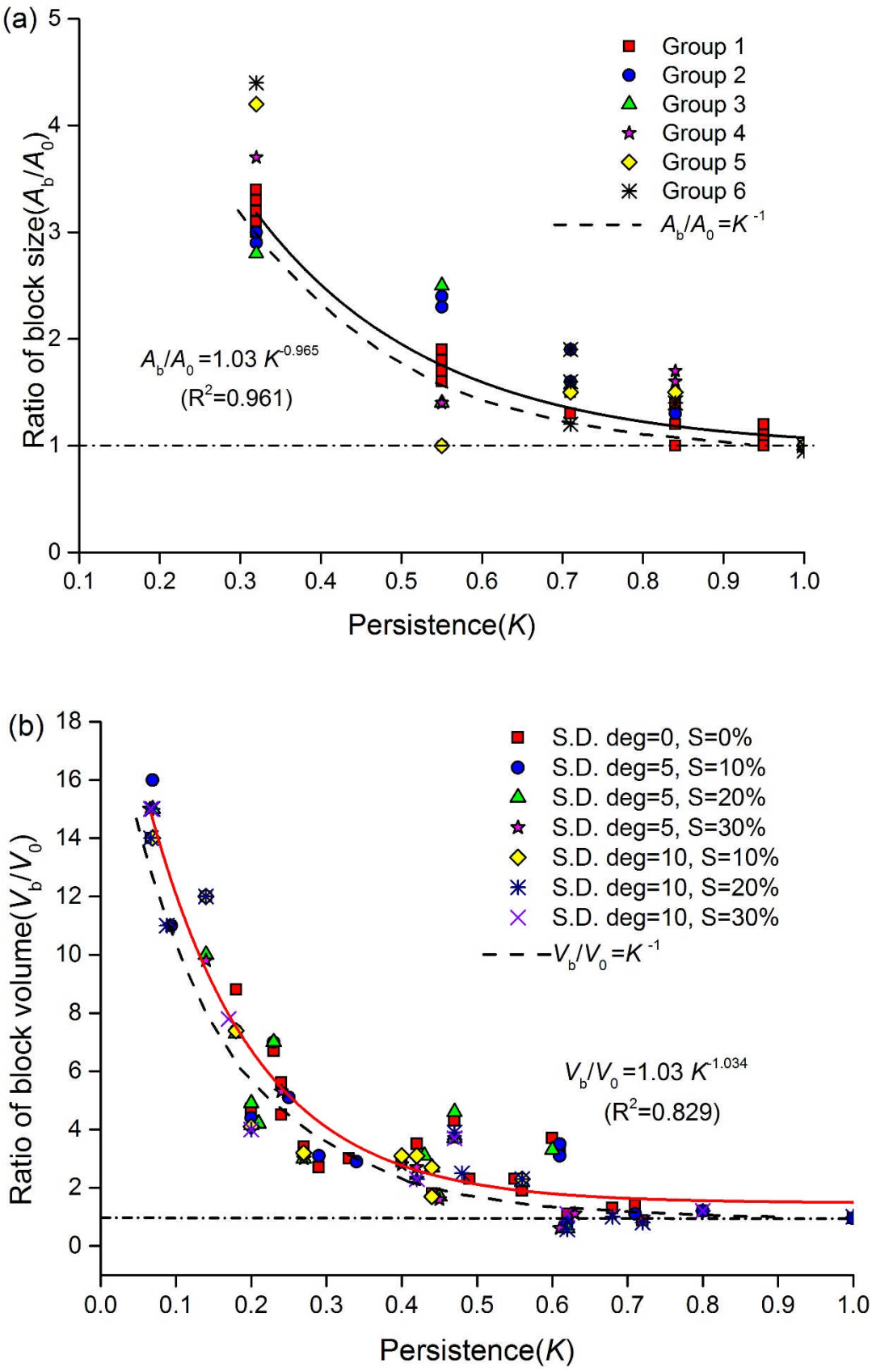

Figure 2.24 Relationship between joint persistence and normalized block size (**a**) and block volume (**b**). Replotted from Kim et al. (2007).

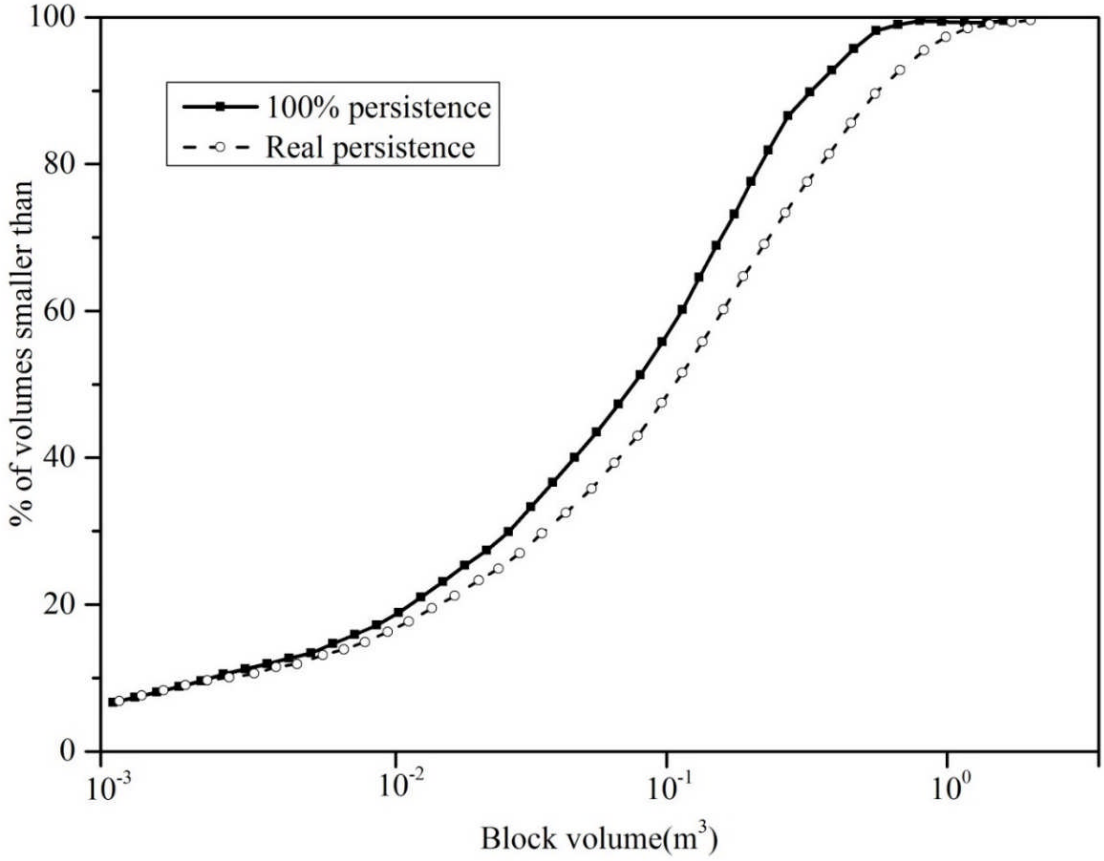

Figure 2.25 Rock block volume distribution for 100% persistence and real persistence. Modified from Longoni et al. (2012).

2.5.2 Mechanical properties and deformability of non-persistently jointed rock masses

2.5.2.1 Influence of persistence on rock mass behaviour

Jointed rock masses, in nature, inevitably contain discontinuities with various orientation, shapes, sizes and persistence. A great number of factors including intact rock matrix strength, discontinuity properties (including shear, tensile strength and any other geometrical properties), discontinuity interactions (stress distribution varies with the number and arrangement of discontinuities (Mughieda 1997)) and the interactions between discontinuities and rock matrix (such as block interlocking) will influence the overall mechanical properties of rock mass. One of these factors, the importance of incipiency of discontinuities (represented as persistence), in the determining of rock block size and volume has been appreciated and investigated, as discussed in section 2.5.1. The incipiency will also influence the overall rock mass behaviour.

There has been several classic mass classification schemes for example RMR (Bieniawski 1973, 1976), Q system (Barton et al. 1974) and GSI (Hoek et al. 1995). Generally these classification schemes are empirically produced to provide a guidance for engineering support (except for GSI, semi-empirically designed for rock mass strength estimation) based on engineering projects or laboratory data. A specific value considering different influential factors is assessed and calculated to reflect the quality of rock masses. But they fail to consider the influence of persistence in the mass strength determination. For example, in GSI system, the discontinuity persistence is only indirectly considered by the interlocking description (Cai et al. 2004) but on a very low level as discontinuities are assumed to be persistent. Bahrani and Kaiser (2013) pointed out that GSI underestimates the overall strength of non-persistently jointed rock mass based on a comparison of intact and non-persistently jointed rocks using the laboratory test results, especially at high confinement when a rapid increase in strength can be seen arising from the interlocking effect.

Rock quality designation (RQD), originally devised by Deere (1968) for use in core logging, is one of the key parameters used in RMR and Q system. Sound core pieces greater than 100 mm in length are summed and expressed as a percentage of total core run. RQD however does not consider and differentiate incipiency of discontinuities involved and often incipient joints are also included in the assessment (which will underestimate rock mass strength) (Hencher 2013, 2015).

Prudencio and Van Sint Jan (2007) conducted laboratory tests on physical models of non-persistently jointed rock mass under biaxial loading condition. In laboratory tests, the influence of discontinuity persistence was considered and non-persistent rock joints were made by inserting steel sheets into the mortar mixture in the sample preparation. It was found that the rock mass failure modes and maximum compressive strength depended on geometrical parameters of discontinuity, loading stresses, ratios of principle and intermediate stresses. Three basic failure modes were found: failure thorough incipient joint plane, stepped failure and rotational failure of rock blocks. But unfortunately no single parametric influence, such as persistence, on overall rock mass has been reported quantitatively as it is difficult to control other parameters to be constant in the laboratory.

Numerical modelling has been effectively used to investigate the influence of persistence on overall mechanical properties of jointed rock masses. Kim et al. (2007a, b) statistically examined how the incipient discontinuities with

varying persistence values affect the mechanical response, represented by shear strength, compressive strength and GSI value, of jointed rock mass. UDEC and 3DEC codes combined with experimental approaches were used in their study. Shear strengths of jointed rock mass with and without considering persistence (represented as τ,τ_0 respectively) and compressive strengths with and without considering persistence (represented as σ_c,σ_{c0} respectively) were simulated, while GSI values considering persistence were calculated using the quantitative approach proposed by Cai et al. (2004), in which the equivalent block volume was derived for non-persistently jointed rock mass. Strength ratios including τ/τ_0, σ_c/σ_{c0} and GSI/GSI$_0$ against discontinuity persistence from these investigations are assembled and plotted in Figure 2.26. It can been seen that shear strength ratio (red curve) of jointed rock masses dramatically decreased when persistence increased, and the ratio approached 4 when persistence approached 0. This finding means that the shear strength of rocks will be underestimated (around 1/4 from real shear strength) if persistence is ignored in the rock mass strength assessment. For the compressive strength ratio (blue curve) and GSI value ratio (green curve) against persistence, the underestimation rule also can been observed but with smaller influences, i.e. within 1.5 time underestimation from the real compressive and GSI value. Note that the variations of compressive strengths ratio (σ_c/σ_{c0}) as well as GSI values ratio (GSI/GSI$_0$) for the same persistence value arise from the different joint spacing parameters adopted in the simulation. That is, upper ratio values corresponded to wider joint spacing, and vice versa. If a strength underestimation (SU) parameter is defined, similar to the definition of strength degradation parameter used by Bahrani and Kaiser (2013), as the reduction in the strength (or GSI value) of full-persistently jointed rock mass from that of non-persistently jointed rock mass. SU of shear strength can reach up to 300%, while SU of compressive strength and GSI can reach 50% according to the findings by Kim et al. (2007a, b). This provides a general and quantitative understanding of the effect of persistence on the strength of non-persistently jointed rock mass.

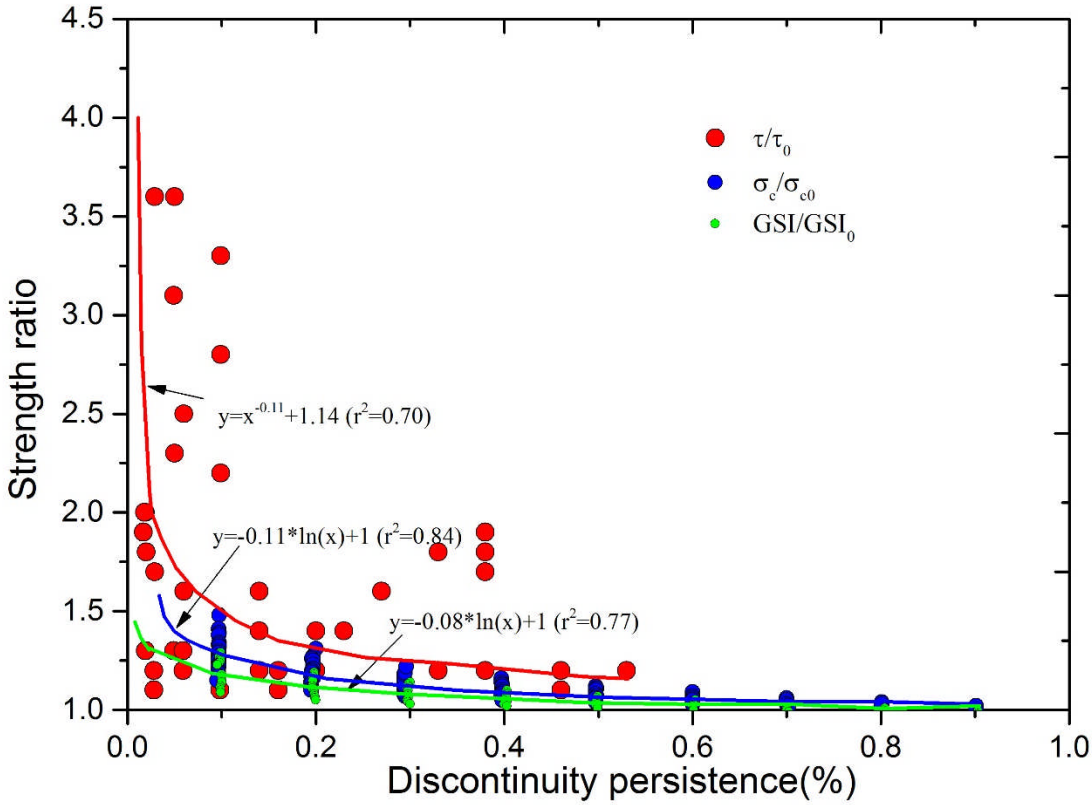

Figure 2.26 Relationship between relative rock mass strengths and persistence. Modified from Kim et al. (2007a, b).

Following the discontinuity geometrical distributions in the laboratory tests conducted by Prudencio and Van Sint Jan (2007), PFC3D code was used by Bahaaddini et al. (2013) as an extension to investigate the effect of discontinuity persistence on the failure mechanism, compressive strength and elastic modulus of rock mass in which multiple layers of coplanar non-persistently discontinuities were arranged while varying geometric parameters (see Figure 2.27).

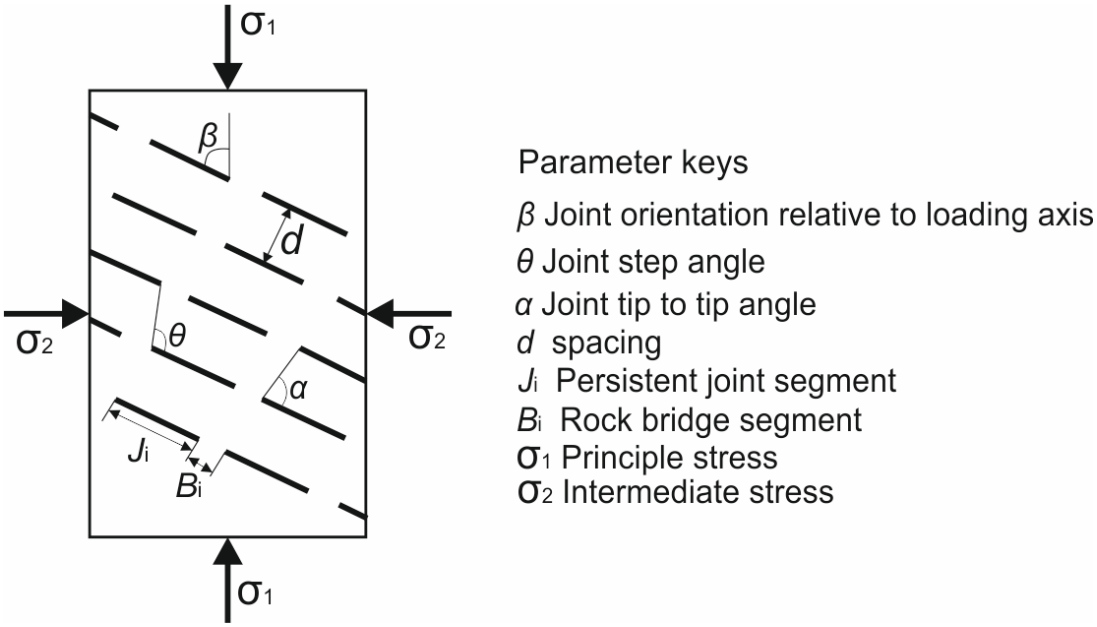

Figure 2.27 Discontinuity geometrical parameters used in the numerical modelling by Bahaaddini et al. (2013). Reproduced from Bahaaddini et al. (2013).

In their study, persistence varied from 0.5 to 0.8 while other geometrical parameters were set to be constant except for β which varied from 0° to 90°. Numerical results were reproduced in Figure 2.28, corresponding failure modes of samples when *K*=0.5 were also included in Figure 2.28a. Note that yellow represents rock matrix in PFC model, green indicates incipient rock joint traces, red indicates tension cracks and blue stands for shear cracks (but rarely can be seen). It was found that compressive strength and elastic modulus of rock mass decreased when persistence increased for the same joint angle relative to loading axis. In addition, strength and modulus varied significantly when β varied from 0° to 90° for the same discontinuity persistence, for all persistence values, these two mechanical parameter all approached the lowest values when $\beta = 60^\circ$. They also found that jointed rock mass containing multiple layers of incipient discontinuities experienced several failure patterns under compression, dependent on discontinuity orientation. For example when *K*=0.5, failure mode changed sequentially from intact rock failure ($\beta = 0^\circ$), planar failure ($\beta = 15^\circ, 30^\circ$), block rotational failure ($\beta = 45^\circ, 60^\circ, 75^\circ$) to intact rock failure again ($\beta = 90^\circ$). It is also worth noting that tensile cracks dominated and decreased dramatically when persistence increased from 0.5 to 0.8 at a constant joint orientation $\beta = 90^\circ$. This phenomenon can be attributed to the reduction of the number of joint tips. A further investigation considering more discontinuity values was reported by Bahaaddini et al. (2016), the same methodology was employed and the similar

results were arrived at to those plotted in Figure 2.28. All these quantitative study results validated the qualitative results originally proposed by Prudencio and Van Sint Jan (2007).

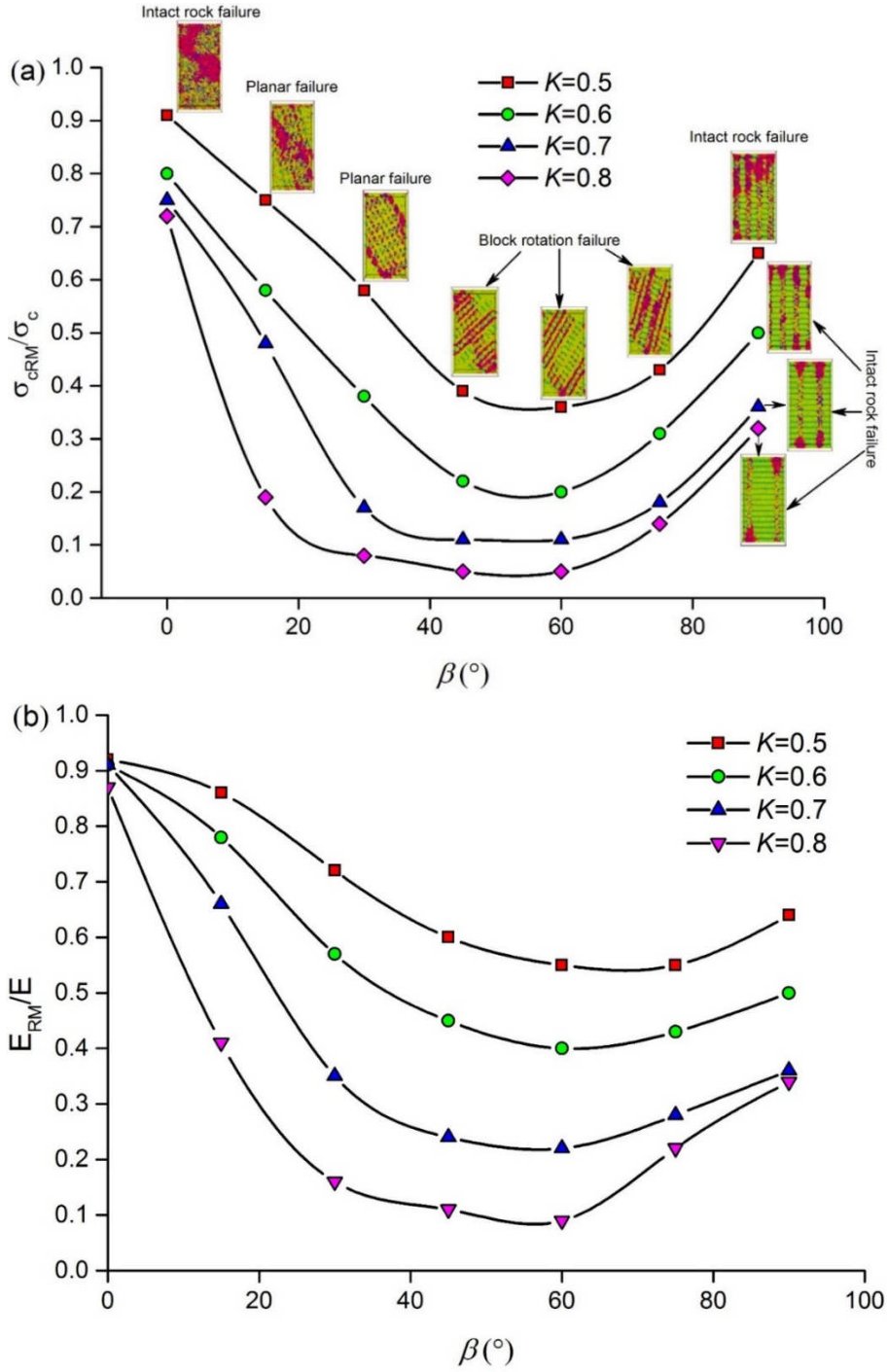

Figure 2.28 Effects of discontinuity persistence on relative compressive strength of rock masses (**a**) and on relative elastic modulus of rock masses (**b**). After and adapted from Bahaaddini et al. (2013).

2.5.2.2 Rock slope stability considering incipient discontinuities

It is agreed that incipient rock discontinuities have significant influence on the mechanical properties and deformability of rock mass thus therefore on the rock slope stability. Compared with local-scale rock mass, large-scale mass (if it is larger compared with joint spacing) can contain more sets of discontinuities therefore much more complex stress distributions, especially where discontinuities appear random. A more challenging difficulty confronting practical rock engineers is that how to consider the incipiency of discontinuities in large scale stability analysis. In addition, the gradual development and coalescence of incipient discontinuities over engineering time may have profound effects on stability. An illustrating engineering example was presented by Hencher (2006), in which movement and development (over many years) of sheeting joints were observed prior to the detachment of a large landslide in Hong Kong.

Einstein et al. (1983) proposed a probabilistic criterion for failure that was related to discontinuity data so as to examine the effect of discontinuity persistence on rock slope stability. Only one set of parallel discontinuities with varying persistence was examined in their study. The “critical path” for a given discontinuity geometry (including coplanar and non-coplanar joint plane, such as en enchelon) was defined to consider strength contributions from discontinuity and intervening rock bridges as well as the spatial variability of discontinuity geometry. For this “critical path” there is a minimum safety margin SM=resisting force-driving force. SLOPESIM code was utilized to find the paths of the minimum SM and achieve probabilistic failure analysis of jointed rock slope. In addition, the effect of the probability distribution of persistence was investigated using the parametric study method.

The notion of representative volume element (RVE) of jointed rock masses was proposed by Pariseau et al. (2007) with an aim to enhance the reliability of large-scale rock mass stability analysis and dramatically reduce computer run time, from hundreds hours to several hours, simultaneously. RVE of a non-persistently jointed rock mass stands for an element that is so large that any other discontinuities contribute little (can be ignored) to the equivalent rock mass properties for the targeted mass volume. Stability of engineered open pit slopes was investigated by utilizing a more practical finite element modelling technique in which RVE was recognised for a given discontinuity geometry. Equivalent discontinuity properties (Pariseau 2003) were calculated for a given persistence for each set of discontinuity evolved in the RVE and then employed in the slope stability analysis. The main benefit of the

RVE approach is that the numerous non-persistent discontinuities within a rock mass at project scale can be effectively dealt with.

Viviana et al. (2015) proposed a method, combining probabilistic technique (mean uniform distribution law) and Yade Open DEM code, to investigate translational sliding failure along an incipient discontinuity within rock slopes. Three different sliding block geometries were investigated, that is, centres of gravity were located in the upper part (Figure 2.29a), lower part (Figure 2.29b) and middle of sliding block (Figure 2.29c), respectively. For each situation, three different dip angles (30°, 50°, and 70°) were used. The relation of slope failure modes (stress distributions) were found to be dependent on the slope geometry and discontinuity persistence. For all situations, tensile and shear stress increased dramatically when persistence decreased which confirms the finding by Bahaaddini et al. (2013) that higher tensile cracking arises from lower discontinuity persistence. For configurations where centres of gravity were located in the upper part (Figure 2.29a) and middle of sliding block (Figure 2.29b), shear cracks predominate, especially for a small dip angle at 30° pure mode II failure can be found. For higher dip angles, rock slope failure was in both mode I and mode II, especially for configuration where centre of gravity is located in the lower part (Figure 2.29b).

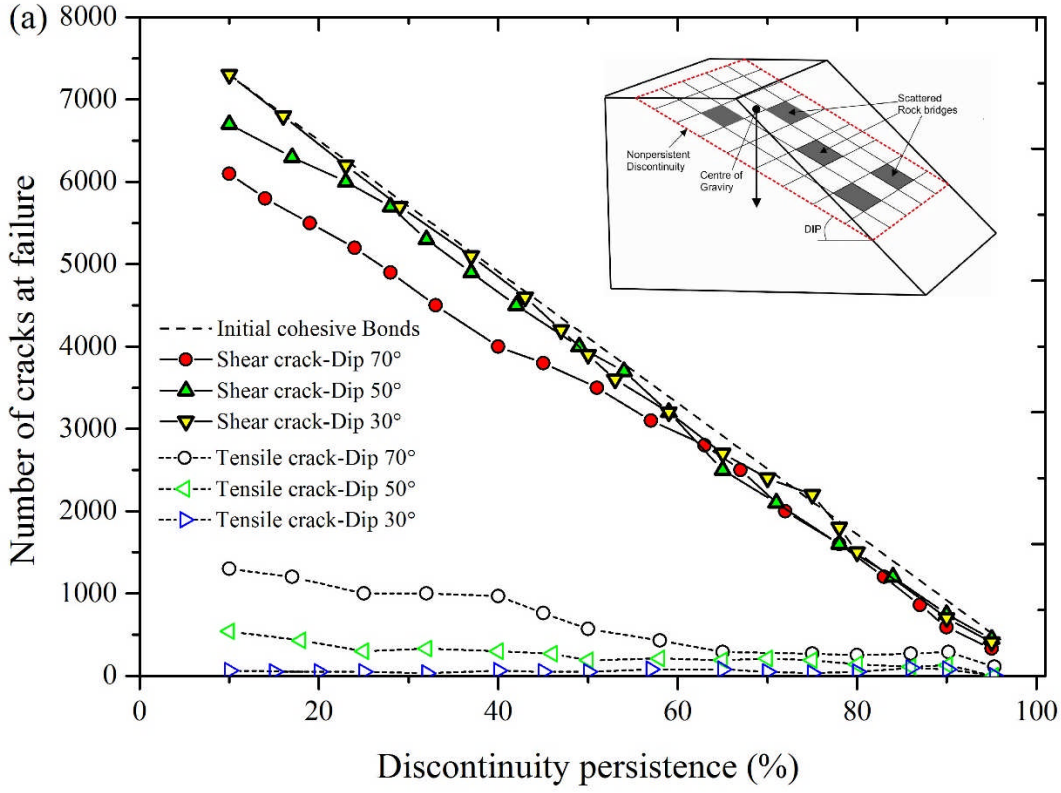

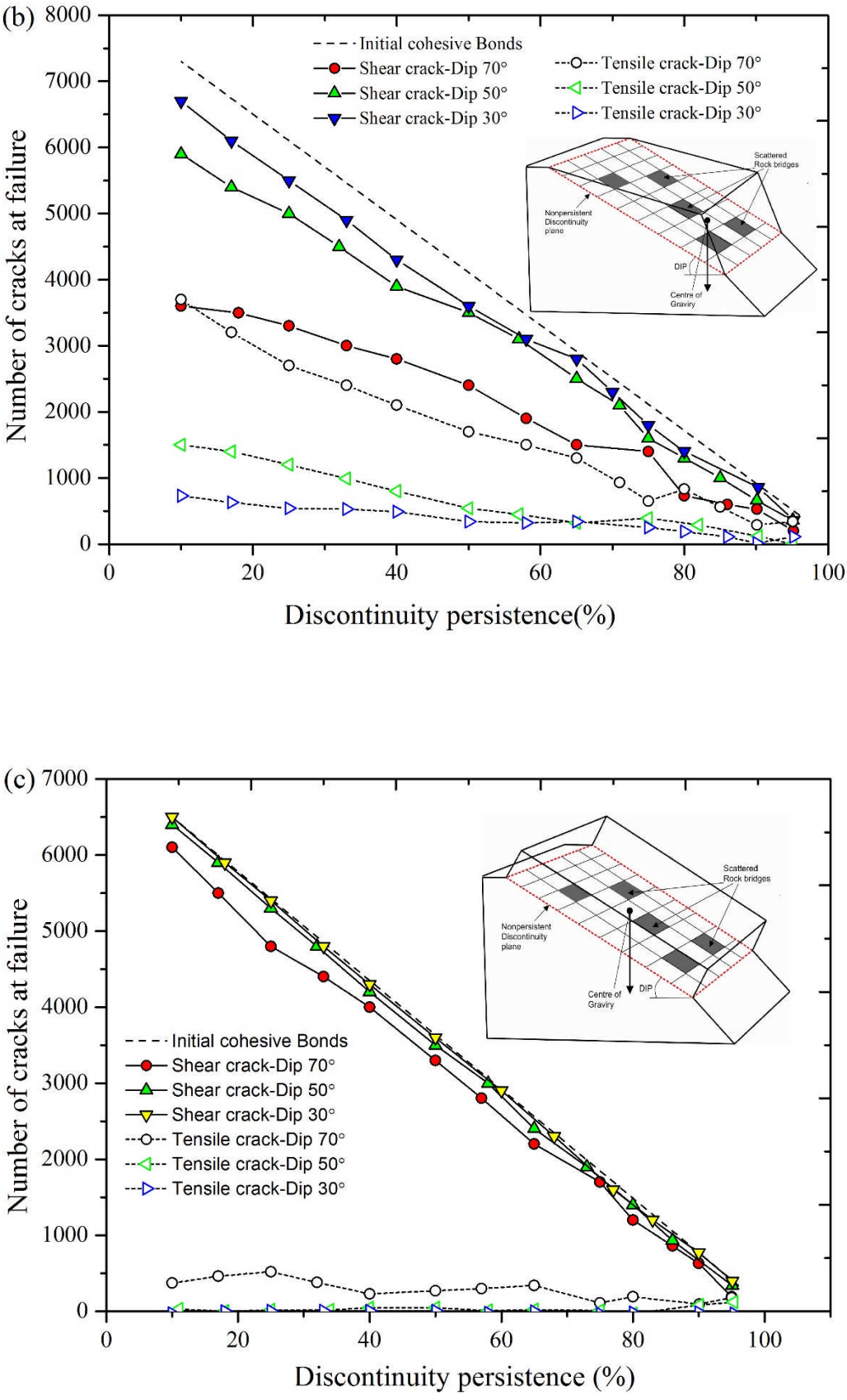

Figure 2.29 Relationship between numbers of tensile and shear cracks occurrences and areal persistence. The dashed lines correspond to tensile crack while continuous lines represent shear crack. Slope dip varied from 30°, 50° to 70°. After and adapted from Viviana et al. (2015)

2.5.3 Summary

In this section, the implication of discontinuity persistence on size and volume of rock blocks, mechanical properties (including shear strength, compressive strength and GSI strength index) of rock masses and deformability of non-persistently jointed rock masses are reviewed. The key findings from this discussion are summarized as follows:

(1) The equivalent volumes of rock blocks within a rock mass can be calculated by Eq. (2-17) on condition that only several sets of parallel joint are interested within the rock mass.

(2) Size and volume of rock blocks within a rock mass are sensitive to discontinuity persistence. Exponential relation (Figure 2.24a) is found about the ratio of rock block size within a non-persistent rock mass and block size within the same rock mass but containing persistent discontinuities. Similar trend is also found about the ratio of block volume (Figure 2.24b).

(3) The results from the research conducted by Longoni et al. (2012) indicate that block volume distribution varied not only with discontinuity persistence but also with lithology and specific geological conditions. These factors should be considered in the assessment of rock block volume and size distribution in the field.

(4) As can be anticipated that strengths of a rock mass will be underestimated if persistence is ignored in the rock mass strength assessment. Shear strength of a non-persistent rock mass will be underestimated to approximately 75% of the real shear strength, while the underestimations of compressive strength and GSI index are both around 33% from real compressive strength and GSI index value, respectively.

(5) Failure mode of a rock mass under compression is mainly affected by the geometrical parameters including joint persistence, orientation and number of joint tips.

(6) For the sliding failure of a rock slope along an incipient discontinuity, persistence of this incipient discontinuity as well as dip angle of the discontinuity plane dominate the failure mode. For a small dip angle (less than 30°), pure mode II failure occurs; while for higher dip angles, slope failure is in both mode I and mode II.

2.6 Quantification of rock discontinuity persistence

The influence of persistence on overall rock mass behaviour has long been known (Hencher 2014; 2015). In practical rock engineering projects, a conservative discontinuity persistence (100% persistence) was adopted or even worse persistence was neglected. This can be attributed to difficulty in the measurement of real persistence. Traditional surveys on exposed rock faces are two-dimensional, thus true persistence inside the rock mass is extremely difficult to determine. Poisson planes and circular discs have been proposed as models for joints by Bridges (1976) and Baecher et al. (1977), on assumption that joint length are approximately equal in strike and dip directions (Robertson 1970). Rawnsley (1990) found that persistence – even as seen in surface exposures - was not predictable on the basis of geological factors or through other observations. As was pointed out by Hencher (2015), the area and extent of a single discontinuity away from an exposure or borehole is difficult to measure. In reality, it is assumed that a rock mass can be regarded as a continuum if there is no particular structural anisotropy relevant to project.

Currently, there are still no recommended methods to measure or predict discontinuity persistence. Trace length of discontinuities obtained from rock exposures was normally used as an approximation of persistence and sometimes 100% persistence was assumed for simplification purpose.

2.6.1 Discontinuity size estimation

An approximation to real discontinuity size can be derived from measured trace length from rock exposures after correcting the sampling bias (e.g. Barcher and Lanney 1978, Einstein et al. 1979, Priest and Hudson 1981, Mauldon 1997, Zhang and Einstein 1998, Zhang et al. 2002, Latham 2006, Zhang et al. 2016). Data acquisition of discontinuities from exposed rock faces, the first step to obtain real trace length, can be grouped into two categories: manual methods (such as scanline sampling (SS) and window sampling (WS)) and computer-aided methods.

(1) Scanline and window sampling methods

At planar or nearly planar rock exposures, statistical sampling methods including scanline and window approaches have been widely used to measure the extent of discontinuities intersected.

Straight scanline, normally a tape laid along rock face, samples the joint traces intersecting the line. Although it has been widely employed in application,

there is still no commonly accepted survey standards. In practice, a typical sample area which contains between 150 and 350 discontinuities is better to be selected. Colour photos of exposed rock faces, setting up of scanline, and scale makers are recommended (Hudson and Priest 1979). Wang (1992) grouped scanline survey into two categories: quick scanline and detailed scanline. For a quick scanline survey, only location of each intersection, plunge and azimuth are recorded. Detailed scanline survey normally comprises chainage of each intersected discontinuity from starting point, discontinuity orientation (dip and dip direction) measured by a compass clinometer, discontinuity types (e.g. joints, bedding, foliation, lamination, cleavage), trace length, aperture and infilling condition, planarity, waviness, termination and water condition(any evidence of seepage). A good example sheet of detailed discontinuity survey was produced and provided by Hencher Associate Limited (HAL, 2015), in which relative strength to parent rock was additionally suggested to be considered.

The scanline survey is subject to some drawbacks, i.e. sampling biases, which have been noted by many researchers since 1970s (e.g. Cruden 1977). Figure 2.30 diagrammatically shows a scanline survey on a planar rock face of limited extent, sampling biases including size bias, orientation bias and censoring bias are illustrated.

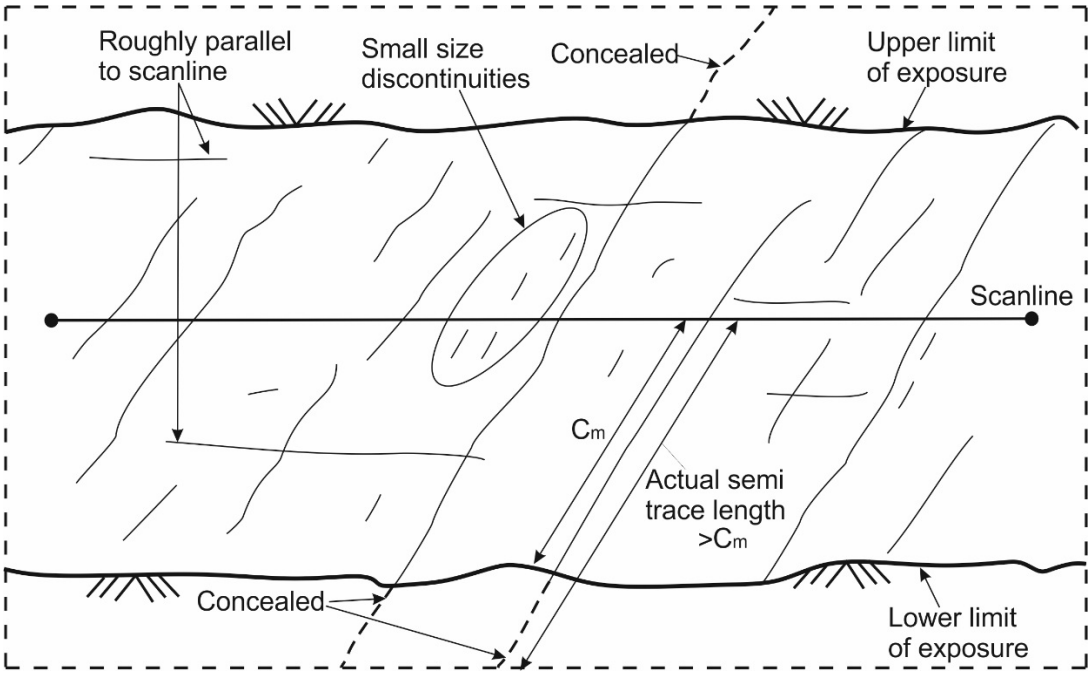

Figure 2.30 Diagrammatic representation of discontinuity traces intersecting a scanline set up on a planar exposure of limited extent. For small size discontinuities or those that are roughly parallel to scanline or concealed, bias will occur when sampling. After and modified from Latham et al. (2006).

These biases are summarised in the following:

(1) Size bias. Scanline will preferentially inserted those discontinuities with a longer trace length and small traces (see Figure 2.30) as low as 10mm on exposures are tend to be neglected. Priest and Hudson (1981) however commented that smaller joint traces will have small effect when mean trace length is in the order of meters.

(2) Orientation bias. Discontinuity striking roughly parallel to the scanline (see Figure 2.30) will be under-represented or excluded from the sampling results. This will lead to a serious misinterpretation of discontinuity extent as some critical information is omitted. Kulatilake (1990) chose seven scanline directions to analysis trace length to eliminate the orientation bias. Priest (1993) suggested that at least three scanlines should be measured at each direction. Park and West (2002) verified and emphasised the orientation bias based on the examination of the differences in results from vertical borehole fracture mapping method and horizontal scanline sampling. In practical rock engineering, three orthogonal line scans are normally recommended to reduce the orientation bias (Hencher 2015)

(3) Censoring bias. Rock exposures are limited and relatively small compared with the persistent joints. Inevitably large discontinuities, one end or both ends (see Figure 2.30), may extend beyond the visible exposure, therefore they are censored at some degree depending on discontinuity size (Cruden 1977). Baecher (1980) pointed out that censoring bias (often related to the geometric variables and shape assumptions) should be considered in size inference.

Window sampling, another manual data acquisition technique, has also been used for sampling the discontinuities exposed at a given rock face. The preliminaries and measurement techniques are similar to scanline survey except that all discontinuities are measured in a finite area, rather than the intersection of the scanline. For setting up window sampling, usually, a rectangle or circular of measuring tapes will be placed on the outcrop. The window should be large enough to reduce the sampling bias, with each side intersecting between 30 and 100 discontinuities. Then the number of discontinuities will be counted and classified into three classes (Pahl 1981 and Zhang and Einstein 2000):

(1) Discontinuities contained in the window: both ends of discontinuities are visible in the sampling domain.

(2) Discontinuities that transect the window: both ends of discontinuities are invisible in the sampling domain, this is, ends beyond the limits of window.

(3) Discontinuities intersect the window: only one end is visible in the window and another one beyond the limits of sampling area.

Although window sampling still confronts the censoring issue, this method normally is able to comprise more and larger discontinuities sets thus will eliminate size bias and orientation bias (Mauldon et al. 2001). In addition, discontinuity termination characteristics can also be logged by using windows sampling (e.g. Dershowitz and Einstein 1988), but it does not provide any information about discontinuity orientation and surface geometry (Priest 1993).

Manual data acquisition methods suffer from some limitations. The first is that it is labour intensive and time consuming. In order to minimise the sampling bias, sampling should be conducted at many different representative spots. It takes long time to obtain discontinuity data one by one from exposed rock faces, and operator's safety during sampling is another issue. The second is that unbiased discontinuity characterisation requires a skilled interpretation by a rock engineer or geologist. The third, and more serious, manual methods cannot be approved to collect data from the rock exposures that are not accessible. So researchers have paid a lot attention on producing other alternative ways to obtain discontinuity data from outcrop.

(2) Computer aided sampling

Computer aided sampling (automatic or semi-automatic) methods, compared with the manual sampling methods above, are more effective. The image analysis technique, perhaps the pioneer work towards this topic, was proposed by Ord and Cheung (1991) to describe discontinuities on outcrop automatically. Afterwards, computer-aided techniques were increasingly to be studied and have been developed. Roberts (2000) proposed a digital photogrammetric technique to investigate three dimensional models of rock faces. Feng et al. (2001) proposed a portal system, in which a laser range finder was firstly used, to measure discontinuities in outcrops. Several computed aided techniques including digital photogrammetry (Tuckey and Stead 2016), ground-based LiDAR, and digital trace mapping have been

involved in the project at Simon Fraser University aiming to develop a standardized and adaptable methodology for assessing discontinuity persistence (trace length). An example of their work was reproduced in Figure 2.31(Tuckey et al. 2012). The open-source image processing code ImageJ was used to trace discontinuities and infer rock bridges, obtained results were used to supplement field window sampling. Umili et al. (2013) developed an automatic method to map and identify discontinuity traces based on digital surface model (DSM), which consists of a triangulated point cloud that approximates the true surface. Terrestrial Laser Scanner (TLS) and Terrestrial digital photogrammetry (TDP), by contrast, are more popular and have been widely used in characterising discontinuities and rock face morphology (e.g. Rosser et al. 2005, Sturzenegger and Stread 2009 a, b , Slob 2010, Sturzenegger et al. 2011 and Lato and Voge 2012). Antonio et al. (2014) comprehensively reviewed the application of TLS technique to rock exposure characterization. These methods are generally based on the segmentation of the rock exposures, and discontinuity traces are obtained as the boundaries of the identified planes (Umili et al. 2013). Collected data are statistically examined and used for rock discontinuity or mass characterisation. Geological exposures however are usually complex thus sometimes will frustrate these statistical sampling approaches (Hencher 2015).

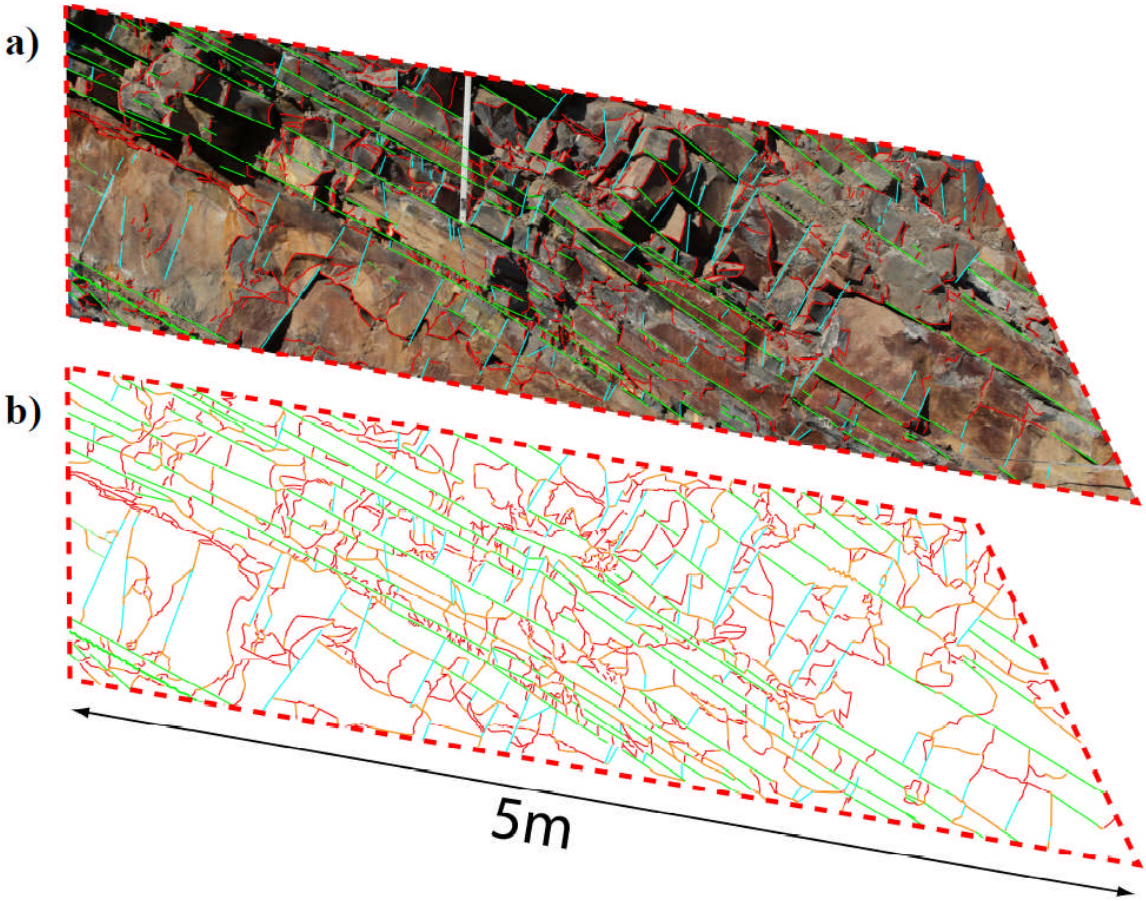

Figure 2.31 a Digital trace mapping of incipient discontinuities and blast-induced fractures over photographs; **b** Discontinuity traces were analysed after tracing. Green and blue lines correspond to incipient discontinuities (two sets), red lines stand for blast induced fractures and orange lines correspond to rock bridges. From Tuckey et al. (2012).

(3) Discontinuity size estimation from censored measurements

Discontinuity size estimation has received extensive attention in rock mechanics literature. This work is based on the censored sampling measurements above. Probability distributions have been used to study the sampling bias thus provide analytical methods to estimate the discontinuity size (or trace length) distribution. Well formulated probability sampling planes should be used otherwise errors will occur (Baecher and Lanney 1978). Table 2.2 presents a selection of publications on this topic.

2.6.2 Subsurface geological discontinuity persistence

All of the above sampling methods are only limited to surface, thus internal discontinuity geometric parameters such as aperture, spacing and persistence cannot be obtained, extrapolation data of surface to subsurface has to be employed. Bieniawski (1989) pointed out that the use of traditional

surface geological sampling was not sufficient to collect accurate discontinuity geometry characteristics thus affecting the reliability of fractured rock mass model. A rock cliff examined by Hencher (2014) demonstrated that it might not be reasonable to carry out discontinuity survey in one area and extrapolate data to elsewhere.

Geophysical techniques perhaps can only be able to provide an approach to investigate internal structure of discontinuities (e.g. Grandjean and Gourry 1996 and Heike et al. 2008). Work by Longoni et al. (2012) provided illustrating insights into the reliable application of radar in the investigation of subsurface real discontinuity persistence. In their work, ground penetrating radar surveys were conducted to image the 3D discontinuity planes inside sedimentary Triassic rocks (limestones, marls and dolomites), thereafter real discontinuity persistence was calculated according to the ISRM (1978) defined persistence shown by Eq. (2-2). Figure 2.32 presents GPR data and interpretation process of real discontinuity persistence. The geophysical approach requires a high resolution thus be able to sample data in deep targets, an experienced operator also is needed to process and interpret discontinuities within radar datasets.

Table 2.2 Selection of typical contributions into the discontinuity size (trace length) estimation from censored measurements.

Methods	Major contributions	Remarks	Sampling methods	References
Censored exponential distribution	Field procedure was set out to provide a method for characterizing and estimating trace length. The number of data collection was dramatically reduced bases this procedure.	The analysis does not consider type of discontinuity termination. The method tends to overestimate larger trace length.	Scanline sampling	Cruden 1977
Moment estimate	Moment estimation of unconditional radius distribution of joints was presented.	Reliable results depend on the probability function assumed.	Scanline sampling	Baecher and Lanney (1978)
Probability distribution analysis	Four simple probability distributions were used to study bias in scanline sampling. The relations between these distributions provide analytical methods of estimating mean discontinuity trace length.	Reliable results depend on the probability function assumed.	Scanline sampling	Priest and Hudson (1981)

Table 2.2 Continued.

Methods	Major contributions	Remarks	Sampling methods	References
Probability distribution function	A technique was proposed for estimating mean trace length on infinite exposures. The method did not require lengths and density function of observed traces.	This method is only applicable discontinuities whose orientation is described by a probability distribution function.	Window sampling	Kulatilake and Wu (1984)
Distribution-free methods	The three simple estimator including end-point estimator, an end-point estimator and stereological estimator were developed for the estimation of variably oriented fracture trace length as well as trace density.	Reliable results depend on the probability function assumed, and underlying distribution of trace length is generally unknown.	Window sampling	Mauldon (1998)
Probability analysis, numerical and analytical methods	Joint trace length distribution was estimated for the Poisson disc joint model. Joint diameter distribution was also numerically and analytically investigated	Relying on the assumption that joint length are similar in strike and dip directions. However, may not real in some cases.	Window sampling	Song and Lee (2001)

Table 2.2 Continued.

Methods	Major contributions	Remarks	Sampling methods	References
Stereological relation analysis	Expressions were derived using stereological analysis to estimate size distributions of elliptical discontinuity from true trace length distribution.	Discontinuity should be planar and elliptical in shape. In some cases these assumptions may not be valid	Sampling and windows sampling	Zhang and Einstein (2002)
Maximum likelihood method	Providing	Derived results only apply for joint traces normal to top and bottom window.	Window sampling	Lyman (2003)
Statistical graphical approach	A flexible method for inference of trace length was formulated using statistical graphical model based on observations at rock outcrops.		Window sampling	Jimenez-Rodriguez and Sitar (2006)
Probability weighted moments (PWM) and L-moments	A distribution-free method was developed to estimate fracture trace length distributions in the light of the estimation of PWM and L-moments of truce trace length.		Window sampling	Li et al. (2014)

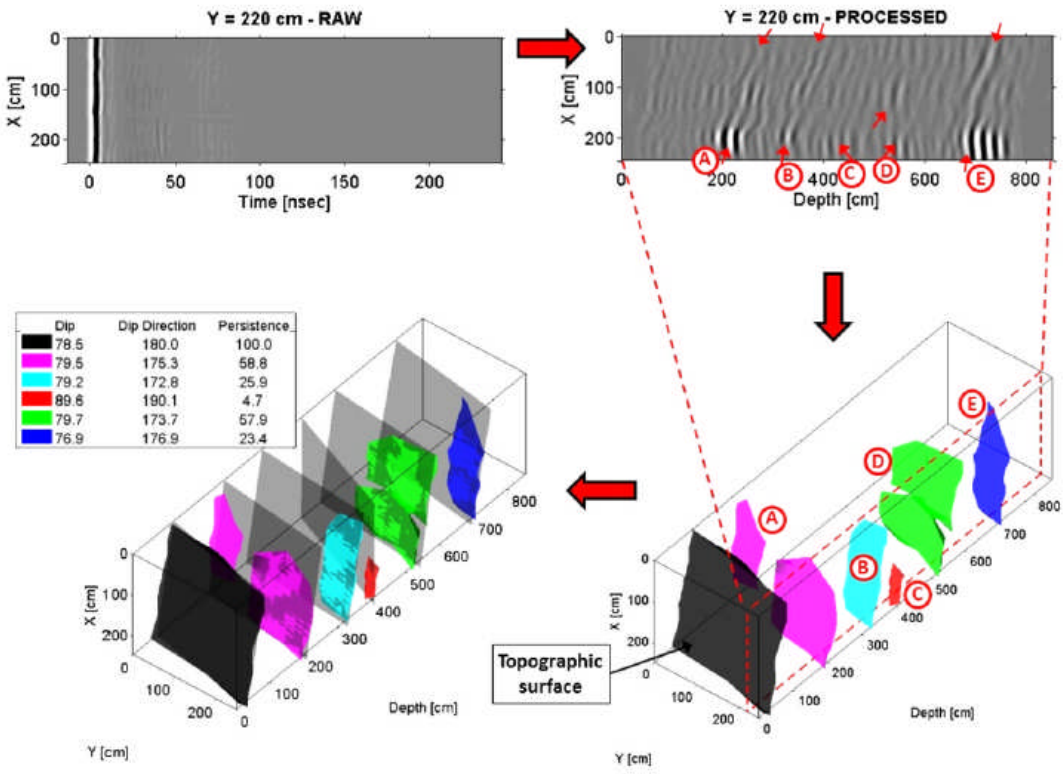

Figure 2.32 Example of GPR data and processing scheme. Raw profile of study area was collected first (top left), and processed profile (top right) was made after picking discontinuities encountered, six interpolated persistent joint areas (bottom right) were obtained and reference planes were fitted respectively(bottom left). Persistence values were then calculated according to Eq. (2-2) and orientations of incipient joint planes were also measured (shown in bottom left). After Longoni et al. (2012).

2.7 Summary

This chapter presented fundamentals of geological discontinuity persistence from general definitions (incipient and mechanical discontinuities and persistence) to stress fields which govern the incipiency of discontinuities. Mechanical properties of single incipient rock discontinuity as well as rock masses containing incipient rock joints were discussed. State-of-the-art methodologies in the quantification of persistence or its approximation were examined.

The review should facilitate rock practitioners and researchers in realising this problematic issue in rock engineering and in applying the current available and most applicable methods to measure or predict persistence in rock engineering projects. Most importantly, it is clear that more research in the development of real persistence quantification standards is needed as well as

better characterisation of incipient discontinuities individually. The study in the following text will be a small step towards this achievement.

Chapter 3
Uniaxial tensile strength of incipient rock discontinuities

It is evident that incipient rock discontinuities (sometimes termed as non-persistent discontinuities in past literature) often have a controlling influence on rock mass strength (e.g. Kim 2013 and Bahaaddini et al. 2013) and stability in rock engineering projects (e.g. Viviana et al. 2015) as well as on other mass properties including deformability and hydraulic conductivity but the degree of incipiency is often very difficult to assess or quantify. Tensile failure of incipient fractures is often the 'final straw' leading to the instability of rock masses (Paronuzzi and Serafini 2009). The recognised relatively low tensile strength value, combined with the conservative assumption of fully persistent of discontinuities in engineering practice lead to the common neglect of tensile strength of discontinuities (Diederichs and Kaiser, 1999). In real situations, for example, there are many stable overhanging rock blocks or slabs due to a sound linking of pre-existing incipient joints which fully demonstrates the supporting capability of incipient rock discontinuities. Unfortunately, in the field, it is extremely difficult to quantify the contribution of the natural defects to the overall strength of rock masses because the information about rock bridges (size, shape and distribution) or filling conditions is never rigorously known in advance(Tuckey and Stead 2016).

In this chapter, a laboratory investigation is presented on the tensile strength of incipient geological discontinuities including incipient bedding, mineral veins and joints. Indirect 'Brazilian' tests were conducted on some intact rock samples but for other samples of both intact rock and containing incipient discontinuities a uniaxial pulling arrangement has been adopted. Meanwhile, the strength origin of different kinds of rock discontinuities were examined by analysis of the mineralogy, nature of the infill and rock bridges. Degree of incipiency was quantified based on the relative tensile strength of discontinuities to that of parent rock.

3.1 Geology and sites description

Figure 3.1 depicts geology of two study areas and shows the locations and overviews of Dry Rigg Quarry (DRQ) and Blackhill Quarry (BQ). DRQ is located in Horton-in-Ribblesdale, north Yorkshire, producing a stone with exceptional wearing and skid-resistant properties used for road improvements.

The quarried rock at DRQ is from Horton Formation siltstone formed approximately 421 to 423 million years ago in the Silurian period and are typically medium to dark grey siltstone. The study area is within the Lower Palaeozoic rock of Ribblesdale, where folding is complex and includes a lot of minor arches, bedding planes, slickensides, and joints (see Figures 3.2, 3.3 and 3.4). These complex geological structures can be viewed on the quarry exposures; bedding in this region is dipping between 65 and 80 degrees to the north north east. Inversion of pre-existing Dinantian extensional faults occurred, accompanied by folding and erosion of the Carboniferous strata (Smedley et al. 2005). Evidence for the late-Namurian tectonics can be seen in the DRQ where there is an irregular morphology including a fold (see Figure 3.3). Incipient rock discontinuities are wide spread in the quarry and some of them are filled with calcite.

Blackhill quarry is in Bramhope (on the edge of Golden Acre Park, near Kings Road), Leeds, West Yorkshire, UK. Quarrying has taken place for over a century and stone products are in a wide range from sand, grit to dimensional stone etc.

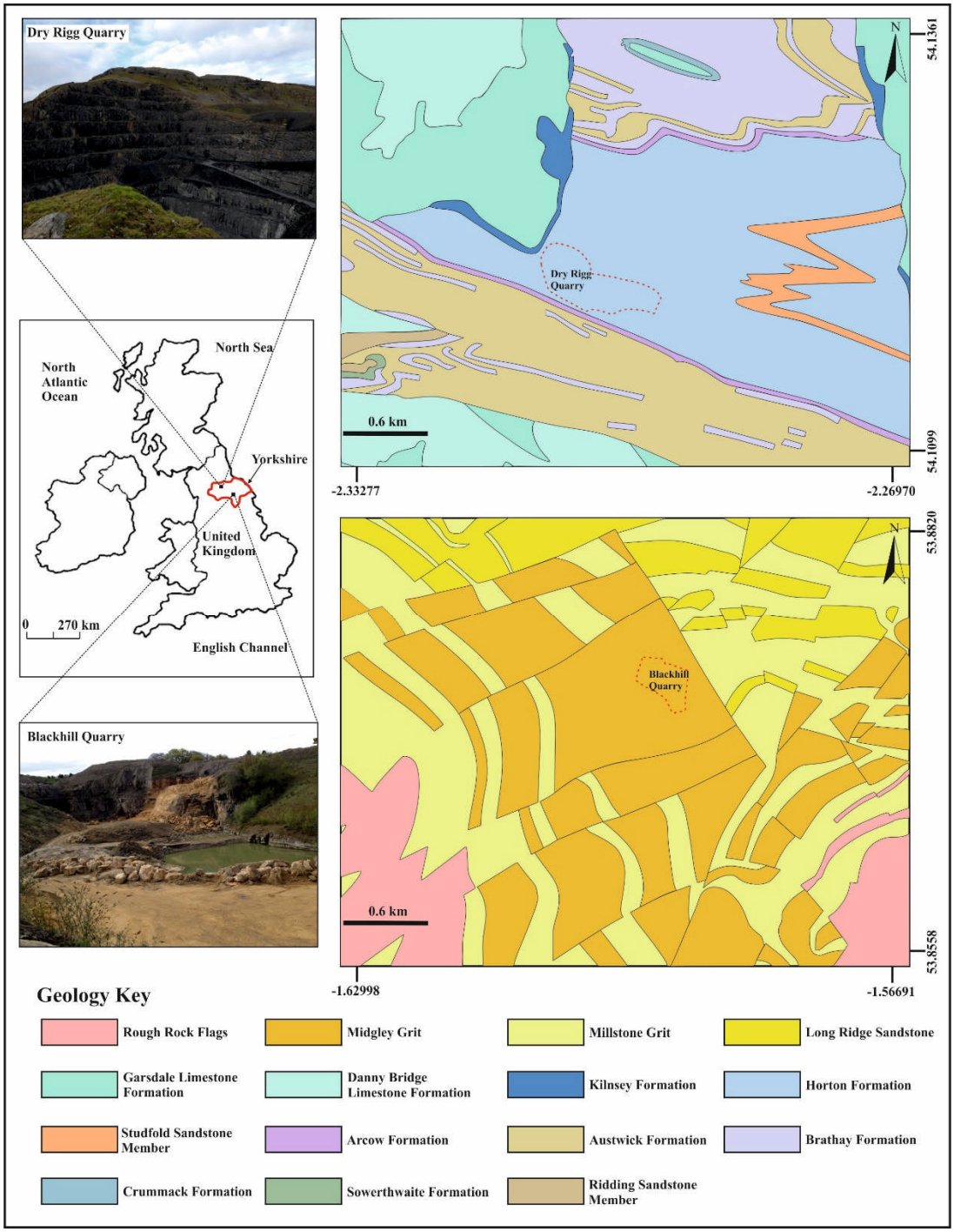

Figure 3.1 Geological maps and locations of Blackhill quarry and Dry Rigg quarry in Yorkshire, United Kingdom. Quarry overviews are also included. Geological maps were produced by sketching and simplifying selected site areas on the complex geological map from the British Geological Survey website.

Figure 3.2 North rock face of DRQ showing predominantly orthogonal discontinuities (horizontal incipient joints and near vertical beds).

Figure 3.3 West exposure of DRQ showing a fold structure and incipient discontinuities including inclined beds and joints.

Figure 3.4 A slickenside surface at DRQ, Yorkshire, England. Seepage can be noticed on the right part of surface.

The sedimentary bedrock at BQ is Midgley Grit Sandstone formed approximately 314 to 315 million years ago in the Upper Carboniferous period. Thick sands laid down at this time formed a sequence of massive sandstones and gritstones. The sandstone is normally well cemented and groundwater transport is controlled mainly by fractures. These rocks form the building blocks of most of the Pennines (Bobbie et al. 2006). The depositional environment was dominated by rivers. The deposit is between 20 and 30 metres in thickness and is made up of a sequence of loosely consolidated sands. The Midgley Grit generally comprises coarse-grained sandstone, commonly with a significantly shaly mudstone parting up to 6 m in thickness. Iron oxides occurs as pore linings and pore fillings and replace ferromagnesian grains such as biotite (Smedley et al. 2005)

3.2 Experimental preparation and preliminary research

3.2.1 Sample preparation

Rock samples containing “simple” incipient discontinuities which are orthogonal to loading axis were prepared for extensive laboratory test. They were prepared from large rock block samples containing a single incipient discontinuity. Block samples and samples containing incipient discontinuities

were collected from two locations. Samples of siltstone with incipient mineral veins were taken from DRQ, Horton-in-Ribblesdale, North Yorkshire, United Kingdom. Samples of medium-grained sandstone containing incipient bedding planes and joints were collected from BQ, West Yorkshire, United Kingdom.

Intact samples as well as samples with incipient discontinuities were prepared. Three sets of samples were tested. The first comprised intact samples (50 mm and 70 mm in diameter). The second sets comprised siltstone samples (50 mm and 70 mm in diameter) containing mineral veins. The third set comprised sandstone samples (70 mm in diameter) containing incipient bedding planes and incipient joints. Figure 3.5 presents diagrammatic illustration of tested samples containing incipient discontinuities.

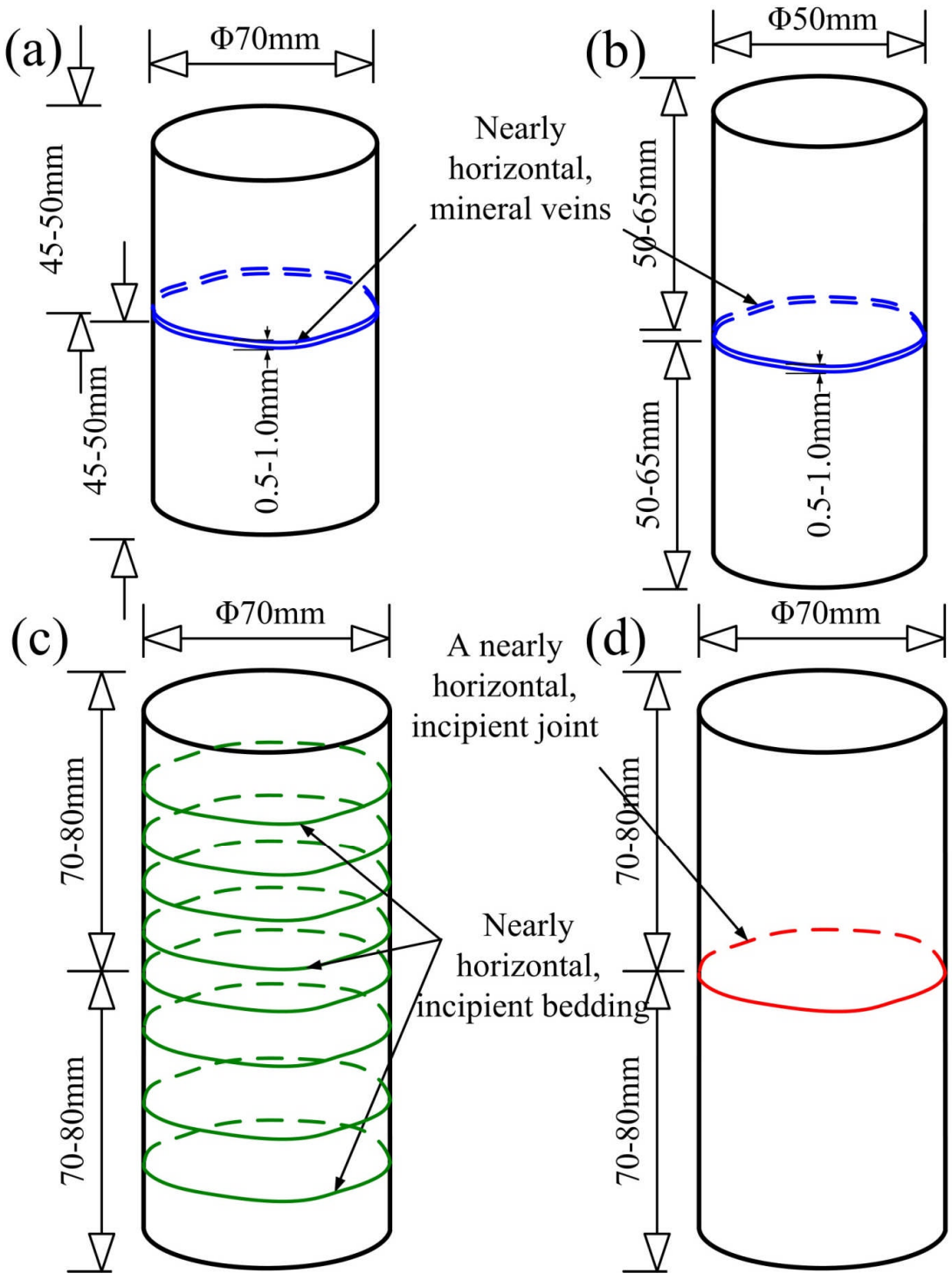

Figure 3.5 Diagrammatic illustration of tested samples containing horizontal incipient discontinuities: (a) Horton Formation siltstone sample contains a filled vein with a diameter of 70 mm; (b) Horton Formation sample contains a filled vein with a diameter of 50 mm; (c) Midgley Grit Sandstone contains horizontal bedding planes and (d) Midgley Grit Sandstone contains a horizontal incipient joint.

(1) Intact sample preparation

Intact rock samples used for uniaxial tension tests and indirect 'Brazilian' tests were obtained in accordance with ISRM standard. Figure 3.6 presents parts of prepared intact rock samples.

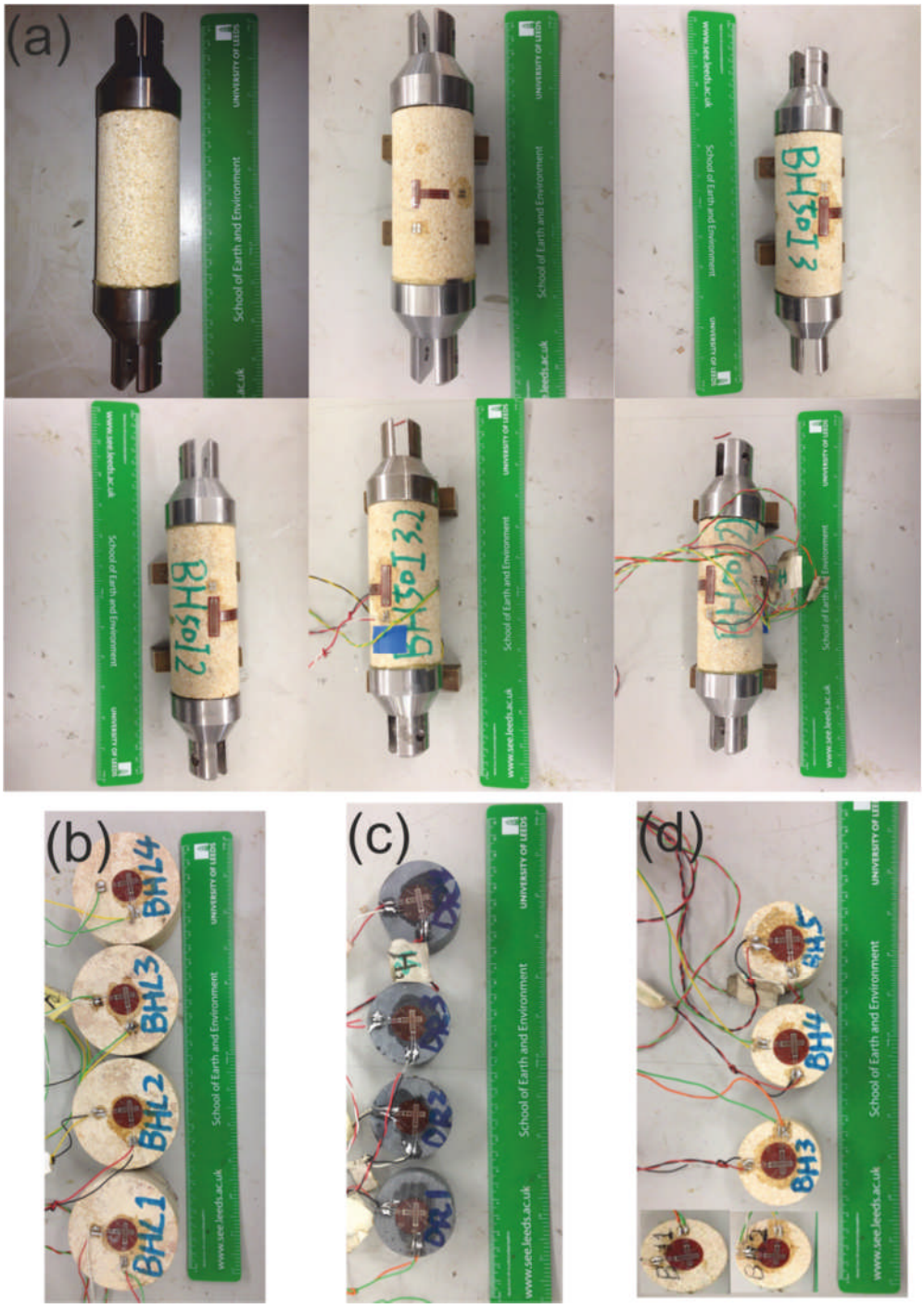

Figure 3.6 Intact rock samples. (a) Midgley Grit Sandstone with diameter of 50 mm; (b) Midgley Grit Sandstone discs with diameter of 70 mm; (c) Horton Formation discs with diameter of 50 mm and (d) Midgley Grit Sandstone discs with diameter of 50 mm.

(2) Samples containing incipient rock discontinuities

Figure 3.7a presents a Midgley Grit Sandstone block containing a large incipient joint. The trace of this joint is intermittent as can be seen from surface. Block sample was trimmed firstly then samples were cored perpendicular to the incipient joint as illustrated in Figure 3.7b.

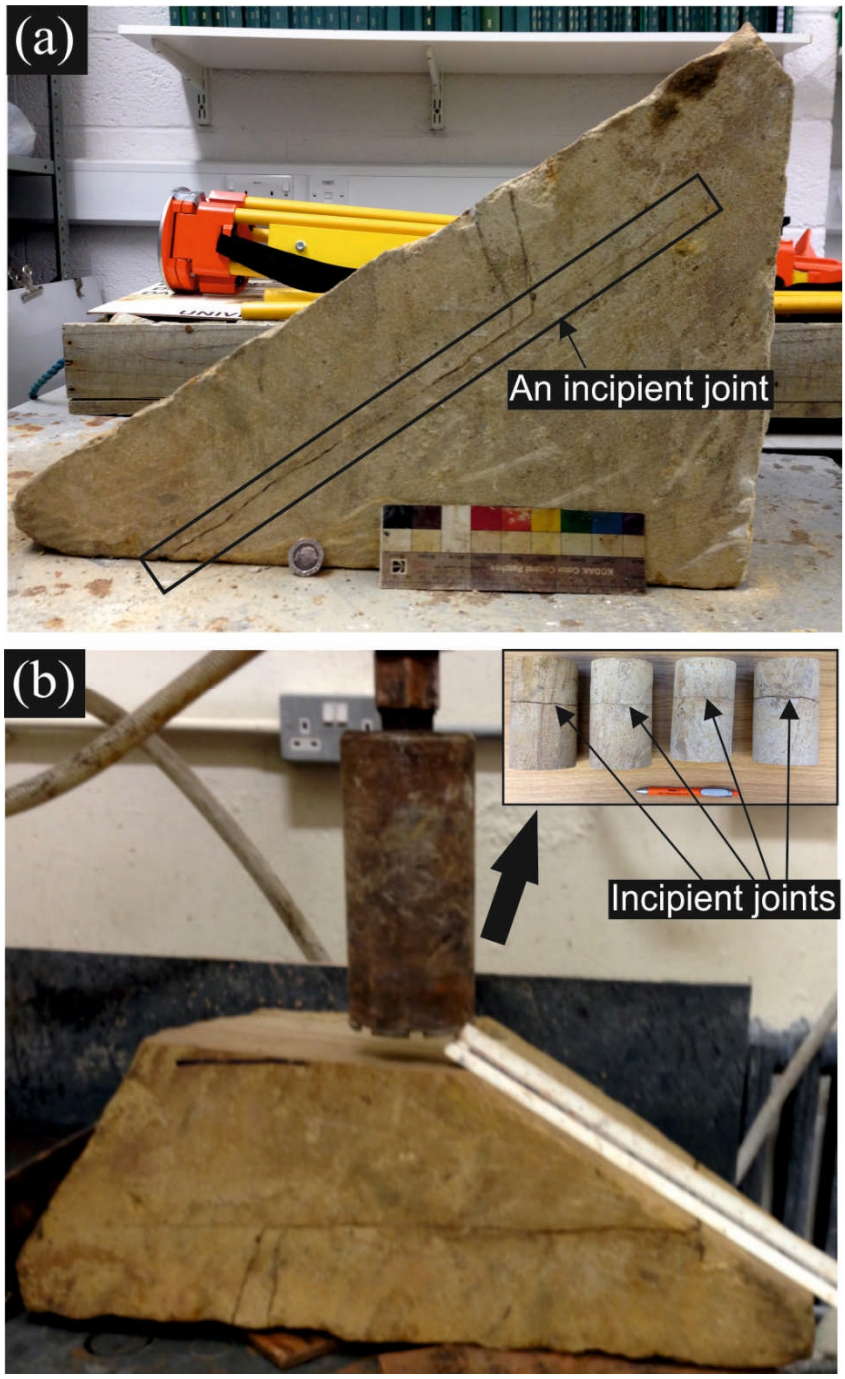

Figure 3.7 Midgley Grit Formation samples cored from a large rock block containing a large incipient joint. (a) A Midgley Grit Sandstone sample containing an incipient joint with aperture ranging from about 0.2 mm to 3.0 mm; (b) Samples drilled perpendicular to the incipient rock joint.

Sample ends were ground flat. In order to minimise stress concentration epoxy resin (araldite) with tensile strength of more than 20 MPa, was employed to cement metal caps to the sample ends (See Figure 3.8). Prepared samples were left more than 5 hours to allow the adhesive to reach full strength.

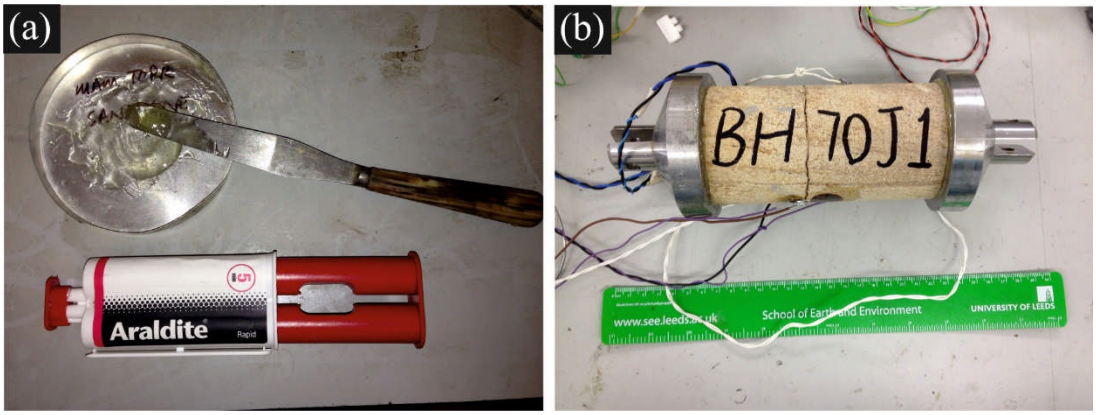

Figure 3.8 Araldite was used to cement metal caps to rock sample ends. (a) Araldite with tensile strength of more than 20 MPa which is higher than tensile strength of most rocks; (b) A prepared sandstone sample with an incipient rock joint for direct tension test.

Similarly, rock samples containing incipient bedding planes and mineral veins were prepared, as shown in Figure 3.9.

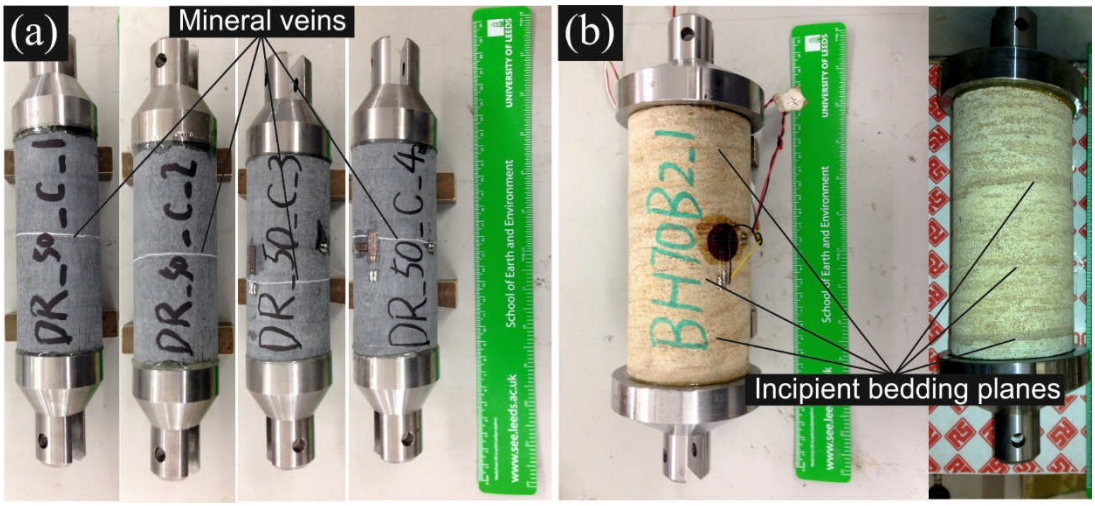

Figure 3.9 Part of prepared rock samples containing incipient rock discontinuities.(a) Horton Formation samples containing mineral veins; (b) Midgley Grit with horizontal incipient bedding.

3.2.2 Testing apparatus set up and verification

A servo-controlled loading machine (MAND), with a capacity of 250 kN, was used for the uniaxial tensile testing as illustrated schematically in Figure 3.10.

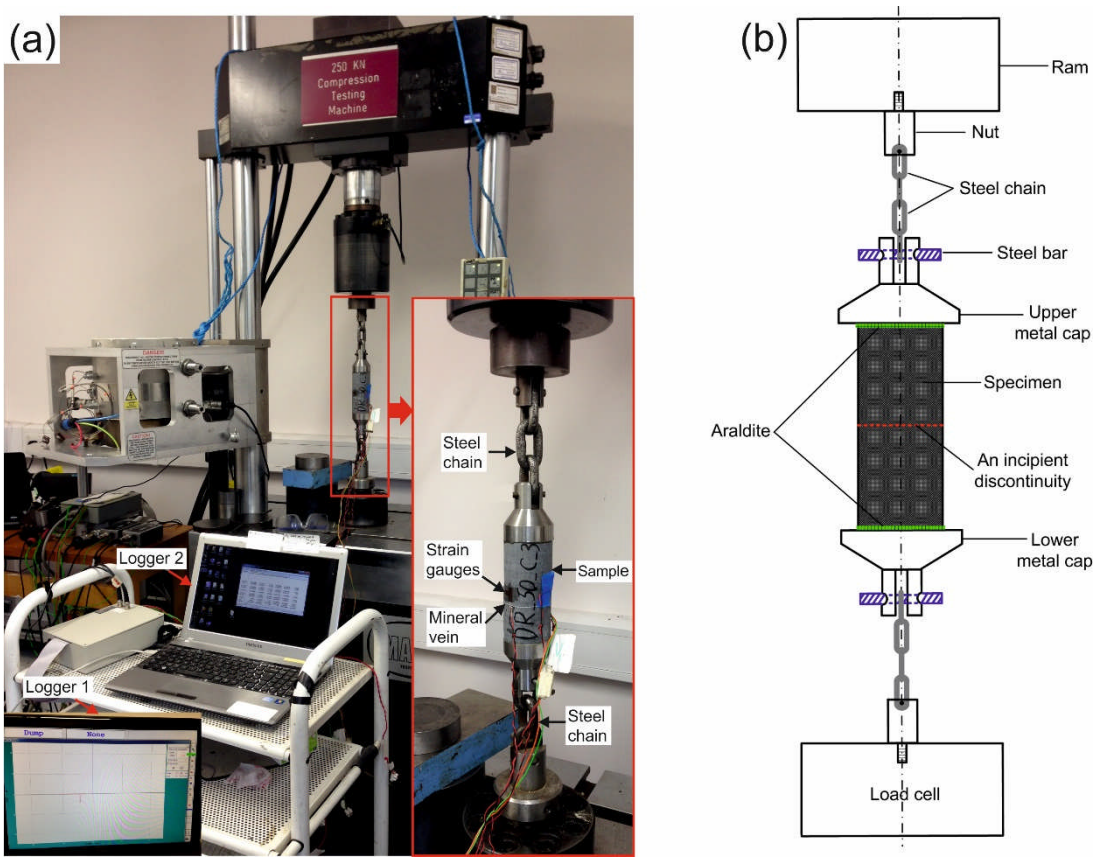

Figure 3.10 (a) Photo of the experimental setup on a sample containing a single incipient mineral vein and (b) schematic diagram of set up for uniaxial tension test (not to scale).

Steel chains were employed as connectors to minimise bending and torsion. In each test, the sample was loaded uniformly at the loading rate of 40 N/s until failure. Strain was calculated by dividing the displacement of the loading platens by sample length, while elongation of chains was deducted for the calculation.

In this test, alignment and gripping of samples are the main problems but, in addition, minor sample inhomogeneity can result in bending and stress concentration (Pells, 1993). High-strength adhesive has been employed to connect samples and connectors together with steel chains as linkage systems to minimise the effect of bending and torsion following the methodologies of Liao et al. (1997), Kwasniewski (2009), Wang (2009) and

Mier and Shi (2002). Note that adhesive should be placed equally and kept to a minimum thickness to obtain an acceptable result.

To validate the test set-up, a preliminary test was carried out on ostensibly homogeneous sample of Midgley Grit Sandstone (lacking visible fabric), using a similar set up to that of Okubo (1996) and Hashiba (2014). Four strain gauges (10 mm in length) were attached to the middle of the samples to measure the macrostrains of samples under tension. Figure 3.11 shows the nature of failure for one sample.

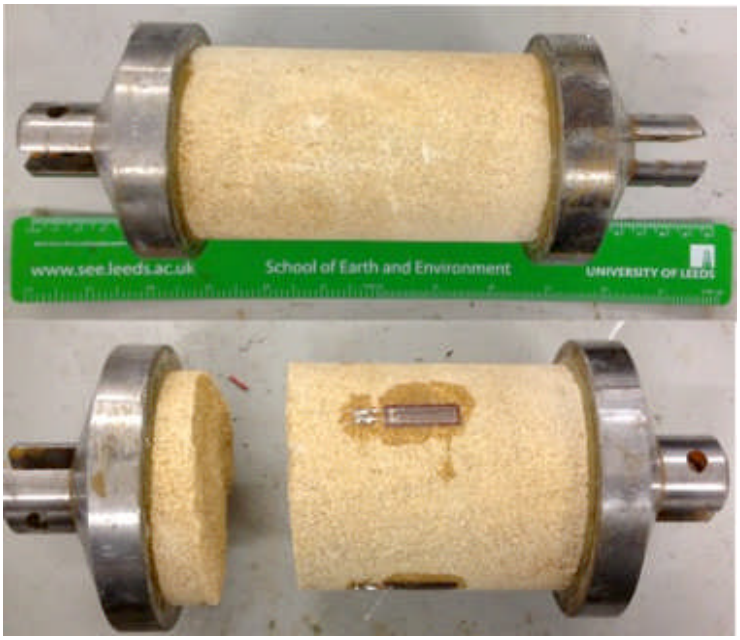

Figure 3.11 Ostensibly homogeneous Midgley Grit Sandstone sample before and after uniaxial tensile test.

Micro-strain curves plotted against time (Figure 3.12) for this test confirm similar strain at the four measurement locations, which provides some confidence in the alignment of the testing set-up as used for the subsequent uniaxial tension tests on incipient discontinuities. Brazilian tests were also conducted on a series of similar homogeneous samples of the sandstone. Data presented in Table 3.1 show that the average measured tensile strength for samples tested uniaxially was 2.08 MPa; the Brazilian test results were generally slightly higher with an average of 2.44 MPa. This finding agrees well with the conclusion in the work by Perras and Diederichs (2014) in which Brazilian tensile strength of sedimentary rock consistently showed a higher value (10% to 30% higher) than uniaxial tensile strength. The differences perhaps reflect aspects of the process of fracture initiation and propagation in

the different testing methods and the way that strength is calculated but further work would be necessary to establish whether there is some consistent explanation. For the purposes of this current work, it is sufficient to observe that the uniaxial test setup gave results that are broadly consistent with the Brazilian test.

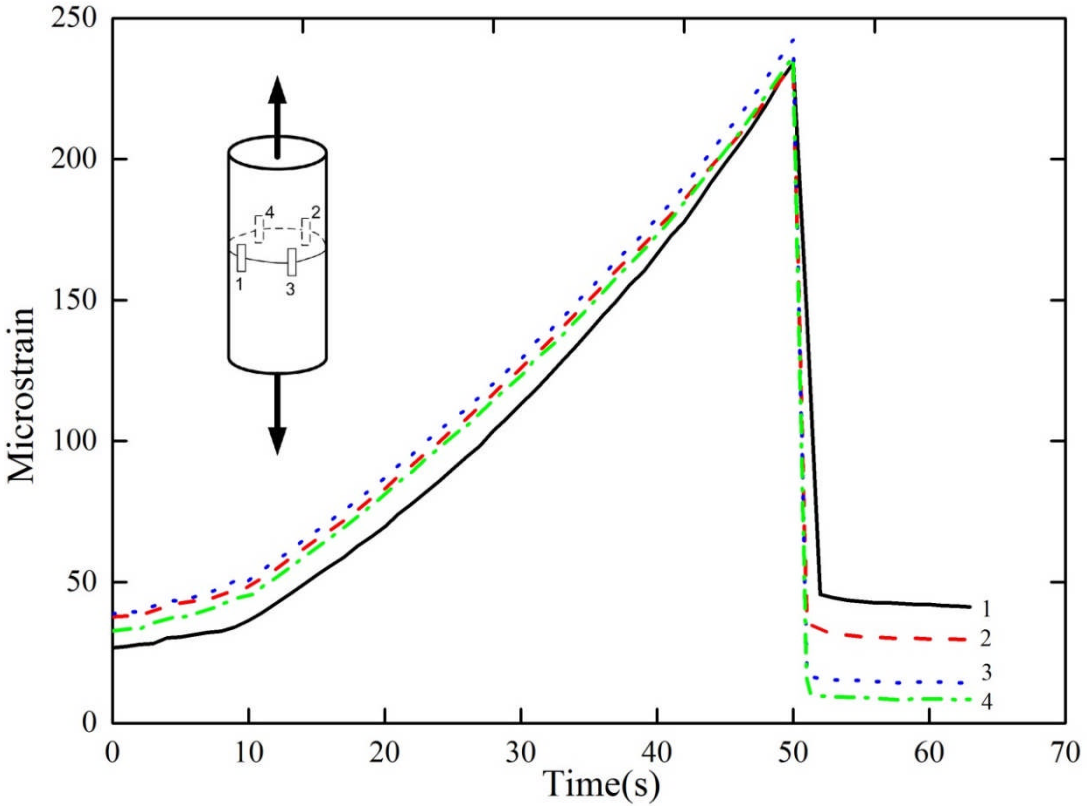

Figure 3.12 Micro-strain vs. time curves for verification tests for uniaxial tension set-up. Four strain gauges were affixed as shown on the diagram.

3.3 Tensile test on intact sandstone and siltstone

3.3.1 Tensile strength of intact rocks

Direct and indirect tensile (Brazilian) tests were undertaken on intact Midgley Grit Sandstone and Horton Formation siltstone samples. The principal properties of samples and uniaxial tensile strength are listed in Table 3.1.

Table 3.1 Principal properties and tensile strength of intact rock samples

Samples		Diameter (mm)	Height (mm)	Weight (g)	Thickness (mm)	Tensile strength (MPa)		Test method
Sandstone	1_1	70	145	1480		2.1	2.1 ±0.2	Uniaxial tension
	1_2	70	142	1402		2.3		
	1_3	70	135	1359		2.0		
	1_4	70	139	1385		1.9		
	1_5	70	149	1520		2.2		
Sandstone	BH1	48		96	24	2.5	2.4 ±0.1	Brazilian tension
	BH2	48		94	22	2.3		
	BH3	49		97	24	2.4		
	BH4	47		95	23	2.5		
	BH5	50		99	25	2.5		
Siltstone	DR1	50		124	25	12.7	12.5 ±0.3	Brazilian tension
	DR2	50		118	23	12.2		
	DR3	50		126	26	12.2		
	DR4	50		130	27	12.9		

3.3.2 Fracture initiation and propagation of Midgley Grit Sandstone under Brazilian tension

During the Brazilian tension tests, a high speed camera (Figure 3.13 top) with was used to log the initiation and development of fractures. The development of fracture of samples BH1, BH2 and BH3 in the Brazilian tension test is presented in Figure 3.14.

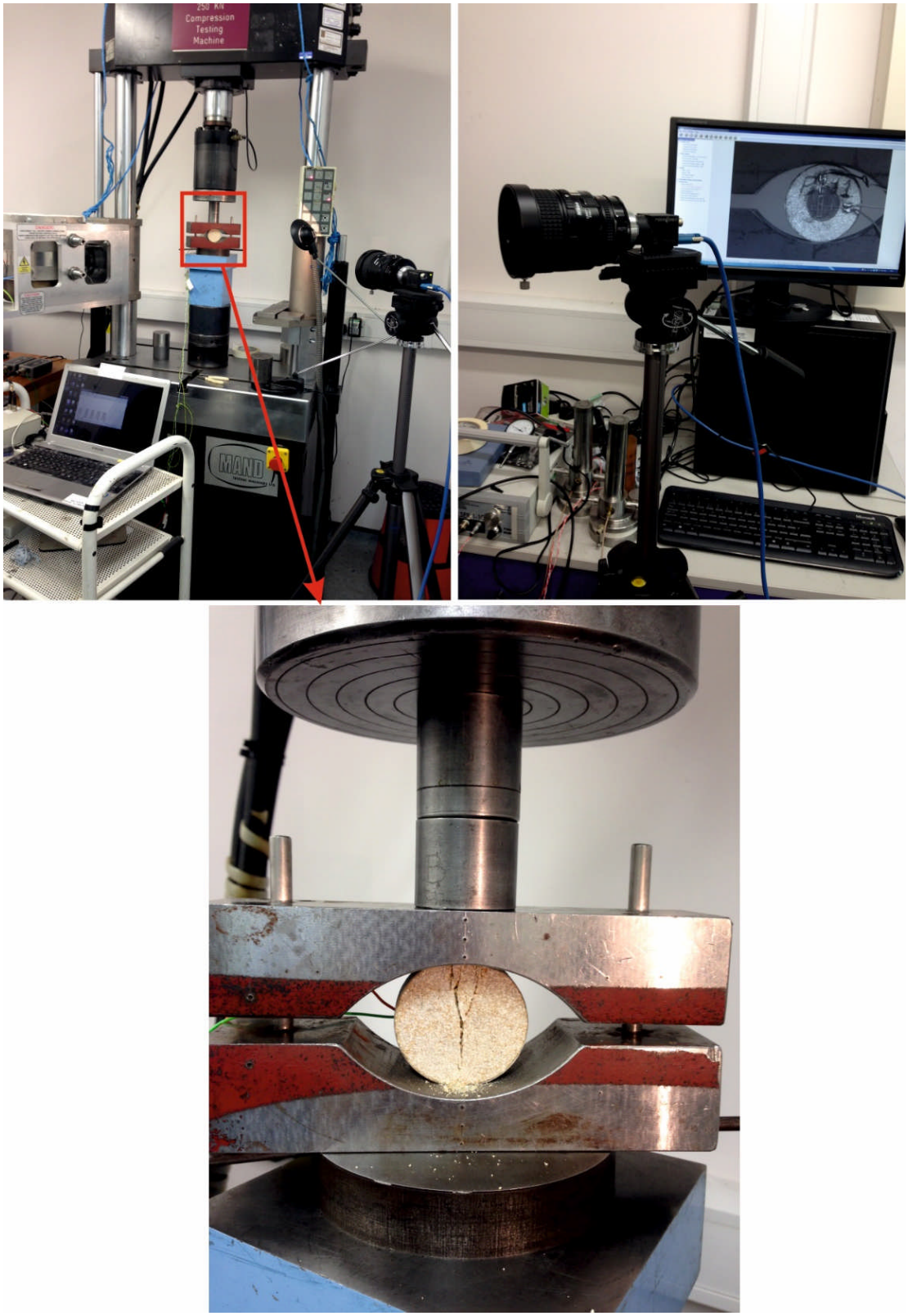

Figure 3.13 A high speed camera was used for logging the fracture initiation and propagation of sample under Brazilian tension.

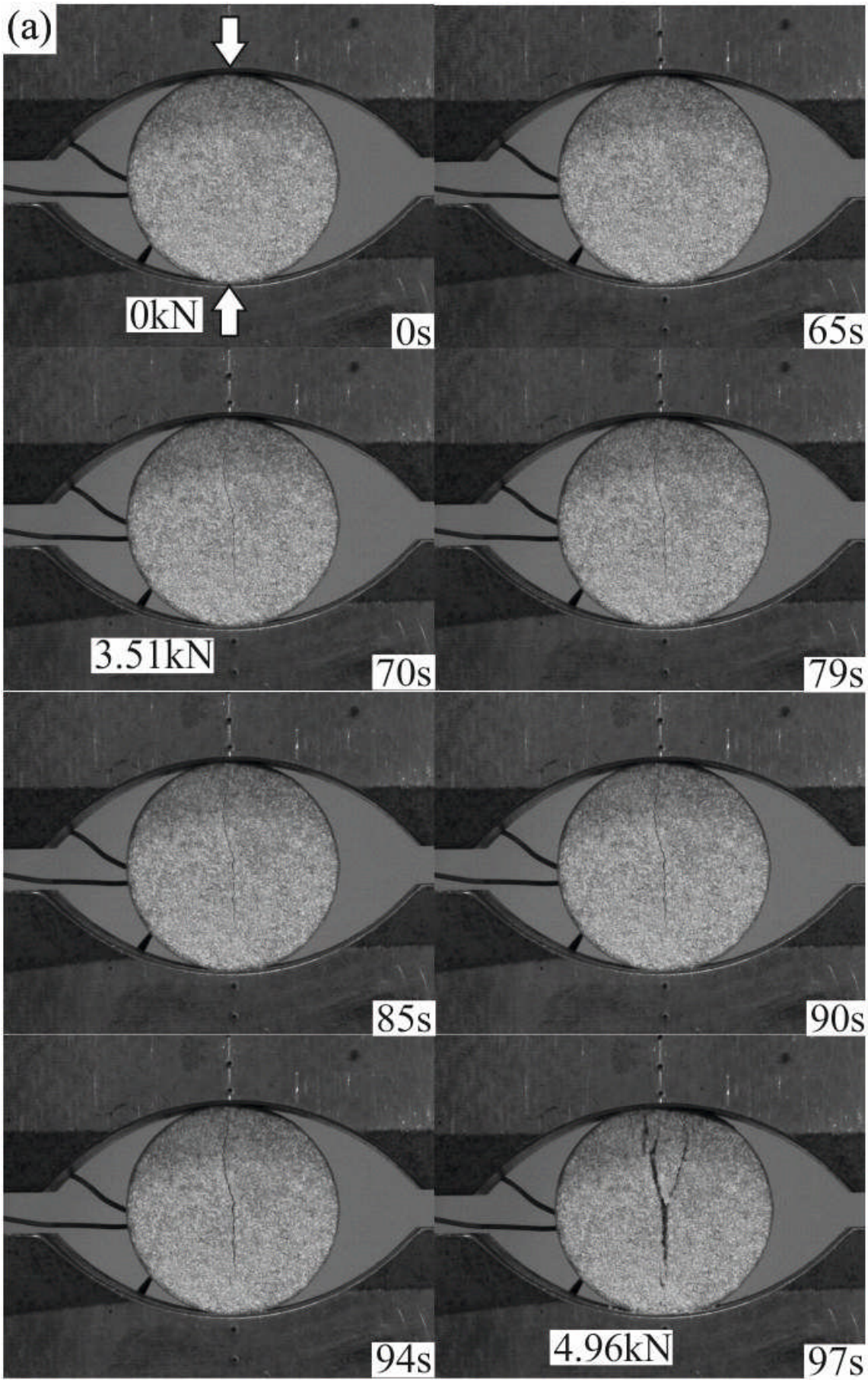
(a)
0kN
0s
65s
3.51kN
70s
79s
85s
90s
94s
4.96kN
97s

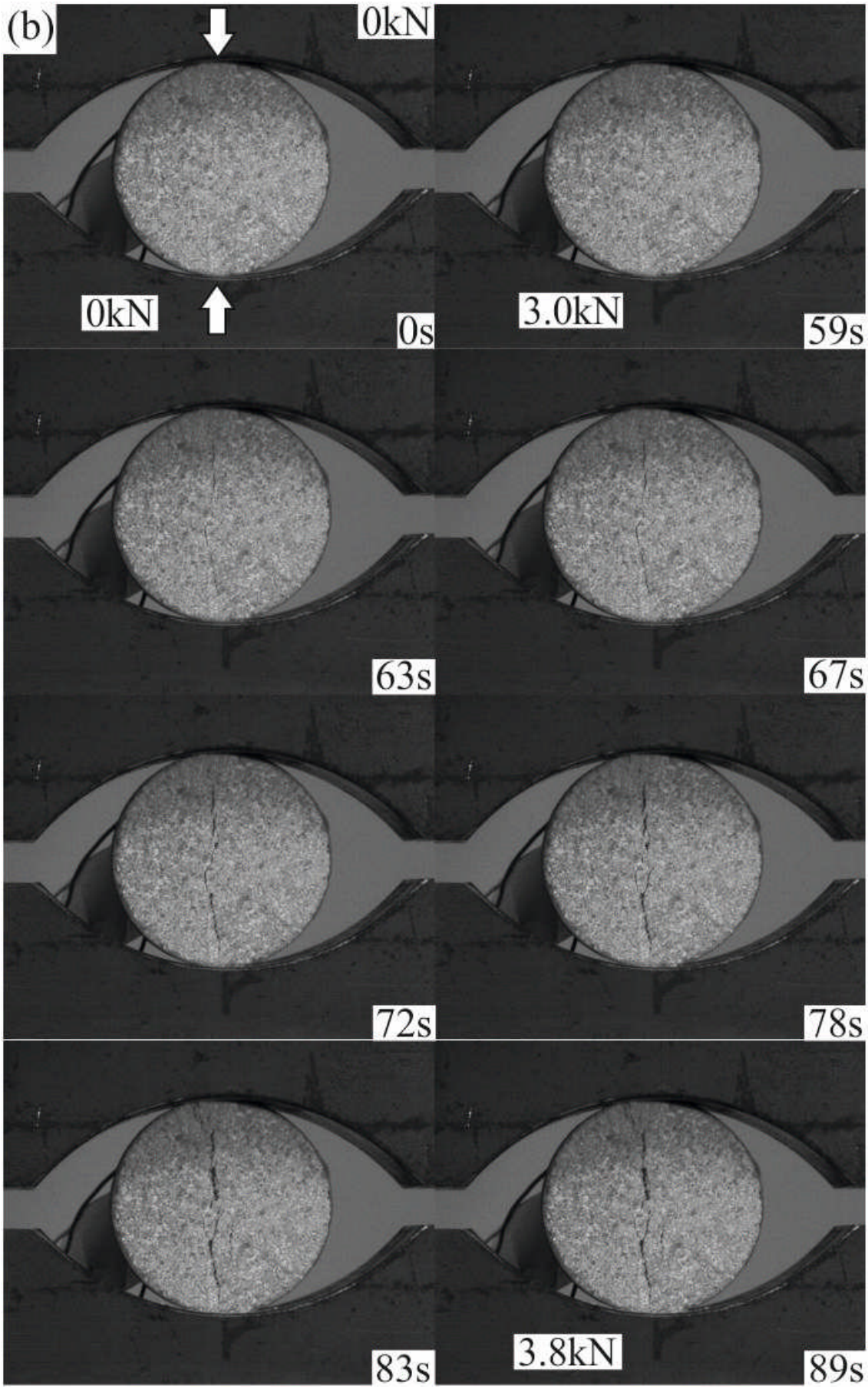
(b)
0kN
0kN
0s
3.0kN
59s
63s
67s
72s
78s
83s
3.8kN
89s

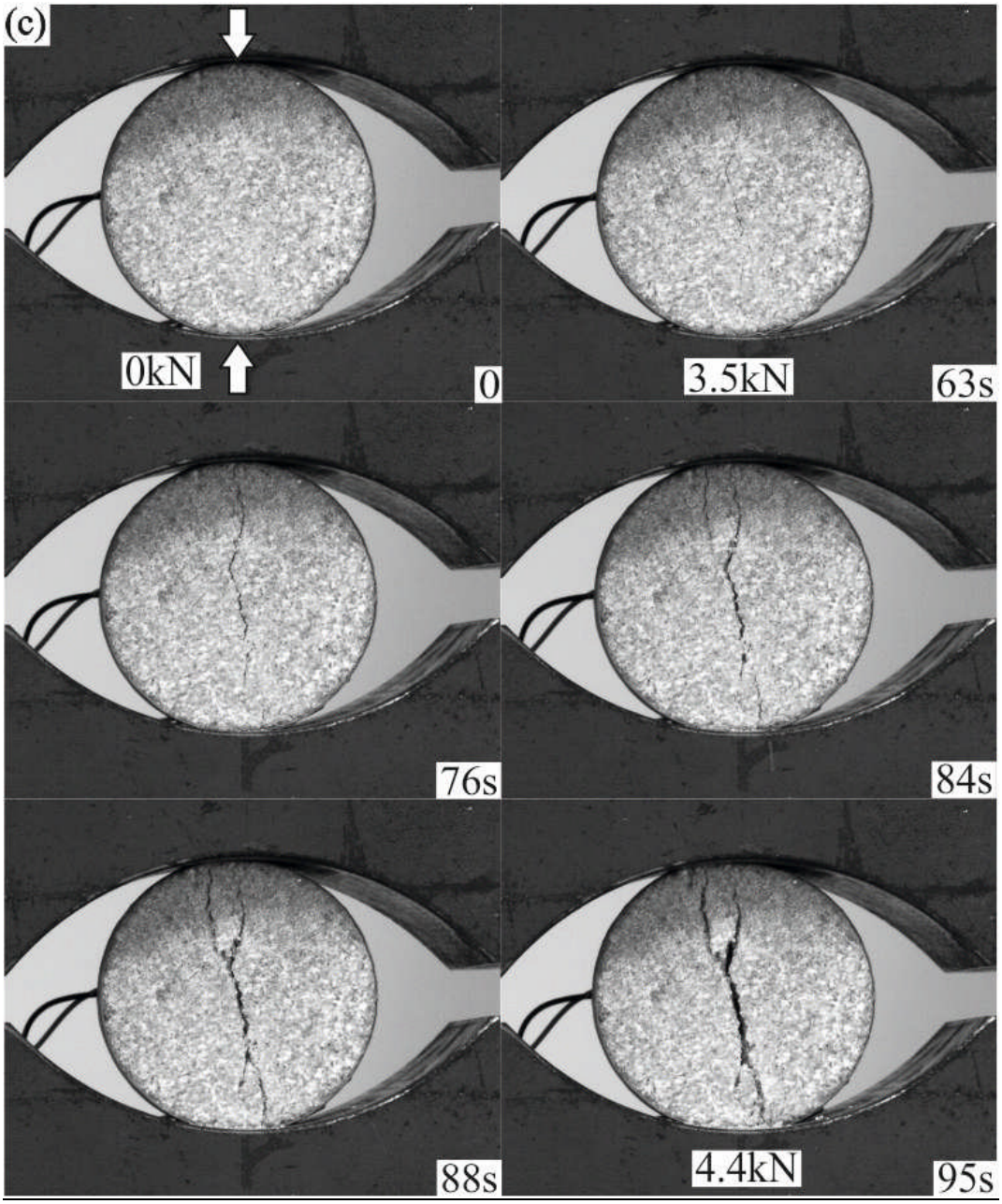

Figure 3.14 Fracture initiation and propagation within intact sandstone samples during a Brazilian tension test. **a** Sample BH1, **b** sample BH2 and **c** sample BH3. Loading was applied vertically relative to the photos, which were taken using a high-speed camera (numbers on the right corners are sequences of frames from test initiation). Note that fracture generally initiated at 70%-80% of ultimate failure load in this test.

It can be noted that all induced fractures initiated approximately from the disc centre and then propagated along loading direction (except for sample BH3) until sample failed. This phenomenon agrees with the conventional assumption about the crack initiation and propagation in Brazilian testing (Wang et al. 2004). For a special case (sample BH3) reported in Figure 3.14,

induced macro-fracture was slightly inclined relative to the loading axis. This probably can be attributed to the local stress concentration or the existing of non-visible pre-existing weakness plane, like bedding lamination.

3.4 Uniaxial tension tests on incipient rock discontinuities

3.4.1 Samples with incipient rock bedding planes

A series of uniaxial tension tests were conducted on sandstone samples with incipient bedding planes approximately perpendicular to the loading axis. Figure 3.15 presents set-up of the uniaxial tension test on a Midgley Grit Sandstone sample containing bedding planes.

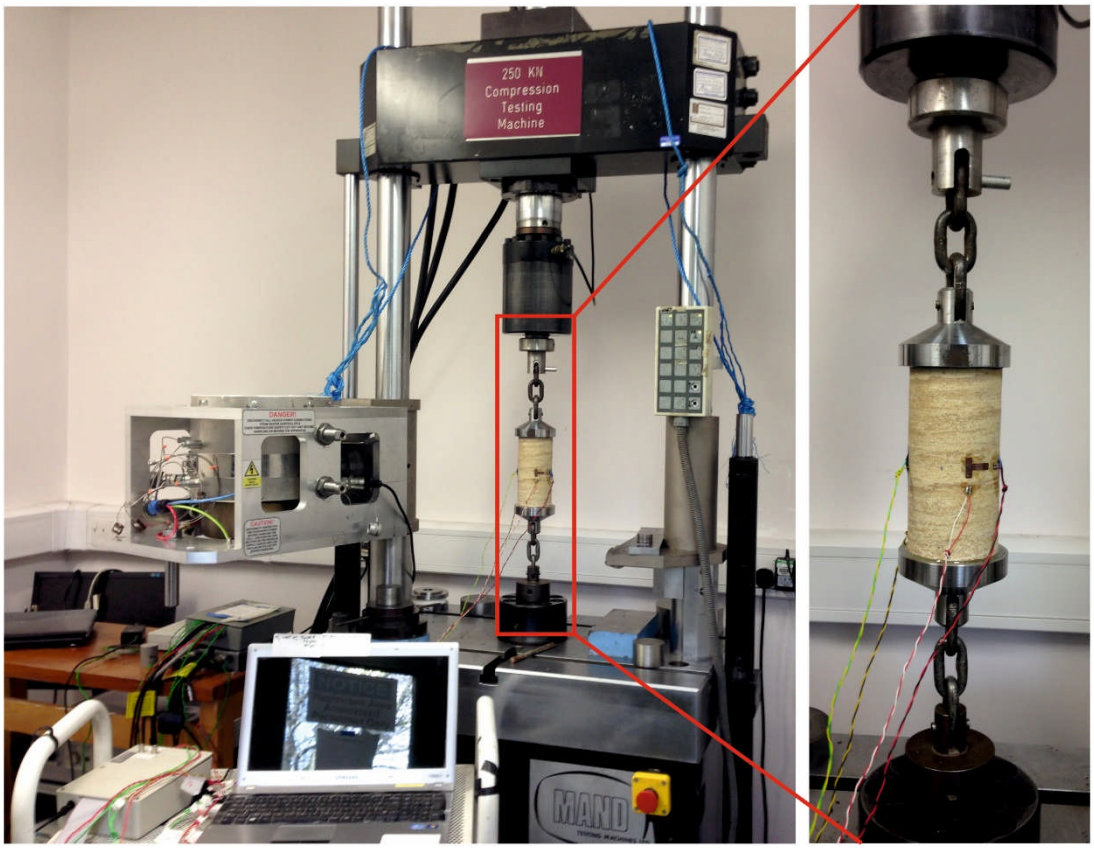

Figure 3.15 Set-up of uniaxial tension test on a Midgley Grit Sandstone sample containing bedding planes.

In some cases, after testing, sample were glued together again by adhesive (generally much stronger than the rock bedding) and the sample retested. In others, where the failure occurred close to a platen, the sample was cut flat and ground prior to gluing the platen on the fresh surface. Following this experimental technique, in each subsequent test run, the samples failed along

progressively stronger discontinuities. It is assumed that few micro-fractures were induced at earlier tests and they do not influence later test results.

Table 3.2 lists tensile strengths for failures on incipient bedding planes and these strengths are expressed as a proportion of the strength of the homogeneous parent rock tested in the same manner (Table 3.1).

Table 3.2 Tensile strength of incipient bedding planes.

Sample	Height (mm)	Tensile strength (MPa)	Percentage to UTS of intact rock (%)	Average tensile strength (MPa)
BH1-1	149	0.67	32.2	
BH1-2	132	1.22	58.7	
BH1-3	112	1.69	81.3	
BH1-4	110	1.82	87.5	1.45
BH2-1	152	1.51	72.6	
BH2-2	150	1.79	86.1	

The UTS of the weakest bedding plane tested in this way was 0.67 MPa, which is approximately 32% that of the parent rock. The strength of the strongest incipient bedding plane on which failure occurred was 1.82 MPa, which is about 88% the tensile strength of the intact sandstone. Average UTS of incipient bedding planes from these tests on Midgley Grit sandstone was1.45 MPa with a standard deviation of 0.4 MPa, i.e. about 70% of the intact rock UTS. The listed data show that measured tensile strengths increased progressively with reducing sample height as samples were trimmed and reset. For example, sample BH1-1 with an original height of 149 mm failed at 0.67 MPa. For the 2nd test on this same sample (but now lacking the weakest incipient discontinuity) the UTS was 1.22 MPa and then progressively 1.69 and 1.82 MPa. The weakest link failed first, followed by progressively stronger surfaces though the same sample.

Stress-strain relationships of sample BH1 are shown in Figure 3.16. The stress-axial strain curves represent the full sample length, rather than locally at the strain gauges. These curves are essentially linear up to failure. Figure

3.17 presents photographs of the failure patterns. It can be seen that samples break along stronger bedding planes each time.

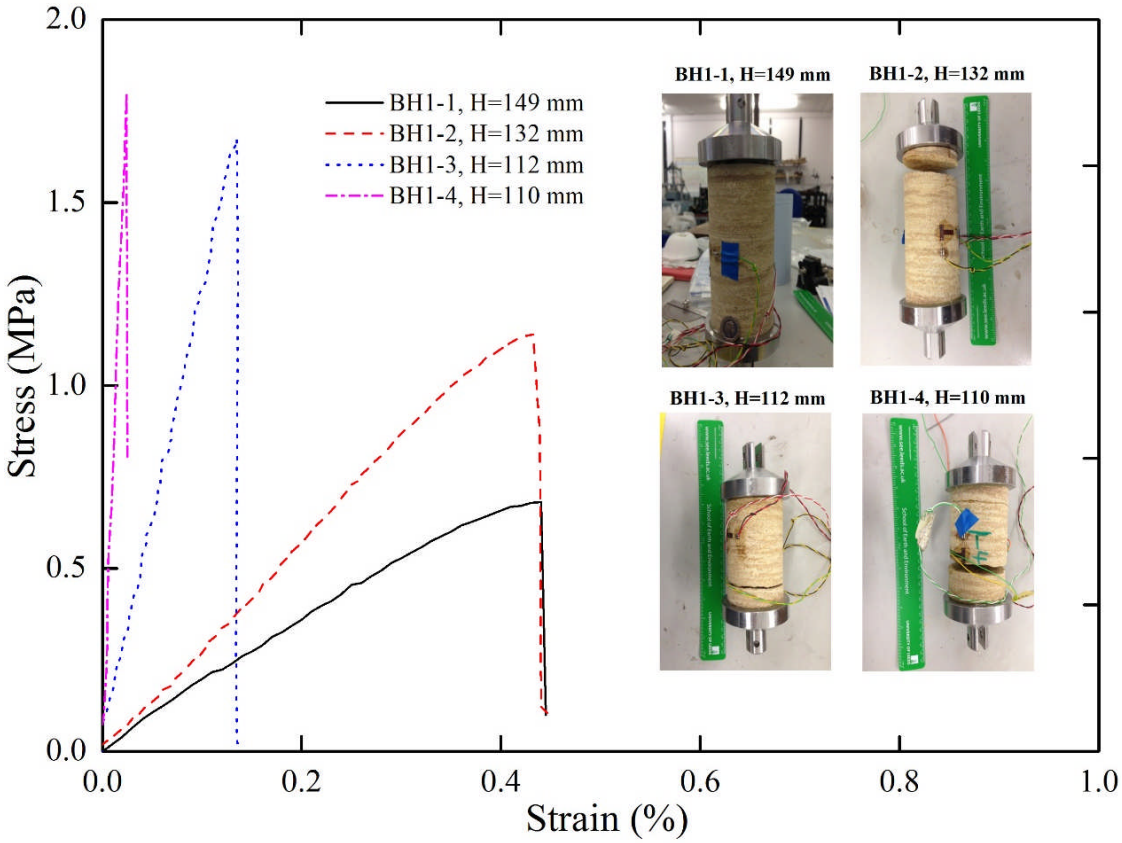

Figure 3.16 Stress vs. axial strain curves of a single sample containing incipient bedding planes, tested under uniaxial tension. Following each test run, the sample was re-cemented using araldite or, where necessary, the sample recut and new platens attached prior to further testing. Note that peak strength increases with decreasing length of the sample. This reflects the progressive exposure of the 'weakest link' bedding planes as the test progressed.

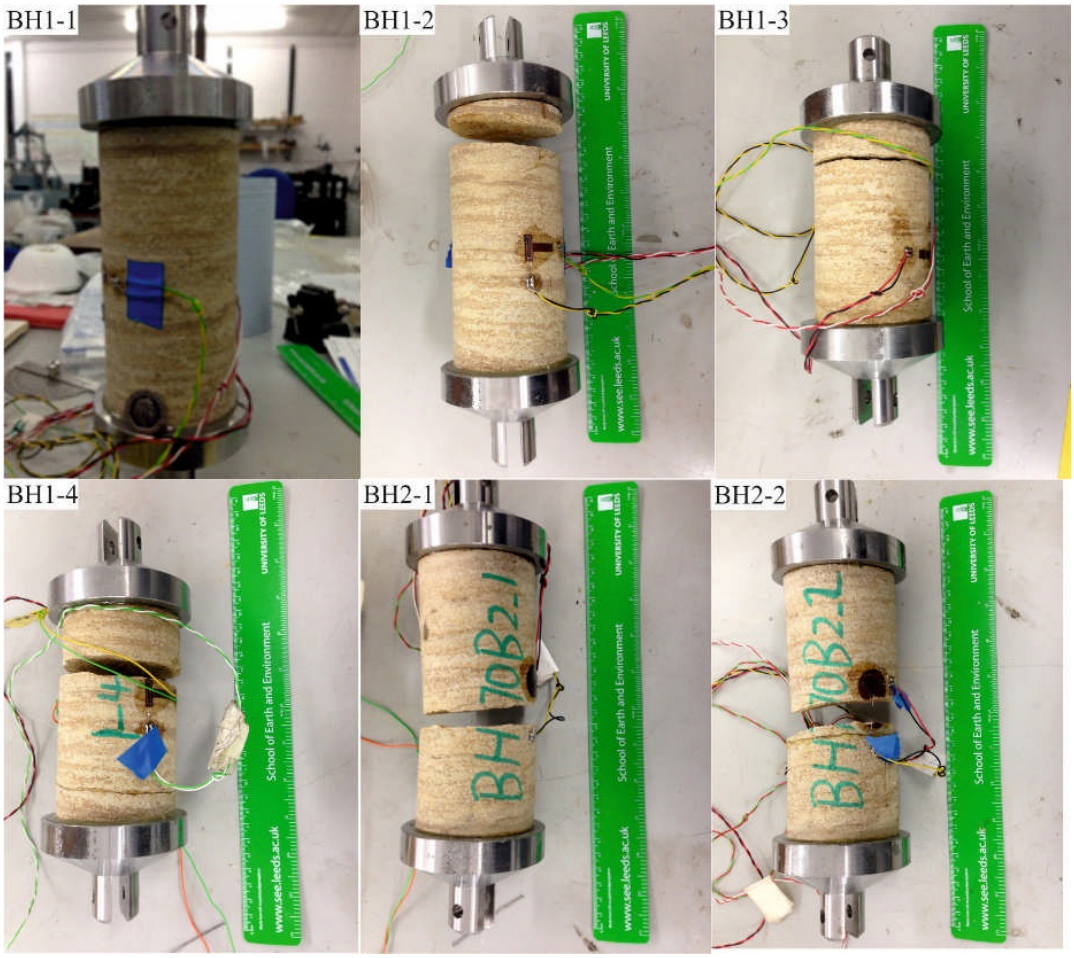

Figure 3.17 Failure patterns of incipient rock beddings under direct tension test.

3.4.2 Samples with incipient joints

Direct tension tests were conducted on samples of ostensibly homogeneous Midgley Grit Sandstone containing incipient joints, with the samples drilled so that the joints were approximately orthogonal to the tensile force. Setup and failure of a sample is shown in Figure 3.18. Stress vs. axial strain curves are presented in Figure 3.19. The inset photos illustrate that failure always occurred along the incipient joint planes. All six samples with incipient joints underwent brittle failure at a relatively low axial strain (0.05%-0.2%) compared to some of the tests on incipient bedding planes (Figure 3.15). Table 3.3 shows that UTS values for these incipient joints varied from 0.48 MPa (sample BH70J2) to 1.34 MPa (sample BH70J5).

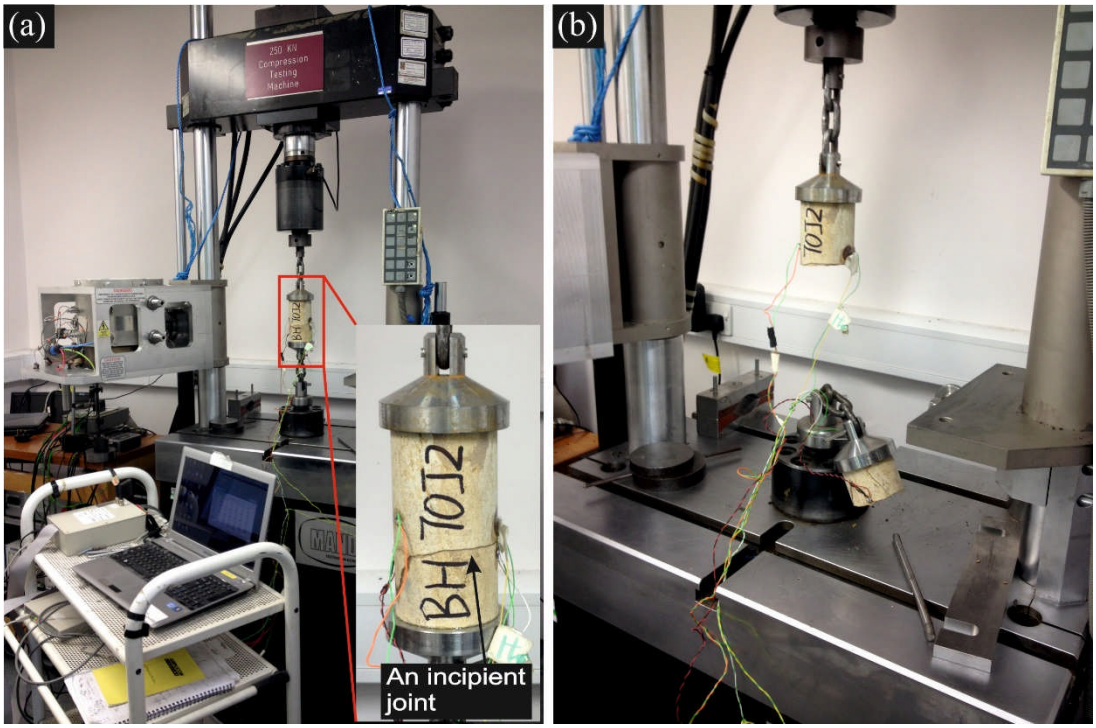

Figure 3.18 a Direct tension set up of Midgley Grit Sandstone containing a nearly horizontal incipient joint; **b** Post tension test of the same sample, note that sample broke along this pre-existing incipient joint plane.

The joint surfaces were described according using a four-colour classification, i.e. fresh and light-brown, reddish-brown, greyish-brown and black-mottled as illustrated in Figure 3.20. Visual inspection of the broken surfaces suggested that the light-brown areas, more or less represented intact rock bridges, were present and these ranged from approximately 23% to 70% of the total area for different samples. The other colours represent areas with coatings of iron oxide on persistent, open sections of discontinuity. These coatings are associated with the general chemical weathering process (including propagation and opening up of incipient joints). Such portions of the joint surfaces would not be expected to offer much tensile resistance. In the final column of Table 3.3, assuming that all tensile strength was derived from the rock bridges (light-brown segments), the UTS of these rock bridges were calculated based on their visible areas; the calculated values (2.07 – 2.14 MPa) are very close to that measured for the intact homogeneous sandstone (Table 3.1). This result confirms that the variability in strength between different incipient joints results from variations in the rock bridge area as might be anticipated. The other mineral coatings contributed very little to the measured tensile strength although it is acknowledged that precipitation of

iron oxides in some joints can sometimes lead to significantly increased tensile and shear strength (Tating et al., 2015).

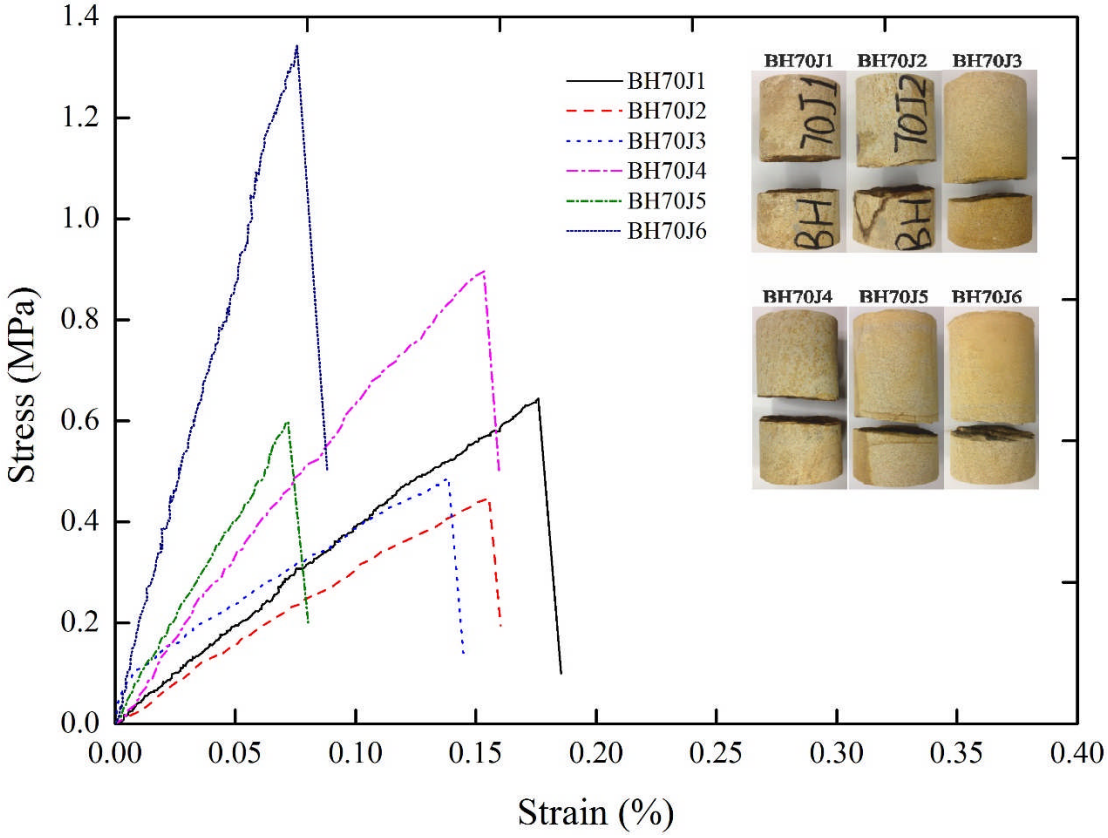

Figure 3.19 Stress vs. axial strain curves for different samples, each containing a single, visible incipient joint, under uniaxial tension. Note that elastic moduli (stress/strain gradient) varied as well as ultimate strength for the different incipient joints.

Four thin section samples were produced by cutting locally from different coloured areas on joint surfaces to investigate their optical properties. Figure 3.21 presents photomicrographs from an essentially unweathered joint surface (probably part of a rock bridge) in Figure 3.21a to a heavily discoloured part of the surface in Figure 21d. Clear grains are quartz; cloudy grains are feldspar ($KAlSi_3O_8$). A large amount of iron oxides (Haematite) are also present in Figures 3.21c, 3.21d. Although it is difficult to quantify the rate at which weathering proceeds (Turkington and Paradise, 2005), the progressive increase in quantity of iron oxide minerals from images 3.21a – d may indicate how degree of weathering gives varying colours to joint surfaces.

Table 3.3 Tensile strength of incipient rock joints.

Sample	Diameter (mm)	Tensile strength (MPa)	Percentage to UTS of intact rock (%)	UTS of rock bridges (MPa)
BH70J1	70	0.63	30.3	2.10
BH70J2	70	0.48	23.1	2.09
BH70J3	70	0.90	42.3	2.14
BH70J4	70	0.55	26.4	2.12
BH70J5	70	1.34	64.4	2.09
BH70J6	70	0.60	28.8	2.07

Note: Rock bridge areas are approximately measured as are in Figure 3.20.

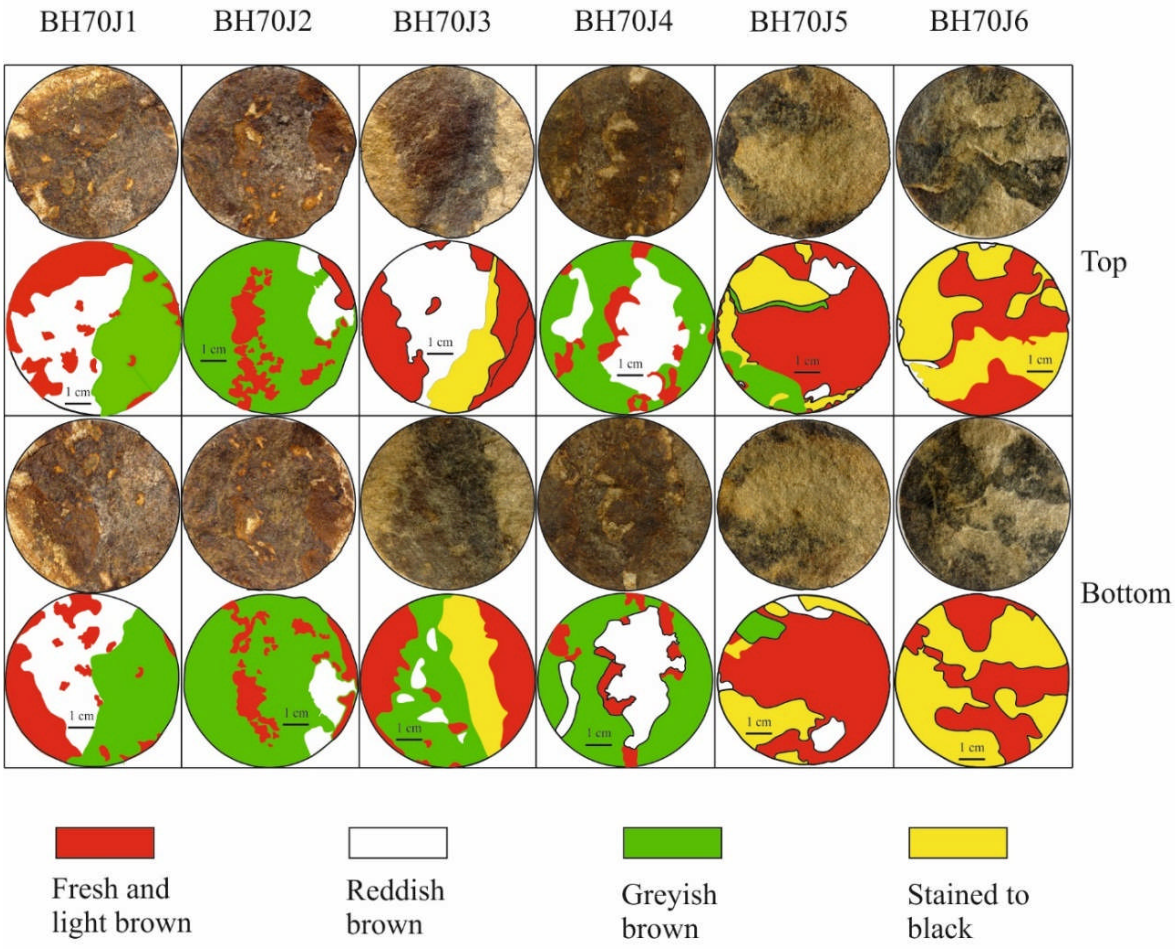

Figure 3.20 Photograph of incipient joint surfaces after failure in uniaxial tension (top images); classification of surfaces according to colour (lower images) which may reflect the degrees of weathering. More details see text.

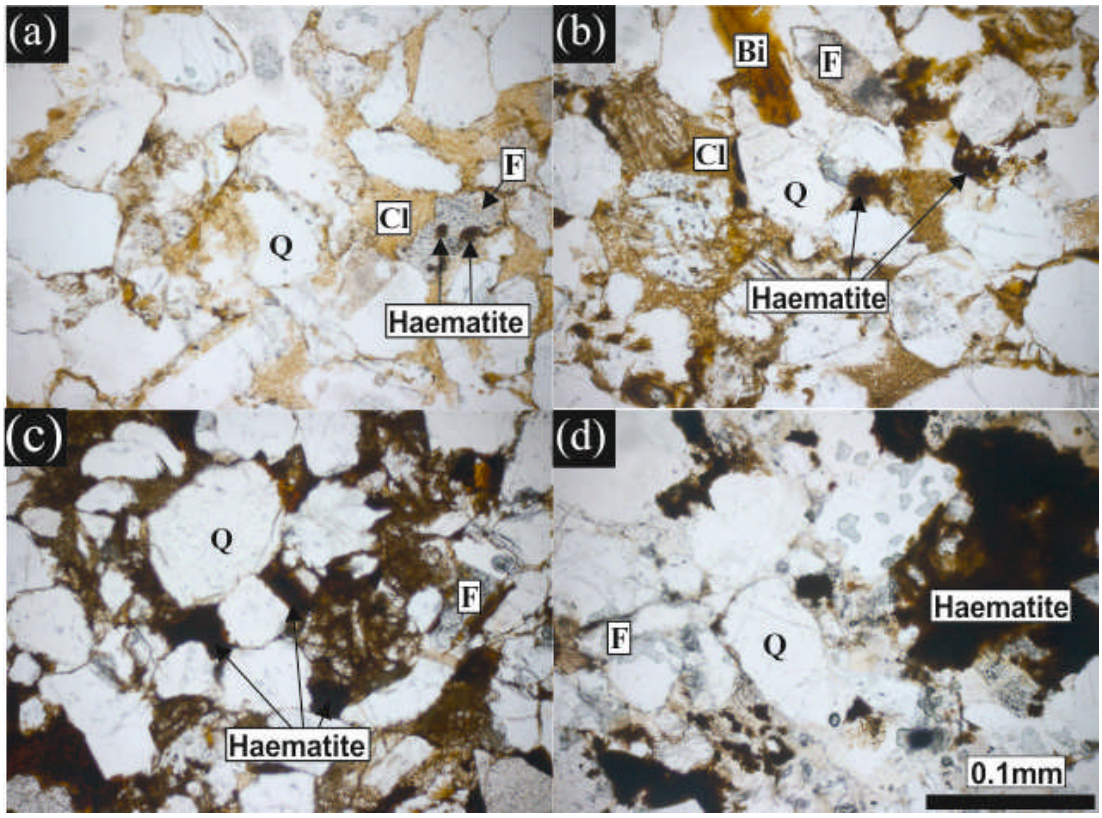

Figure 3.21 Photomicrographs of thin sections from different coloured areas on incipient joint surfaces. Thin section samples were produced by cutting locally from each area (approximately parallel to joint surface), i.e., **a** light brown area representing a rock bridge, i.e. essentially fresh rock; **b** reddish brown area; **c** and **d** greyish brown and black mottled areas. Clear grains are quartz (Q); cloudy grains are feldspar ($KAlSi_3O_8$) (F). Mottled light brown areas present in **a** and **b** are Clay (Cl). A small amount of biotite (Bi) exhibiting pleochrosim is also present in **b**. Iron oxides (Haematite) is present in increasing quantities in **a** and **b**, **c** and **d** respectively, perhaps indicating that this represents a weathering product on the discontinuity surface.

3.4.3 Samples containing mineral veins

For veined rocks, fracturing and strength are controlled by veins. Mineral veins often have complex geological histories and therefore their geometries, thicknesses, terminations and compositions are similarly complex, even at a small scale (Turichshev and Hadjigeorgou, 2014). In this set of tests, samples were cored with diameters of 50 mm and 70 mm and incipient predominantly calcite vein thicknesses typically 0.5-1.0 mm (see Figures 3.5a, b). For this test series all samples failed at the vein walls. Figure 3.22 shows the setup of direct tension test on a sample containing mineral vein and its failure state

and Table 3.4 provides a summary of test results, which varied between 0.11 to 7.13 MPa.

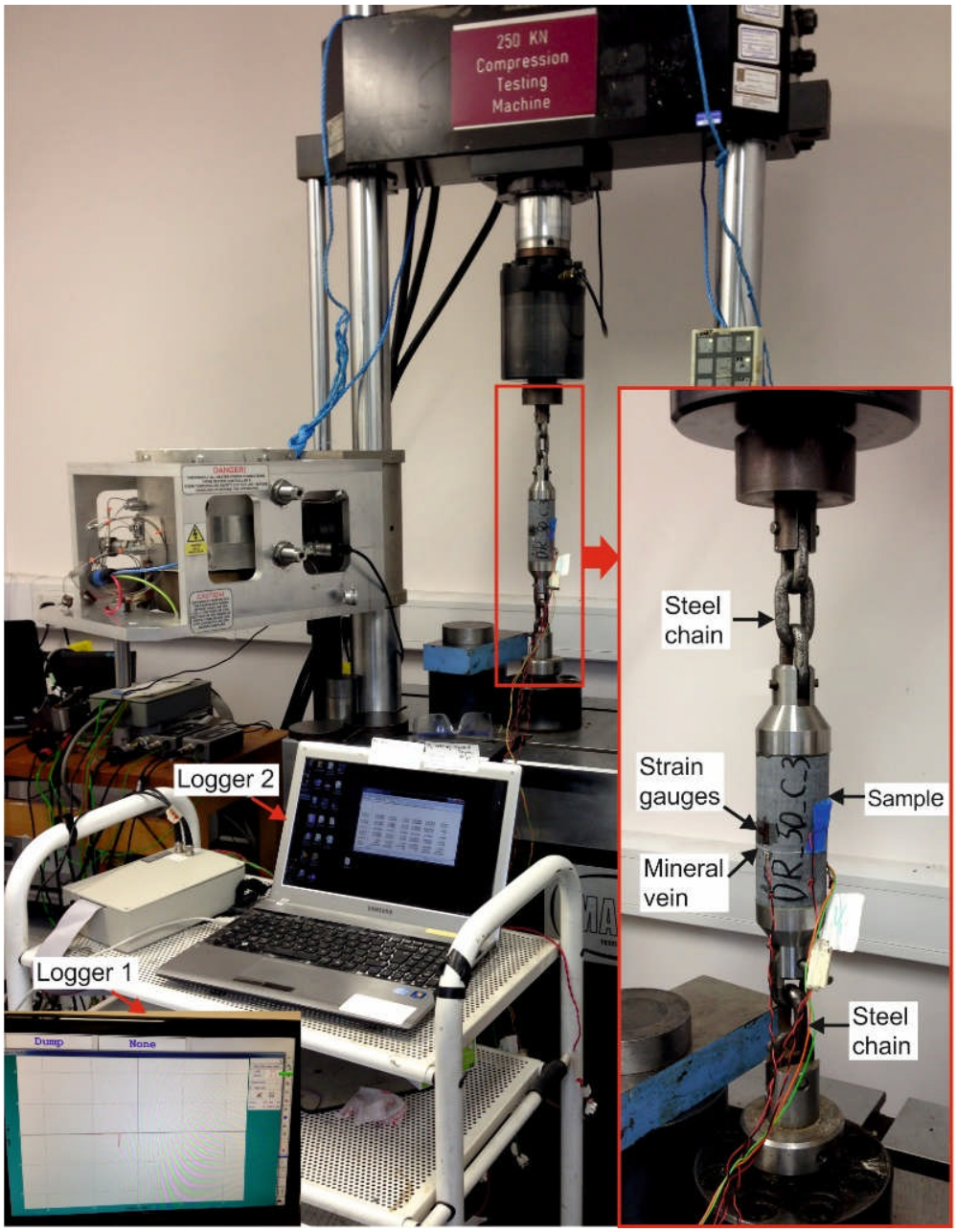

Figure 3.22 Direct tension setup of a sample of Horton Formation siltstone containing mineral vein.

Table 3.4 Tensile strength of incipient filled veins.

Samples	Diameter (mm)	Tensile strength (MPa)	Average strength (MPa)
DR50C1	50	0.49	
DR50C2	50	0.62	
DR50C3	50	1.15	
DR50C4	50	1.09	0.84 ± 0.29
DR50C5	50	7.13	
DR70C1	70	0.29	
DR70C2	70	0.44	
DR70C3	70	0.11	0.28 ± 0.19
DR70C4	70	6.68	

Note: Samples DR50C5 and DR70C4 are not included in the process of average strength calculation

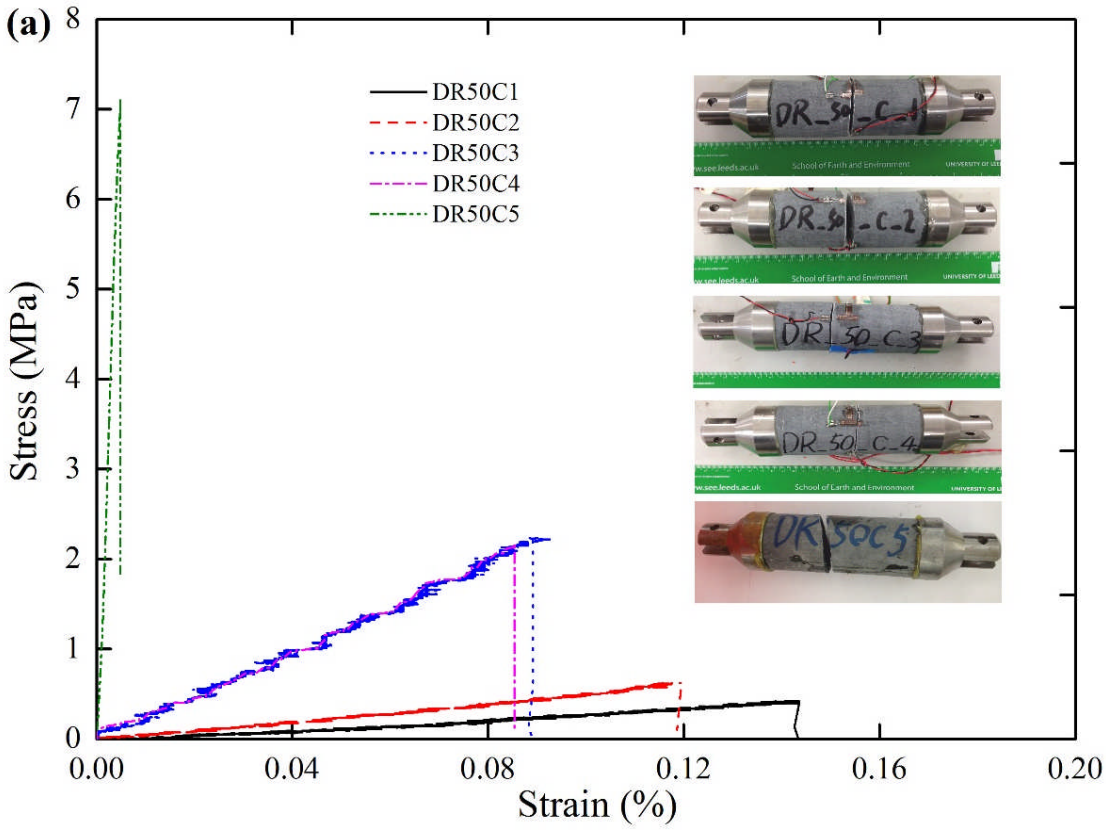

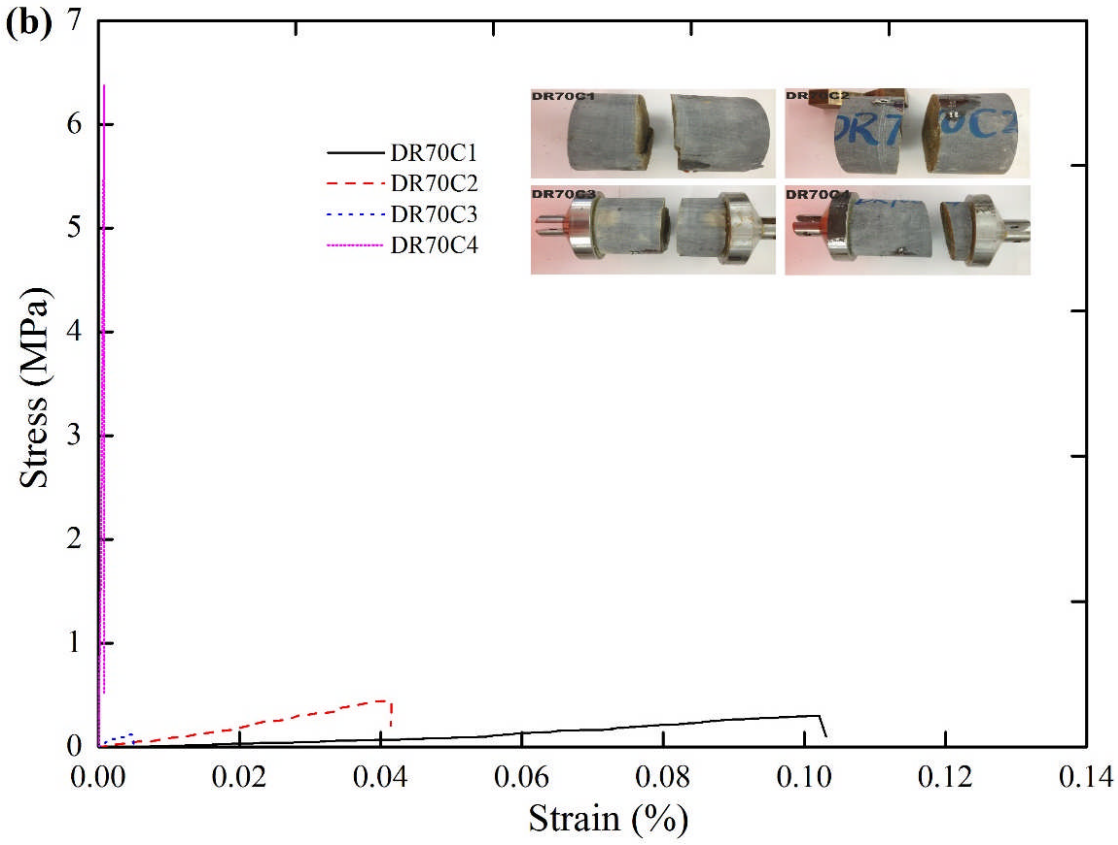

Figure 3.23 Stress vs. axial strain curves of samples with mineral veins under uniaxial tension. **a** sample with a diameter of 50 mm. **b** Sample with a diameter of 70 mm. Each sample failed at the incipient mineral vein.

Figure 3.23a presents the stress vs. strain curves for the 50 mm diameter samples together with photographs of each test; Figure 3.23b presents data from the 70 mm diameter specimens. As for the tests on incipient bedding planes presented in Figure 3.16, stress-strain curves are essentially linear before failure for all samples.

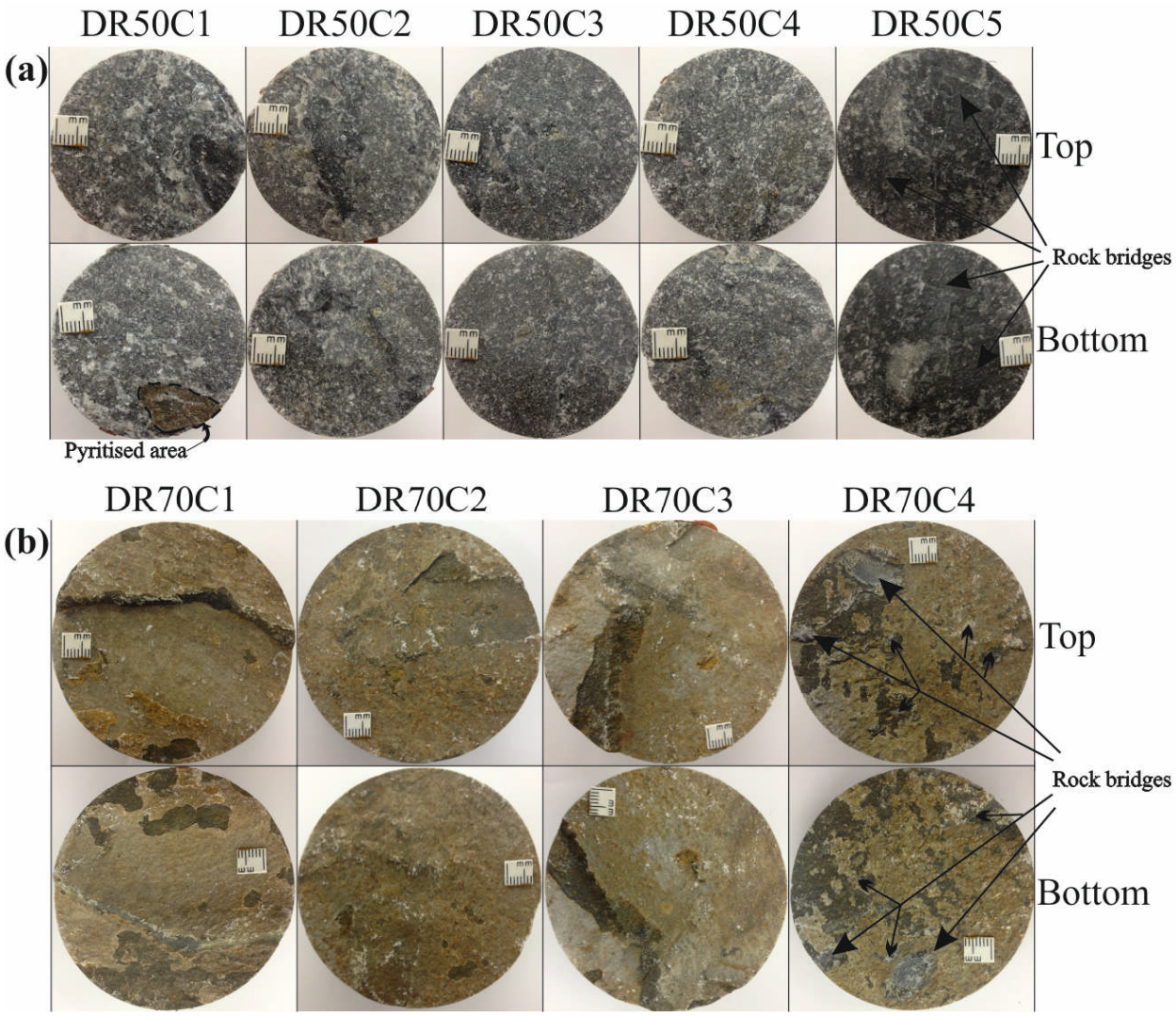

Figure 3.24 Photographs of profiles of filled veins after uniaxial tension tests. **a** vein profile with a diameter of 50 mm. **b** vein profile with a diameter of 70 mm. Samples failed at one of the walls of the incipient veins. Rock bridges along veins were revealed in sample DR50C5 (scattered fresh dark areas indicated by arrows) and in sample DR70C4 (Small scattered bridges cannot be indicated individually). A small pyritised area was revealed on sample DR50C1.

Figure 3.24 shows the surfaces exposed after failure. The data in Table 3.4 show that for two tests, much higher strengths were measured (6.68 and 7.13 MPa) than for all others, for which the measured UTS was typically less than 1 MPa. The feature that distinguishes these two samples is the presence of rock bridges of intact rock (with no mineral infill or coating). For sample DR50C5 the broken rock bridges are the discrete dark areas indicated by arrows in Figure 3.24a. For sample DR70C4 there is one main rock bridge accompanying by many discrete smaller rock bridges (Figure 3.24b).

X-Ray Diffraction analysis was used to identify the mineral composition of the veins, as shown in Figure 3.25. Three samples were prepared by scraping from pyritised and white vein segments respectively from sample DR50C1 (see Figure 3.24a) and from the orange-tinted coating from sample DR70C1 (Figure 3.24b).

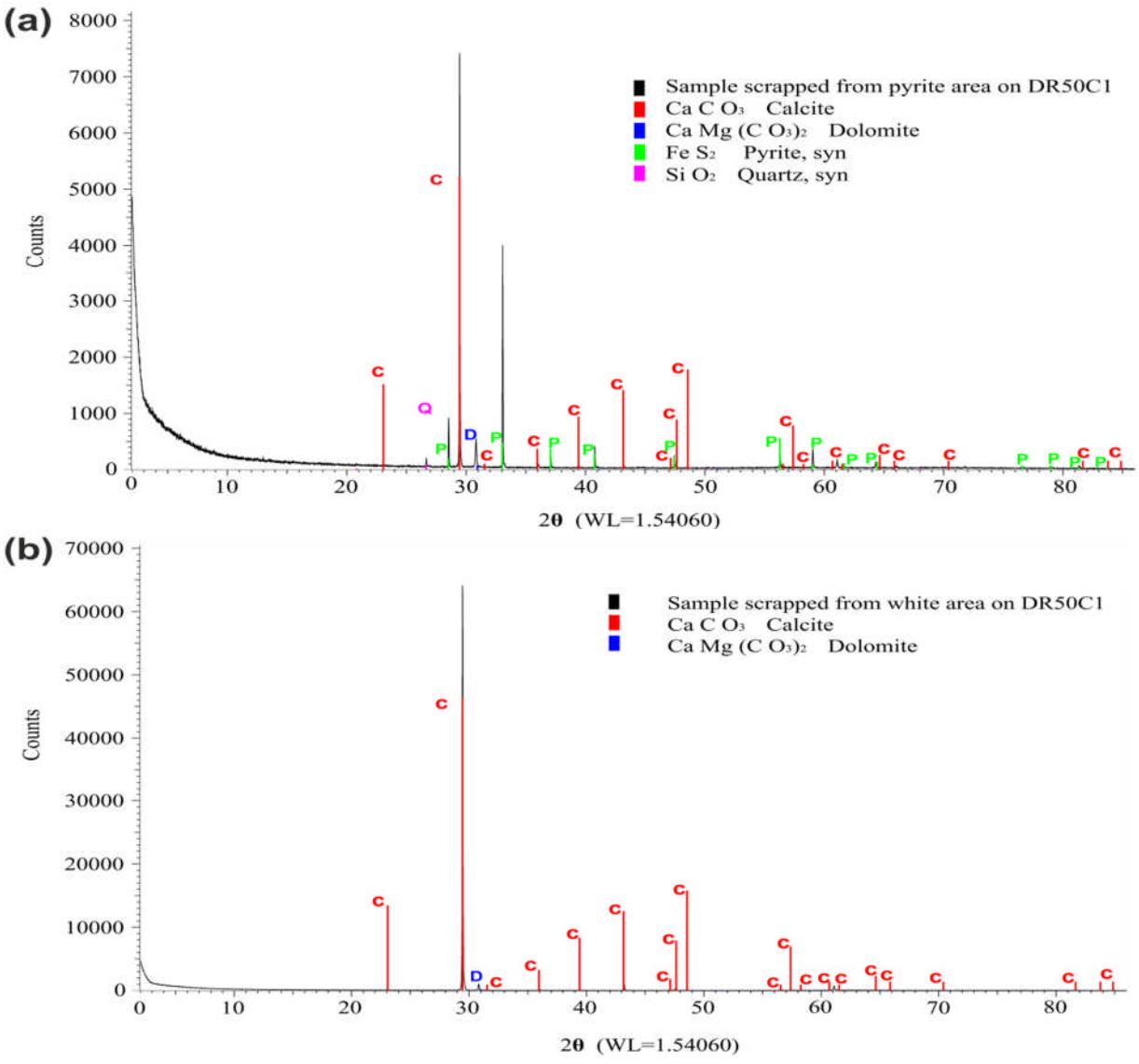

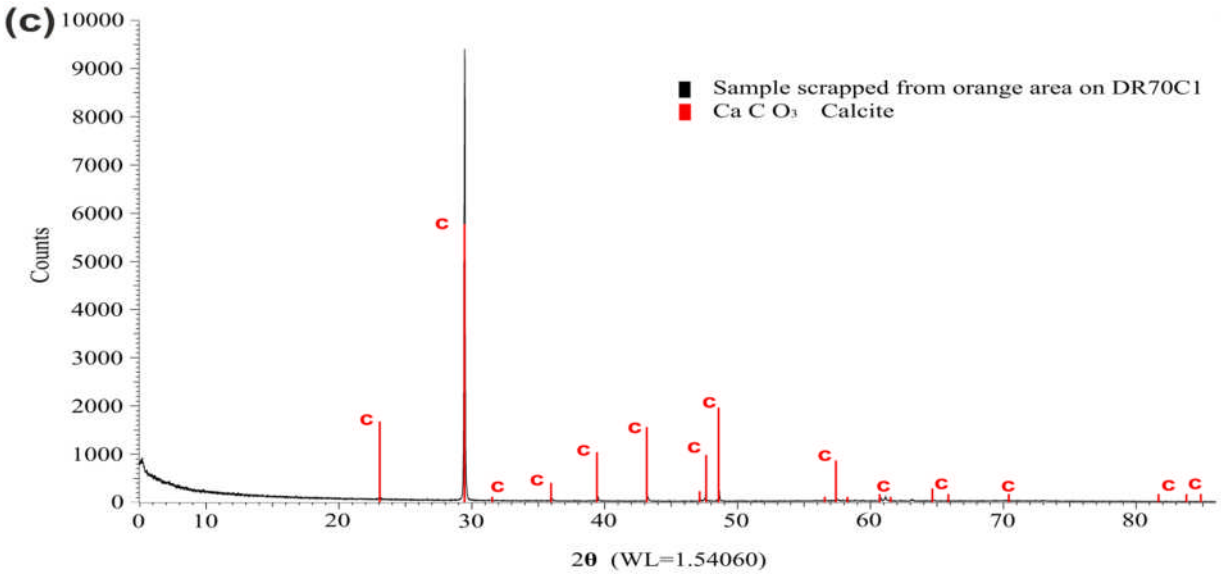

Figure 3.25 X-ray diffraction diagrams of mineral compounds of infill and pyrite area: **a** Pyrite segment on specimen DR50C1, **b** White segments on specimen DR50C1 and **c** Orange segments on sample DR70C1. Samples used for XRD analysis were scraped from veins. C=calcite, D=dolomite, P=pyrite and Q=quartz.

Test results confirmed that calcite is the major mineral infill for all samples. The orange discolouration on the 70 mm diameter samples is probably from iron oxide staining. The pyritised area from Sample DR50C1 was confirmed as pyrite but there is also calcite and a small amount of dolomite and quartz. For samples DR50C1, DR50C2, DR50C3 and DR50C4, failure surfaces were completely coated by calcite. As can be seen, samples DR50C5 and DR70C4 had rock bridges of intact siltstone with no mineral coating. Evidently these rock bridges have survived intact and unchanged from the original propagation of a fracture around them, leaving them as remnant intact rock, and the mineral infilling. The fracturing and mineralisation probably accompanied a mountain building episode in the late Silurian to early Devonian (Soper and Dunning, 2005) as evident from the observed relationships between mineralization, folding and faulting within the quarry.

3.5 Discussion

It has been found that all tested bedding planes have UTS less than the homogeneous sections of the rock and it can be concluded that the incipiency of different bedding planes can be roughly characterised by percentage of UTS to that of the parent rock. For an individual bedding plane, UTS is likely to reduce with geological time from original stronger state to weaker and

eventually, fully persistent bedding-parallel discontinuity. As can be seen in Figure 3.16, axial strain reduced markedly with measured UTS for equivalent stress levels; i.e. the tangent elastic modulus increased progressively as stronger bedding planes (and adjacent relatively weak rock) were removed. It follows that the modulus must be extremely variable locally within a sample containing incipient discontinuities of differing strength. The cohesion of an incipient joint can be caused by mineral bonding over areas of distinct rock bridge and by secondary cementation (Hoek, 2007; Hencher, 2012). For intermediate unfilled incipient joints (the type of incipient joints tested in the sandstone samples reported in this paper), joint planes can be broadly divided into the discrete rock bridges segments and the persistent fracture segments (persistent areas). Hencher and Richards (2014) reported shear test data from an intact rock bridge, revealed after shearing an incipient joint, with a cohesive strength of around 750 kPa for the rock bridge area; persistent sections of joint contribute to shear strength but only in terms of friction and roughness interactions.

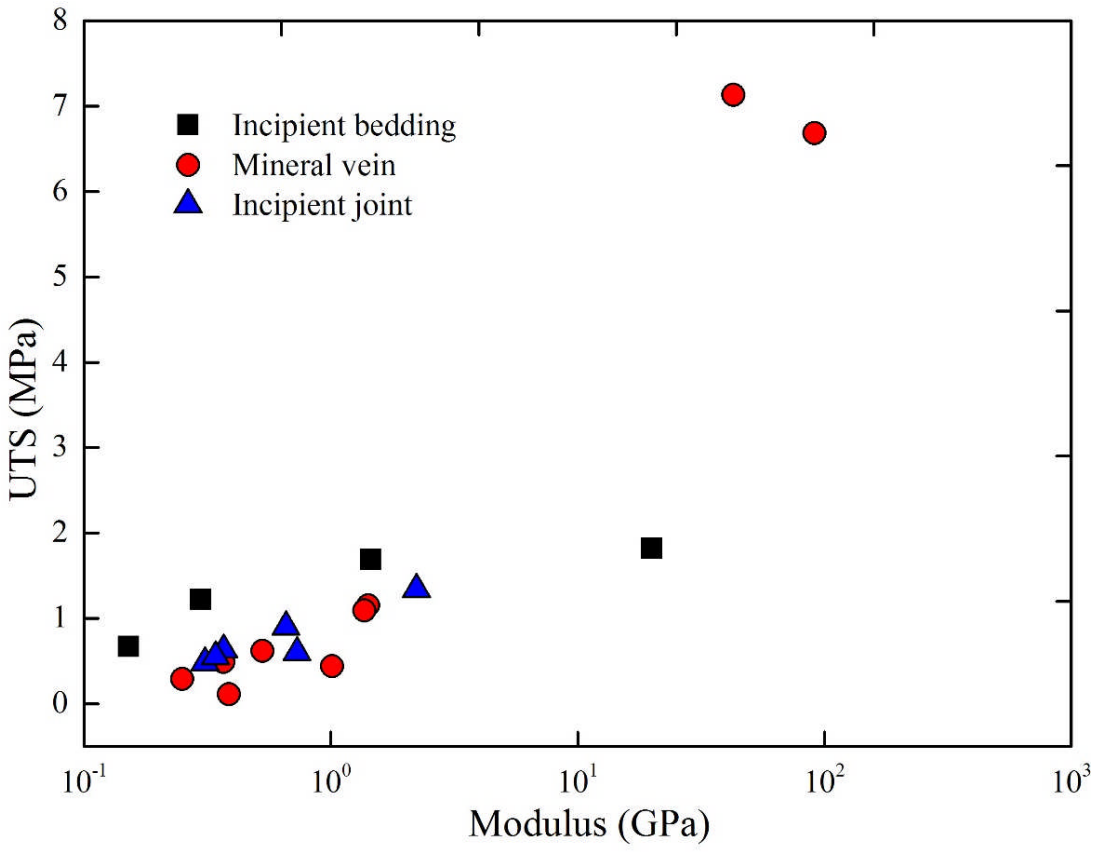

Figure 3.26 Elastic modulus vs. uniaxial tensile strength of geological discontinuities.

In relation to the UTS and modulus of incipient joints (Figure 3.26), moduli of tested samples scattered from 0.5 to 5 GPa where UTS varied from 0.5 to 2 MPa. Moduli of samples containing incipient mineral veins, similarly to that of incipient joints, scattered between 0.5 and 2 MPa, expect two cases (samples DR50C5 and sample DR70C4) which rock bridges exist.

Different sections of incipient discontinuity in the field may have different characteristics with some areas characterised by discrete rock bridges elsewhere, mineral infill or precipitated weathering products and some sections open and with zero tensile strength. A methodology is thereby anticipated whereby strength contributions from different segments of the discontinuity can be used to predict the overall strength of the feature. This would be supported by geological analysis as to the origin and geological history that have resulted in the discontinuity characteristics in conjunction with strength tests. This subsequently might allow the predication of overall UTS of incipient joints with the same lithology and geological history based on visual inspection. In the tests reported here, colour variations of joint surfaces were associated with different weathering degrees and/or mineral alteration products and hence potentially different tensile strengths. In this particular case (for the tests on joints), the strengths of rock bridges overshadowed contributions from coatings on persistent sections but there will be situations where contributions will come from various factors and sources.

Brzovic and Villaescusa (2007) produced a classification of mineral infill based on strength, and calcite (the major component of vein infill tested here) was graded as ‘soft’ This is supported by the results of vein tests from this paper (Table 3.4) which show that the tensile strength is much lower for samples with calcite veins than the intact rock. Where veins were non-persistent so that there were rock bridges of intact rock then the strength was higher and in one case apparently much higher even than might be anticipated based on the main rock bridge area (DR70C4). For this case, the rock bridge areas are approximately 1555 mm^2 (about 42 % of the total cross section area). The tensile strength of these rock bridges of intact rock was calculated as 17.8 MPa assuming zero strength elsewhere. This compares to the Brazilian tensile strength (12.5 MPa) for the intact rock. This might reflect some internal cementation and strengthening within the rock bridge area compared to the parent rock.

3.6 Summary

In this chapter, a series of uniaxial tension tests were carried on incipient geological discontinuities in cylindrical samples at laboratory scale including incipient bedding, mineral veins and incipient rock joints. Natural rock samples were cored perpendicular to the incipient rock discontinuities in large rock block samples (Figure 3.7). Tensile strength of these incipient features was identified.

Average UTS of incipient bedding planes from the tests on Midgley Grit Sandstone was 1.45 MPa. The UTS of the weakest bedding plane tested in this chapter was 0.67 MPa, which is approximately 32% that of the parent rock (2.08 MPa). The strength of the strongest incipient bedding plane on which failure occurred was 1.82 MPa, which is about 88% the tensile strength of the intact sandstone.

Tensile strength of incipient joints varied between 0.48 MPa and 1.34 MPa. UTS of rock bridges on joint surfaces were calculated (2.07 – 2.14 MPa) which are very close to that of intact rock (2.08 MPa).

For mineral veins under direct tension, all samples failed along vein walls. Tensile strength of these veins varied between 0.11 and 7.13 MPa. Two cases with much higher tensile strength measured (6.68 MPa and 7.13 MPa) were due to the presence of rock bridges.

Chapter 4
Development of the original methodology to quantify the tensile strength of large-scale incipient rock discontinuities

4.1 Introduction

Uniaxial tensile strength of incipient discontinuities has been measured using natural rock samples (70 mm in diameter) in the laboratory (see Chapter 3). Some incipient discontinuities/joints which are partially developed indeed have tensile strength mainly arising from residual rock bridges.

Like the traditional mechanical tests in the laboratory, in the uniaxial tension test, a servo-controlled loading machine was used to apply tensile force to small regular cylinder samples. To investigate the tensile strength of larger-scale samples with irregular incipient joints, an original methodology has been developed in the laboratory which uses an expansive compound to develop the tensile force is described in this chapter.

4.2 Experimental apparatus

(1) Cordless drill

A set of 36V cordless drill (Model: Makita, see Figure 4.1) with three operation modes (rotation, hammering and rotation plus hammering) was used to drill holes in rock material as well as along incipient rock joint planes. The drill has a vibration absorbing handle and a soft grip; drill bits with varying diameters up to 26 mm can be used to drill in rock or concrete materials. Four 18V-2.6Ah Li-ion batteries BL3626 and two 36V battery chargers were employed so that the drill can work continuously for a test run.

Figure 4.1 36V cordless drill (Makita) was employed to drill holes for the tests described in this chapter.

(2) Chemical splitter

In the test, an expansive chemical splitter was used to apply pressure to the sample instead of a traditional servo-controlled loading machine. The expansive grout is a mixture of Dexpan power (Non-toxic material generally comprising SiO_2, Al_2O_3, Fe_2O_3, CaO, MgO and SO_3 (Huynh and Laefer 2009) and water with a recommended ratio of 3.3 kg/L.

Dexpan is a commercial product used to crack rocks and concrete in engineering projects where no vibrations or blasting are allowed. According to the manufacturer, the expansive strength can reach 124 MPa arising from the chemical reaction when mixed with common water. The strength capacity depends on various factors including grout concentration, working/rock temperature and the amount of grout used. Three different types of Dexpan are available according to varying temperatures (type 1 from -5 °C to 10°C, type 2 from 10 °C to 25°C and type 3 from 25 °C to 40°C). For these tests, type 2 Dexpan has been used in the laboratory. Generally, it takes 24 hours for Dexpan to generate its full force and the rock or concrete will break within that period depending on their strength.

(3) Proving ring and its calibration

A 50 kN proving ring (PR) was used to install LVDT in the lab test. A servo-controlled compression testing machine (MAND) with a capacity of 250 kN was used to calibrate the PR, as shown in Figure 4.2. The tensile loading rate of 33 N/s was adopted to apply tensile force gradually. The relationship of tensile force to displacement of the PR was found, as shown in Figure 4.3. The stiffness constant of the 50 kN PR used in the tests is 0.06 (mm / kN) with a R^2 of 0.999. It can be noted that the PR works well as there is no initial resistance force.

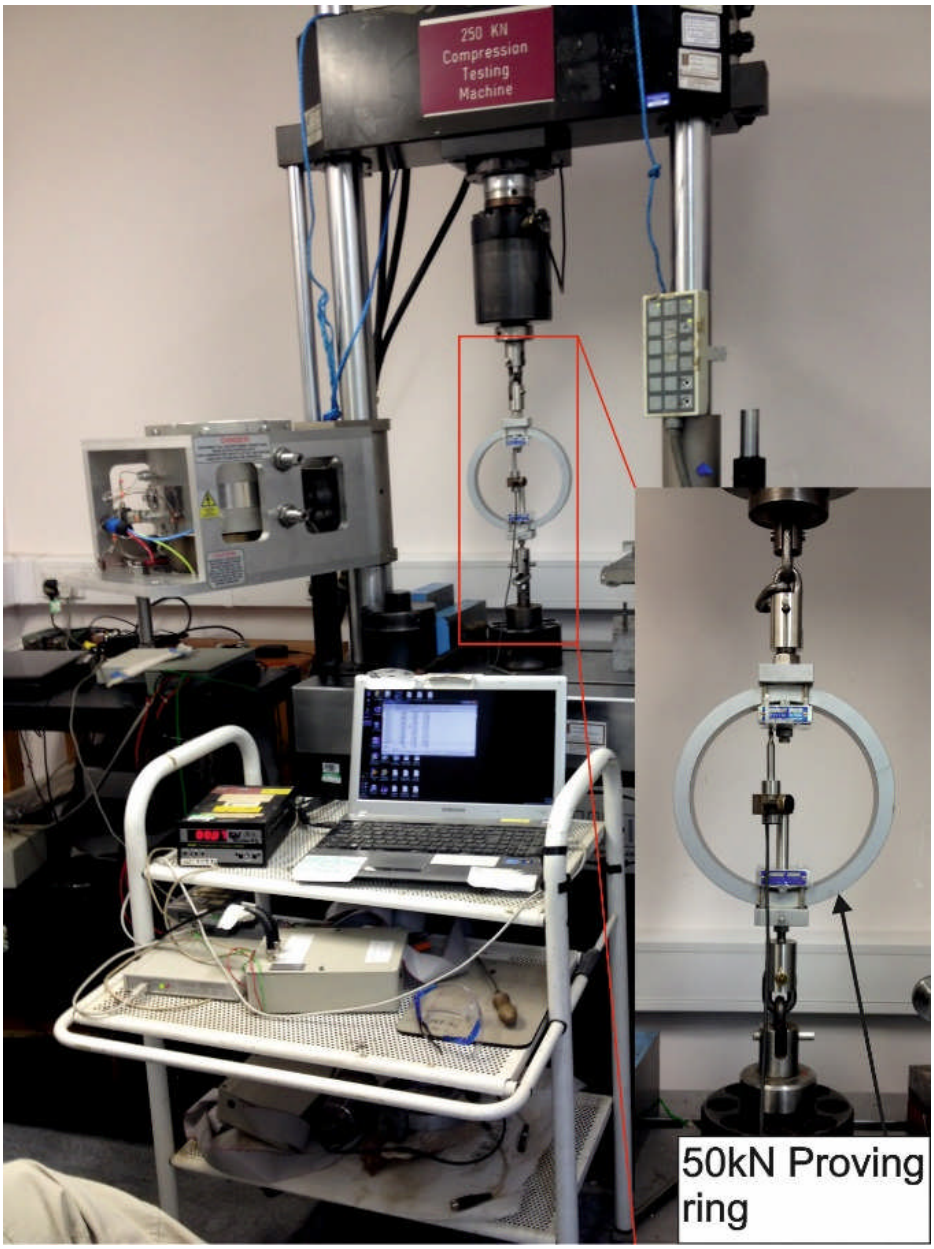

Figure 4.2 Calibration of a 50 kN proving ring (PR) using the 250 kN compression machine under a loading rate of 33 N/s. LVDT was installed in the middle of PR. Applied tensile force and corresponding displacement were logged by a laptop.

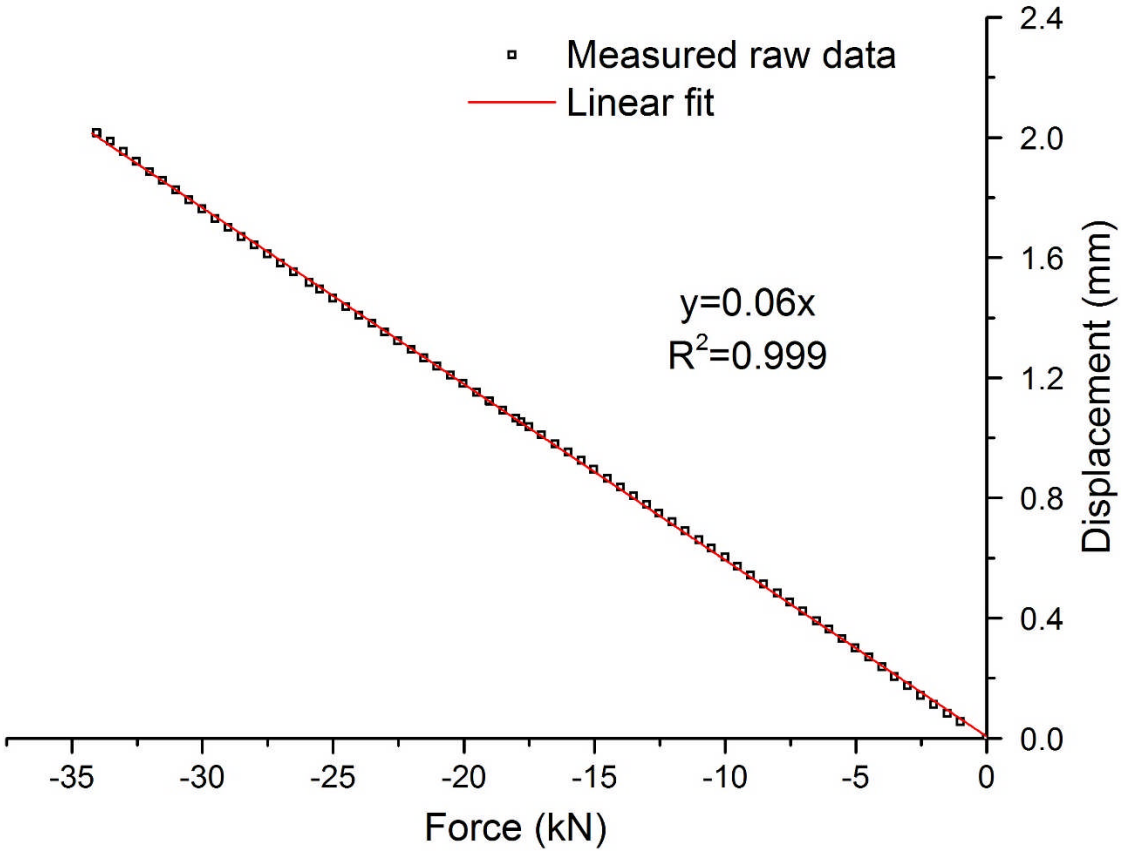

Figure 4.3 Relationship between the applied tensile force and displacement of the 50 kN proving ring used in the tests. The measured stiffness of the PR used is 0.06 (mm / kN).

(4) Other equipment

Other accessories used in the test include button-compression load cells (0 - 50 kN), heavy duty adjustable clamps, a linear variable differential transformer (LVDT) (0 - 30 mm), spectrum plasticine, manufactured metal connectors, threaded rods and nuts suitable for the test, wood pieces and a base for the test.

Three button-compression load cells and compatible instrumentation were used in the tension tests. One is a readily available small button style load cell with a capacity of 50 kN that was used to measure the force generated from the chemical splitter. Two other large button style load cells with the same capacity were specially manufactured by Nova tech Measurements Ltd to the size suitable for the tests. The tensile force arising from chemical splitter was re-measured using the twin load cells as a verification.

A linear variable differential transformer (LVDT) with a high accuracy of ±0.1% up to 0-5 mm was used with the PR for the accurate measurement of displacement of PR under tension.

Two 600 mm heavy duty adjustable clamps, manufactured metal connectors suitable for the PR, 15 mm threaded rods and nuts were used to install load cells and the PR in the test. Grey spectrum plasticine, an excellent modelling material which is soft and pliable, was used to seal open edges and bottoms of holes to prevent expansive grout from leaking.

4.3 Experimental model: schemes and concepts

4.3.1 Abbreviations

The abbreviations used in the test are as follows:

$F_{D(t)}$: Applied radial force (kN) from chemical splitter, which varies time, grout concentration, room temperature, and grout amount involved, see Figure 4.4a.

F_r: Resisting force (kN) of intact rock material / incipient joint to be split.

F_i: Resisting force (kN) of rock material / incipient joint at the point of fracture initiation.

F_m: Maximum resisting force (kN) of rock material / incipient joint at sample failure, i.e. the tensile strength of the large-scale rock material or incipient joint (espressed in force units).

F_{LC}: Measured force (kN) using load cell.

F_{LCA} and F_{LCB}: Measured force (kN) using load cell A and load cell B, respectively.

F_{PR}: Measured force (kN) using PR.

$ETF_{(t)}$: The total expansive tensile force (kN) perpendicular to the splitting plane from chemical splitter (as a function of time t, see Figure 4.4c)

Figure 4.4 schematically shows the ETF arising from chemical splitter.

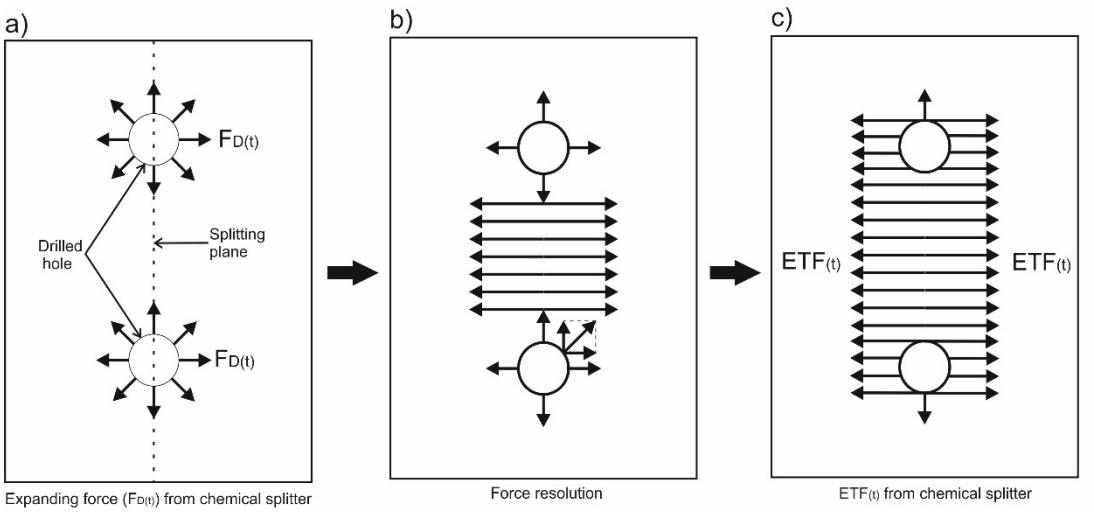

Figure 4.4 Diagram of expanding force from chemical splitter and its resolution and expansive tensile force. Figure not to scale.

4.3.2 Experimental scheme and conceptual model

In this section, a conceptual test model of the proposed methodology is described (see Figure 4.5). Each test comprises two phases: Phase i test and Phase ii test. The Phase i test reports the actual test on the sample i.e. either intact rock or incipient discontinuity. The Phase ii test is done on the broken sample to establish the ETF generated by the splitter. Two parameters including the failure time of sample under tension (measured in the Phase i test) and the $ETF_{(t)}$ (measured in the Phase ii test) at this time are measured. It is assumed that ETF measured in the Phase ii test represents the ETF at the same time in the Phase i test.

Simplified experimental graphs at some key points in each phase of test are presented in Figure 4.5. Schematic curves measured in each phase of test are also included. The Phase i test was conducted on an ostensibly homogeneous block sample with or without an incipient joint to find the time of sample failure. An LVDT together with a PR was installed at the top of sample, and there was no constraint at the base. Chemical splitter was employed to apply tensile force parallel to the LVDT in the middle. For the purpose of analysis, the whole test is assumed to occur under a state of static equilibrium due to the slow chemical reaction of splitter.

Figure 4.6 presents simplified force diagrams in the Phase i test. At the initiation of test (t_0 in Figure 4.6), there will be no forces as chemical splitter takes time to generate force.

After initiation of the Phase i test, chemical splitter expanded gradually to apply tensile force acting on the plane through the chemical splitter filled holes. LVDT measured essentially zero displacement until at the time when sample failured (see Figure 4.5i).

At the point when sample failed in the Phase i test, EFT equalled to F_m (at t_2 in Figure 4.5(ii)). A fracture plane shown in the second image in the Phase i test in Figure 4.5 was induced along the plane through chemical splitter filled holes. At this time LDVT started to measure displacement (under compression) as schematically shown in Figure 4.5i. A gap was generated at the base of sample once the sample failed, because of the unconfined condition of the sample bottom.

The broken sample containing the open fracture was re-employed in the Phase ii test (see right column in Figure 4.5). Two load cells were installed parallel and ETF generated by chemical splitter was measured. Figure 4.5 (ii) schematically shows the measured force vs. time. ETF at the time t_2 (sample failure time in the Phase i test) was identified at which time it was assumed ETF was equal to F_m the maximum resisting force of rock material. Figure 4.6 shows the progressive development of the ETF, which is opposite by F_r when the sample fail at t_2. Figure 4.7 presents the relationship between forces measured by load cells and ETF in the Phase ii test.

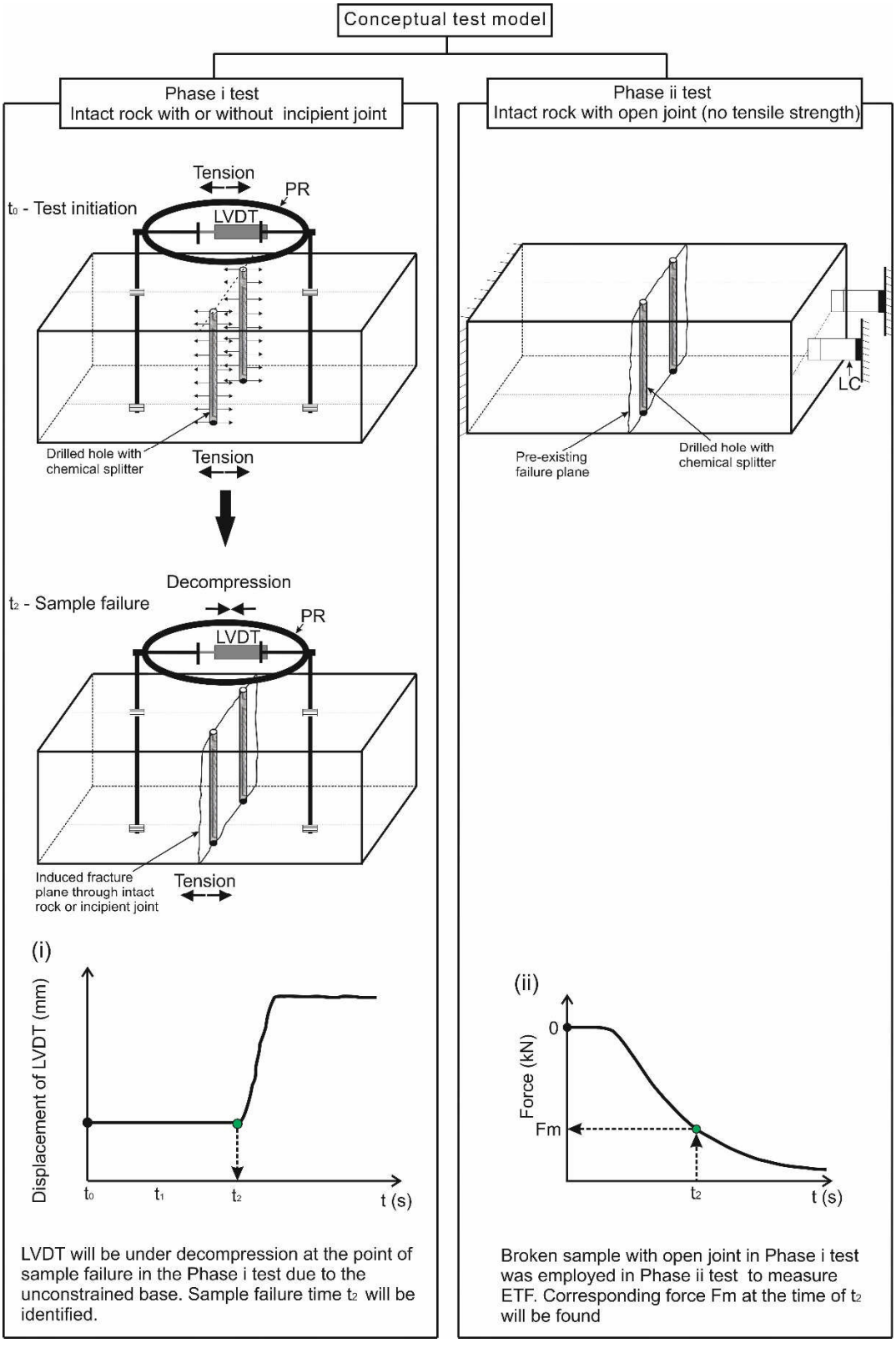

Figure 4.5 Phase i and Phase ii setup. The Phase i test: experimental schematic of tension test on intact rock sample with or without incipient joint (left column). The Phase ii test is conducted to measure ETF (right column). Simplified graphs at particular time are presented. Schematic diagrams of displacement of LVDT vs. time measured in the Phase i test and force vs. time measured in the Phase ii test are also included. For details see text.

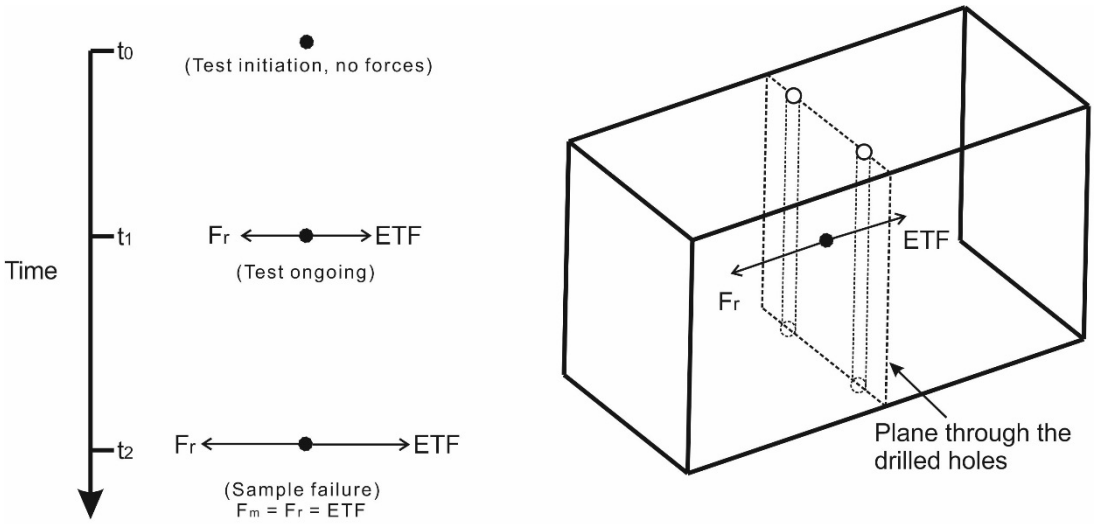

Figure 4.6 Schematic force diagrams during different procedures in the Phase i test.

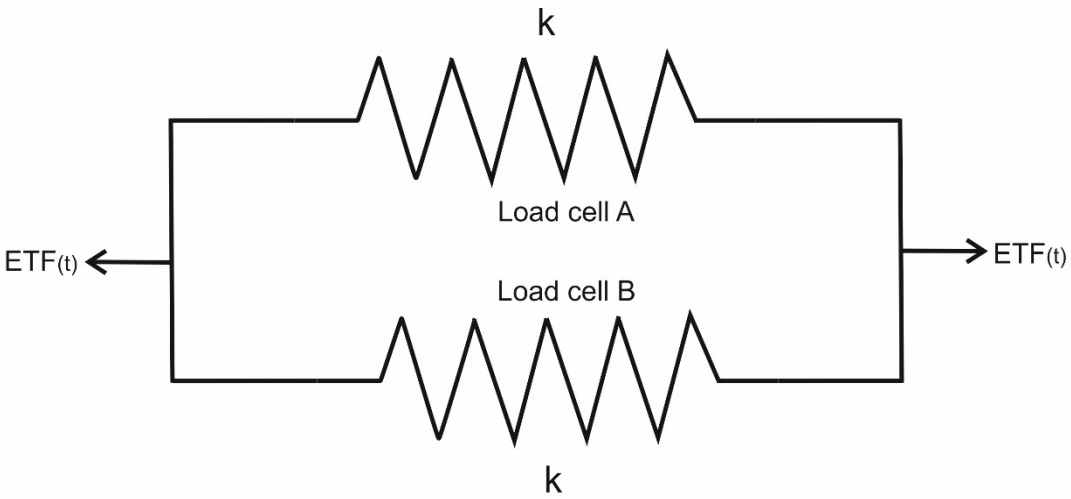

Figure 4.7 Simplified force diagram for the Phase ii test.

4.3.3 Tensile strength calculation

Tensile strength of the plane through the chemical splitter filled holes was calculated by dividing the $ETF_{(t)}$ when sample failed by the area (A) of failure plane, which can be expressed by the following equation:

$$\sigma_t = \frac{ETF_{(t)}}{A} \tag{4.1}$$

Note that tensile force is negative in this study.

4.4 Experimental setup

In this section, detailed experimental setups on intact rock sample without incipient joints, sample containing single incipient joint (Phase i test) and broken sample containing the induced fracture in phase 1 test (Phase ii test) were described.

4.4.1 Experimental setup on intact block without incipient joints (the Phase i test)

Figure 4.8 shows experimental setup on intact block sample without incipient joint. Apart from the chemical splitter filled holes, two additional holes with the same diameter as the threaded rods were drilled to install the PR, nuts were used to make sure the rigid connection between PR and sample. A LVDT was employed to measure displacement and hence identify the point of sample failure as stated in the conceptual model.

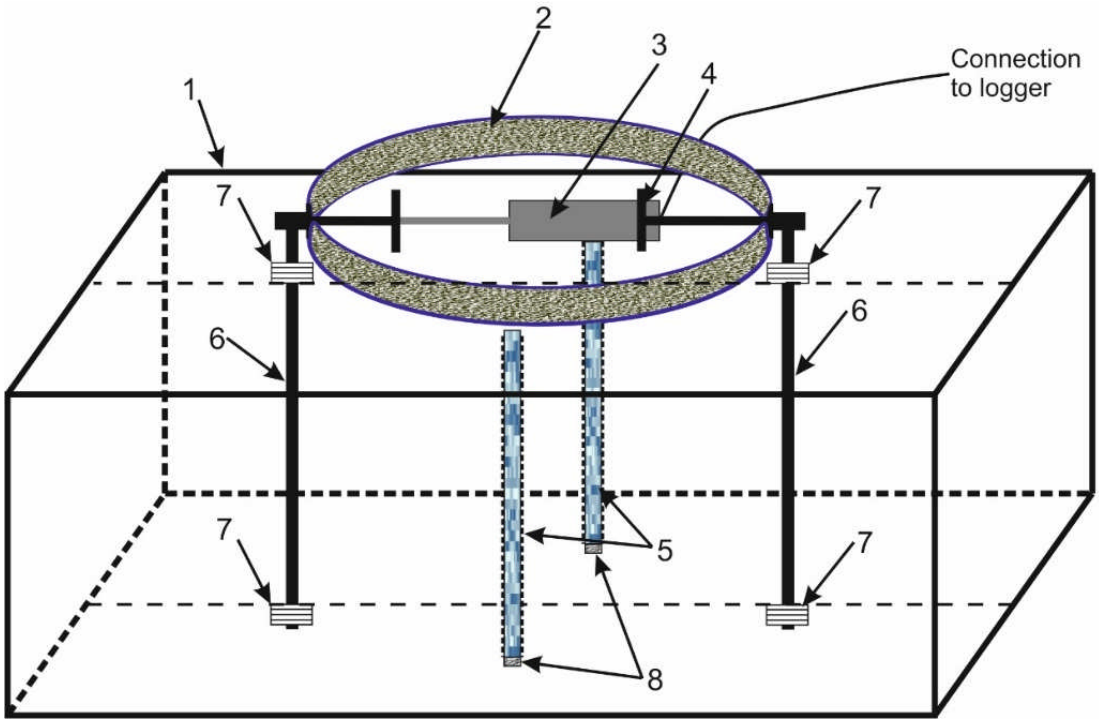

Figure 4.8 Diagram of experimental setup on intact rock block without incipient joint. For details see text. 1 - intact rock sample without incipient joints, 2 - proving ring (50 kN), 3 - LVDT, 4 - LVDT holder, 5 - chemical splitter, 6 - threaded rods, 7 - nuts, 8 - spectrum plasticine on the bottom. Figure not to scale.

4.4.2 Experimental setup on intact block containing single incipient joint (the Phase i test)

Figure 4.9 shows experimental setup on intact rock block containing a vertical incipient joint. The setup procedure is similar to that described in Figure 4.8. The main difference is that two holes were drilled along incipient joint plane in this test (assuming that the joint surface is planar). Similarly, the point of failure of incipient joint under tension can be logged during this test.

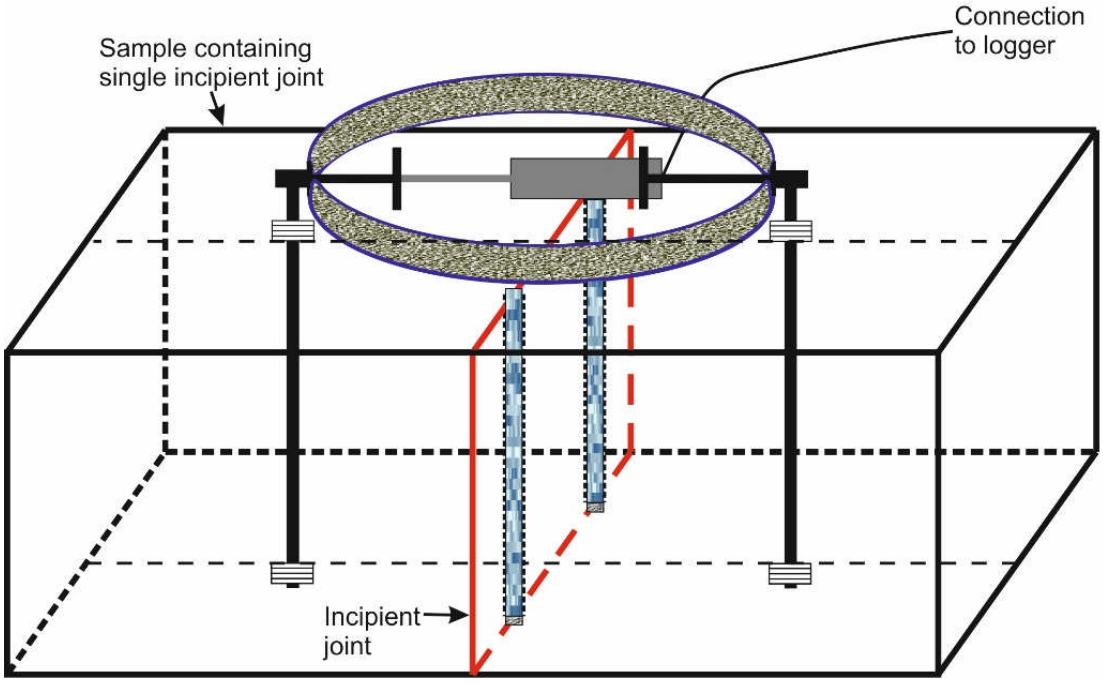

Figure 4.9 Diagram of experimental setup on intact rock block sample containing single vertical incipient joint. For details see text. Figure not to scale.

4.4.3 Experimental setup on intact block containing single induced fracture (the Phase ii test)

Experimental setups shown in Figure 4.8 and 4.9 were employed in the Phase i test to identify the failure point of intact rock or an incipient joint under tension. Subsequently the Phase ii test was conducted on same samples tested in Figure 4.8 and 4.9 but containing the fracture opened in the Phase i test (to measure ETF). Figure 4.10 shows two different experimental setups on the rock samples containing mechanical joints.

Prior to testing, spectrum plasticine was used to seal the broken edges of holes and bottom of holes to prevent chemical splitter from leaking. The PR (stiffness: k_1) and load cell (stiffness: k_2) described in section 4.2 were installed parallel on the top and base of sample separately (see Figure 4.10a).

$ETF_{(t)}$ can be calculated by adding up two readings of forces from the PR ($F_{(PR)}$) and load cell ($F_{(LC)}$). In a second arrangement, in order to eliminate the influence of stiffness difference between the PR and load cell in the measurement of $ETF_{(t)}$ (see Figure 4.10a), Load cell A and load cell B with the same stiffness were employed in this test specially manufactured by the Novatech Measurements Ltd. The twin load cells were installed symmetrically as shown in Figure 4.10b. $ETF_{(t)}$ was then obtained by adding up two readings from twin load cells ($F_{(LCA)}$ and $F_{(LCB)}$).

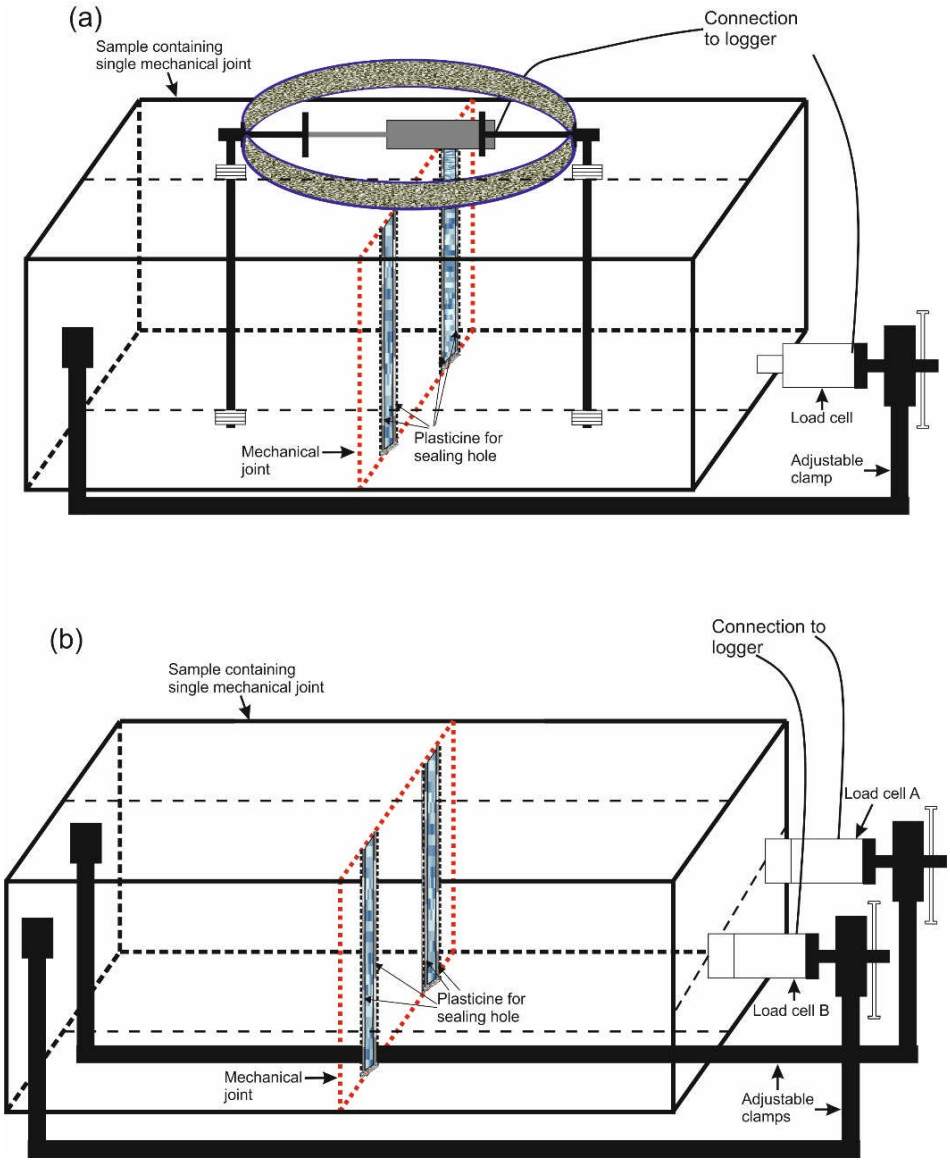

Figure 4.10 Diagram of experimental setups on rock block samples containing the fractures opened in the Phase i test (to measure ETF). **a** The PR and load cell were installed to measure ETF; **b** Load cell A and B with same stiffness were installed to measure ETF. For details see text. Figure not to scale.

4.5 Tensile tests on large-scale intact sandstone sample without incipient joint

Experimental schemes on ostensibly homogeneous rock samples and samples containing an incipient joint were the same. Tension tests on intact Thornhill Rock Sandstone and Midgley Grit Sandstone samples without incipient joints were firstly conducted to establish this methodology.

4.5.1 Tensile tests on intact Thornhill Rock Sandstone without incipient joint

(1) Sample description

Suitable samples of Thornhill Rock Sandstone with a pale greyish colour and uniform texture were collected. Sample ends were trimmed parallel and flat. The prepared sample (see Figure 4.11a) with approximate dimensions of 150 mm (H) X 280 mm (L) X 170 mm (W) was used in the test. The block sample was stored in air dry condition in engineering geology laboratory, University of Leeds. Some physical and mechanical properties including water content (3.8%), Schmidt hammer rebound hardness (43 ± 2), uniaxial compressive strength (49 ± 2.8 MPa) and point load strength $I_{s(50)}$ (1.9 ± 0.1 MPa) were measured according to ISRM standards (ISRM 2007 and 2014). The procedures for measuring these properties were briefly summarised below.

a) Water content

Small irregular samples were weighed using an electronic precision balance and drying oven setting at around 105 °C was used to dry samples for 24 hours. The weight difference of specimen prior to and after drying was used to find the water content.

b) Schmidt hammer rebound hardness

A saw-cut intact air-dried Thornhill Rock Sandstone sample with a thickness of 120 mm at point of impact was used for the measurement of Schmidt hammer rebound hardness (ISRM 2014). In this test, the block was placed on the ground and was clamped by another two larger rock blocks to prevent the sample from sliding or moving during testing. A L-type hammer was impacted roughly normal to the rock surface. Mean rebound value of 43 with a standard deviation of 2 was obtained in this test.

c) Uniaxial compressive strength

Five 25 mm-diameter core samples were prepared for the uniaxial compression test. In this test, a servo-controlled loading machine was used to apply load continuously at a constant loading rate of 1 MPa/s until sample failure.

d) Point load strength

Ten core-based samples (25 mm in diameter) with length / diameter ratio ranging from 0.8 to 1.0 were prepared for point load testing. The size correction factor was 0.75 during the strength calculation, and the mean point load strength values were calculated by deleting two highest and lowest values.

(2) Testing procedures

a) The Phase i test

Figure 4.11 presents the experimental setup on intact Thornhill Rock Sandstone (without incipient joint). Two symmetrical holes with diameter of 25 mm were drilled through rock material vertically at a spacing of 30 mm. Spectrum plasticine was used to seal the bottoms of pre-drilled holes to prevent the expansive grout (chemical splitter) from leaking. A LVDT together with a 50 kN PR was installed on the top of sample. The measuring jug, syringe and soft drink bottle were used to measure Dexpan power and water to the suggested ratio (3.3 kg / L). A metal stick was employed to mix the Dexpan power and water in a plastic bucket. Personal protective equipment (PPE) including goggles, FFP3 masks, rubber gloves and protective clothing were worn all the time when handling chemical splitter. A measuring jug and syringe were used to fill and measure the amount of chemical splitter involved in the pre-drilled holes. The metal stick was also used to agitate the expansive grout in the holes making sure no air was trapped in holes. A laptop was used to log the displacement of the LVDT during this test.

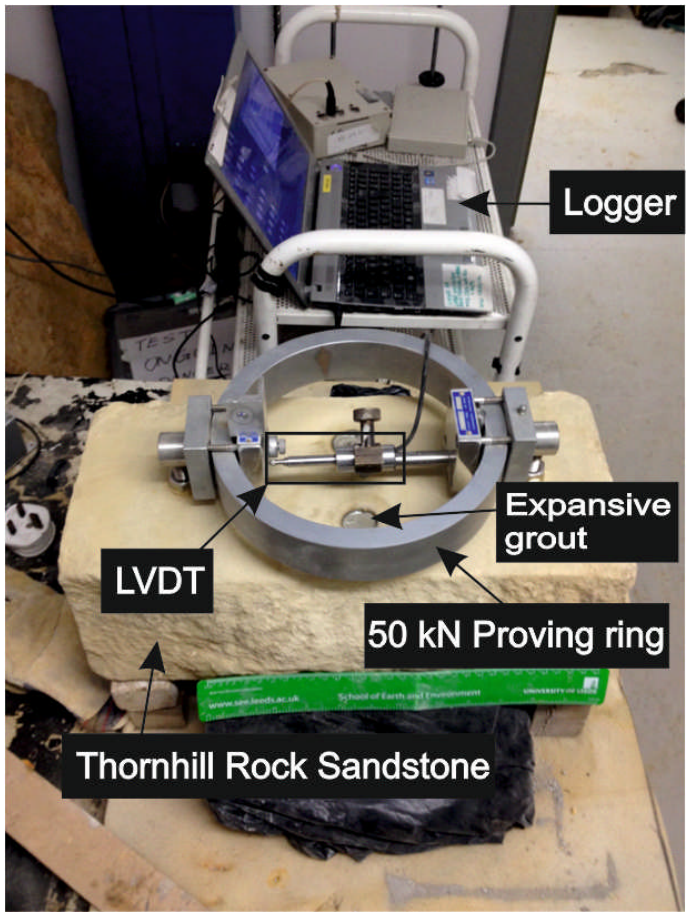

Figure 4.11 Experimental setup of the Phase i test on an intact Thornhill Rock Sandstone sample. Rule for scale is 350 mm in length.

b) The Phase ii test

The ETF arising from expansive grout was measured in the Phase ii test in which same sample used in the Phase i test but containing induced fracture was employed, as illustrated in Figure 4.12. In the test, the open fractures were placed together but had no cohesion (true tensile strength). Spectrum plasticine was used to seal the open hole edges and bottoms of holes. The Phase ii test was conducted and repeated on the same sample; the ETF was measured several times and average value was calculated.

It should be noted that two different methods of setup were employed in the Phase ii test. The first comprised the PR and load cell, as shown by Figure 4.12a. One cylinder load cell (150 mm x 50 mm) was installed at the base of sample using a clamp, other setup procedures were similar to those in Figure 4.11. Wood wedges were placed on the bottom of load cells so as to make sure the alignment of the long axis of load cell and horizontal reference axis. The initial reading of load cell was set to be 0 kN in such a manner as to ensure same initial confinement of the load cell and PR. Amount and

concentration of chemical splitter (3.3 Kg/L) was controlled to be the same as in the Phase i test. In terms of the second method (Figure 4.12b), two same load cells with same stiffness were employed to verify the validity of the ETF measured by the first method described above.

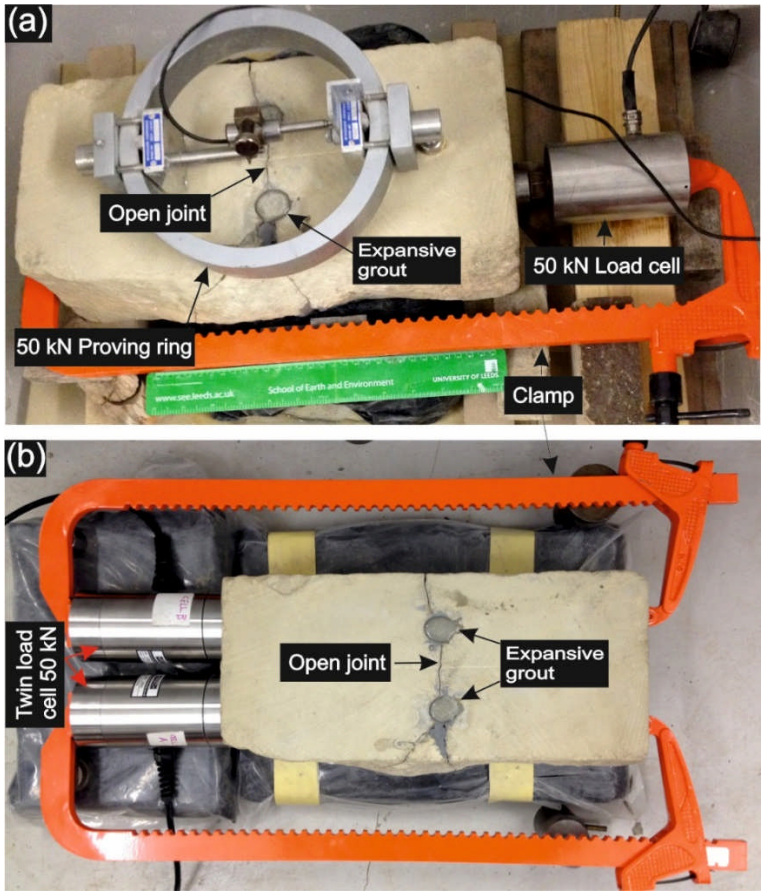

Figure 4.12 Experimental setups of the Phase ii test on an intact Thornhill Rock Sandstone sample containing open joint. **a** Type 1 re-setup method: The PR and load cell were employed in the measurement of ETF and **b** Type 2 re-setup method: Twin load cells with same stiffness were employed instead. Rule for scale is 350 mm in length.

(3) Sample failure patterns in the Phase i test

The induced fractures were irregular as can be seen in Figure 4.13a. Two fracture planes were induced on one side of the sample (Figure 4.13b), while only one fracture plane was generated on the other side (Figure 4.13c). The irregular failure pattern can be attributed to the inhomogeneity of rock sample tested. Although an irregular failure plane was induced, the plane perpendicular to the direction of ETF shown in Figure 4.13d was treated as the failure plane under tension, and its projected area was used in the

calculation of tensile strength. A gap was observed at the base of sample (see Figure 4.13c, image captured after 24 hours), the explanation for this has been made in the conceptual model (is due to confinement of the sample at the top only, by the proving ring).

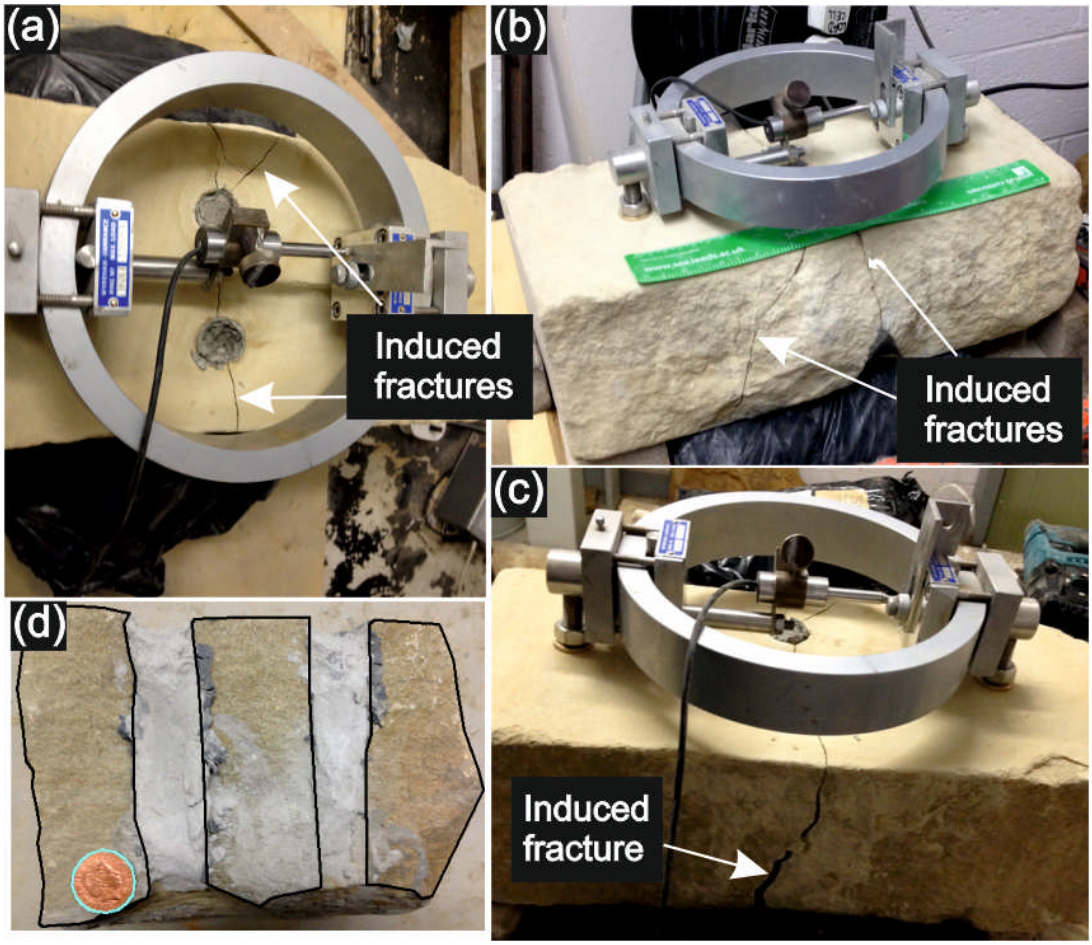

Figure 4.13 Failure patterns of the Thornhill Rock Sandstone sample under tension in the Phase i test described in Figure 4.11. **a** Front view, **b** left side view and **c** right side view. One failure surface was presented in **d**. Rule for scale is 350 mm in length, coin for scale is 29 mm in diameter

(4) Test results and tensile strength calculation

Figure 4.14 (i) shows the measured displacement of LVDT against time in the phase 1 test shown in Figure 4.11. The Phase ii tests were conducted three times and all forces measured using PR and load cell were presented in Figure 4.14 (ii).

Two turning points (point b and c) were observed in Figure 4.14 (i). At point b, LVDT (in tension state) started to measure displacement of sample. This point can be treated as the initiation of macro-fracture. At point c, LVDT started to decompress which indicates the complete failure of the sample under tension,

i.e. this is when the crack at the base of the sample opened causing the proving ring started to decompress. Thus point c corresponds to the time t_2 described in the conceptual model.

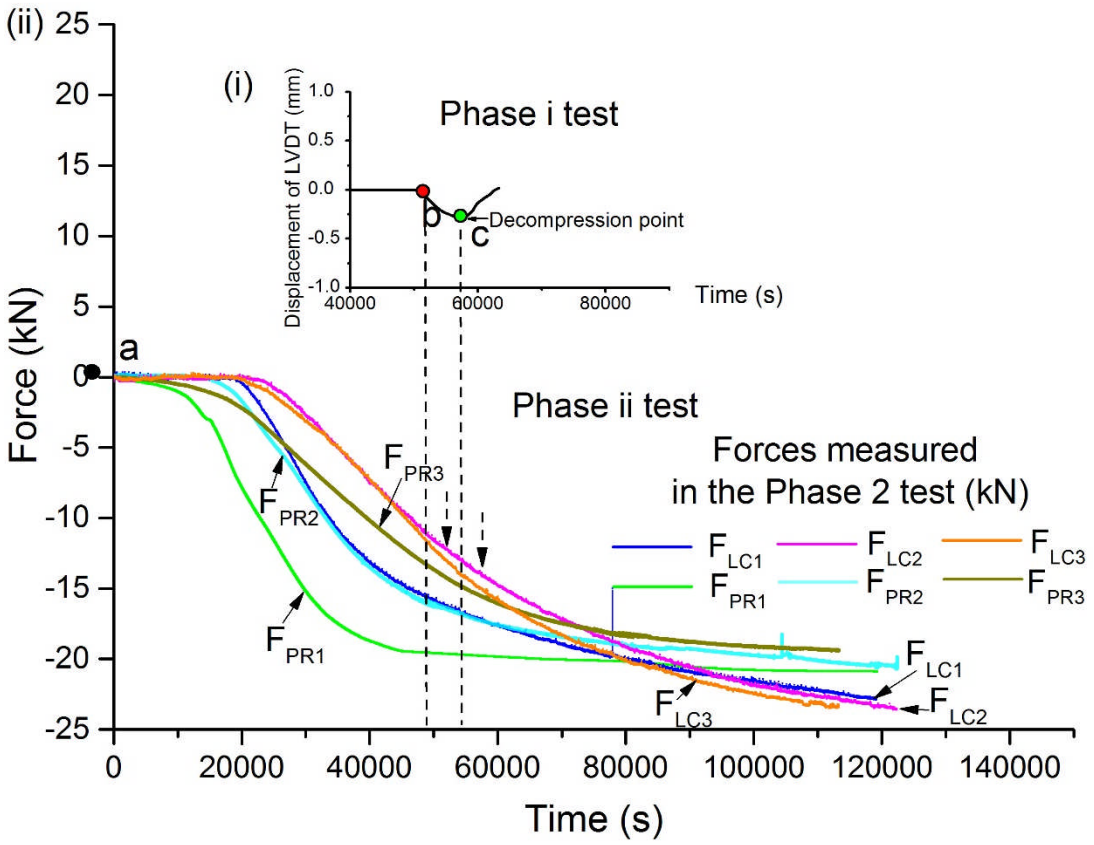

Figure 4.14 (i) Displacement of LVDT vs. time measured in the Phase i test on the intact Thornhill Rock Sandstone sample shown in Figure 4.11. **(ii)** Measured forces vs. time in the Phase ii test using the type 1 re-setup shown in Figure 4.12a. Forces were measured three times and average values were calculated in the calculation of tensile strength.

According to Figure 4.14 (i), the time at point b when macro-fracture initiated was 51514s after test initiation while it was 58417s at the point c when sample failure (as the PR started to decompress). Table 4.1 lists the parameters and forces measured at point c in the Phase ii test. $ETF_{(58417s)}$ was calculated by adding up the values of forces measured by the PR and load cell. And average ETF of -33.4 kN for this sample setup (last column in Table 4.1) was calculated.

Table 4.1 Parameters and forces measured in the Phase ii test on the Thornhill Rock Sandstone sample shown in Figure 4.11 (Hole diameter is 25 mm).

Time (s)	Test number	Amount of expansive grout (ml)	T (°C)	FPR (kN)	FLC (kN)	ETF (kN)	
58417	1	65.6	23	-19.8	-17.4	-37.2	-33.4 ± 3.3
	2	71	20	-17.4	-14.3	-31.7	
	3	72.6	19	-15.8	-15.4	-31.2	

The tensile strength of the tested large-scale rock sample was calculated according to Eq 4.1. The area of failure plane (18,192 mm^2) was measured by AutoCAD. Thus, tensile strength of the tested large-scale intact Thornhill Rock Sandstone sample was -1.8 ± 0.2 MPa.

For comparision, Brazilian discs of Thornhill Rock Sandstone were prepared according to the ISRM standard. Average Brazilian tensile strength was obtained (3.5 ± 0.7) as shown in the last column in Table 4.2. It can be seen that the tensile strength of large-scale sample measured in this test (1.8 ± 0.2 MPa) was approximately half of that obtained from Brazilian test (3.5 ± 0.5 MPa).

Table 4.2 Brazilian tensile strength of the Thornhill Rock Sandstone.

Sample	D (mm)	L (mm)	Maximum load (kN)	Stress (MPa)	Average stress (MPa)
1	54	28	7.8	3.3	3.5 ± 0.5
2	54	29	6.9	2.8	
3	54	27.5	8.7	3.7	
4	54	23	7.1	3.6	
5	54	24	8.5	4.2	
6	54	28.5	7.4	3.1	

Figure 4.15 (ii) presents the measured forces vs. time using the type 2 re-setup method described in Figure 4.12b (i.e. two load cells rather than one LC and PR). Results (LVDT displacement vs. time) in the Phase i test was also included (Figure 4.15 (i)).

It can be seen from Figure 4.15 (ii) that the ETF was -33.9 kN at the time of 58417s. The type 2 result was in the range of ETF values (7^{th} column in Table

4.1) obtained by the type 1 re-setup method (proving ring + load cell). It is also interesting to note that this value (-33.9 kN) was very close to the average ETF (-33.4 kN). This gave some evidence that the ETF results obtained by type 1 re-setup test using proving ring and load cell are acceptable, despite the difference in stiffness between the PR and LC.

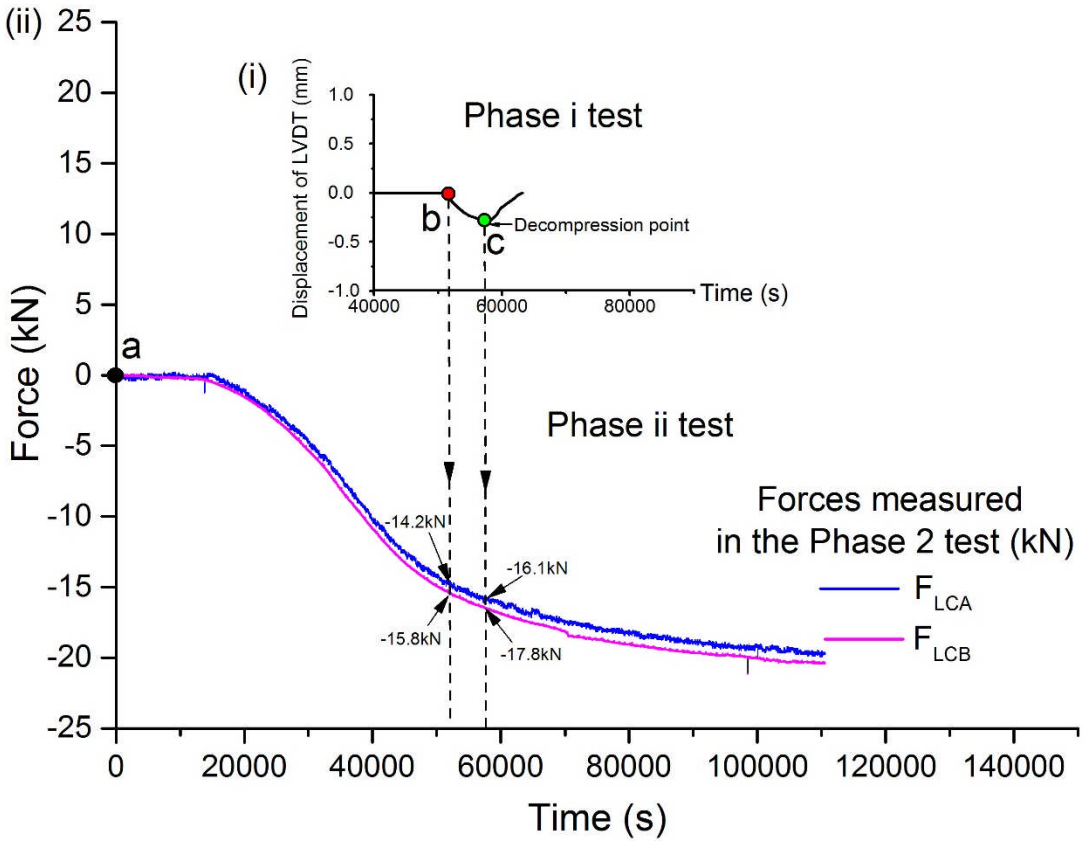

Figure 4.15 (i) Displacement of LVDT vs. time measured in the Phase i test on the intact Thornhill Rock Sandstone sample shown in Figure 4.11. **(ii)** Measured forces vs. time in the Phase ii test using the type 2 re-setup shown in Figure 4.12b.

4.5.2 Tensile tests on intact Midgley Grit Sandstone without incipient joint

This section describes the second preliminary tension test on a block of intact Midgley Grit Sandstone (dimensions: 100 mm (H) X 380 mm (L) X 170 mm (W)). The rock type was the same as those samples described in Chapter 3. The sample was stored in the engineering geology lab in Leeds University prior to testing. Some physical and mechanical properties including water content (3.2%), Schmidt hammer rebound hardness (20.8 ± 4.2), uniaxial compressive strength (25 ± 3.1 MPa) and point load strength $I_{s(50)}$ (1.4 ± 0.3 MPa) were measured according to ISRM standards. The test procedures are the same to those described in the section 4.5.1.

(1) Test procedure and sample failure pattern

The test comprised two phases: the Phase i test on the intact Midgley Grit Sandstone sample without incipient joint and the Phase ii test on the same sample but containing the induced fracture.

a) The Phase i test

The test procedures are similar to those described in the tension test on the Thornhill Rock Sandstone sample in section 4.5.1. The major difference of setup to the previous test is that two cuts with aperture of approximately 2 mm were produced using a diamond wheel saw from the edge of block sample to the holes for chemical splitter, as shown in Figure 4.16a, so as to get a regular failure plane at the edge. Figure 4.16b presents the photo at the completion of the Phase i test. A larger gap (see Figure 16b_1) was created at the base of sample. One induced fracture approximately perpendicular to the direction of ETF can be seen on the top of sample (see Figure 16b_2). The areas of failure surfaces presented in Figure 4.16c_1, c_2 were measured by AutoCAD which were 8105 mm^2 and 8596 mm^2, respectively.

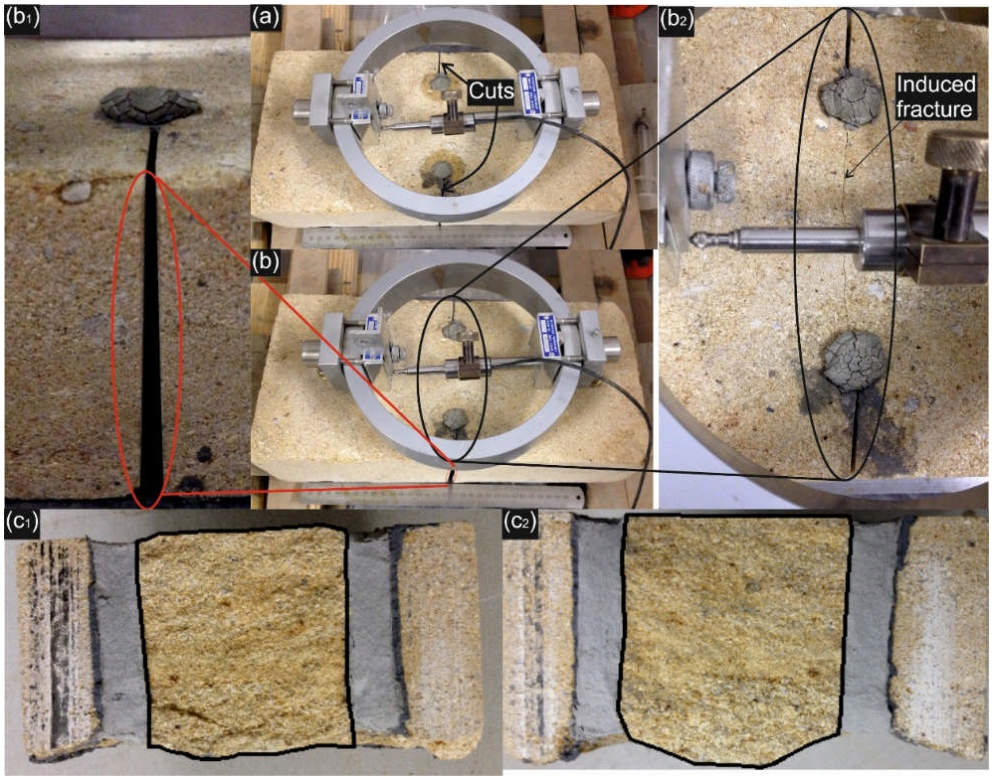

Figure 4.16 Experimental setup of the Phase i tension test on a block of intact Midgley Grit Sandstone. **a** The initiation of test and **b** The completion of test. The induced fractures were presented in **b_1** and **b_2**. **c_1, c_2** Failure surfaces between chemical splitter filled holes (areas enclosed by black lines). More details see text.

b) The Phase ii test

Again, two different types of re-setup methods (Figure 4.17a and 4.17c) were employed in the Phase ii test to measure the force from chemical splitter used. The procedures were the same as those described in Figure 4.12.

The fracture induced in the Phase i test was re-opened again to an aperture of around 1.5 mm shown in Figure 17b_1 and Figure 4.17d_1 (images were taken after 24 hours).

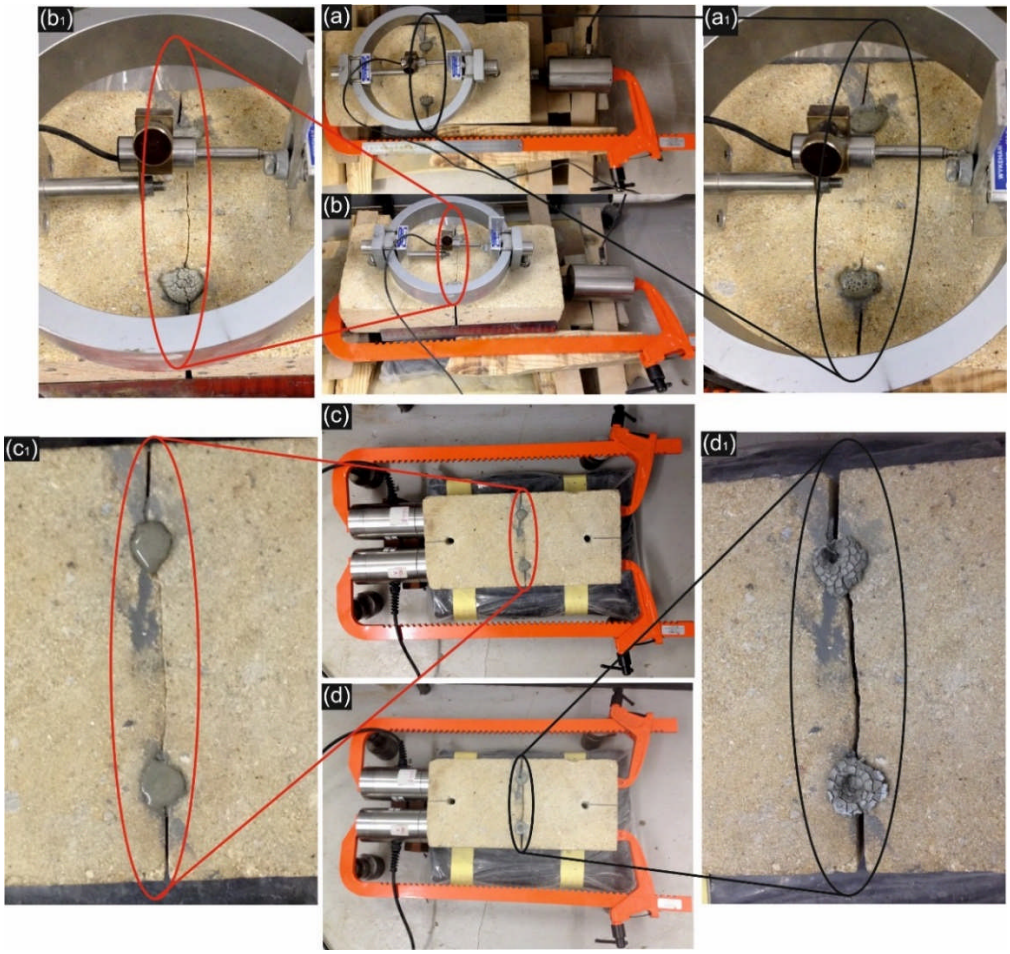

Figure 4.17 The Phase ii test conducted on the broken sample of Midgley Grit Sandstone after the Phase i test shown in Figure 4.16. **a** and **b** Photos of the initiation and completion of the type 1 re-setup test. **c** and **d** Photos of the initiation and completion of the type 2 re-setup test. More details see text.

(2) Test results and tensile strength calculation

Figure 4.18 (i) shows the displacement of LVDT vs. time measured using the setup shown in Figure 4.16a. The Phase i test curve demonstrated the time

(20339s) for initination of failure (at point b) and the time (34724s) for complete failure (at point c). Figure 4.18 (ii) presents the force vs. time of the chemical splitter measured in the Phase ii test shown in Figure 4.17. The parameters and forces meraured in the Phase ii test were listed in Table 4.3 and 4.4.

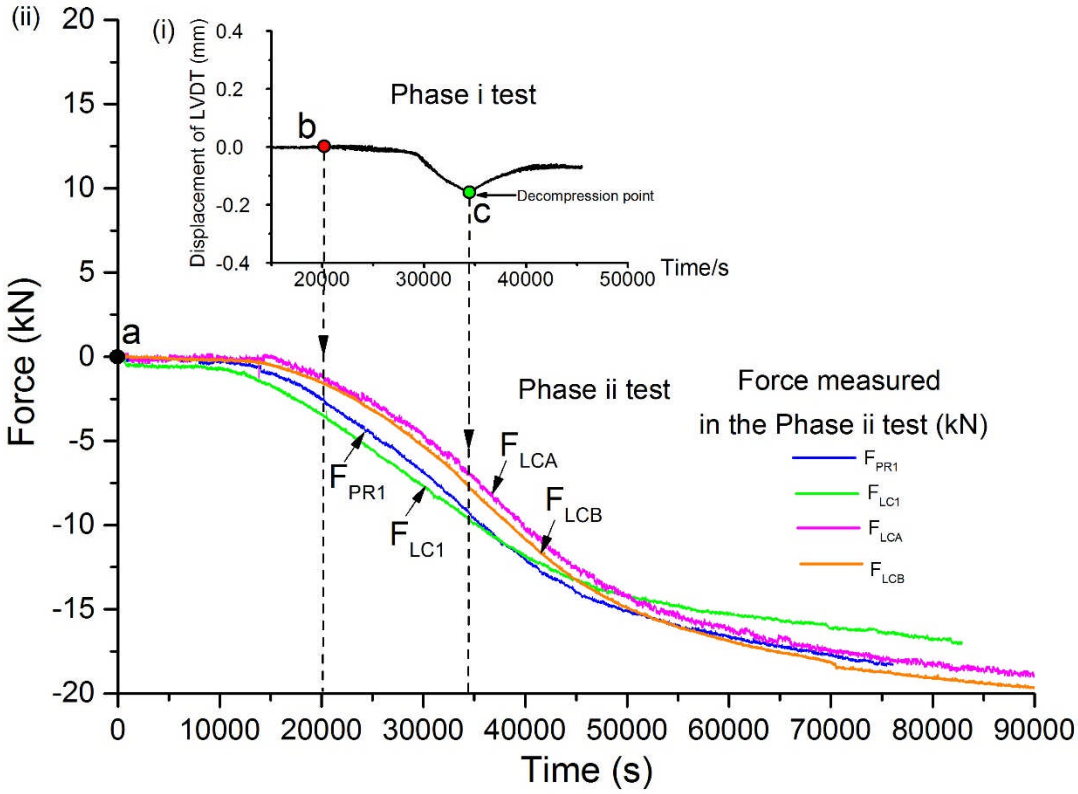

Figure 4.18 (i) Displacement of LVDT vs. time during the Phase i test on the Midgley Grit Sandstone sample using the setup shown in Figure 4.16. **(ii)** ETF from chemical splitter poured into the drilled holes (17 mm in diameter) were measured in the Phase ii test using two different re-setup methods shown in Figure 4.17.

The average ETF value was calculated (-16.7 ± 3.9 kN, i.e. average of (F_{LCA} + F_{LCB}) and (F_{PR1} + F_{LC1})) at the time of 34724s corresponding to sample failure in the Phase i test. The failed area between the two drill holes was 8351 mm^2 (because of the saw cuts at the sides, see Figure 4.17). So the tensile strength of the Midgley Grit Sandstone sample tested was 2.0 ± 0.2 MPa. The implied tensile strength of large-scale Midgley Grit Sandstone is less than the average value measured by Brazilian test (2.4 MPa), but it lies below the range of tested values (2.29 - 2.52 MPa). It is however worth to be noting that the strength (2.0 ± 0.2 MPa) measured in this test lies in the strength range (2.08

± 0.22) values measured using uniaxial tensile method on smaller cylinder samples and reported in Chapter 3 (Table 3.1).

Table 4.3 Parameters and forces measured by the type 1 re-setup method in the Phase ii test on the Midgley Grit Sandstone sample shown in Figure 4.17a (hole diameter is 17 mm).

Time (s)	Expansive grout volume (ml)	Temperature (°C)	F_{PR} (kN)	F_{LC} (kN)	ETF (kN)
20339	42.6	20	-2.69	-3.56	-6.25
34724	42.6	20	-9.57	-9.79	-19.36

Table 4.4 Parameters and forces measured by the type 2 re-setup method in the Phase ii test on the Midgley Grit Sandstone sample shown in Figure 4.17a (hole diameter is 17 mm).

Time (s)	Expansive grout volume (ml)	Temperature (°C)	F_{LCA} (kN)	F_{LCB} (kN)	ETF (kN)
20339	43.5	20	-1.72	-2.01	-3.73
34724	43.5	20	-6.32	-7.52	-13.84

4.6 Tensile tests on large-scale sandstone sample containing single incipient joint

The results of Tests undertaken on intact sandstone blocks without incipient joints indicate that a smaller tensile strength was measured using the proposed method than standard methods. Discussion of this will be given in section 4.7. Below, tensile strength of block-scale and irregular incipient joints was measured using the new approach.

4.6.1 Sample description

Midgley Grit Sandstone samples containing incipient rock joint were collected in the BQ, UK. Figure 4.19 shows two samples selected for testing containing incipient joints. It can be seen that these two samples are irregular in shape, but containing apparently continuous joint traces. It is evident that the two incipient joints retain some strength. It should be noted that incipient joint 1 in block BHQ7 inclined at about 40 degree to ground, while incipient joint 2 in sample BHQ5 was nearly vertical with respect to ground. Two holes with diameter of 17mm were drilled along the plane of incipient joint 2.

The sample BHQ 5 was stained brown due to the presence of the FeO. As can be seen in Figure 4.19, the stained bedding laminations were nearly

perpendicular to incipient joint planes. Again, some physical and mechanical properties including water content (3.3%), Schmidt hammer rebound hardness (22.8 ± 2.9), uniaxial compressive strength (24.2 ± 5.1 MPa) and point load index $I_{s(50)}$ (1.2 ± 0.1 MPa) were measured according to ISRM standards. The test procedures were the same to those used in the section 4.5.1.

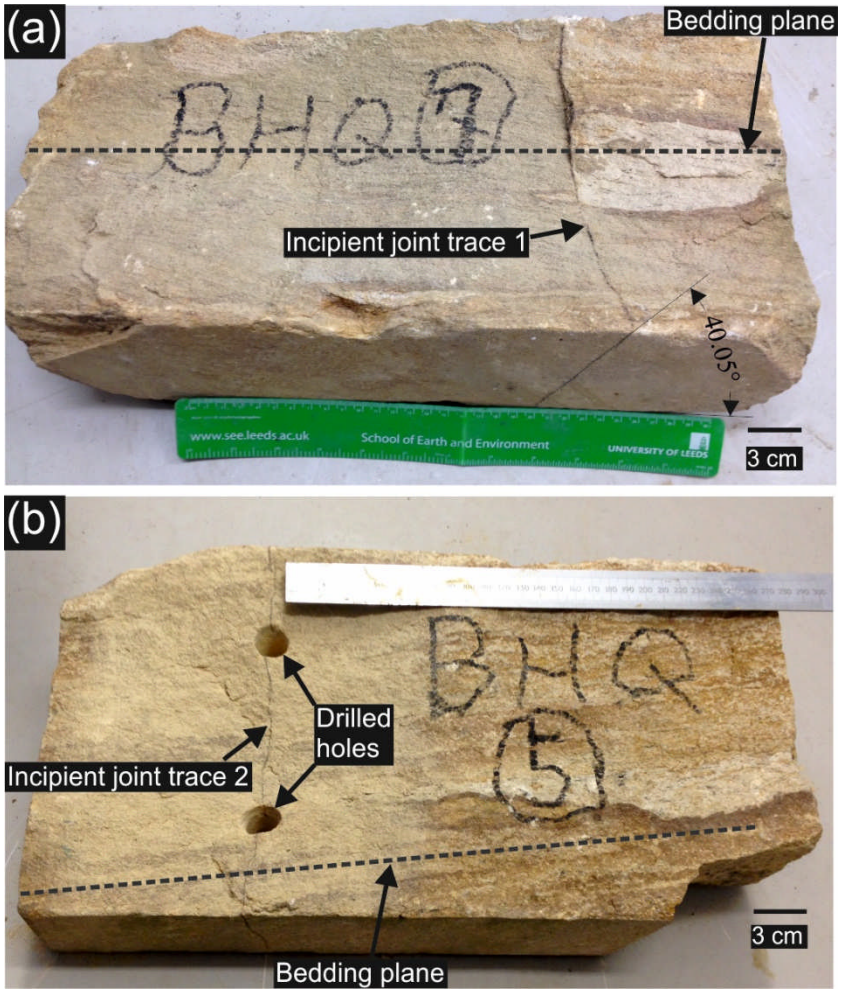

Figure 4.19 Irregular Blackhill sandstone blocks (BHQ 5 and BHQ 7) containing incipient joints. **a** An inclined incipient joint 1 that is expressed at a certain trace around the block. **b** An nearly vertical incipient joint 2 with a continuous trace at the surface of the block.

4.6.2 Experimental setup and failure surfaces

Figure 4.20 shows the experimental setup on sample BHQ 7 which is similar to that used for the tests on intact rocks described earlier. During drilling, care needs to be taken to drill exactly along the joint plane as far as possible assuming that the joint is planar in shape and follows the trace as exposed at

the surface. Unlike the test carried out on intact Midgley Grit Sandstone, no cuts were made in the sample.

Figure 4.20 b and c illustrate the failure modes of the incipient joint 1 after testing. As anticipated the sample broke along this joint plane. As in tests on intact blocks, the aperture at the bottom of the fracture was larger than that at the top (see Figure 4.20c).

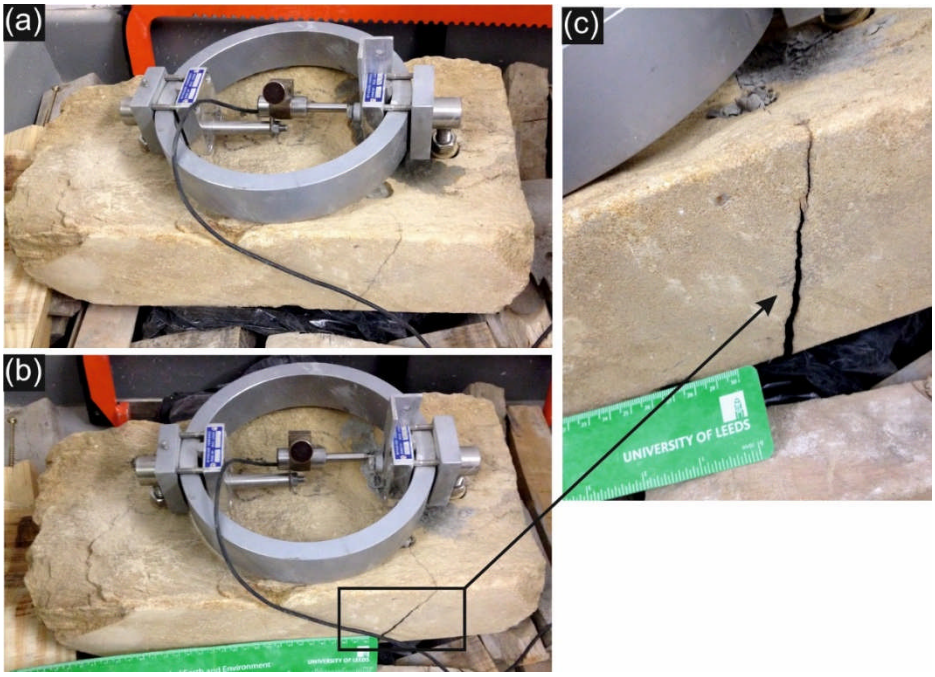

Figure 4.20 Experimental setup of the Phase i tension test on a block of the Midgley Grit Sandstone with the incipient joint 1. **a** Initiation of test and **b** Completion of test. The sample broke exactly along the pre-existing incipient joint and aperture (**c**)

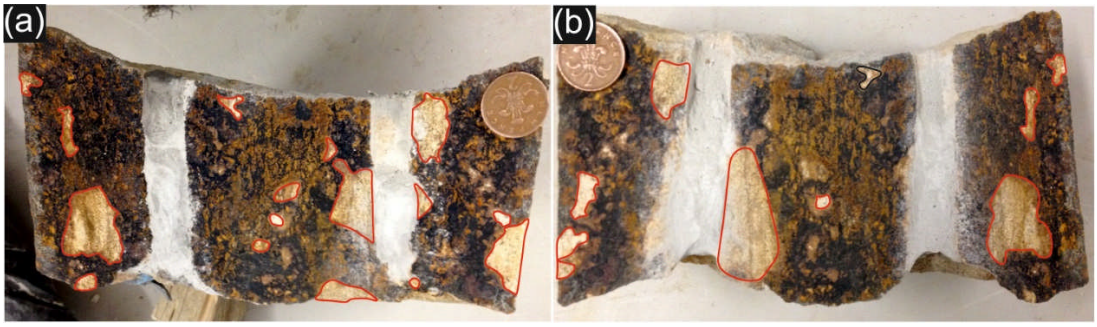

Figure 4.21 Two surfaces of incipient joint 1 after the tension test. The persistent areas (dark brown mottled black) have been weathered. The slightly stained or fresh areas representing rock bridges, as enclosed by red curves. 2p coins for scale are 25.9 mm in diameter.

Figure 4.21 shows the failure surfaces of the incipient joint 1. As for incipient joint surfaces of core samples (Figure 3.20), revealed after uniaxial tension and discussed in Chapter 3, the exposed areas show staining to a variable degree across their surfaces. It can be seen that the incipient joint 1 was not fully persistent in contrast to the continuity shown by the exposed trace on the block (BHQ 5) selected for testing. The persistent areas (dark brown and black mottled) have been highly weathered. If it is assumed that the areas enclosed by red lines were non-persistent, a persistence of 75% of the incpient joint 1 was calculated according to the definition of areal persistence in Chapter 2 (ratio of persistent area to the total area).

Figure 4.22 shows the experimental setup on incipient joint 2 within BHQ5 which is the same to that setup on incipient joint 1. Two failure surfaces after testing are shown in Figure 4.23. An areal persistence of 63% was calculated.

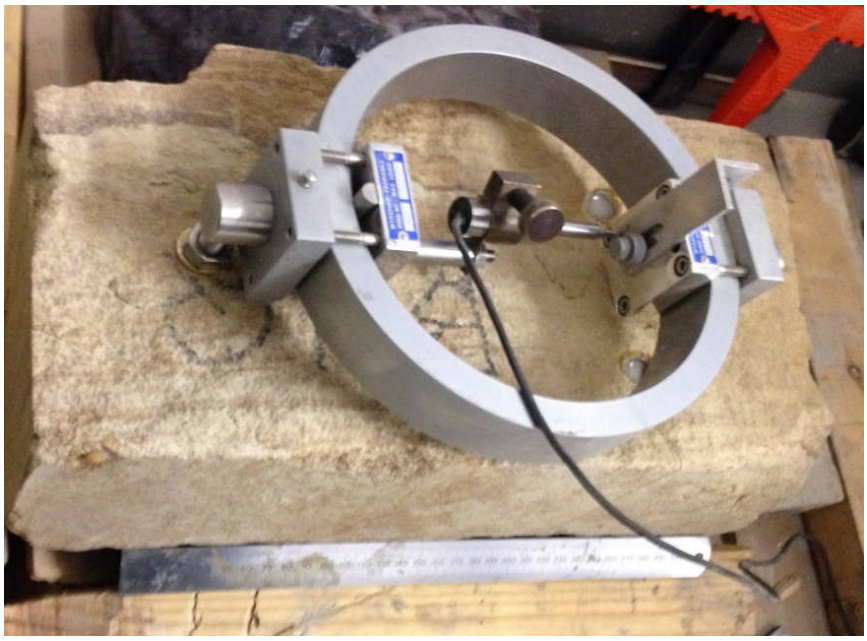

Figure 4.22 Experimental setup of the Phase i tension test on a block of the Midgley Grit Sandstone with the incipient joint 2.

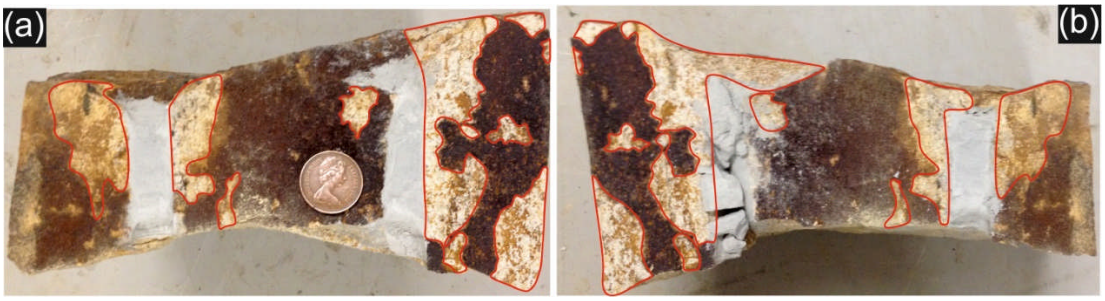

Figure 4.23 Two surfaces of incipient joint 2 after the tension test. The persistent areas (dark brown and black mottled) have been weathered. The slightly stained areas representing rock bridges, as enclosed by red curves. 2p coins for scale are 25.9 mm in diameter.

4.6.3 Tensile strength of large-scale incipient rock joints

Phase ii tests were conducted on the borken open joints to measure the ETF from the chemical splitter. Again, two different methods were employed which is similar to the tests on intact rocks described earlier. Figure 4.24 presents the test results of both Phase i and Phase ii tests. Table 4.5 and 4.6 list the parameters and forces measured in the Phase ii tests.

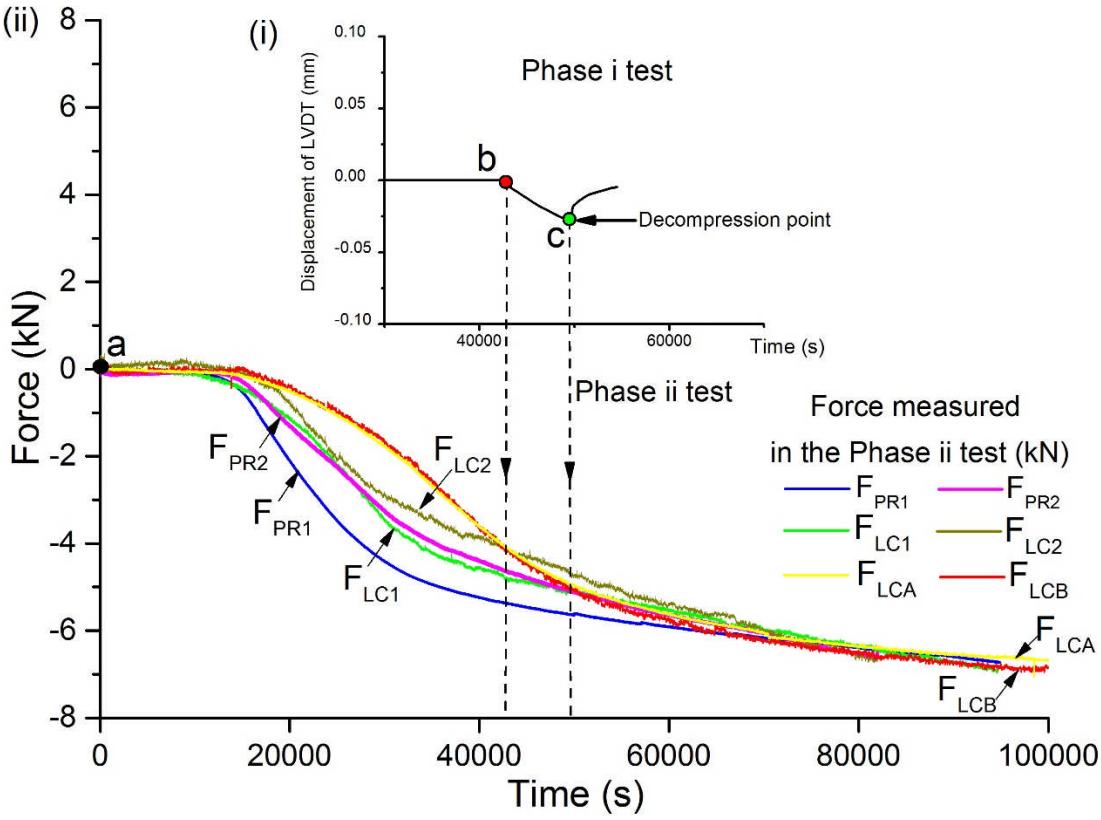

Figure 4.24 (i) Displacement of LVDT vs. time measured in the Phase i test on the BHQ 7 containing incipient joint 1. **(ii)** Measured forces vs. time in the Phase ii test.

It can be seen from Figure 4.24 that It took 49642s for incipient joint 1 to break (at point c). And average EFT measured by the type 1 and type 2 methods at the same time in the phase 2 test was -10 ± 0.5 kN.

The irregular surface areas of incipient joint 1 (Figure 4.21) were traced and the projected areas were measured by AutoCAD and the value was 19475 mm^2. Then the tensile strength of incipient joint 1 was 0.5 ± 0.03 MPa.

Similarly, it takes 34876s for incipient joint 2 to break (at point c in Figure 4.25). The average ETF at the time of 34876s was 12.3 ± 2.3 (8 kN / sin40.05°) kN. The measured surface areas of incipit joint 2 (see Figure 4.23) was 15899 mm^2. Thus the tensile strength of incipient joint 2 was 0.77 ± 0.1 MPa

Table 4.5 Parameters and forces measured by the type 1 setup method in the Phase ii tests on incipient joints (hole diameter is 17mm).

Sample	Time (s)	Expansive grout volume (ml)	T (°C)	F_{PR} (kN)	F_{LC} (kN)	ETF (kN)
Incipient joint 1	42884	35.6	19	-5.4	-4.8	-10.2
		31	20	-4.6	-4.1	-8.7
	49642	35.6	19	-5.4	-5.1	-10.5
		31	20	-5.1	-5.0	-9.6
Incipient joint 2	19797	28.5	20	-2.6	-1.5	-4.1
	34876	28.5	20	-4.7	-5.0	-9.7

Table 4.6 Parameters and forces measured by the type 2 setup method in the Phase ii tests on incipient joints (hole diameter is 17mm).

	Time (s)	Expansive grout volume (ml)	T (°C)	F_{LCA} (kN)	F_{LCB} (Kn)	ETF (kN)
Incipient joint 1	42884	35.6	20	-4.02	-4.03	-8.05
	49642	35.6	20	-4.82	-4.88	-9.70
Incipient joint 2	19797	28.5	21	-0.43	-0.43	-0.86
	34876	28.5	21	-2.85	-3.54	-6.39

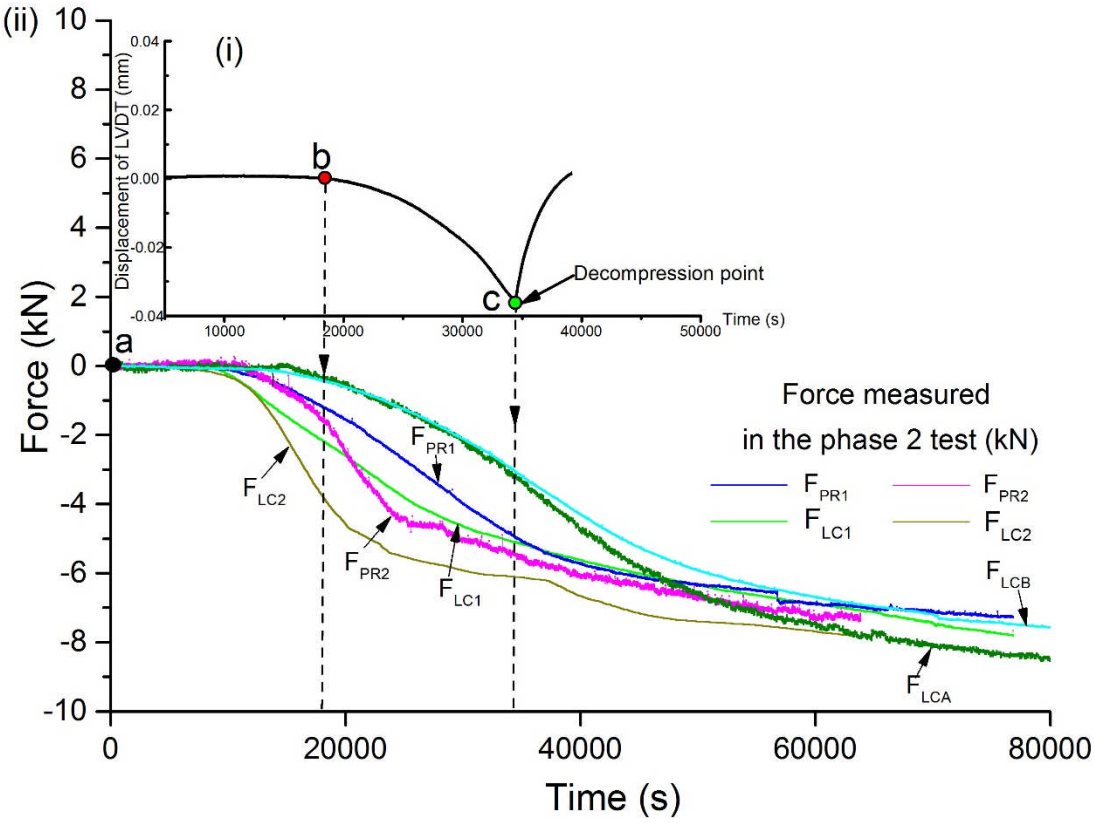

Figure 4.25 (1) Displacement of LVDT vs. time measured in the Phase i test on the BHQ 5 containing incipient joint 2. **(2)** Measured forces vs. time in the Phase ii test.

4.7 Discussion

4.7.1 ETF arising from the chemical splitter

The tensile strength calculation relies on the assumption that ETF measured in the Phase ii test represent the ETF at the same time in the Phase i test. Three main parameters including grout concentration, room/rock temperature and amount of grout will potentially influence the magnitude of ETF from chemical splitter in the test. Same samples containing the fractures that induced in the Phase i test were employed in the Phase ii test to measure ETF, so as to keep the amount of chemical splitter evolved in Phase ii and Phase ii tests to be the same. All tests were conducted at the recommended grout concentration of 3.3 kg/L and in the engineering geology lab (room temperature at 20 ± 1°C), University of Leeds. The ETF normal to the failure plane was measured using two different setup methods in the Phase ii test. The PR and 50 kN load cell were employed in the type 1 setup method (Figure 4.10a) and twin load cells with same stiffness were used in the type 2 setup

method (Figure 4.10b). The ETF were calculated by adding up the readings of PR and LC in the type 1 method, and of twin load cells in the type 2 method.

It was found that ETF measured by the type 2 method lay between values measured by the type 1 method (Figure 4.14ii and 4.15ii). This indicates that the measured ETF gives a reasonable and acceptable result in the two different setup methods. For some tests (Figure 4.14ii and 4.25ii), however, there were some differences at earlier stage of testing but similar ultimate ETF values at the end of each test run. For example, the curve labelled as F_{PR1} in Figure 4.14ii, much larger force was measured before 50000s compared with other test results. This probably be attributed to the higher working temperature (see the fourth column in Figure 4.1) during this test which quicken the chemical reaction of splitter. Average ETF therefore is suggested to be used in the tensile strength calculation.

4.7.2 Effects of scale on the strength of rock materials

The scale effect on the strength of rock and discontinuities has been investigated by many researchers (e.g. Thuro et al. 2001, Zhang et al. 2011, Fredrik 2016, Manuchehr et al. 2015, Sheshede and Cheshomi 2015). The common agreement about scale effect is that increase in strength values corresponds with decrease in sample size. This phenomenon can be attributed to the anisotropic nature of rock materials. Besides, material with a larger volume is able to contain more defects, thus it is easier to break under external loading.

The failed rock surface areas of the large-scale block of samples reported in this chapter were about 5 times larger than that of the cylindrical sample with a diameter of 50 mm. It is interesting however to note that the measured tensile strength (2.0 MPa) of the large-scale Midgley Grit Sandstone sample was larger than the lowest value (1.86 MPa) of measured tensile strength of intact sample using the uniaxial tension method. This means that tension test carried out on this large-scale intact Midgley Grit Sandstone sample give a reasonable result. The slightly difference in the setup of tension method (two cuts were made in the intact Midgley Grit Sandstone sample, see Figure 4.16a) as well as failure patterns of the two samples may give a possible explanation. It can be seen that two regular failure planes (Figure 4.16c_1, c_2) were obtained at the end of test run. Failure planes however were irregular in the tension test on the Thornhill Rock Sandstone sample (Figure 4.13). Two induced fractures were produced on one side of sample and only one fracture was induced on the other side. The irregular failure plane will influence the tensile strength calculation process because it will influence the projected

areas used in the strength calculation. In addition, the force acting the irregular plane is complex which also influence the strength calculation. As is reported by Gholamreza et al. 2015, failure patterns (reflected by the fracture length) of sandstone samples under Brazilian indirect tension were related to the average tensile strength.

Tension tests for the large-scale incipient rock joints which give two strength values of 0.5 MPa and 0.77 MPa, respectively. Although It is diffcult to verify the validity the the two values but a back calculation of the strength of non-persistent areas may give some clue, as is the same approach adopted in Chapter 3. For the tested incipient rock joints, the non-persistent areas(red envelopes in Figure 4.21 and 4.23) were clearly not intact rocks but have been stained to some degree. The enveloped areas on incipient joint plane 1 and 2 were measured (4927 mm^2 and 5914 mm^2) approximately using AutoCAD. The calculated tensile strength of these non-persistent areas were 1.8 MPa and 1.6 MPa which were smaller than the intact rock uniaxial tensile strength (2.08 MPa). This means that the slightly stained segments on the non-persistent areas on failure surfaces have strength somewhat less than the intact rock strength.

In Chapter 3, uniaxial tension tests were carried out on incipient rock joints within smaller cylindrical samples with diameter of 70 mm. Two areal extent values (72% and 62%) of samples BH70J1 and BH70J3 are quite close to that (74.7% and 62.8%) of the samples tested in this chapter. The tensile strength (0.63 MPa and 0.90 MPa) of sample BH70J1 and BH70J3, however, were somewhat larger than the tensile strength (0.5 MPa and 0.77 MPa) of the large-scale incipient joints. The larger failed incipient joint surface area (compared to the failed areas of samller cylinder samples tested in Chapter 3) may be responsible, although distributions (location) and shapes of rock bridge can also influence the strength (Ghazvinian 2007).

4.7.3 Stress concentration during the tension test

Laboratory methods including direct and indirect tensile tests were employed to measure the tensile strength of rock materials (e.g. Hobbs 1965, Baela and Innaurato 1973, Luong 1988, Liao et al. 1997, Li et al. 2013). In those tests, uniformly distributed stresses along failure planes are the basis of valid results. Efforts have been made to reduce the anomalous concentrated stresses within rocks during testing (e.g. Wuerker 1955 and Hoke 1964).

In order to understand the stress distribution on the failure plane in the proposed test, the lineral elastic fracture mechanics analysis was employed

under the assumption that rock material is elastic-plastic. Analytical models were constructed as shown by Figures A 4.1, A 4.2 and A 4.2. Figures A 4.4 and A 4.5 (see appendix A) present the stresses along and perpendicular to the failure plane along chemical splitter filled holes. The analytical stress distribution results were based on a ratio of $d / r_i = 5$, with $r_i = 20$ mm, and when the internal pressure of chemical splitter was 50 MPa. It is found that the maximum stress concentrated around hole edges and tensile stresses normal to the plane between two holes were not equally distributed, but decreased from 59.5 MPa in the edge by the holes to 20.8 MPa in the middle of the holes. Thus it is resonable to expect that, in the tension test, fracture will initiate at the hole edges and propagate progressively to the centre. This is not the same to the situation for the stress distribution in Brazilian tensile test in which fracture theoretically initiates at the exact center of discs (Li et al. 2015). Fracture initiation in Brazilian discs were observed in Chapter 3 (Figure 3.10).

The anomalous concentrated stress distributions in the block tests give an explanation to the smaller laboratory test results compared with those measued by the Brazilian test. Another consideration is that for tension tests carried out on incipient rock joints, stress would also concentrated around rock bridge tips. This may actually represent the field situation or insitu stress condition because of the intrinsic nature of incipient rock joints.

4.7.4 Effects of Pressurization rate and water on strength of rock material

Strength of rock materials varies with the loading rate(Kumar 1968, Sangha and Dhir 1972, Kittitep and Numchok 2010, Kittitep et al. 2012, Sopon et al. 2015, Zhou et al. 2015 and Chang and Jo 2015). It was found that the tensile strength of rock materials can also vary depending on test method as well as the loading rate, leading to uncertainty (Chang and Jo 2015). In this study, chemical splitter (a kind of expansive grout made from mixturing Dexpan power and pure water with a recommended ratio of 3.3 Kg/L) was employed to apply ETF. As can be expected that the influential factors including working temperature, concentration and amount of chemical splitter evolved in each test will influence the pressurization rate of chemical splitter. As can be seen from the test results, it took several hours for chemical splitter to break intact rock as well as incipient rock joints. Obviously, that is much longer than conventional tensile tests, i.e., a very small loading rate was applied on the rock materials in the test. We suspect that the smaller strength obtained is may be attributed to the small loading rate. It agrees with the findings by Mellor

and Hawkes (1971) that tensile stength of rock will decrease with decresing of loading rate.

In addition, water in the chemical splitter can infitrate and diffuse into the rock matrix in the test, which in turn will probably degrade the rock strength (Chang and Jo, 2015).

4.8 Summary

An original methodology to quantify the tensile strength of large-scale incipient joints was trying to be developed in this chapter. In this method, chemical splitter was employed to generate tensile forces normal to incipient joint planes. Each test comprised of two phases: Phase i test and Phase ii test (see the conceptual model in Figure 4.5). Failure time of sample (with or without an incipient joint) under tension was measured in the Phase i test. Expansive tensile force (ETF) arising from chemical splitter was measured in the Phase ii test using the same sample broken in the Phase i test. The magnitude of ETF (measured in the Phase ii test) at the time of sample failure (measured in the Phase i test) was employed to calculate the tensile strength of the plane through chemical splitter filled holes (see Eq. 4.1).

Preliminary tensile tests were conducted first on an large-scale intact Thornhill Rock Sandstone sample (Figure 4.11) and a Midgley Grit Sandstone sample (Figrue 4.16a) to establish the methodology. The measured tensile strength of these two large-scale samples were 1.8 MPa and 2.0 MPa, respectively. It was found that the results were less than average strength values measured from Brazilian tests which were 3.5 ± 0.7 MPa (Table 4.2) and 2.08 ± 0.22 MPa (Table 3.1), respectively.

Tensile strength of large-scale incipient joints were then measured using this new approach. As anticipated sample failured exactly along incipient joint traces and areal extent of persistent areas along incipient joint planes were revealed (see Figures 4.21, 4.23). The tensile strength of incipient joints measured were 0.5 ± 0.03 MPa. and 0.51 ± 0.1 MPa. The calculated tensile strength of non-persistent areas (red envelopes in Figure 4.21 and 4.23) along incipient joint planes were 1.8 MPa and 1.3 MPa. These two values were somewhat smaller than the tensile strength (2.1 ± 0.2 MPa) of intact rock measured in the Chapter 3. The smaller tensile strengths measured using the proposed method may be due to the stress concentration around chemical splitter filled hole edges (see Figure A 4.4 and A 4.5) and low pressurization rate of chemical splliter. Besides, the unavoidable variations of ETF measued

in the Phase ii test may also influence the strength calculation results, even though average ETF was employed in the tensile strength calculation process.

Chapter 5
Investigation into the persistence (areal extent) of incipient rock discontinuities

5.1 Introduction

Persistence is defined as the areal extent of a rock discontinuity (ISRM 1978, see Figure 2.5b in Chapter 2). Its profound implications for rock mechanics and rock engineering projects have been well understood (e.g., Kevin 1980; Einstein et al. 1983; Park 2005; Kim et al. 2007; William et al. 2008; Wasantha et al. 2011; Sarfarazi et al. 2014; Zhang et al. 2015; Viviana et al. 2015), which has been discussed in Chapter 2.

Owing to its three dimensional nature and the limitations of measurement, we know very little about real discontinuity persistence and few publications are available. Rawnsley (1990) found that persistence, even as seen in surface exposures, was not predictable on the basis of geological factors or through other observations. Park (2005) concluded that it was impossible in practice to measure discontinuity area based on field investigation. Norbury (2010) pointed out that quantification of persistence normally requires the extent of rock discontinuity surface to be measured both down dip and across dip.

Some researchers have attempted to quantify this parameter but all restricted to exposed rock faces (e.g. Sturzenegger and Stead 2009 and Ferrero et al. 2009). Currently, in rock engineering and modelling, trace length of discontinuities obtained from outcrop is used as an approximation of real persistence (e.g. Kim et al. 2007, Umili et al. 2013 and Han et al. 2015); sometimes the persistence value of 100% is assumed for simplification purpose (e.g. Park 2005; Jiang et al. 2015). All these approximations and assumptions are geological guesswork. Field observation of the extent of incipient rock discontinuities combining the geological origin and interpreted geomorphological history of site will be a realistic approach towards this difficult topic (Hencher 2015).

In this chapter, a technique, “forensic excavation of incipient rock discontinuities (FEIRD)”, was used to examine the extent of incipient rock discontinuities, therefore providing a small step in quantifying real persistence. Laboratory and field tests were carried out on incipient rock discontinuities within Horton Formation blocks and Midgley Grit Sandstone blocks as application examples. Apparently planar discontinuities were focused in this study primarily due to two reasons. The first is that it is a common practice in

rock engineering to assume that discontinuities are planar in shape (e.g. Priest and Hudson, 1976, Baecher et al., 1977 and Zhang and Einstein 2002). The second is because the persistence definition by ISRM (1978) (see Chapter 2, Eq. (2.2)) used in this study implies a planar discontinuity.

5.3 Methodology: Forensic excavation of incipient rock discontinuity

The term “forensic excavation of incipient rock discontinuity (FEIRD)” in this study refers to the process of non-explosive splitting along a planar or near-planar incipient rock discontinuity; thereafter the three dimensional nature of discontinuity such as areal extent (persistence), roughness as well as fractographic features (if present) can be observed and investigated. There have been some rock splitting methodologies used in rock engineering for example hydraulic rock splitter (Figure 5.1), chemical rock splitter (expansive grout) and rock splitter based on shape memory alloys (Benafan et al. 2016). Chemical rock splitter was used for FEIRD in this study considering its portability and operation simplicity.

5.3.1 Chemical splitter and operation principle

The chemical splitter used in this study is a commercially available powder named Dexpan (generally comprising SiO_2, Al_2O_3, Fe_2O_3, CaO, MgO and SO_3 (Huynh and Laefer 2009)). Mixing with pure water the grout expands considerably through chemical reaction and hydration. The production of the powder can be dated back to 1930’s and it was first commercially available in 1970 (Gani 1997; Huynh and Laefer 2009). Because of major benefits, i.e. no ground vibration and fly rock, chemical splitters have been employed in rock engineering projects where blasting was not allowed (Natanzi and Laefer 2014).

5.3.2 FEIRD testing procedure

FEIRD testing has been carried out in the field on large discrete blocks of rock. The procedures used are generally similar to that presented in Chapter 4 (laboratory test) but there are some differences. Testing generally comprise the following sequential phases (see Figure 5.2):

● Phase 1 - Drilling holes along discontinuities. A battery drill (Makita) was employed to drill holes with diameter of 27 mm and spacing of around 200 mm (larger diameter holes can be used when forensic excavating large-scale rock

masses but not more than 100 mm as blow out may occur). Holes were not drilled through so as to preven.t chemical splitter from leaking. Dust in holes was cleaned after drilling as much as possible for a good result.

● Phase 2 - Chemical splitter preparation: mixing expansive powder with pure water. The recommended ratio of expansive powder /kg to water /L is 3.3 kg/L. A measuring jug, syringe and a soft drink bottle were used to measure the expansive powder and water to the recommended ratio. A metal stick was used to mix the expansive powder and water in a plastic bucket to make sure that the powder was completely dissolved in water. Personal protective equipment (PPE) including goggles, FFP3 masks, rubber gloves and protective clothing were worn all the time when handling the chemical splitter.

● Phase 3 - Filling the pre-drilled holes with the chemical splitter. The measuring jug and syringe were used to fill and measure the amount of chemical splitter injected into each hole. A metal stick was used to agitate the chemical splitter in the holes to make sure no air was trapped. After filling the holes with chemical splitter, a plastic cover was placed over the holes and warning signs were attached. Care must be taken not to look directly into holes as explosive blow out may occur.

● Phase 4 - Opening up of the incipient rock discontinuity. It normally took several hours (up to 24 hours) for the chemical splitter to harden gradually, expand and open up the incipient discontinuity. The actual time varies with temperature, rock lithology and amount of the chemical splitter used. Secondary prising off tools (an excavator, forklift and chisels) were used in the field test.

● Phase 5 - Failure description. After the large blocks had been split, the exposed surfaces were described and interpreted.

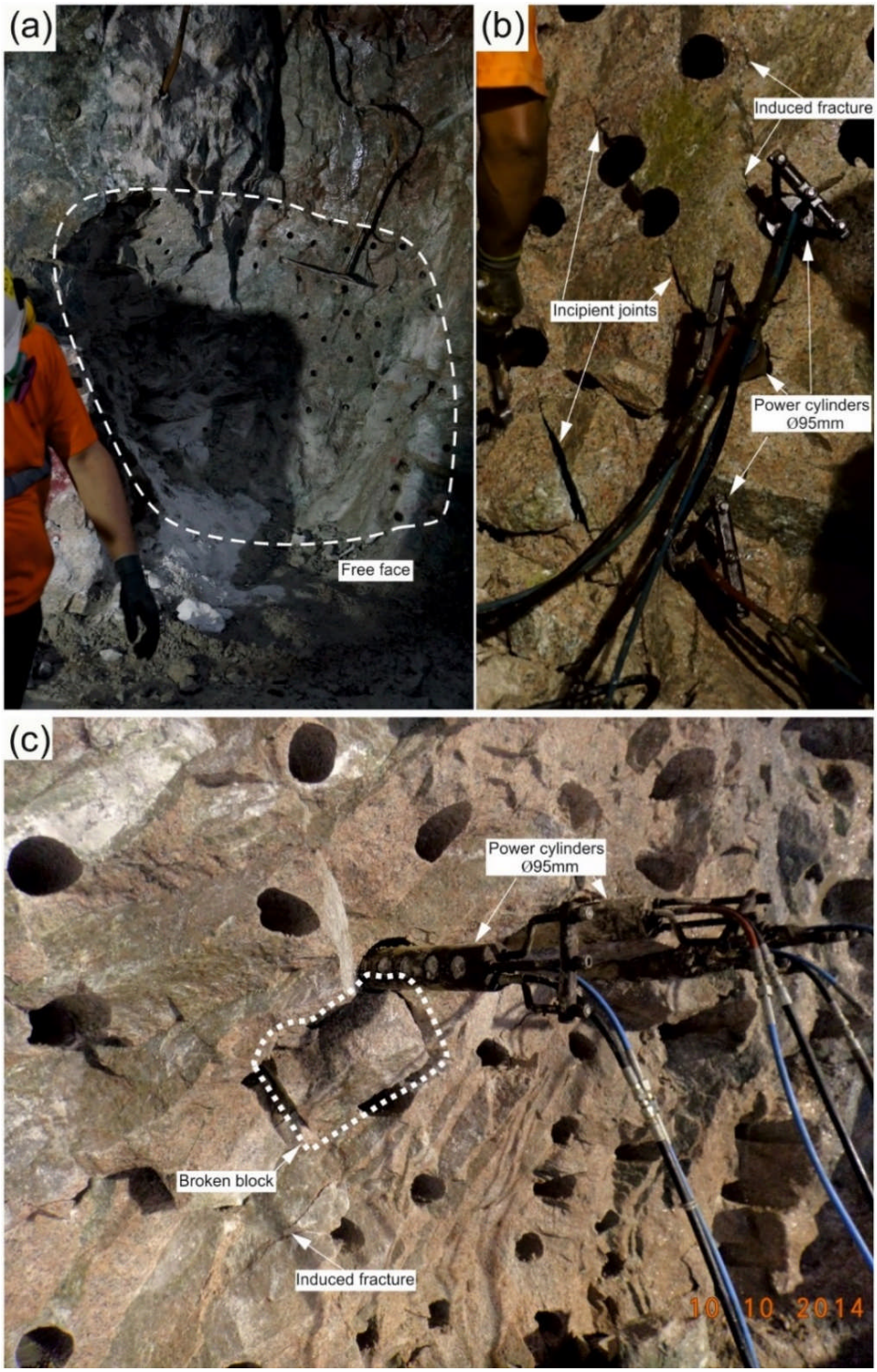

Figure 5.1 Construction of Mass Transit Railway (MTR) - Admiralty section in Hong Kong. A hydraulic rock splitter (model PRS-95) was employed in the excavation of an underground tunnel where blasting was not allowed because of adjacent engineering works. **a** Predrilled holes with diameter of 100 mm on the free face; **b** Holes were drilled along several parallel incipient joints, note that irregular fractures were induced by the upper power cylinder; **c** A small rock block was broken from the free face and an induced fracture can be seen. It took around 2-4 mins for this PRS-95 rock splitter to break rock for each run.

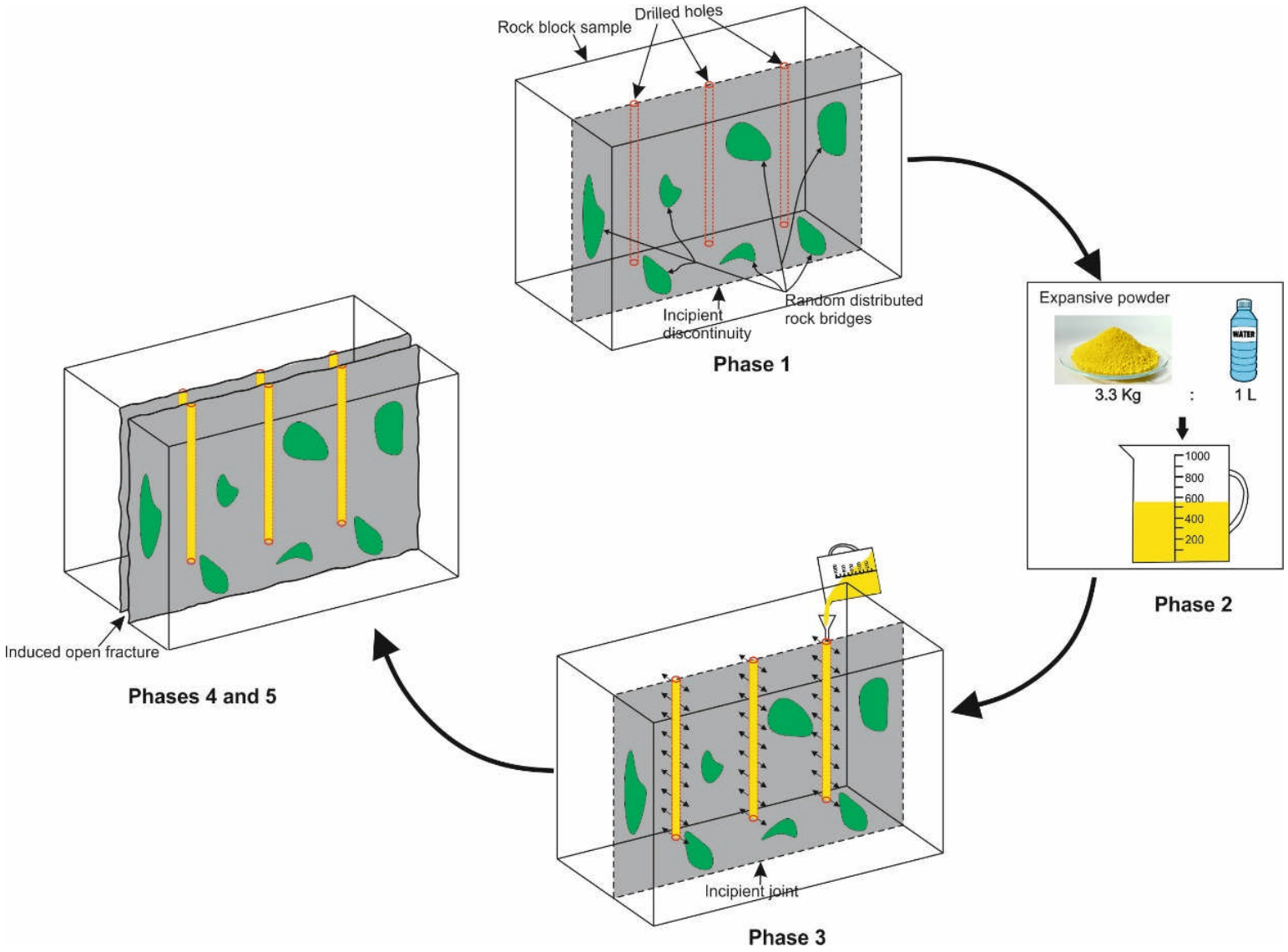

Figure 5.2 Schematic diagram of the FEIRD testing procedure

As for the laboratory tests described in Chapter 4, areal extent (persistence) and roughness were quantified based on examination of the discontinuity surfaces. Factors relating to incipient nature of each discontinuity were investigated. In addition, relationships between roughness and persistence were considered. Interpretations made in knowledge of the geo-histories of incipient discontinuity structures at the specific field sites as deduced by field examination and on the basis of literature review.

5.3.3 Dye technique, a preliminary investigation

A new experimental method was devised using the injection of dye, prior to splitting, in an attempt to identify persistent portions of incipient discontinuities. A preliminary dye test was performed in the laboratory on an irregular Midgley Grit Sandstone block approximately 514 mm long, 400 mm wide and 150 mm depth.

(1) Apparatus and experimental procedure

Figure 5.3 presents the test preparations and apparatus used. An incipient joint (boxed area in Figure 5.3a) within the block sample. Two holes with diameter of 7 mm were drilled either on the top surface or on the side of block sample along the joint trace (see Figure 5.4). A plastic tube containing some pre-drilled small holes was then introduced to each hole in turn which permits the dye penetrant flow through the joint in a uniform inlet pressure (see Figure 5.3b). A metal cap (Figures 5.3b and 5.3c) was attached on the top by using an adhesive (Araldite) to prevent dye from leaking when introduced under pressure.

Fluorescein ($C_{20}H_{12}O_5$), a synthetic organic compound soluble in water, was used in the test (termed as florescent dye here after). It has been used elsewhere for crack detection and non-destructive testing (NDT). Figure 5.3d shows some of the prepared florescent dye.

An advanced Pressure / Volume Controller (ADVDPC) was employed to pump fluorescent dye into the holes drilled to follow the predicted geometry of the incipient discontinuity. The ADVDPC is microprocessor-controlled screw pump for the precise regulation and measurement of fluid, oil or air pressure and volume change.

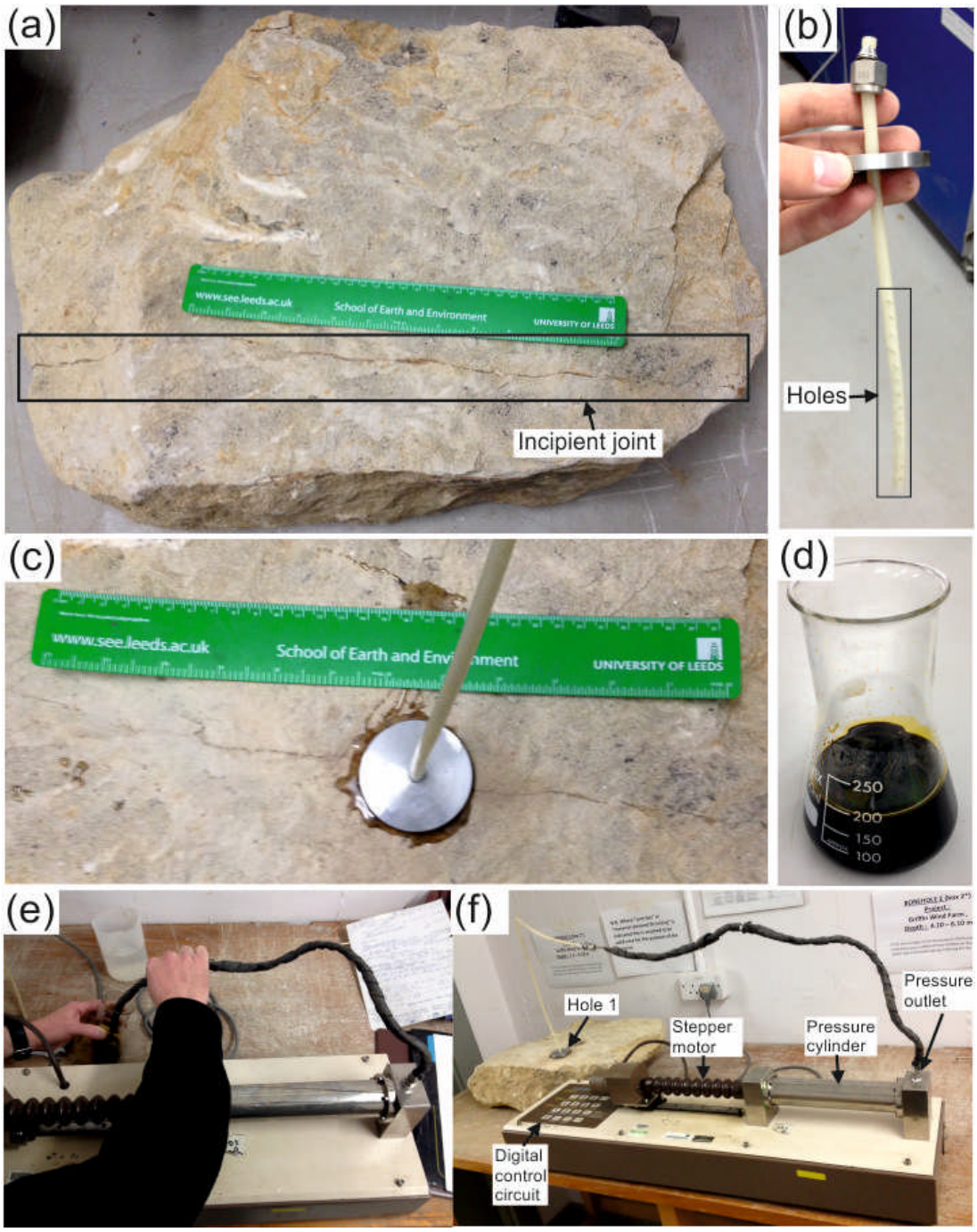

Figure 5.3 a Midgley Grit Sandstone block containing an incipient joint; joint trace (boxed area) is persistent observed at surface. **b** A metal cap and plastic tube containing some pre-drilled holes were used as the conduit of dye penetrant, **c** The tube was inserted into a pre-drilled hole along this incipient joint and the metal cap was glued on the top by Araldite to seal the hole. **d** Fluorescent dye penetrant that was used to colour the persistent areas along incipient joint. **e**, **f** The GDS advanced pressure / volume controller was used to pump fluorescent dye into the incipient joint plane. Rule for scale is 314 mm in length.

Figures 5.3e, f show the ADVDPC used in this preliminary test. Fluorescent dye was firstly introduced to the pressure cylinder (e) and then pumped into the rock block down holes drilled into the incipient joint (f). Several runs were

performed due to the limited volume of the pressure cylinder. A constant pressure control mode (3 MPa) was used for injection. Dye was injected into two holes and this process was stopped when the dye from two holes met as observed from the block surface (see Figure 5.4).

(2) Results and discussion

Figure 5.4 shows the extent of the dye exposed at the surfaces and dye transportation (with time) around the hole 1, dye volumes introduced to the hole 1 are also indicated for steps from (a) to (g). No single fracture flow was achieved at the surfaces as the dye travelled in sub-circular shape, which not only flowed along the expected preferential path (incipient joint plane) but also penetrated into the rock matrix. The high permeability of Midgely Grit Sandstone appears to have first order control of how the fluid behaved, although rough joint surface of course can sometimes give rise to a tortuous flow due to spatially varied aperture (Thomposon and Brown 1991, David et al. 2006). The inhomogeneous nature of Midgley Grit Sandstone can be demonstrated by the scattered transportation of dye, especially along the depth of sample (Figures 5.4e, f).

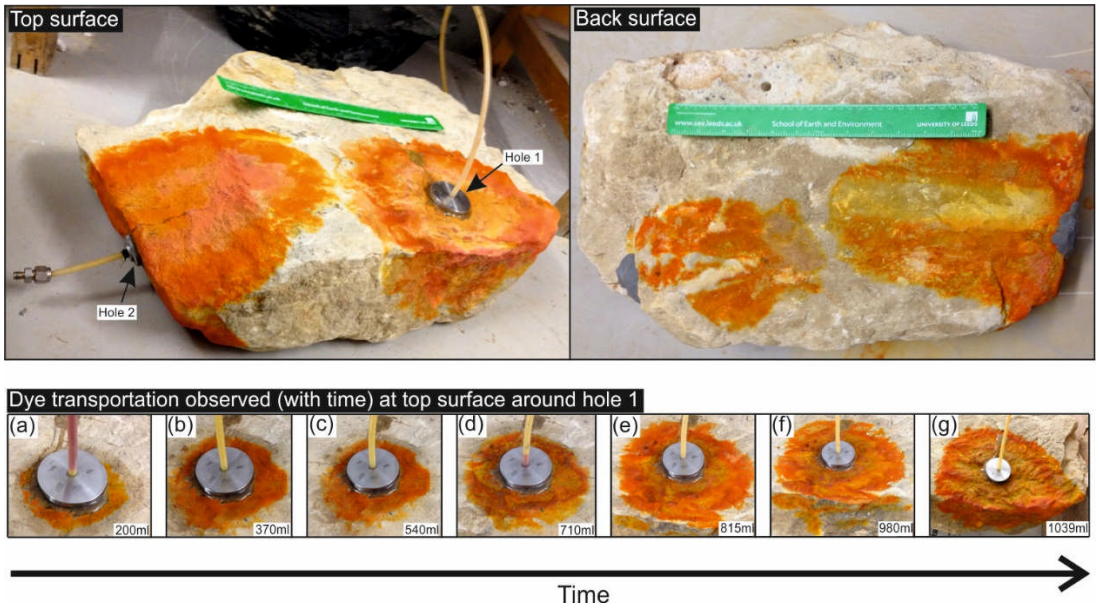

Figure 5.4 Observed dye at the top and back surfaces after the injection process. (a) to (g) show the dye transportation with time around hole 1 observed at the top surface. Rule for scale is 314 mm.

The block sample was left at room temperature around one month and then split. Four holes with diameters of 27 mm were drilled along the joint (assuming planar in shape). Exposed joint surfaces after splitting are presented in Figure 5.5. Both weathered areas (persistent areas) and rock

bridge areas have been stained by dye, which can be attributed to the high rock material permeability. The main mineral on the dark areas is Haematite. It is assumed that incipient joint structure remained the same during the dye pumping procedure although persistent area of joint surface can increase with the applied stress yet at a high pressure up to 20 MPa (Duncan and Hancock 1966, Namdos et al. 1983). According to Eq. (2.2), based on the areal extent of the weathered surfaces, persistence of this planar incipient joint was calculated (approximately 86% assuming all persistent areas have been stained).

From this preliminary test as conducted, it is conclude that the dye technique is not applicable for the high permeability rock such as Midgley Grit Sandstone tested in this study.

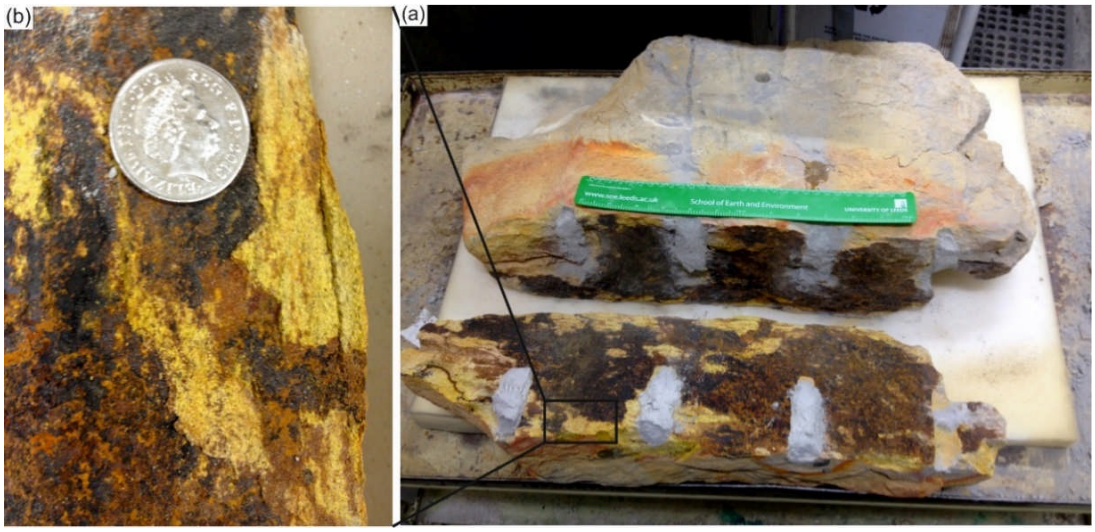

Figure 5.5 Exposed incipient joint surfaces after the FEIRD test conducted on a Midgley Grit Sandstone block sample. Joint surfaces have been coloured entirely including rock bridges (light yellow areas). Coin for scale is 25.9 mm in diameter, rule for scale is 314 mm in length.

5.4 Areal extent of incipient rock discontinuities within Midgley Grit Sandstone: A laboratory FEIRD experiment

5.4.1 Block sample description

A Midgley Grit Sandstone block sample (Figure 5.6) was collected from BQ, West Yorkshire, UK. The irregular shaped sample shown in Figure 5.6 contains six visible traces, labelled from ①-⑥. Incipient joint traces ①, ② and ③ intersected by one another (see Figure 5.6 top view). Incipient bedding is also present. Relative orientations of these discontinuity traces including

exposed surfaces are plotted in Figure 5.7 assuming the north direction was as shown in the top view. Incipient joint ① appears as a trace on all free surfaces, whereas other joints appear to be less well developed.

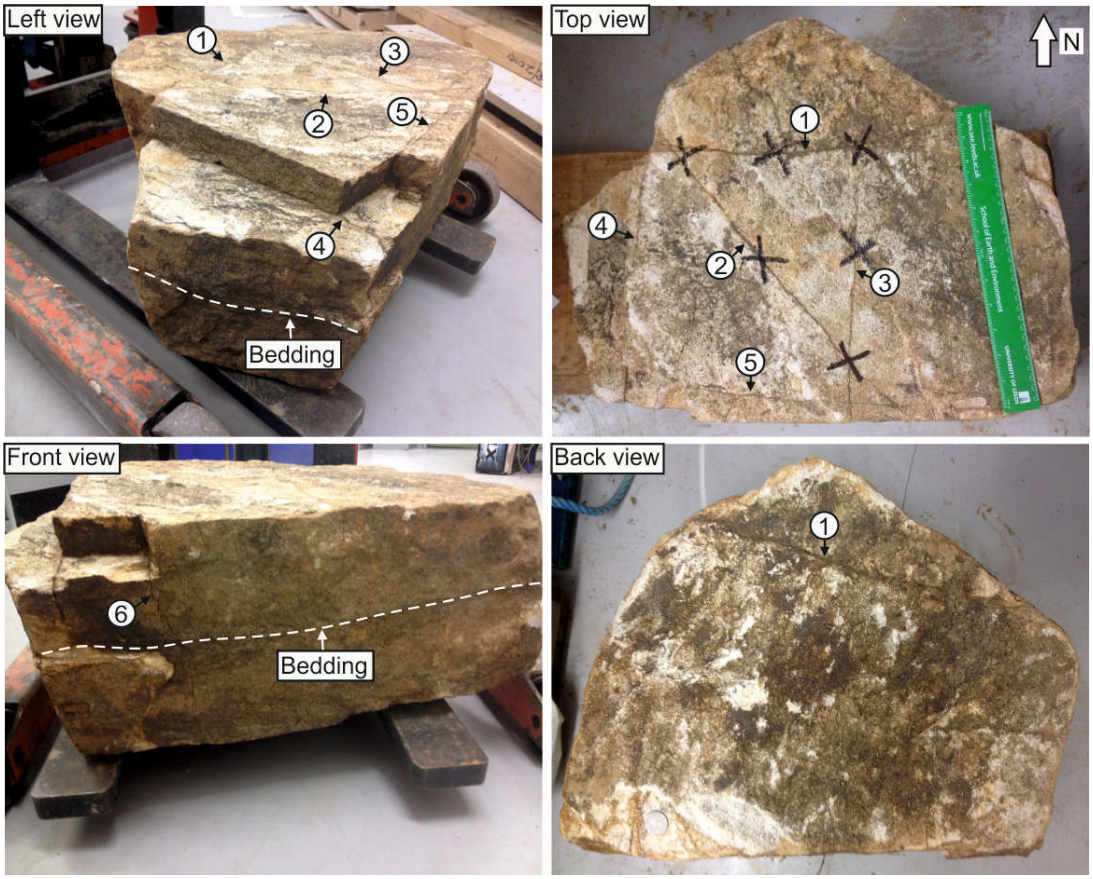

Figure 5.6 View of large block of Midgley Grit Sandstone with incipient bedding and six visible joint traces. Relative orientations are measured taking bedding as horizontal and north as indicated in the top view. The rule for scale is 314 mm.

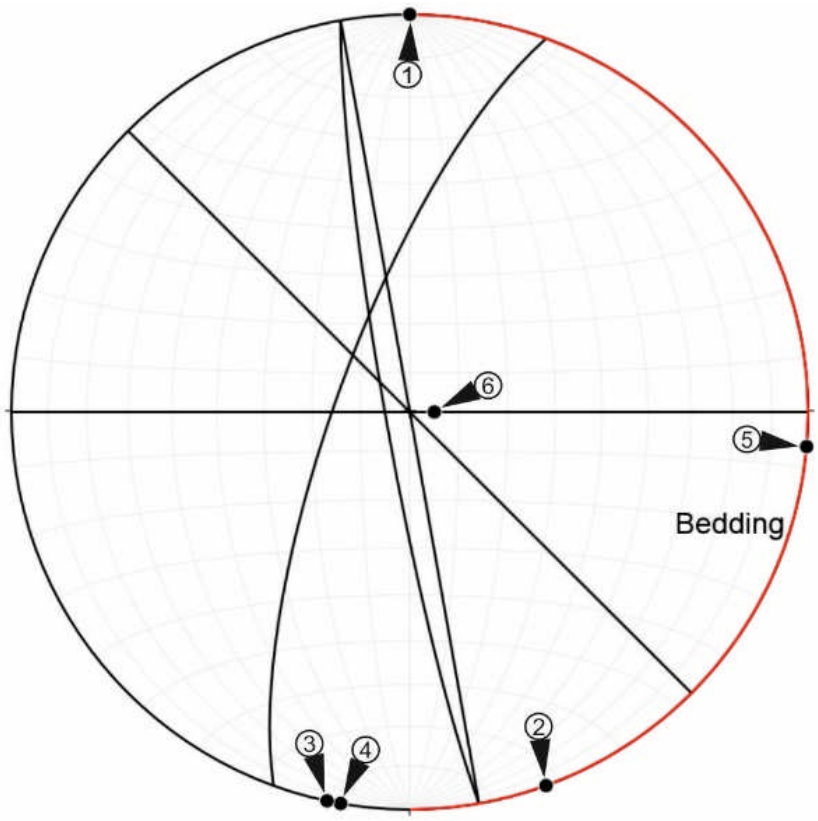

Figure 5.7 Stereographic representative of six incipient joint traces and exposed surfaces shown in Figure 5.6. Bedding is taken as horizontal.

5.4.2 Testing procedure and failure patterns

Figure 5.8 shows how the rock was split. Holes with diameter of 27 mm were drilled only along incipient joint traces ①, ② and ③.

The drilling geometry was adopted assuming that the joints were planar in shape. The chemical splitter was prepared in a measurable bucket and then was injected into the pre-drilled holes (Figures 5.8a, b). Hole spacing was between 100 mm and 120 mm, hole depth 150 mm and injected volumes about 88 ml.

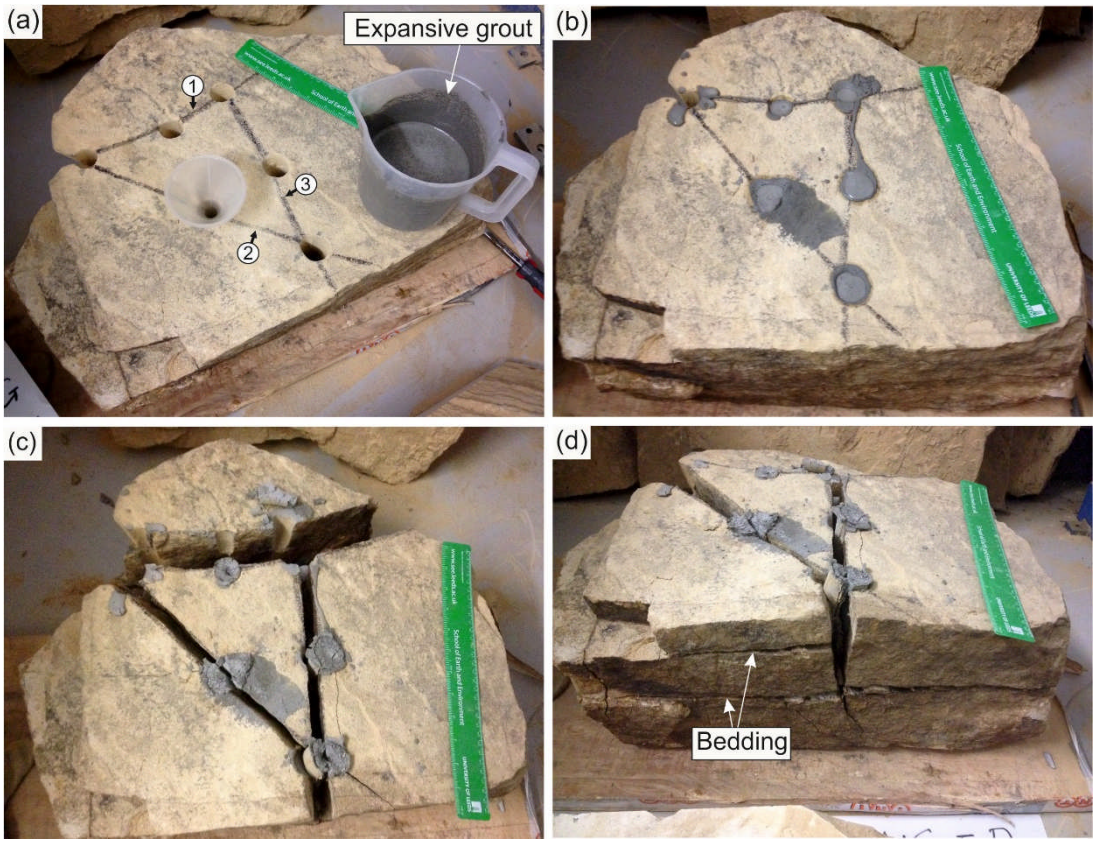

Figure 5.8 FEIRD testing procedure along incipient rock discontinuities ①, ② and ③. **a** Six holes with diameter of 27 mm were drilled along these incipient joints to a depth of 150 mm; **b** The chemical splitter was injected into the pre-drilled holes; **c** Induced fractures along pre-existing incipient joint traces, image was taken after 24 hours; Note that two horizontal parallel fractures were induced along the direction bedding planes as shown in **d**. The rule for scale is 314 mm.

Figure 5.8c and d show the failure patterns after 24 hours. As anticipated, the block sample was split exactly along the pre-existing discontinuity traces. Two horizontal bedding planes were also mobilised because of the expanding forces. It is also interesting to note that the induced fracture along incipient rock joint ③ changed from nearly vertical to incline at below one of the opened bedding plane (Figure 5.8d). The incipient joint ④ was also broken during this test but not deliberately.

5.4.3 Result interpretation and discussion

The split rock block pieces were removed with care and the failure surfaces examined as shown in Figure 5.9. From the revealed joint planes, it can be see that all incipient joints terminated at bedding planes (indicated by red lines).

Generally the persistent joint segments (outlined by white dashed lines) exhibited different degrees of weathering in a similar manner to the samples described in Chapter 3. Intervening rock bridge areas can be distinguished and quantified approximately by using AutoCAD. Persistence values of incipient rock joints ①, ②, ③, and ④ were calculated (85%, 37%, 32% and 90%, respectively). However there has little evidence for the areal extent prior to the FEIRD testing. Scattered weathering areas on incipient joint plane ③ shows some clues that weathering might be expected to the main factor affecting joint incipiency. Residual rock bridges shown on the plane ③ gives some evidences for joint development influenced by weathering, as discussed by Hencher and Knipe (2007).

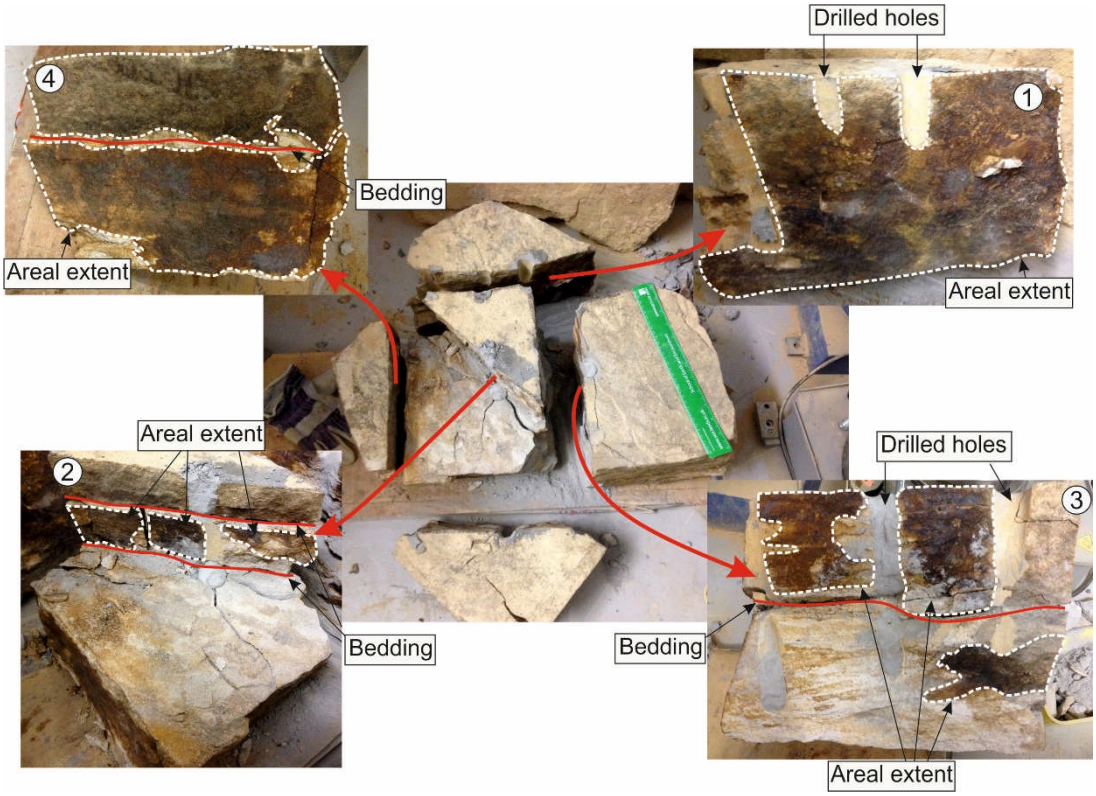

Figure 5.9 Incipient joint surfaces exposed after testing. Red lines correspond to an opened bedding plane. The rule for scale is 314 mm.

Uncertainties and errors in jointing measurements and geological data acquisitions mainly arising from spatial variability of geological formations have long been recognised (e.g. Merritt and Baecher 1981 and Palmstrom 2001), but no recommended methods have been proposed to resolve this issue (Einstein and Baecher 1982). This uncertainty was well demonstrated by the unpredictable areal extent of incipient joints within this small block sample.

Interactions between incipient discontinuities and rock matrix (such as interlocking effects) will influence the overall strength of the rock mass (Mughieda 1997). The incipient nature of joints (existing rock bridges) within this block sample clearly contributes a great deal to the strong interlocking effects. The strong capacity of rock bridges in strength contribution to a rock mass (UCS>200 MPa) was also examined and quantified by Diederichs and Kaiser (1999).

5.5 Areal extent of incipient rock discontinuities: Field FEIRD experiment

5.5.1 Field FEIRD test on Midgley Grit Sandstone Block 1

As can be seen from the overview of Blackhill Quarry in Figure 5.10a, Many large rock blocks were produced unpredictably after blasting due to the existing of incipient rock discontinuities. A hydraulic secondary breaker has to be used to break these large blocks into smaller pieces. Some of these blocks have been broken along incipient joint planes, and an example is shown in Figure 5.10b.

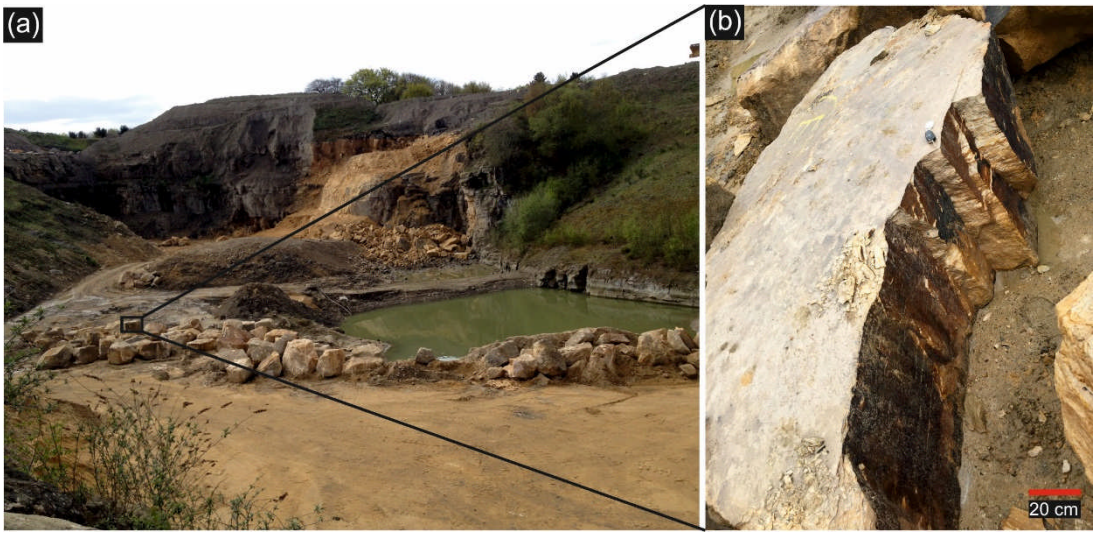

Figure 5.10 a Overview of BQ, West Yorkshire, UK; **b** A Midgley Grit Sandstone block showing one extensive exposed joint surface after blasting in the quarry. Note that light top surface of the block is a feshly exposed bedding plane.

As can be seen in Figure 5.10b, a set of incipient rock joints containing four parallel joints were broken partially along joint planes. It shows that revealed joint surfaces have been weathered significantly (almost no rock bridges can

be seen in the exposed portions) thus expected to have lower strength compared with those segments that were surviving.

Among these blast-induced rock blocks, an irregular Midgley Grit Sandstone block containing a complete incipient rock joint was identified in the BQ. It was removed with care to a spare place in the quarry for FEIRD testing (see Figure 5.11).

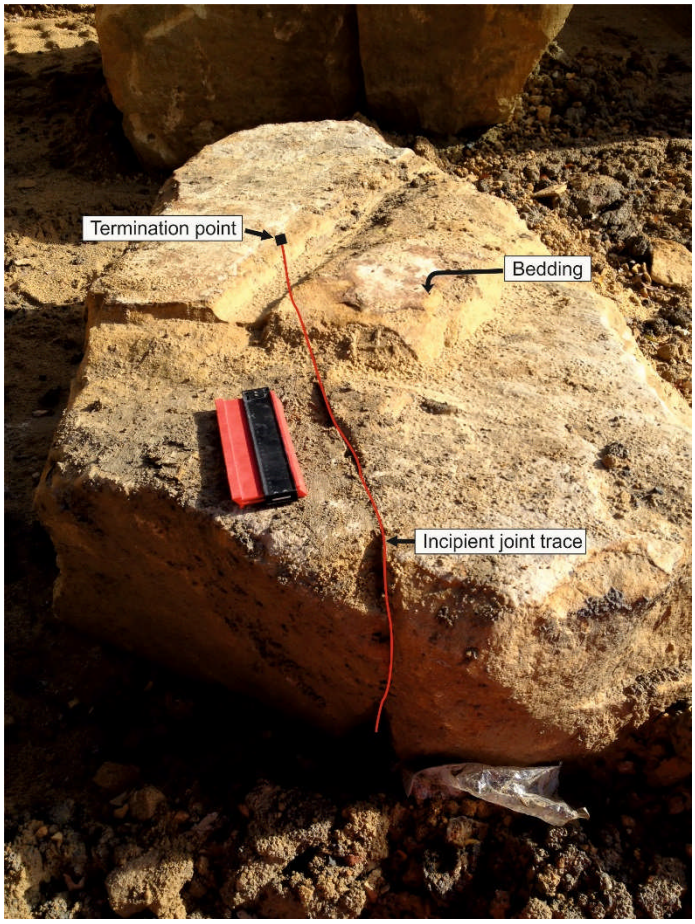

Figure 5.11 Midgley Grit Sandstone Block 1 with irregular dimensions in Blackhill Quarry, West Yorkshire, United Kingdom. An incipient rock joint survived the blasting process. The profile meter for scale is 270 mm.

It can be seen from top surface that the nearly vertical incipient rock joint terminated at rock material (indicated by the black dot), bedding planes approximately perpendicular to this joint plane.

(1) Testing procedures and failure patterns

The rock surface of sample was cleaned to remove any loose sand prior to FEIRD testing. Figure 5.12 illustrates the testing procedure adopted and the failure patterns that were created. All the images were captured after 24 hours.

Four the holes with diameter of 27 mm were drilled with separation of around 200 mm along joint trace on the top surface (Figure 5.12a). Joint trace termination point at hole 4 was indicated by a black rectangular dot. Another two holes with same diameters (27 mm) and spacing of around 230 mm were drilled along the extension line of the persistent joint trace. All holes were drilled to a depth of approximately 280 mm, more than 50% of the block depth. The expansive chemical splitter was prepared according to the specification in section 5.3.2 and injected into holes. The parameters of drilled holes and chemical splitter used in this test are shown in Table 5.2. Block sample was then protected by a plastic cover and warning signs placed to prevent quarry staff from approaching the experiment. Figures 5.12c, d and e show the failure patterns captured after 24 hours. It can be seen clearly that, only single mode I fracture exactly along the persistent joint trace was induced before hole 4 (joint termination point) (Figures 5.12c, e). While beyond the termination point, irregular (mode I opening and mode II shearing) fractures were produced. From Figure 5.12d, it can be noticed that mode II shearing fracture propagated approximately horizontally along weak bedding plane, while another mode II shearing fracture with smaller aperture propagated perpendicular to the bedding. The two separated blocks were removed with care by using a forklift (see Figures 5.12f, g). Two incipient joint surfaces were exposed and examined (see Figures 5.13).

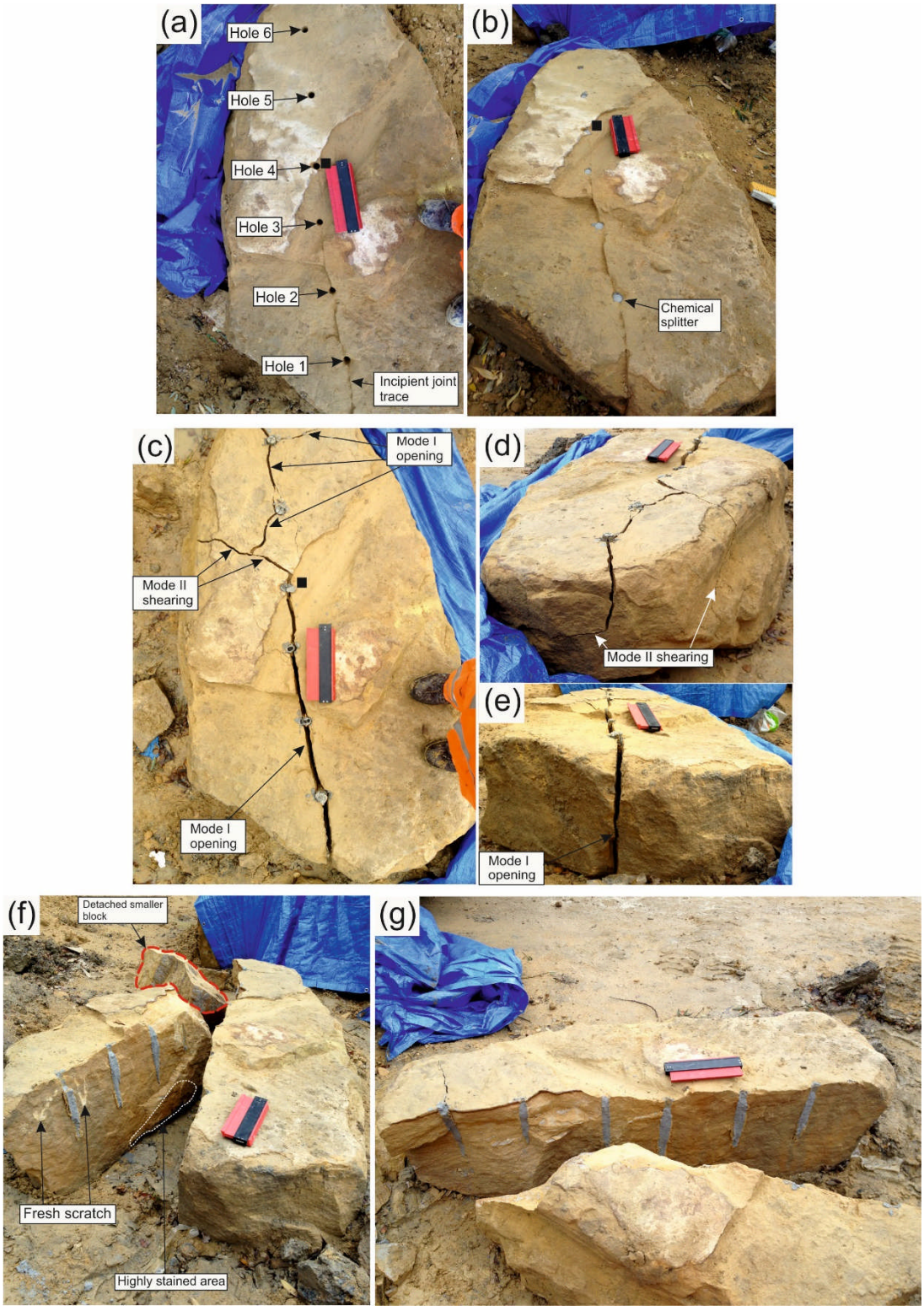

Figure 5.12 Procedures and failure patterns of the FEIRD testing performed on Midgley Grit Sandstone Block 1 in the Blackhill Quarry, West Yorkshire, United Kingdom. **a** Single near-vertical incipient joint terminated at rock matrix, six holes were drilled. **b** Chemical splitter was injected into pre-drilled holes. **c**, **d** and **e** Failure patterns and fractures induced after 24 hours. See text for more details. **g** Two separated blocks. **f** One smaller block was detached. Black rectangular dot shows the joint trace termination point. The profile meter for scale is 270 mm.

Table 5.1 Parameters of pre-drilled holes and chemical splitter used in the FEIRD testing on Midgley Grit Sandstone Blocks 1 and 2 in the field.

Sample	Hole numbers	Hole depth (mm)	Hole diameter (mm)	Hole spacing (mm)	Approximate amount of chemical splitter(ml)
Midelgy Grit Sandstone Block 1	1	280	27	Ranging from 200 to 230	162
	2	280	27		165
	3	280	27		160
	4	280	27		164
	5	280	27		165
	6	280	27		168
Midelgy Grit Sandstone Block 2	1	430	27	Around 240	251
	2	430	27		260
	3	430	27		253
	4	430	27		259
	5	430	27		255
	6	430	27		256
	7	430	27		264

(2) Testing results and discussion

The fracturing along the incipient joint plane shown in Figure 5.12 demonstrates that it propagated in a straight and near-planar way. Incipient joint is of interest within this block sample terminated at rock matrix. This can be attributed to the stress relief and stress around the incipient joint tips being transferred to the adjacent rock material during the initial joint development geologically (Hencher 2015). Notice that the irregular fracturing patterns (mode I and mode II) occurred partly through intact rock materials, probably due to the lithological heterogeneity. These induced fracture planes were opened. Two conditions are necessary for this fracturing in rocks (Fairhurst

1972). The two are: a “stress” condition that is the true cohesive strength (described by tensile strength) should be exceeded when the solid ruptures; and an “energy” condition, i.e. enough energy to form two distinct joint surfaces and to allow the fracture to extend and propagate. Hoek and Martin (2014) concluded that this brittle fracturing process, including fracture initiation and propagation, is predominately controlled by tensile strength of the intact rock including its component grains.

Figure 5.13 presents the exposed joint surfaces and joint roughness profiles. Two fresh scratches (Figure 5.13a) produced by a forklift provide a good reference for identifying the colour changes of the material. Fresh rock bridge (RB) areas on the incipient joint surfaces were distinguished by eye and are enclosed by the dashed lines (see Figures 5.13a, b). Feather markings can also be clearly identified visually. For the exposed joint surface shown in Figure 5.13a, the persistent joint areas (on the left) have been stained slightly indicated by colour changes. Discolouration of rock material on this surface varied gradually from the left part to the edges of rock bridge, i.e. from light grey (slightly stained), through a grey mottled brown transition zone to light brown for the relatively fresh rock bridges. No identifiable feather markings occurred on persistent areas. Apart from this, there are some heavily stained areas (black areas) on the bottom. It also can be seen that the areal extent of the persistent joint segment does not correspond with the termination point of joint trace (indicated by rectangular dot in Figures 5.13a, b) observed from surface.

Roughness profiles of the joint surface in Figure 5.13a were measured by a profile meter. The relative amplitude of eight roughness profiles were quantified with a reference value of 7 cm. This means that real roughness amplitude of any points on profile lines can be obtained by subtracting 7 cm using the each relative amplitude value. Positive corresponds to convex points while negative indicates the concave point. Linear extent values along these eight profile lines were also included correspondingly in Figure 5.13a_1. The terms for medium-scale roughness at centimetres were used to describe the profile according to the definitions by Barton and Choubey (1997) and Norbury (2010). Joint profiles 1-2 were planar, profiles 3-4 were undulating and profiles 5-8 were stepped. There is a general trend between linear extent values and profiles, i.e. linear extent values were changing from 100% for planar and undulating profiles to 20% and 0% for stepped profiles. This illustrates that the induced fracture segment along the persistent incipient joint area was flat,

while in areas of new fracturing the fracture was more variable and rough with high asperities.

Similar observations were made on the opposite exposed joint surface (Figures 5.13b, b_1). Feather markings were seen on the rock bridge areas. Profiles on this surface changed from planar at profile lines 1-3 to undulating at profile lines 4-5 and finally to stepped at profile lines 6-11. Note that rock bridge area on this joint surface (outlined with a white dashed line in Figure 5.13b) contained clear signs of tensile failure, in the form of high level asperities. The rock bridge area on the joint surface was quantified by using AutoCAD, and the areal extent (persistence) of this incipient joint was calculated as 48%. While the linear extent of joint trace from surface is approximately 55% (Figure 5.13a). It is larger than the real persistence (48%) demonstrating that the traditional approximation of real persistence using trace length from rock outcrop may be not reliable, at least for the case in this study, even though the areal extent depends greatly on the geometrical properties of sample and is scale dependent (Lu and Latham 1999, Wasantha et al. 2014).

Linear extent and relative amplitude of each 2D profile are shown in Figure 5.13b_1. A reference value of 9 cm was employed to calculate the variation. Linear extent varied abruptly from 100% for profiles 1-5 to 0% for profiles 6-11.

Schmidt hammer (L-type) tests (SH) were performed on the two joint wall surfaces (Figures 5.13a, b) according to the ISRM standard (1981, 2014) to measure the wall strength. Joint walls were cleaned to eliminate effects from loose thin layers prior to SH testing. Each point was tested two times perpendicular to the surface. Red and green dots on two exposed surfaces (Figures 5.13a, b) correspond to the SH testing points on persistent joint area and rock bridges, separately. For the heavily stained areas on the bottom of failure surfaces, rebound values range from 18 to 24, while the values range from 21 to 34 for slightly and moderately weathered area. The value range 28-45 is higher for the testing points on rock bridge areas.

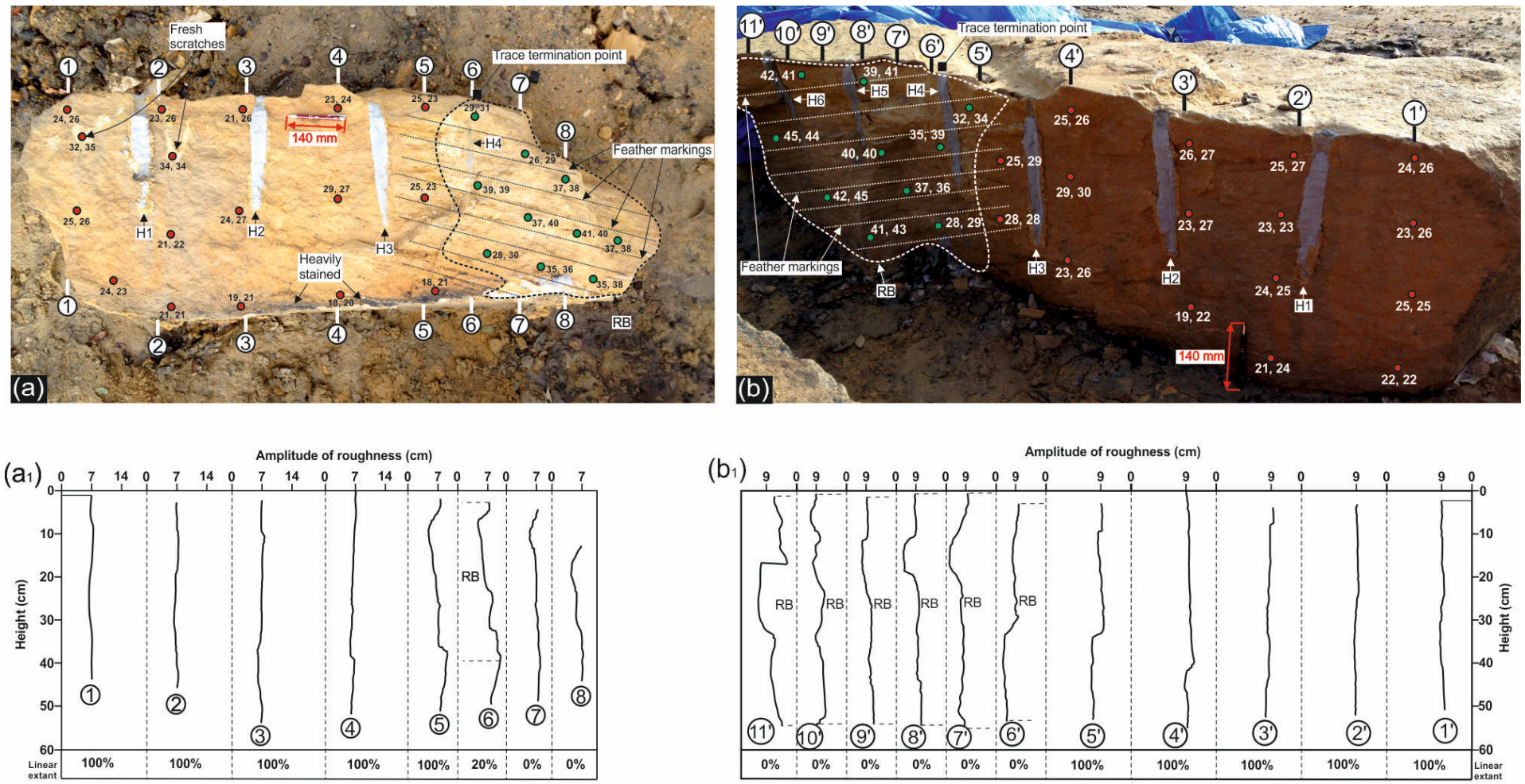

Figure 5.13 Opposite exposed incipient joint surfaces, areal extent and roughness profiles of the incipient joint within the Midgley Grit Sandstone Block 1. Persistent joint areas can be distinguished by discolouration, fresh and relatively fresh rock bridge (RB) areas were enveloped by black dashed line in **a** and white dashed line in **b**. Red and green dots correspond to the L-type Schmidt hammer testing points on persistent joint area and rock bridge area. The ball pen for scale is 140 mm.

5.5.2 Field FEIRD test on Midgley Grit Sandstone Block 2

Figure 5.14 presents another irregular Midgley Grit Sandstone Block sample 2, in Blackhill Quarry, UK. It contained a single vertical incipient joint with visible termination at the black dot shown on surface. The linear extent of the joint trace on the exposed surface is around 56% of the block dimension. No other joint traces within this block sample were identified. Block volume was estimated to be approximately 4 m^3. Sample surface shows different degree of weathering.

Figure 5.14 Midgley Grit Sandstone Block 2 with irregular dimensions in Blackhill Quarry, West Yorkshire, United Kingdom. A vertical incipient rock joint, surviving after blasting, terminated at rock matrix (black dot on surface). The profile meter for scale is 270 mm and van can be another scale.

(1) Testing procedures and failure patterns

FEIRD testing procedures (Figure 5.15) were the same as those used for the Midgley Grit Sandstone Block 1. Seven holes with diameter of 27 mm were drilled along the incipient joint plane (Figure 5.15a), and chemical splitter (Figure 5.15b) was poured into the pre-drilled holes according to the preparation requirements described in section 5.3.2. Sample was then protected by a plastic cover for 24 hours. Figures 5.18c and d show the failure patterns. It can been seen that an induced fracture with aperture of around 3.3

cm was produced exactly along the pre-existing incipient joint trace on the top surface. Mode I and mode II fractures appeared (Figures 5.15c, d); beyond the termination point, a stepped induced fracture occurred (Figure 5.15d). A forklift was used to prise off one broken part to expose the incipient joint surfaces, shown in Figure 5.15e.

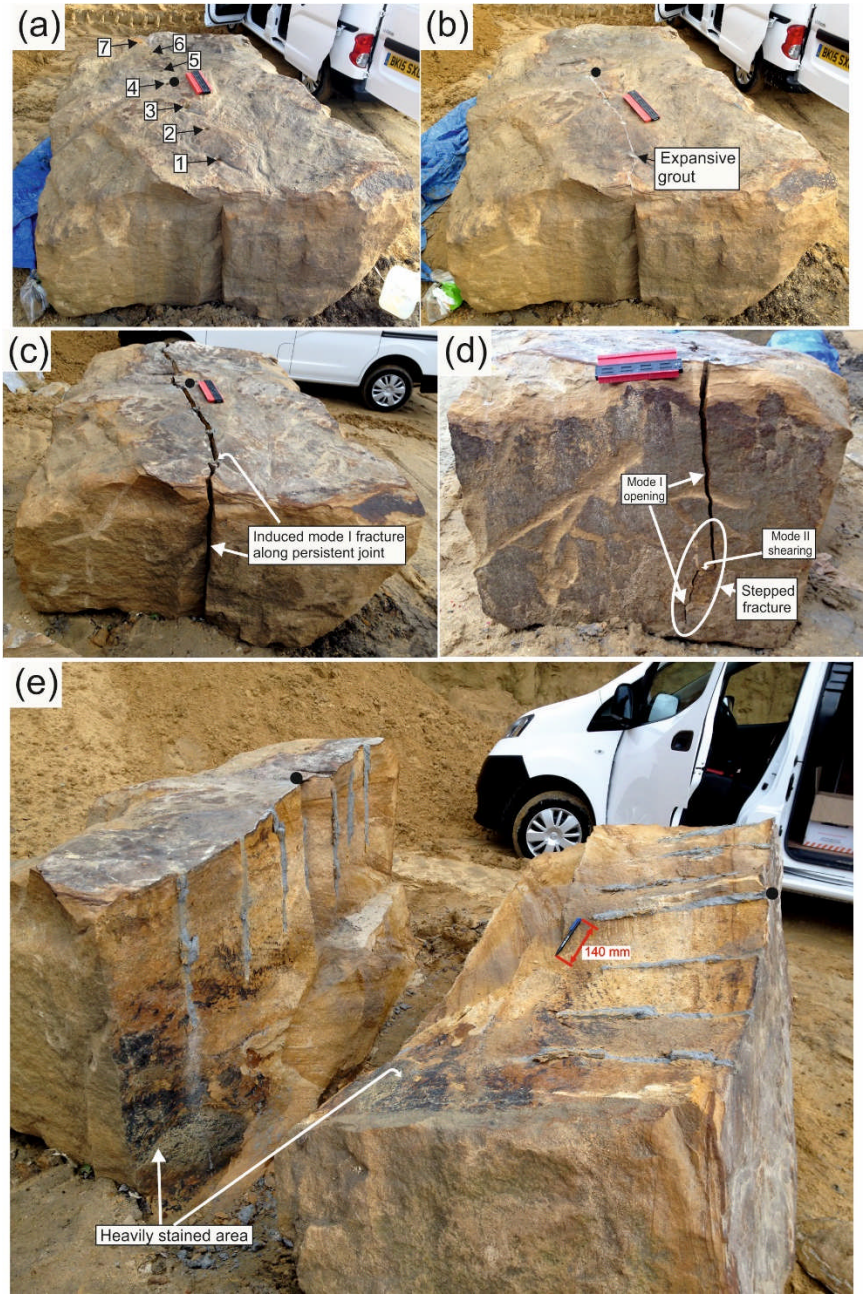

Figure 5.15 a and **b** Procedures of forensic excavation of incipient rock discontinuity within the Midgley Grit Sandstone Block 2. Failure patterns were shown in **c** and **d**. The two blocks were separated by a forklift and the exposed joint surfaces are shown in **e**. The profile meter for scale is 270 mm, ballpoint pen for scale is 140 mm in length. Black dot indicates the joint trace termination point at top free surface.

(2) Testing results and discussion

As can be seen in Figures 5.15 c and d, induced fracture predominately occurred in mode I opening and near planar in shape along pre-existing incipient joint trace, except for a small stepped mode II shearing fracture (Figure 5.15d). Stresses around joint tips control the joint-propagation path (see discussion in Chapter 2, section 2.3). Once fracture naturally initiates under mode I loading, it tends to propagate in a plane if the principal stress remains consistent along the extension of joint plane (Pollard and Aydin 1988). This is evident from the planar incipient joint plane. It can be seen that the failure pattern in this test is different to the situation in previous FEIRD test shown in Figure 5.12c, in which induced non-planar fractures with mode I and mode II passed through the matrix. This might can be related to, except for principal stress orientation, the large increment of dimension of Midgley Grit Sandstone Block 2 (compared with that of Block 1). Chemical weathering process left a clear morphological signatures (stained sections) on surfaces due to redox reactions, i.e. oxidation (Figure 5.15e).

Figure 5.16 presents the exposed incipient joint surfaces and roughness profiles. A general trend of degree of weathering was clear. The persistent area was stained heavily to black at the bottom and it varied gradually to reddish brown and grey towards the top of the block. Similarly degree of weathering decreased gradually from the edges to inner areas. This demonstrates, in the medium scale, the progressively development of discontinuity with time from incipient state to finally mechanical state due to weathering (see further discussion in Hencher and Knipe (2007)).

As for the Block 1, feather markings were not identifiable on the persistent joint areas; while they appeared in the relatively fresh rock bridge areas. Stained feather markings were noticed at the transition zones from persistent joint area to rock bridge area (Figures 5.16a, b). Note that weathering (discolouration) was along feather markings, primarily due to the water flow along or parallel to the marks. The feather markings on the non-persistent areas were traced by white dashed lines (Figures 5.16a, b). Similarly fresh scratches were left because of the action of the forklift.

The joint trace termination point on the top free surface was indicated by black dots in Figures 5.16a, b. Again, the rock bridge area was distinguished by discolouration to the persistent joint surfaces. Unlike the situations in relation to joint trace termination point and areal extent within Block 1, the joint trace

terminated beyond the edge of areal extent of stained area, i.e. the areal extent value (persistence) might be smaller than its approximation from the trace length observed at surface. Areal extent values of the two opposite joint surfaces were calculated as 28% and 33%, respectively, thus average areal extent of this incipient joint was 31%; while the trace length (approximation of persistence) of the incipient joint was 56%, approximately 74% larger than the real persistence. This is based on the assumption that persistent areas have been stained. The large difference cannot be neglected. This means that the traditional approximation of areal extent (persistent) using trace length on outcrop may not be reliable, at least for the case in this test.

Again, L-type SH tests were carried out on the exposed joint surfaces to measure the wall strength according to ISRM standards. Testing points were indicated by red dots and green dots separately on the rock bridge areas and persistent stained areas (Figures 5.16a, b). Rebound values ranged from 25 to 46 for rock bridge area while for persistent stained areas, the values varied from 12 to 32.

Medium scale roughness profiles and corresponding relative amplitude of two exposed joint surfaces were quantified. It should be noted that amplitude, shown in Figures 5.16 a_1, b_1, compared to a reference value of 7 cm. For roughness profiles shown in Figure 5.16a_1, it changed from planar (① and ②) in persistent area to undulating (③ and ④) in transition zone, and finally to stepped (⑤-⑩) in the rock bridge area. Linear extent values of these three areas varied from 100% (persistent area), 52% and 56% (transition zone), and approximately approaching to 0% (rock bridge). While for the roughness of the opposite joint surface (Figure 5.16b_1), a similar trend can be seen. Roughness profiles varied from planar (①-③) in the stained persistent area to undulating in the transition zone (④), and eventually to stepped in rock bridge area (⑤-⑩). Linear extent changed from 100%, 50% and 0% for these three zones separately. Note that the stepped roughness profiles in the rock bridge areas were closely related to the stepped failure of rock material shown in Figures 5.16a, b.

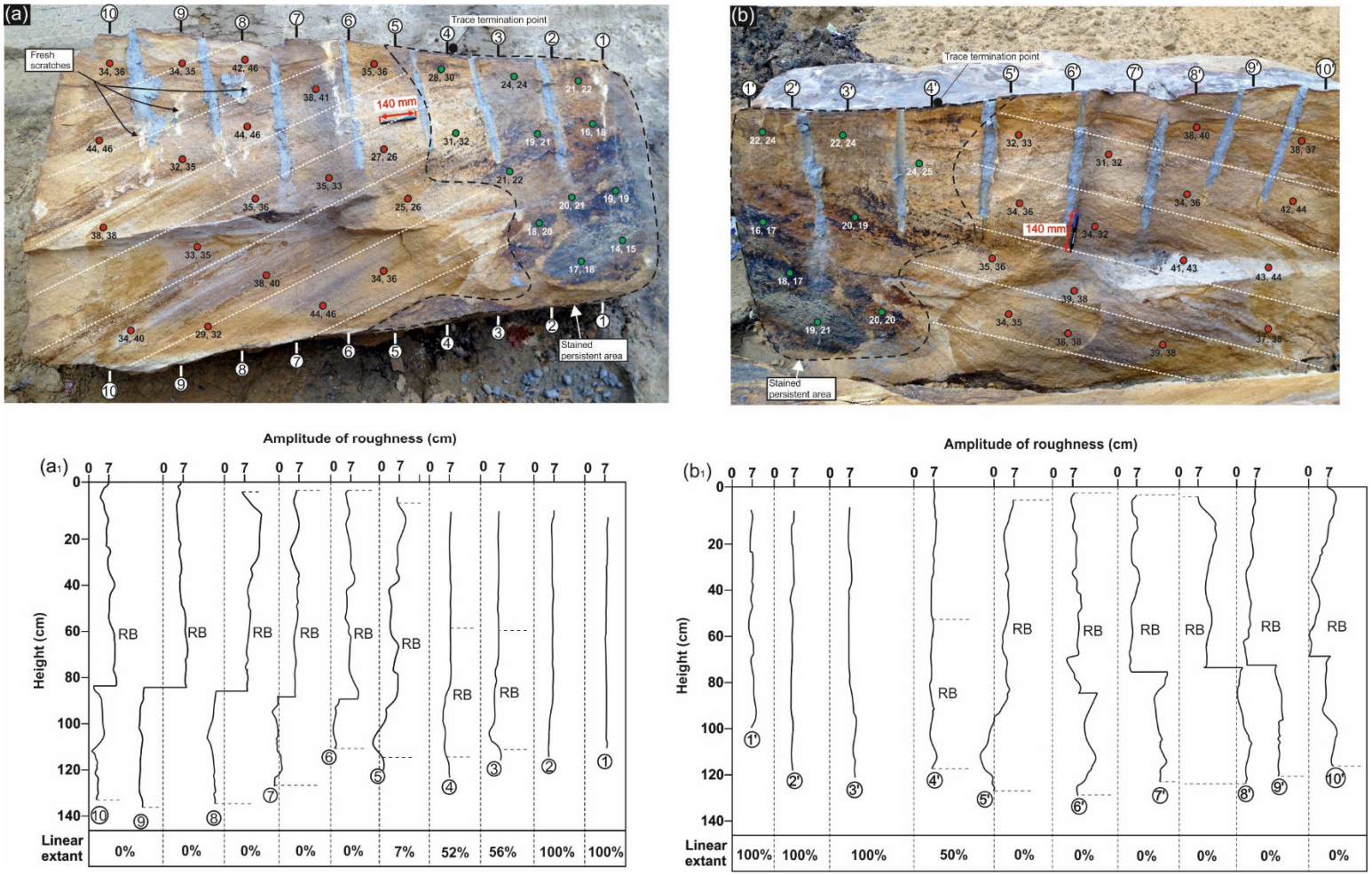

Figure 5.16 a and **b** Opposite exposed incipient joint surfaces and areal extent of the incipient joint after FEIRD testing. Stained areas were enveloped by black dashed lines; Feather markings were traced by white dashed lines. SH testing (L-type) on joint walls were carried out and testing points were indicated by red and green dots on rock bridge areas and persistent stained areas, respectively. Medium scale roughness was quantified and shown in $\mathbf{a_1}$ and $\mathbf{b_1}$.

5.5.3 Field FEIRD tests on Horton Formation siltstone block

FEIRD testing was conducted on a fractured Horton Formation siltstone block at Dry Rigg Quarry, North Yorkshire, United Kingdom. Figure 5.17 presents the tested rock block containing various incipient rock discontinuities from different views. This block has been removed and placed at the edge of car park area by the quarry staff. Seven incipient joint traces were identified from top free surface; bedding plane slightly inclined as was indicated by black dashed line in the front view image. Incipient joint traces on the back exposed surface were traced by white chalk. Note that parts of exposed surfaces on the front and left view surfaces have been coated by quartz.

This jointed rock block was going to be forensic excavated slab by slab along planar or near-planar incipient joint traces on the top surface to investigate the areal extent of incipient rock discontinuities. Prior to the forensic excavations, dye was injected considering the low-permeability of siltstone interested (dye will preferentially flow along persistent joint segments instead of matrix).

Figure 5.17 Horton Formation siltstone block at Dry Rigg Quarry, North Yorkshire, United Kingdom. The rule for scale is 314 mm, geological hammer for scale is 310 mm.

(1) Relative orientation of discontinuities

Seven visible incipient traces can be seen from the top view in Figure 5.17. Note that the top view image only shows the left part of the original block after splitting of a slab along joint ①. A bedding plane, indicated by the black dashed line in the front view, was inclined relative to the ground and perpendicular to the front exposed block surface. Parts of a closed and non-infilled incipient joint ① can be seen from the left view, while another partially exposed joint surface enclosed by black line in this joint set was coated by quartz (left view). From the back view of this block, many planar and non-planar incipient joint traces appear which have been traced by white chalk in the field. Bedding traces were also clearly displayed. Relative orientation of these incipient discontinuity traces (only consider planar or near-planar traces) including exposed free surfaces are plotted in Figure 5.18 assuming a North direction towards to the strike of bedding plane (see front view in Figure 5.17).

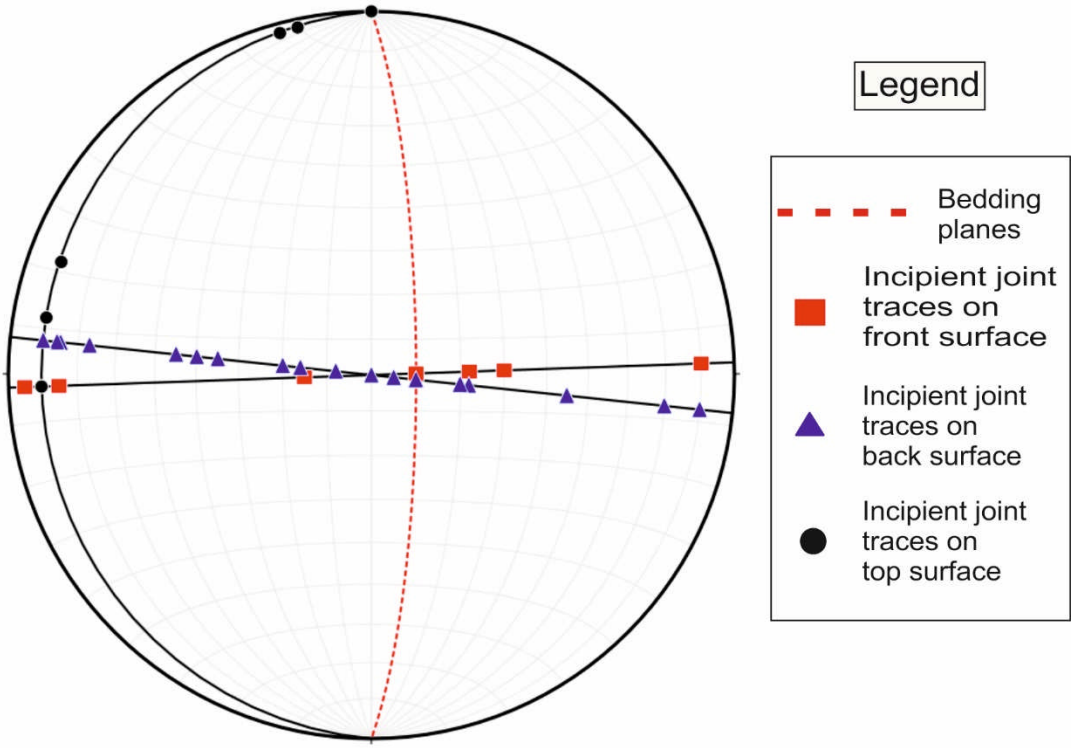

Figure 5.18 Relative orientations of planar incipient discontinuities and exposed free surfaces on the Horton Formation siltstone block in Figure 5.17.

(2) First run of FEIRD testing

a) Testing procedures and failure patterns

Five holes with depth of approximately 450 mm were drilled along incipient rock joint trace ①. Note that, because of the high strength of the siltstone in this site (UCS approaching 200 MPa Duckering (2015).) and the limitation of the hand drill used, only the first drilled hole was 27 mm in diameter; the other four holes were drilled at 17 mm in diameter (see Table 5.3). Prior to the forensic excavation, dye was injected in an attempt to colour the persistent joint segments. The block was then protected by a plastic cover and left for 24 hours for dye to penetrate over gravity. Figure 5.19 shows the procedures and dye flow results after 24 hours.

Figure 5.20 shows the procedures of the first run of FEIRD testing. There was a slight difference between the procedure tested here and that described in section 5.3.2. Secondary prise-off tools included steel and wood chisels and an excavator. These were needed because after splitting, the block remained partially intact. This was probably because the insufficient depth of holes drilled leaving remnant intact rock bridges towards the bottom of the incipient joint plane. A fracture with an aperture of around 2 mm was induced after 24 hours (Figure 5.20b). It is interesting to see that the induced fracture exactly followed the joint trace ① which terminated at hole 2 and then followed a zigzag pattern between hole 2 and hole 3. Unexpectedly, it did not pass through hole 3. Secondary prise-off work was conducted, as shown in Figures 5.20 c-g. A zigzag induced fracture shape was also noticed in Figure 5.20d for a crack through intact rock material. A high tensile strength contribution (true cohesion) arising from rock bridges along this incipient rock joint was evident as the slab was still intact even though the fracture aperture at the top approaches 130 mm (Figure 5.20f). This slab was eventually detached by an excavator (Figure 5.23g), and the exposed joint surfaces are presented in Figure 5.20h.

Figure 5.19 Dye technique used to colour persistent joint areas. **a** Fluorescent dye ($C_{20}H_{12}O_5$) was poured into holes using a syringe prior to the first run of forensic excavation. **b** and **c** Dye flowed out along persistent joint segments after 24 hours. Red dot indicates the termination point of incipient joint trace ①.

Table 5.2 Parameters of pre-drilled holes and chemical splitter used in FEIRD testing on Horton Formation siltstone in the field.

	Hole numbers	Hole depth (mm)	Hole diameter (mm)	Hole spacing (mm)	Amount of chemical splitter (ml)
First run of testing	1	450	27	Ranging from 200 to 230	260
	2	450	19		131
	3	450	19		130
	4	450	19		128
	5	450	19		127
Second run of testing	1	450	19	Ranging from 200 to 230	131
	2	450	19		135
	3	450	19		125
	4	450	19		126
	5	450	19		125
	6	450	19		130

b) Results and discussion

It is interesting that seepage appeared from one incipient joint trace on the front exposed surface (Figure 5.19c) and from the left part of incipient joint trace ① (Figure 5.19b). This can be related to the fluid flows along persistent joints within rock masses. Persistent joint segments in turn might be coloured.

Figure 5.21 presents the exposed joint surfaces and medium scale roughness profiles. It can be seen that persistent areas on the exposed surfaces have been contaminated (however no clear colour traces from the dye can be noticed). The seepage phenomenon observed in Figures 5.19b, c can be explained and verified by the persistent nature of joint areas on the left part of exposed surfaces as well as the joint trace indicated by red line in Figures 5.21a, b. Fresh rock bridge areas were embraced by black dashed line in Figure 5.21a and the white dashed line in Figure 5.21b. Areal extent (projected) of this incipient joint was calculated (62%) by averaging the areal extent values (59% and 64%) from the two exposed surfaces. The real

persistent value (62%) calculated from exposed incipient joint surface is about two times larger than its approximation (32.4%) traditionally from joint trace from the exposure.

Figure 5.20 Procedures of the first run of FEIRD testing along incipient joint ① within a Horton Formation siltstone block. **a** Chemical splitter was poured into pre-drilled holes, and one fracture with an aperture of about 2 mm was induced after around 24 hours in **b**. **c**-**f** Metal and wood chisels were employed to prise off the pre-split rock slab, it is however still stable even though the aperture on the top exceeded 130 mm as seen in **f**. An excavator eventually helped to prise off the slab in **g** and the exposed incipient joint surfaces were shown in **h**. Red dot indicates the termination point of the incipient joint trace ①. The rule for scale is 314 mm, and geological hammer for scale is 310 mm.

As is evident from this study, fractography features including hackles and rib marks were observed. The hackles (indicated by white lines in Figures 5.21a, b) were noticed on two exposed joint surfaces, which was first described and named “feather structure” by Woodworth (1896), and later named “plumose” by Hodgson (1961). In this study, the hackles radiated from the edges of persistent joint rather than from a point (which is often observed in the field (Pollard and Aydin 1988) or on the rock surface broken by impact with hammer (Hencher 2015)). This different feature may be due to the different way of fracture propagation in the FERID testing, demonstrating the local joint propagation orientation. Rib marks, curvilinear ridges structures indicating incremental interrupted growth, are normally oriented at right angles to hackles (Woodworth 1896 and Bankwitz 1965). This is evident from this study that ribs profiles (white dashed line in Figure 5.21a and black line in Figure 5.21b) occurred on the exposed joint surface were parabolic and were normal to the hackles, which are similar to those reported (e.g. Engelder, 1987 and Ameen 1995) and the classic surface structures described in Chapter 2.

The randomly distributed joint traces on both exposed surfaces were traced by black lines, and for a special case (allowing seepage seen in Figure 5.19c), traced by red lines. The persistent joint areas shown on exposed surfaces combining the conjugated red-traced joints on both surfaces worked as the conduits for fluid flow.

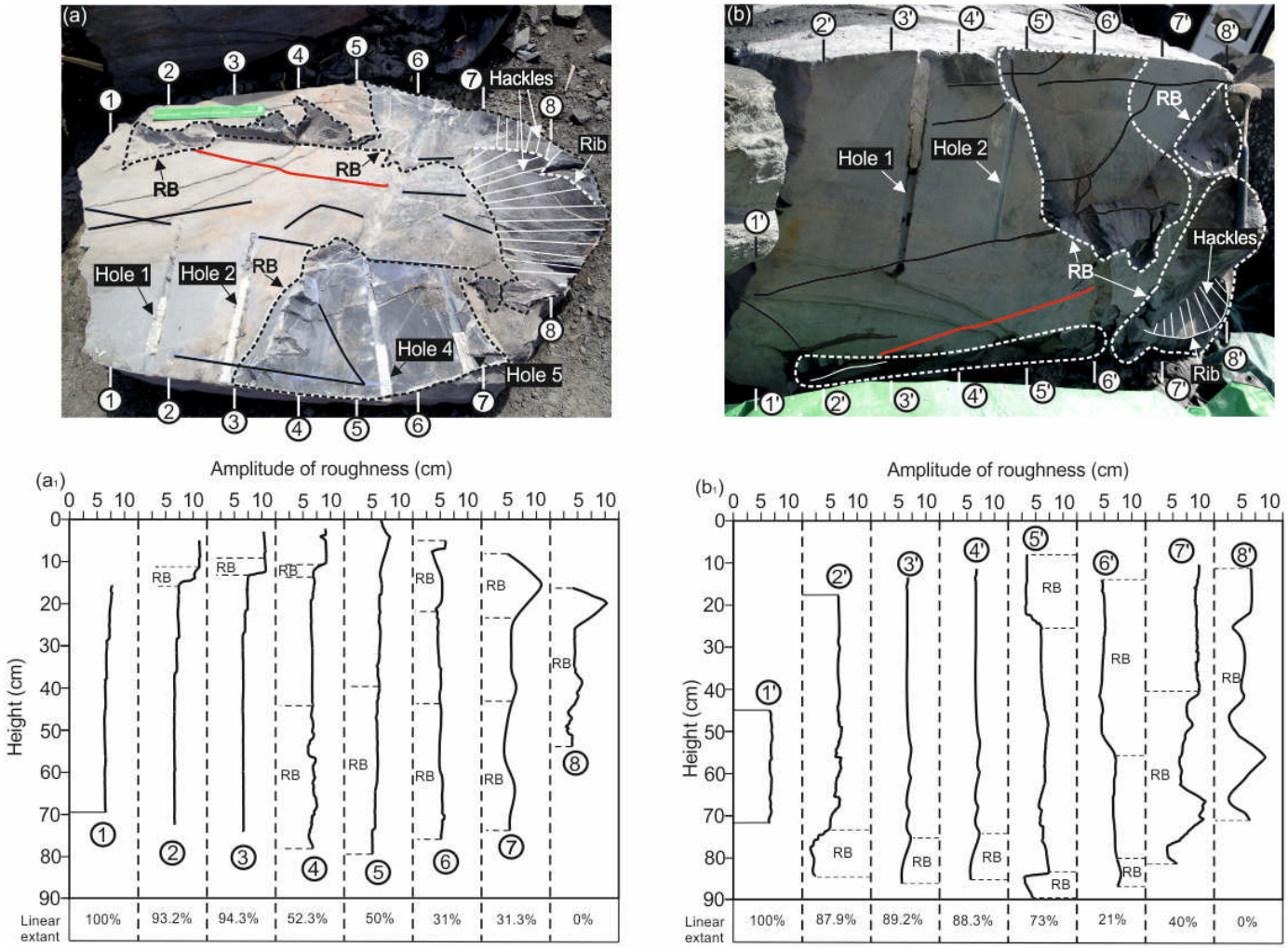

Figure 5.21 Exposed incipient joint surfaces and roughness profiles. The main rock bridge (RB) areas were enveloped by black dashed line in **a** and by white dashed line in **b**; Incipient joint traces on exposed surfaces were indicated by black lines. $\mathbf{a_1}$ and $\mathbf{b_1}$ Linear extent of 2D roughness profiles on both exposed surfaces varied from 0% to 100%. Red dot indicates the termination point of incipient joint trace ①. The rule for scale is 314 mm, and geological hammer for scale is 310 mm.

Medium scale roughness profiles were measured by a profile meter, the relative amplitude of roughness profiles were quantified with a reference to a plane of height of 7 cm. Rock bridges (RB) were indicated on the 2D profiles. It is interesting to note that most of the rock bridge areas correspond to a higher profile amplitude. This can be explained by the nature of fracture propagation in the test, thus generally irregular fractures were tend to be reduced when cracking intact rock (rock bridge areas in this test). This is similar to situations observed in the FEIRD in Midgley Girt Sandstone. In addition, unlike surface profile shown in Figure 5.13 and Figure 5.16, no clear changing trend in profile shape can be noticed. Linear extent of 2D profiles are scattered between 0% and 100% with no abrupt changes.

(3) Second run of FEIRD testing

a) Testing procedures and failure pattern

The second run of FEIRD testing was carried out on the same block along incipient joint trace ④. Note that dye technique was not employed in the second run of testing as the text (using gravity seepage) was unsuccessful for the first test run. Figure 5.22 illustrates the testing procedures and failure patterns. Four holes were drilled along the joint trace ④ while another two holes were drilled along the extension of the straight line of trace, so as to produce a slab. Table 5.3 shows the parameters of holes and chemical splitter used in each hole. The fracture induced on the top surface (Figure 5.25b) followed the pre-existing joint trace ④ as anticipated. It also followed on induced joint traces on one of the exposed joint surfaces after the first run of FEIRD testing (Figures 5.22b, c). Steel chisels were used to prise off the rock block which was not fully broken using the chemical splitter. Unlike the situation in the first FEIRD (a whole slab was produced), two blocks were mobilized rather than a whole rock slab.

b) Testing results and discussion

Figure 5.23 shows the exposed joint surfaces after the second run of FEIRD testing on Horton Formation siltstone. Not as expected, several irregular blocks were produced rather than a whole single slab from the first run of testing. From the exposed surface in Figure 5.23f, it can be seen that incipient joint plane ④ was non-planar in shape (curved and dipping into rock masses indicated by arrow). This give an explanation for the irregular failure patterns obtained. No areal extent (persistence) value of the incipient joint ④ was

obtained because of the unsuitability of the persistence definition in this study based on the assumption that discontinuities are planar in shape.

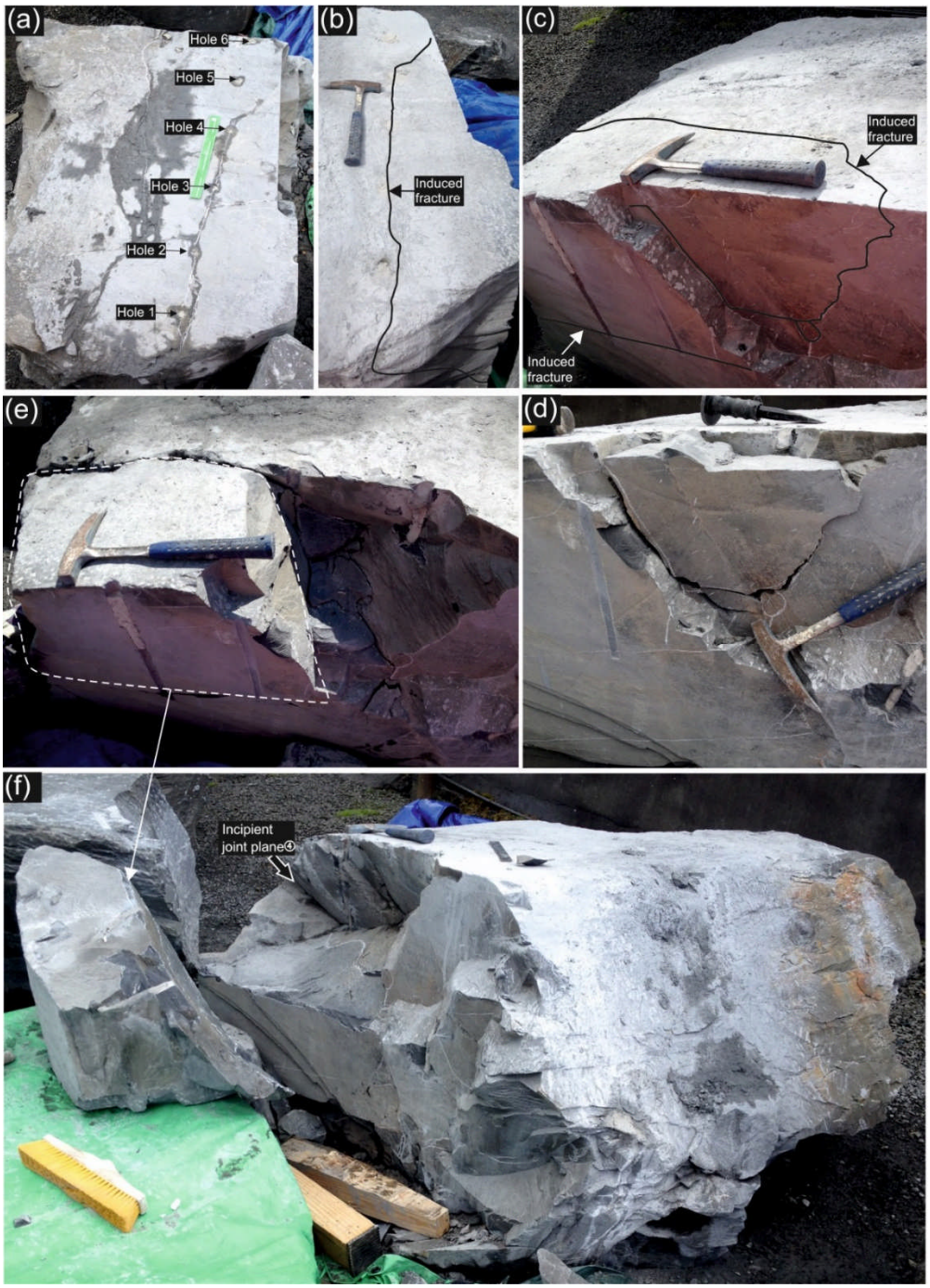

Figure 5.22 Procedures of the second run of FEIRD testing along the incipient joint trace ④. **a** Four holes were drilled along the joint trace while another two holes were drilled into intact rock material aiming to produce a rock slab as for the first run of FEIRD testing. Induced fractures were produced after 24 hours (**b** and **c**). Two blocks were eased off by a chisel (**e**-**f**). It was found that incipient joint ④ dipping into rock mass and was non-planar. Rule for scale is 314 mm, and geological hammer for scale is 310 mm.

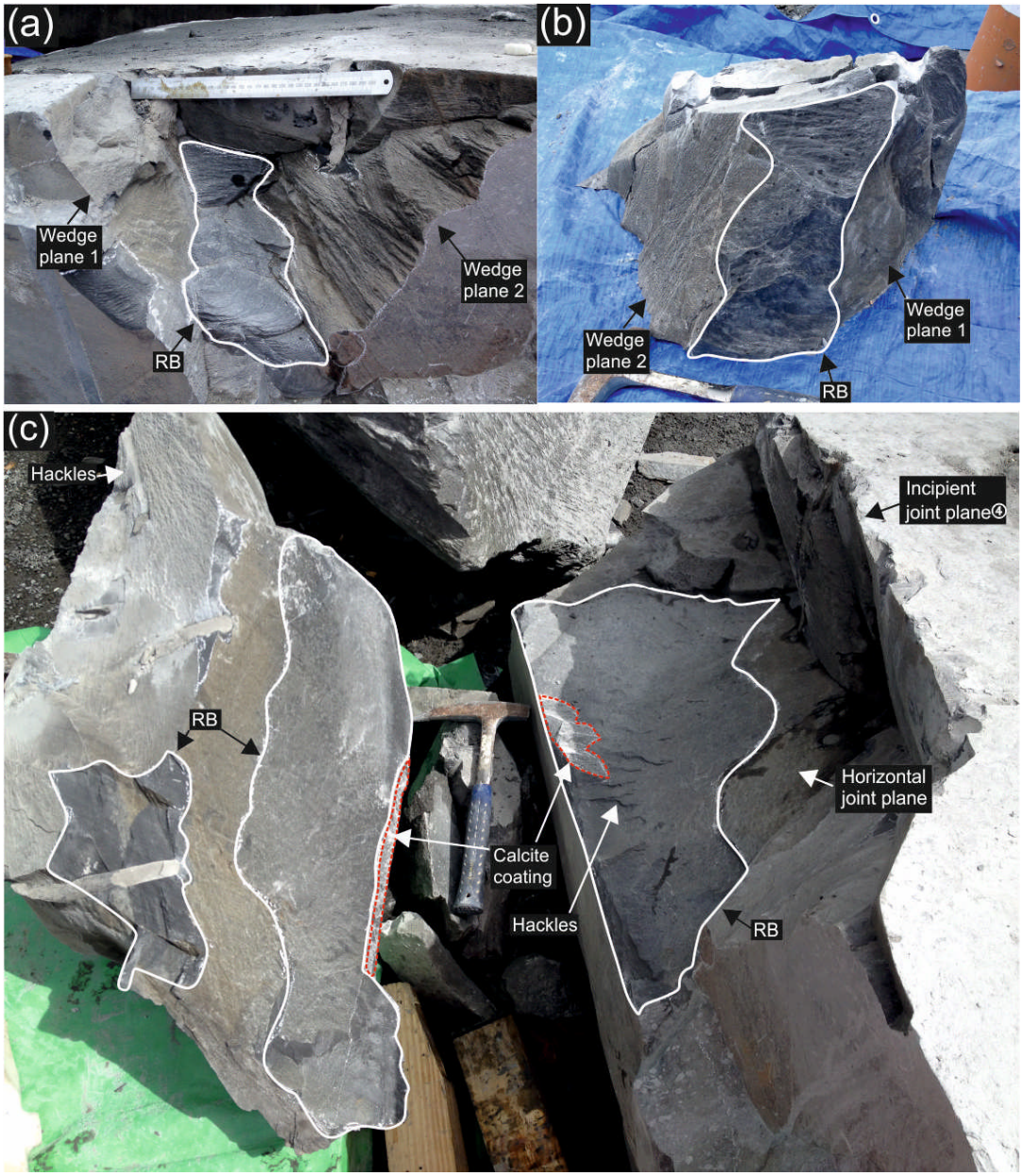

Figure 5.23 Irregular exposures after second run of FEIRD testing. Two main irregular rock blocks were produced rather that a whole slab. **a** Two wedge planes and intervening rock bridge (enveloped by white line). **b** A mobilized wedge-shaped block was produced. **c** A larger irregular block prised off showing the rock bridges (white enveloped areas) and calcite coating on joint planes (red dashed areas). Steel rule for scale is 300 mm, and geological hammer for scale is 310 mm.

Two wedge planes and intervening rock bridges are shown in Figure 5.23a, giving rise to a wedge-shaped block (Figure 5.23b). Only the exposed parts of these two wedge planes can be seen, there are no clue about how far they persist into this rock block. Another larger block was produced because of the intersection of curved incipient joint plane ④ and a near horizontal incipient joint. Fresh rock bridges on these exposed incipient joint planes were

identified visually and enclosed by white lines. It was observed that calcite coating areas (red enclosed areas) were exposed partially on joint surfaces (Figure 5.23c). All the exposed fracture surfaces lacked visible surface patterns, but exposed surfaces through rock bridges showed some hackle markings (see Figure 5.23c).

Large block volumes tend to be produced due to the incipient nature of rock discontinuities (Wang et al. 1991 and Longoni et al. 2012), this is demonstrated by the second run of testing. The large rock bridge areas (white enveloped areas) provide a considerable strength contribution to rock masses.

5.6 Summary and conclusions

In this chapter, a technique “Forensic excavation of incipient rock discontinuity (FEIRD)” has been developed to investigate discontinuity persistence (areal extent). Laboratory and field based FEIRD testing on different rocks of lithology were performed as application examples. A preliminary investigation into using dye technique to permeate persistent areas along incipient discontinuity plane was conducted in the lab. Main conclusions are drawn as follows:

(1) FEIRD is useful in the investigation of areal extent (persistence) of planar discontinuity. It was found that traditional approximation of persistence from trace mapping on rock exposures is not reliable and this might have major consequences for rock mass classification.

(2) The dye technique was attempt in the laboratory to colour the persistent sections of incipient discontinuities. It was found that this technique did not allow the persistent segments along incipient discontinuities to be fully identified, especially for permeable rocks (such as Midgley Grit Sandstone). For the Midgley Grit Sandstone tested in this study, natural discolouration of failed surfaces provided a much better clue to quantify persistence, assuming that persistent areas have been stained or weathered at the time of testing.

(3) Persistent sections of natural incipient rock joints were often near-planar in shape with low level of asperities during splitting in the FEIRD. While a high level of asperities on failed rock surface appeared when breaking rock bridges.

(4) Feather markings on the split rock surfaces in the FEIRD testing radiated around edges of rock bridges rather than from a point (which is often the case in the field), this relates to the specific test methodology and fracture propagation.

Chapter 6
Synthesis

6.1 Fundamental understanding of discontinuity development

Geological discontinuities can develop from incipient states into mechanical fractures in response to a number of triggers including gradual processes such as weathering and unloading and more rapid processes including seismic shaking and human activities (e.g. blasting). Discontinuities can be found in nature at different stages of geological development. Examples of discontinuities at early incipient stages are joints 1 and 2 in Figure 2.4, Chapter 2; an example of a joint at a later incipient stage is joint 3 in Figure 2.4, Chapter 2. Figure 2.1 (in Chapter 2) illustrates how an incipient joint, given time, will develop into a mechanical fracture lacking tensile strength.

Assessment of rock engineering project regarding stability and engineering performance should consider the development of discontinuities encountered with respect to the specific geological history in the site, as discussed by Hencher and Knipe (2007). In-situ monitoring of the long-term creep behaviour of a specific discontinuity over many years can improve our understanding of how incipient discontinuities develop (e.g. Collins and Stock, 2016).

6.2 Characterisation of incipiency

The term ‘incipiency’ relates to geological discontinuities that are only partially developed. Incipient discontinuities may be observed as visible traces or simply discerned as a mechanical anisotropy when rock is tested or in engineering performance (such as rift and grain weakness directions in quarrying). Investigation of tensile and shear strength of incipient discontinuities has been addressed in Chapter 2. It has been noted that rock bridges along incipient discontinuities will contribute to increased shear strength as discussed previously by Lajtai (1969). As can be anticipated, shear strength of incipient rock discontinuities will vary with the spatial distributions and geometries of rock bridges (Ghazvinian, 2007). Strength variation will relate in part to stress conditions at leading and developing fronts of persistent sections of fractures, as discussed in Chapter 2.

The degree of incipiency of discontinuities can be characterised and quantified relative to the tensile strength of the parent rock (see Chapter 3). Different discontinuities have different characteristics and it follows that the factors contributing to their incipiency are also different. For incipient bedding, as in the sample tests reported in Chapter 3, the nature of incipiency mainly varies with the geological formation of each bedding surface (including subsequent diagenetic history) and thereby the mineral bonding strength across the bedding surface (grain bonding and secondary cementation). Partially developed fracturing leads to the presence of incipient joints (that may themselves be weathered or even locally re-cemented, for example by iron oxides) separated by residual bridges of intact rock (see Chapter 3, Figure 3.20 and Figure 3.24). Another class of incipient discontinuity is where they are infilled unevenly with minerals such as quartz and calcite along previously persistent sections of incipient joint (see Chapter 3, Figure 3.24).

For natural incipient discontinuities, stress distributions around tips of rock bridges (if present) are complex which in turn will affect their tensile strengths. A proportional linear relationship has been found between mode-I fracture toughness (a description of tensile stresses near fracture tips) and tensile strength of rock (see Chapter 2, Figure 2.16).

It is self-evident that natural discontinuities in later stages (more fully developed) will be comparatively sensitive to disturbance from external triggers (and may open up during ground investigation). For example, weak incipient joints tend to break in the process of blasting. Stronger incipient features may survive the blasting. From the data presented in Chapter 3, it is asserted that only those geological discontinuities that are in the later incipient states (very weak) should be assumed as fully persistent for rock engineering, as distinct from current practice of treating all discontinuities as having little tensile strength.

6.3 Scale effect of incipiency

The scale effect of properties of rock materials and discontinuities has been a subject of interest for many decades. Mechanical properties such as compressive or shear strength are normally obtained in the laboratory based on small-scale samples. Strength of large-scale rock masses is then estimated empirically using the factors derived from laboratory studies (e.g. Hoek & Brown, 1997) or on the basis of other reasoning (e.g. Hencher & Richards, 2015).

It is postulated that there may well be a scale effect for tensile strength of incipient discontinuities but no scale effect can be discerned for the limited number of samples tested in the laboratory during this study.

Tensile strength of block-scale incipient joints was investigated using the methodology described in Chapter 4. Lower tensile strengths were measured than for smaller samples and the possible reasons have been discussed in section 4.7 in Chapter 4. It is suspected that stress concentration around chemical splitter filled hole edges (see the analysis in Appendix A) led to the propagation of the fractures along the lines of incipient joints (proto-joints) and progressive failure (see Figures A 4.4 and A 4.5) and that this was related to specific geometry and test set up rather than any fundamental scale effect.

6.4 Scale effect of persistence

The alternative definitions for persistence of planar incipient rock discontinuities have been addressed in section 2.2 of Chapter 2. Areal extent of discontinuity defined by Eq. (2-2) is recommended for the quantification of persistence allowing for the three dimensional nature of real discontinuities. Discontinuity persistence should be treated relative to the problem size as discussed by Sainsbury et al. (2008). Areal extent (persistence) of incipient discontinuities calculated in this thesis, either at laboratory sample scale (Chapter 3) or at a larger block-scale in the field (Chapters 4 and 5), was treated relative to sample dimension.

A limiting aspect in defining a scale effect of persistence is that the persistence value calculated is a percentage (ranging from 0 to 100%) according to the definition by Eq. (2-2) (in Chapter 2). Figure 5.24 schematically shows three scales of incipient joint planes ordered from small-scale (laboratory scale), through medium-scale (block scale, such as samples tested in Chapter 5) to large-scale (project scale). Shaded areas delineate rock bridges. Values of persistence of these three incipient joint planes are the same (50%).

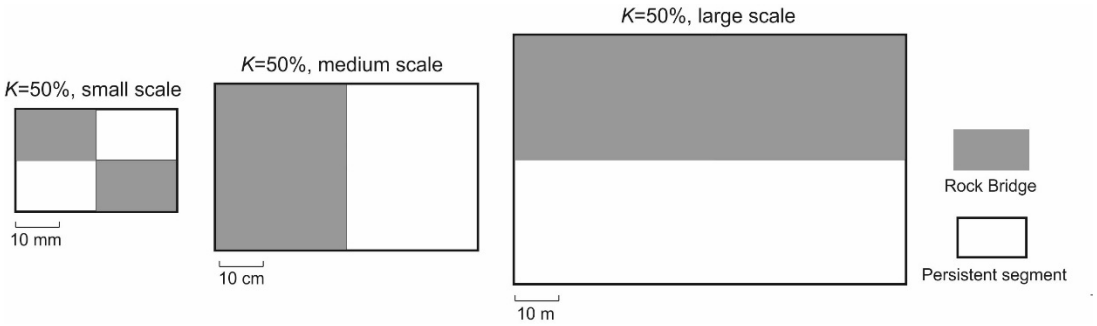

Figure 6.1 Three scales (laboratory small scale, block medium-scale and project large scale) of incipient joint planes with same persistence (50%). No scale effect of persistence (in terms of strength or conductivity) would be anticipated for these cases.

6.5 Practical strength of rock masses

As discussed in Chapter 2, current widely used rock mass classification schemes such as RMR (Bieniawski 1973, 1976), Q system (Barton et al. 1974) and GSI (Hoek et al. 1995) fail to consider the influence of persistence in the mass strength determination. This no doubt relates to the difficulty in determining persistence in any practical manner in geotechnical investigation. It is a matter of practical limitation. It is self-evident that a rock mass where the contained (and visible) fracture network is incipient will have completely different mass behaviour to one in which the discontinuities are either open or may be opened readily due to some stress change.

Studies regarding the implications of discontinuity persistence for rock mass strength have been reviewed in section 2.5 in Chapter 2. Previous work indicates that strengths of rock mass will be underestimated if persistence is underestimated or ignored in the rock mass strength assessment. Size and volume of rock blocks within rock masses are sensitive to discontinuity persistence. It is found that distributions of block size and volume are exponentially related to persistence (see Chapter 2, Figure 2.24). For some cases, shear strength of a non-persistent rock mass can be underestimated to approximately 75% of the real shear strength, while the underestimations of compressive strength and GSI index are both around 33% from real compressive strength and GSI index value, respectively (see Chapter 2, Figure 2.26).

As stated earlier in this section, a number of factors (rock bridges, infill and mineral bonding) may contribute to the strength of incipient discontinuities. Yet in many cases, rock bridges overshadow the efficacy of other factors, as much more energy and strength are expected to reserve within intact rock bridge.

For example, the cases tested on incipient joints in Chapter 2 in which rock bridges dominated the magnitude of tensile strength. Similarly this also can be seen in the field tests reported in Chapter 5, incipient joints terminated at rock matrix (see Chapter 5, Figures 5.11 and 5.14) which should be mobilized first prior to the rupture of incipient joints. The shearing test reported by Hencher (1984) revealed a rock bridge with a strength contribution of 750 kPa (see Chapter 2, Figure 2.20). It has been noted that the capacity of 1% rock bridge areas (equivalent to 100 cm^2 per $1m^2$) in a strong rock (for example fresh granite) can be equivalent to the capacity of at least a cablebolt. Rock bridges along incipient discontinuity plane will also enhance the efficacy of the interlocking effect (see chapter, Figure 5.9), especially under a high confining stress as in some underground excavations.

It can be concluded that a more realistic rock mass strength assessment can be achieved when strength contribution of rock bridges is considered in the classification schemes but this will require considerable effort to achieve. Potentially however, this approach towards the assessment of practical rock mass strength would be much better than the current practice (which often assume a 100% persistence - even though in practice most discontinuities are actually only incipient). To make this next step, the database on underground opening stability would need to be revisited, taking better account of actual geological conditions and discontinuity incipiency - no mean task, but with considerable imagined benefit. Two areas where the cost-effectiveness of such consideration might be realised is in nuclear waste studies and petroleum reservoir engineering.

6.6 Implement of incipiency/persistence in numerical simulations

Numerical simulations provide an innovative approach that can be used to further our understanding of rock engineering performance. In the current numerical modelling codes like FLAC, UDEC, RFPA, discontinuities (mainly joints) are often treated as fully persistent lacking any tensile strength. The incipiency or areal extent of modelled joints are often ignored with a tacit acknowledgement that it is a simplification of the actual situation. In fact, the incipient nature of many discontinuities within the rock mass will significantly affect mechanical behaviour of rock masses and stability of rock project. Any correlation between such modelling and field performance must be tempered with a realisation that the models are inherently flawed (and that correlations are strictly empirical rather than deterministic or scientific).

In the future it is anticipated that more realistic numerical codes, accounting for the incipiency of discontinuities should improve the development of numerical simulation study, and further our understanding of rock mass behaviours.

Chapter 7
Summary and conclusions

The chapter summarises the works presented in Chapters 3 to Chapter 5 and presents the main findings from this research. The implications of these findings and scope for future research are addressed at the end of this chapter.

7.1 Tensile strength of incipient discontinuities in cylindrical rock samples

A series of uniaxial tension tests were carried on incipient geological discontinuities in cylindrical samples at laboratory scale including incipient bedding (bedding laminations), mineral veins and incipient rock joints. Natural rock samples were cored perpendicular to incipient rock discontinuities in large rock block samples. Tensile strength of these incipient features was quantified. Main conclusions drawn from these tests are as follows:

- The direct tension test is useful to measure and research the UTS of visible and discrete incipient geological discontinuities. Incipient discontinuities can indeed have high tensile strength. In this series of experiments some discontinuities had tensile strength approaching that of the parent rock. For examples, the tensile strengths (see Table 3.2) of the incipient bedding in Midgley Grit Sandstone samples BH1-3, BH1-4 and BH2-2 (1.69 MPa, 1.82 MPa and 1.79 MPa) were of the order of 80% of that of the parent rock (2.08 MPa). Tensile strength of some incipient joints within Midgley Grit Sandstone samples were far weaker. Example tensile strengths are of samples BH1-1 (0.67 MPa), BH70J1 (0.63 MPa), BH70J2 (0.48 MPa) and BH70J6 (0.60 MPa) and that were about 30% that of parent rock (2.08 MPa).

- Tests on weathered but incipient rock joints (with rock bridges) showed a clear relationship between UTS and the area of rock bridges exposed after the tests. Mineralogy was investigated using an optical microscope (Figure 3.21). Quartz, feldspar and haematite were present on the exposed joint surfaces. The pre-existing open and mineral coated sections of the joints contributed little to the tensile strength.

- For tests on mineral veins within Horton Formation siltstone samples the UTS was considerably lower than that of the intact rock. Where rock

bridges were present as well as mineral infill, then the rock bridge strength dominated behaviour. XRD analysis was used to investigate mineral composition of veins (see Figure 3.25) and calcite was found to the major mineral infill for all samples, although a small amount of dolomite and quartz were also found.

- Midgley Grit Sandstone samples containing incipient bedding and joints and Horton Formation siltstone samples containing mineral veins always broke along these weaker planes under direct tension. These geological discontinuities tested all underwent brittle failure after direct tension at a low axial strain (within 0.5%).

- In relation to the elastic modulus vs. UTS. The tangent elastic modulus increases as weaker bedding planes are progressively removed, i.e. the higher tensile strength, the higher the tensile modulus. For mineral veins and incipient joints, the measured moduli were vary variable, ranging from 0.5 to 5 GPa.

7.2 Tensile strength of incipient discontinuities in large-scale rock blocks

An original approach has been employed to quantify tensile strength of large-scale incipient rock joints in rock blocks. In this method, an expansive compound was used to exert a tensile force normal to incipient joint planes.

Preliminary tests were firstly conducted on intact Thornhill Rock Sandstone and Midgley Grit Sandstone samples, lacking visible incipient joints, to establish the methodology. Tensile strength of large-scale and irregular incipient joints was then measured using the new approach. Conclusions drawn from the preliminary tension tests are as follows:

- The proposed method allowed measurement of the tensile strength of large-scale rock blocks as well as incipient rock joints, despite limitations as explained in Section 4.7 (Chapter 4).

- Tensile strength of intact rock as well as incipient joints measured using the expansive grout method were somewhat smaller than determined from either direct tensile tests or Brazilian methods. Some factors may contribute to this:

(1) Stresses arising from the chemical compound expansion were likely concentrated around edges of drillholes (Figures A 4.4 and A 4.5), and this focus for crack propagation contributed to the smaller tensile strengths measured. It is noted that similar stress concentration around joint tips within incipient joint plane in natural conditions may also contribute to relatively low tensile strength being developed for rock bridges than might be otherwise theoretically possible.

(2) Variations (even small) of the expansive tensile force (ETF) (normal to failure plane)arising from the chemical splitter between tests will influence the calculated tensile strengths which rely on the ETF developing at the same rate in tests on broken and unbroken blocks.

(3) The low pressurization rate of chemical splitter on rock samples is likely to lead to a relatively smaller tensile strength being mobilised in these tests as discussed in Section 4.7.4 (Chapter 4).

(4) It is speculated that diffusion of water from chemical grout splitter into rock matrix will, to a certain degree, degrade the strength of incipient rock joints or intact rock.

7.3 Factors contributing to tensile strength of incipient rock discontinuities

Based on the samples tested for this study, factors contributing to the tensile strength of incipient rock discontinuities have been investigated and characterised, which include:

(1) Partially developed discontinuities with localised residual rock bridges, which contribute significantly to tensile strength (for laboratory-scale, see Figure 3.24 and for block scale see Figure 5.21).

(2) Weathering variations of the open sections along the incipient discontinuity plane (see Figures 3.20, 4.21 and 4.23) result in variable strength contributions to the magnitude of overall tensile strength. A methodology has been proposed whereby strength contributions from different segments can be used to predict tensile strength of incipient discontinuities.

(3) Secondary cementation of opened (or partially opened) discontinuities by minerals as veins or partial cementation (see Figure 3.24), which provides tensile strength (real cohesion). Tensile strength will vary with vein structure including type of fill mineral, vein thickness, wall contact conditions and spatial variations. XRD results show that calcite was the major component of mineral in the veins within Horton Formation siltstone samples tests reported in Chapter 3.

7.4 Persistence (areal extent) of incipient discontinuities

Forensic Excavation of Incipient Rock Discontinuities (FEIRD) has been proposed and developed to investigate the areal extent of planar incipient rock discontinuities. Details for this technique have been described (see Section 5.3.2). Applications of FEIRD in the quantification of areal extent have been presented from laboratory and field studies. One finding is that estimation of persistence from trace length in exposures can lead to large errors and this might have major consequences for rock mass characterisation.

Natural incipient rock joints exposed in these studies were often approximately planar in shape. Flat and straight mode I fractures normally followed the pre-existing planar sections of incipient joint planes, while fresh fractures induced within rock bridges were more irregular in surface characteristics due to the complex stress distributions and lithological heterogeneity (see Figure 5.12c). Amplitude of surface roughness of the broken discontinuity surfaces within rock bridges was normally larger than that of the sections of pre-existing, persistent sections of incipient joint planes. Failure patterns of rock in the field are influenced by various factors including principal stress orientations, dimensions of rock as well as the heterogeneity of rock matrix at the time that the fracturing was induced (e.g. diagenetic, cooling, tectonic, unloading). For strong rocks, like the Horton Formation siltstone samples tested (UCS approaching 200 MPa), zigzag fracture shapes were often induced within the intact rock bridges under these strictly tensile and unconfined conditions. Investigation of the fractography features (such as rib and hackle marks) of such failed surface helps to understand the fracture initiation and propagation, especially for hard rock materials.

Spatial variability of geological formations and geological uncertainties is paralleled by the unpredictable areal extent of failed incipient joints (Figure 5.16), even in a small block sample (see Figure 5.9). This is one area where future studies might make considerable progress from a fuller study of the

linkage between rock bridge areal extent and geological history at a site including formation, tectonics, unloading and weathering.

A dye injection technique was attempted in the laboratory to colour persistent segments of an incipient joint within Midgley Grit Sandstone sample. It was found that this technique (preliminary) did not allow the persistent areas of incipient joint to be uniquely identified because, for a permeable rock such as that used in the experiment the dye penetrated the rock matrix at the adopted pressures. The methodology however has scope for improvement and potential as a useful tool. For the Midgley Grit Sandstone tested here, natural discolouration of failed surfaces provided a much better clue to quantify persistence, assuming that all persistent segments have been weathered.

7.5 Implications of findings

In rock mass and engineering projects, discontinuities are normally considered as weak features, lacking tensile strength, regardless of actual strength. For conservative purposes or safety in excavation, discontinuities are assumed as fully persistent (lacking any tensile strength) which is not true in real situations and sometimes may cause problems for rock engineering.

Based on the tests in Chapters 3 and 4 in this thesis, it is concluded that discontinuities encountered in rock engineering can be differentiated on the degree of incipiency and that this can best be done with reference to the tensile strength relative to that of parent rock. The approach proposed in Chapter 3 is advised to quantify tensile strength of incipient discontinuities, which would bridge the gap of current knowledge. Potential benefits of differentiating incipient discontinuities in rock engineering are as follows:

- More accurate estimation of overall rock mass strength. The relative strength of discontinuities to parent rock can be used to improve the current rock mass classification schemes such as RMR or the Q system which do not account for the variable tensile strength of incipient rock discontinuities (visible traces).

- Development of numerical codes that would achieve more realistic modelling of rock engineering projects that could then be related to performance on a more scientific basis.

- Better practical rock engineering design, for example in selection of equipment like cutters in TBM or diaphragm walling; more accurate

estimation of the progress of engineering project which can avoid contractual problems.

- Potential to reduce additional rock support, which would lower the budget.

The methodology established in Chapter 4 demonstrated lower tensile strengths than standard tensile methods. Stress concentrations at the edges of drillholes filled with expansive grout probably contributed to this. Even despite this perceived limitation, the proposed method is considered be a step towards the quantification of the tensile strength of large-scale incipient discontinuities, thereafter linking the incipiency (relative tensile strength to that of parent rock) and persistence in the field scale.

The study shows that the traditional approximation of persistence from the trace length from exposures is not reliable, even resulting in large errors. As can be seen from smaller block samples in the lab (Figure 4.19), even where joint traces are apparently persistent on exposed surfaces, true areal extent (persistence) is not as full as anticipated (see Figure 4.21 and 4.23). The non-persistent areas (red envelopes in Figure 4.21 and 4.23) contribute some tensile strength. Such studies and experiments further our understanding about the strength contributions arising from residual rock bridges.

The technique of FEIRD was established which can be used to investigate areal extent of incipient discontinuities either in the laboratory or in the field. Discolouration (if present) of persistent areas exposed following testing gives some indication of the areal extent of incipient discontinuity planes and this can help us to quantify persistence of discontinuity in the field with due regard to the geological factors at a site. FEIRD may also be useful for the investigation of geological uncertainty regarding the spatial variability of rock bridges and roughness of discontinuity surface. Rock bridge areas after breaking in tension were found to be much rougher than pre-existing areas of persistent joints (of those tested) and this observation may be useful for understanding the areal extent (persistence) of incipient joints in field studies and rock mass characterisation.

Rock masses preferentially break along planar incipient joint planes subjecting to external loads. Mixed modes of fractures (mode I and mode II) occur in the failure of rock bridges. This failure mode observed in the process of FEIRD testing in the field may further our understanding of the rupture of rock engineering at the field scale.

7.6 Recommendations for future research

This project has improved our understanding of the implications of persistence of geological discontinuities. It has also allowed identification of some research gaps for current knowledge. Differentiation of geological discontinuities (weakly incipient through to fully persistent and open) as a useful tool for rock engineering is highlighted as an important study area and a practical method to achieve this has been proposed in Chapters 3 and 4. A technique for the investigation of persistence has been established and discussed in Chapter 5. This method allows the observation of real persistence of planar incipient geological discontinuities.

Below are several topics that might be taken up for future research.

(i) The current definitions of persistence imply that discontinuities are planar in shape. Research and applications based on this assumption will unavoidably have some limitations as many discontinuities observed in the field are non-planar. Thus there is a need to define persistence for non-planar discontinuities, thereafter to achieve a more reliable application and to further our understanding of implications of persistence.

(ii) Tensile strength of incipient rock discontinuities has been investigated, but limited ranges of natural rock samples have been investigated. Scale effects regarding tensile strength can be investigated further if additional data were available.

(iii) Quantification of incipiency of discontinuities has been achieved, and differentiation of discontinuities according to incipiency/persistence is advised in rock engineering. The difficulty is then how to implement this notion into practical applications. Better representation of persistence within numerical modelling codes would allow a more realistic estimation of overall rock mass strength as well as further our understanding of rock mass behaviour, like stability and permeability.

(iv) Further study of the degree of persistence (enabled by the FIERD approach) should be linked to basic geological studies of those factors responsible for the condition (persistence and openness) of discontinuities. Factors include geological formation, later tectonics, unloading and weathering.

(v) The proposed FIERD method in this thesis to quantify persistence only applies to single incipient rock discontinuity. Discontinuities have to be broken first to achieve this goal. Non-invasive quantification of persistence might well be investigated by using geophysics, which if successful will greatly improve the advanced prediction of rock mass properties and to provide a fruitful opportunity for the future advance of rock mechanics.

Appendix A

Analytical solution of stress distributions in rock subjected to symmetrical concaved pressure

Assuming two symmetrical pre-drilled holes with same radius of r_i in elastic-plastic rock mediums. The internal pressure $p_{(t)}$ generated from expansive grout acts on the inside wall of holes. The problem could be treated as the interactions of two thick-walled cylinders internally pressurised. Figure A 4.1 presents the front view of symmetrical holes internally pressurized and stress acting on element arising from hole 2. The inner radius is r_i and outer radius r_0 equals to two hole distance d. This problem can be simplified to plane strain problem under the assumptions.

The pre-drilled hole 1 and surrounding rock material in Figure A 4.1 can be treated as a thick-walled cylinder ($2r_i$ / (d-r_i) ≤ 40) like a pipe under hydraulic pressure, in polar coordinates, the general stress equations of equilibrium without body force can be given as (Mendelson 1968 and Chakrabarty 1987)

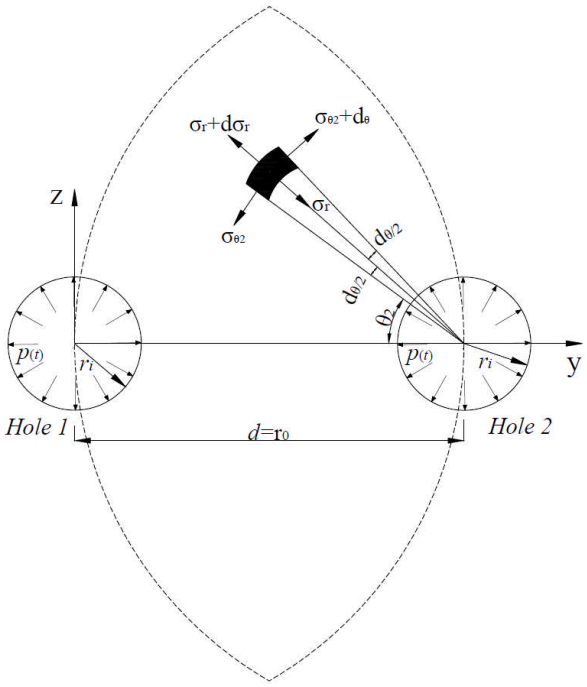

Figure A 4.1 Sketch of front view of symmetrical holes internally pressurized. Stresses acting on element solely arising from one hole is presented in polar coordinate. r is the radius and θ is the azimuth in polar coordinates

$$\begin{aligned}
&\frac{\partial \sigma_r}{\partial r}+\frac{1}{r}\frac{\partial \sigma_{r\theta}}{\partial \theta}+\frac{\partial \sigma_{rx}}{\partial z}+\frac{\sigma_r-\sigma_\theta}{r}=0\\
&\frac{\partial \tau_{\theta r}}{\partial r}+\frac{1}{r}\frac{\partial \sigma_\theta}{\partial \theta}+\frac{\partial \tau_{\theta x}}{\partial z}+2\frac{\tau_{\theta r}}{r}=0\\
&\frac{\partial \tau_{xr}}{\partial r}+\frac{1}{r}\frac{\partial \sigma_{x\theta}}{\partial \theta}+\frac{\partial \sigma_x}{\partial z}+\frac{\tau_{xr}}{r}=0
\end{aligned} \qquad \text{(A - 1)}$$

where r is the radius in polar coordinates and θ is the azimuth in polar coordinates. x-axis direction is along the line of hole spacing.

In the plane strain situation, the free expand of hole ends $\sigma_x = 0$, thus the general equations can be rewritten as

$$\begin{aligned}
&\frac{\partial \sigma_r}{\partial r}+\frac{1}{r}\frac{\partial \sigma_{r\theta}}{\partial \theta}+\frac{\sigma_r-\sigma_\theta}{r}=0\\
&\frac{\partial \tau_{\theta r}}{\partial r}+\frac{1}{r}\frac{\partial \sigma_\theta}{\partial \theta}+\frac{\partial \tau_{\theta z}}{\partial z}+2\frac{\tau_{\theta r}}{r}=0\\
&\frac{\partial \tau_{zr}}{\partial r}+\frac{\tau_{zr}}{r}=0
\end{aligned} \qquad \text{(A - 2)}$$

This problem is asymmetry about x-axis $\frac{\partial}{\partial \theta}=0$, and uniform radial deformation, Eq. (11) reduces to

$$\frac{\partial \sigma_r}{\partial r}+\frac{\sigma_r-\sigma_\theta}{r}=0 \qquad \text{(A - 3)}$$

A standard solution for equation (A - 3) is $\sigma_r = c\, r^n$ (*c* and *n* are constants), and the boundary conditions for a thick cylinder with internal pressure $p_{(t)}$ is:

at $r=r_i, \sigma_r=-p_{(t)}$ and at $r = r_0 = d$, $\sigma_r = 0$. Substituting this in equation (A - 3), we can obtain the radial and circumferential stresses:

$$\begin{aligned}
\sigma_r &= \frac{r_i^2 p_{(t)}(1-\frac{d^2}{r})}{d^2-r_i^2}\\
\sigma_\theta &= \frac{r_i^2 p_{(t)}(1+\frac{d^2}{r})}{d^2-r_i^2}
\end{aligned} \qquad \text{(A - 4)}$$

In order to obtain the stresses on element generated by two symmetrical internally pressurised holes, the stresses in polar coordinates need to be transformed into Cartesian coordinates. Assuming the y-axis direction along the spacing line of two holes, and z-axis direction normal to the line of spacing, as is shown in Figure A 4.1. The equations transforming from polar to Cartesian coordinates can be written as

$$\sigma_{yy} = \sigma_r \cos^2_\theta + \sigma_\theta \sin^2_\theta$$
$$\sigma_{zz} = \sigma_r \sin^2_\theta + \sigma_\theta \cos^2_\theta \qquad \text{(A - 5)}$$

where σ_{yy} is the principle stress along the spacing line of two pre-drilled holes in Cartesian coordinate system, σ_{zz} is the principle stress perpendicular to the spacing line. Note that if σ_{yy} and σ_{zz} work out to be positive, it is tensile and if it is negative, it is compressive.

Now from Eq. (A - 4) and (A - 5), we can find out the stress distribution in rocks subjected to two symmetrical concaved pressure $p_{(t)}$:

For the stress at any point perpendicular to hole spacing,

$$\begin{aligned}\sigma_{zz} &= \frac{r_i^2 p_{(t)}}{d^2 - r_i^2}\left(\sin^2_{\theta_1} - \frac{d^2}{r_1^2}\sin^2_{\theta_1} + \cos^2_{\theta_1} + \frac{d^2}{r_1^2}\cos^2_{\theta_1} + \sin^2_{\theta_2} - \frac{d^2}{r_2^2}\sin^2_{\theta_2} + \cos^2_{\theta_2} + \frac{d^2}{r_2^2}\cos^2_{\theta_2}\right) \\ &= \frac{r_i^2 p_{(t)}}{d^2 - r_i^2}\left[2 + \frac{d^2}{r_1^2}\left(\cos^2_{\theta_1} - \sin^2_{\theta_1}\right) + \frac{d^2}{r_2^2}\left(\cos^2_{\theta_2} - \sin^2_{\theta_2}\right)\right] \\ &= \frac{r_i^2 p_{(t)}}{d^2 - r_i^2}\left[2 + d^2\left(\frac{1 - 2\sin^2_{\theta_1}}{r_1^2} + \frac{1 - 2\sin^2_{\theta_2}}{r_2^2}\right]\right.\end{aligned} \qquad \text{(A - 6)}$$

where r_1 and r_2 are the distance from any point to centres of hole 1 and hole 2 respectively. θ_1 and θ_2 are illustrated in Figure A 4.2. From the geometrical relation, $r_1 \sin\theta_1 = r_2 \sin\theta_2$.

Two symmetrical holes with diameters of 20 mm ($r_i = 20mm$) are assumed be placed in a distance of 100mm from centre ($d = 100mm, d / r_i = 5$). Because of the symmetrical nature, stresses distributed around two holes are only investigated in three areas, i.e. area A ($0^\circ \le \theta_1 \le 12^\circ, 0^\circ \le \theta_2 \le 78^\circ$), area B ($15^\circ \le \theta_2 \le 60^\circ, 15^\circ \le \theta_1 \le 60^\circ$) and area C ($90^\circ \le \theta_2 \le 180^\circ$), respectively, as is shown in Figure A 4.2 and Figure A 4.3. Stresses distributed in the other areas can be symmetrically obtained.

At the time when internal pressure from expansive grout arrives at 50 MPa, the distribution of stress perpendicular to spacing line is shown in Figure A 4.4. Figure A 4.4 a indicates that stress in not equally distributed in the area when $0^\circ \le \theta_1 \le 12^\circ, 0^\circ \le \theta_2 \le 78^\circ$. Specially, tensile stresses distribute at the majority of this area except for a small part (when $\theta_1 = 12^\circ \, and \, 11.1^\circ$) where stresses are compressive. The maximum tensile stress (59.5 MPa) appears at the hole edges on the spacing line and decreases to 20.8 MPa in the middle. This phenomenon agrees well with the progressive failure of large-scale rock specimen under tension which has been observed in the previous laboratory

test. It also can be seen that the tensile stresses on the middle line in this area are the same (20.8 MPa), i.e., $\sigma_{zz} = \frac{10 r_i^2 p_{(t)}}{d^2 - r_i^2}$ ($\theta_1 = \theta_2 = 0, r_1 = r_2 = \frac{d}{2}$).

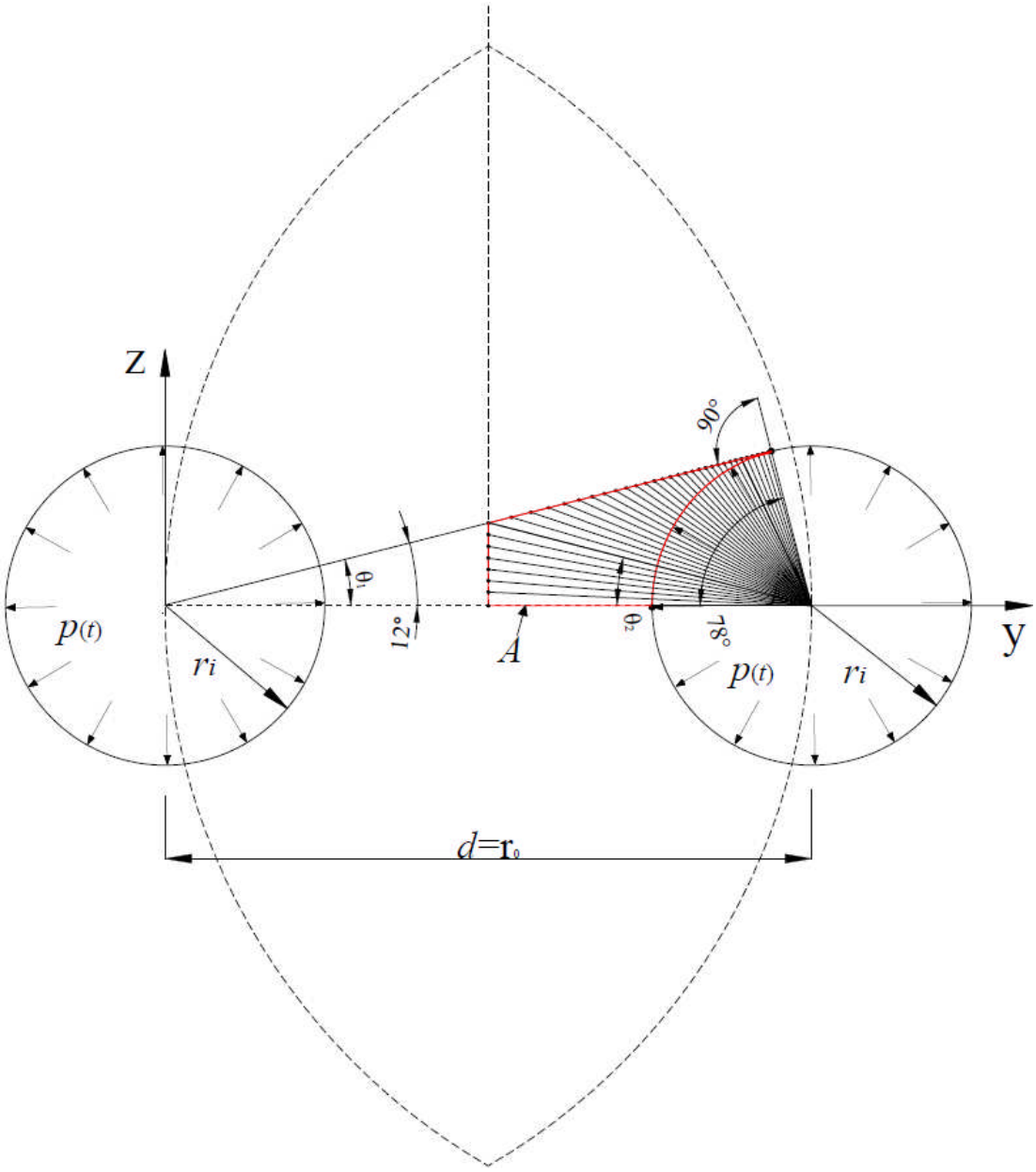

Figure A 4.2 Element within the red hatched area A when θ_2 decreases from 78° to 0° with an interval of 2°, while θ_1 correspondingly decreases from 12°, 11.1°, 9.6°, 8.9°, 8°, 7.2°, 6.1°, 5°, 3.8°, to 0° with varying intervals ($0^\circ \le \theta_1 \le 12^\circ, 0^\circ \le \theta_2 \le 78^\circ$,).

Stresses also are not equally distributed when $15^\circ \le \theta_2 \le 60^\circ, 15^\circ \le \theta_1 \le 90^\circ$, as is shown by the left part in Figure A 4.4b. Tensile stress along the middle line in this area decreases from 17.6 MPa when $\theta_1 = \theta_2 = 15^\circ$ to 2.1 MPa when $\theta_1 = \theta_2 = 60^\circ$.

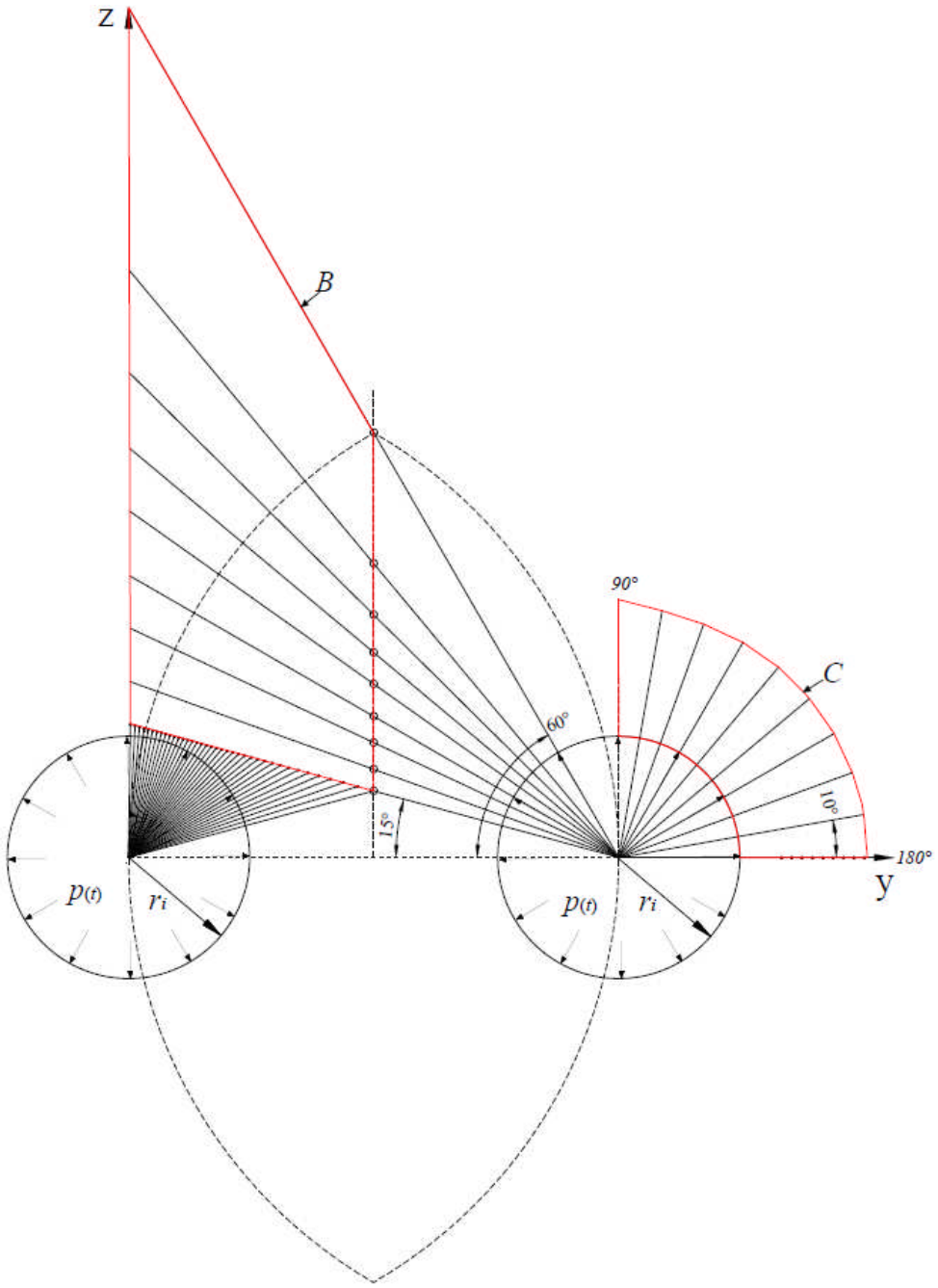

Figure A 4.3 Element within the red hatched area B when θ_2 increases from 15° to 60° with intervals from 5° to 10°, while θ_1 correspondingly increases from 15° to 90° with varying intervals ($15^\circ \le \theta_2 \le 60^\circ, 15^\circ \le \theta_1 \le 90^\circ$). Element within the red hatched area C when θ_2 increases from 90° to 180° with an interval of 10°, assuming stresses arising from hole 1 acting on element in this area can be neglected according to the Saint-Venant's Principle.

It also can be noticed that stresses far from the pressurised holes tend to be zero as can be anticipated. Stresses distributed in the edge of hole 2 (when

$90^{\circ} \le \theta_2 \le 180^{\circ}$) is presented in Figure A 4.4 c assuming stress generated from hole 1 acting on element in this area can be neglected according to Saint-Venant's Principle. Stresses in this area transfers from compression (when $90^{\circ} \le \theta_2 \le 130^{\circ}$) to tension(when $130^{\circ} \le \theta_2 \le 180^{\circ}$). In addition, it can be seen that stresses tend to be zero far from the centre of hole 2.

(a)

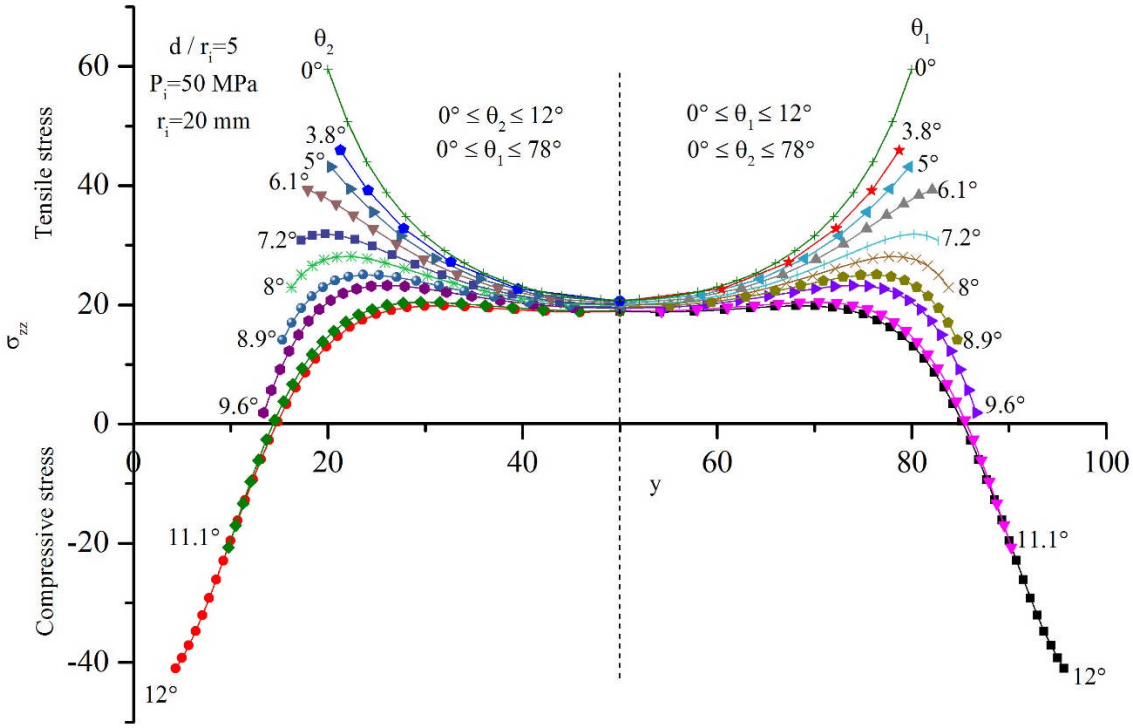

(b)

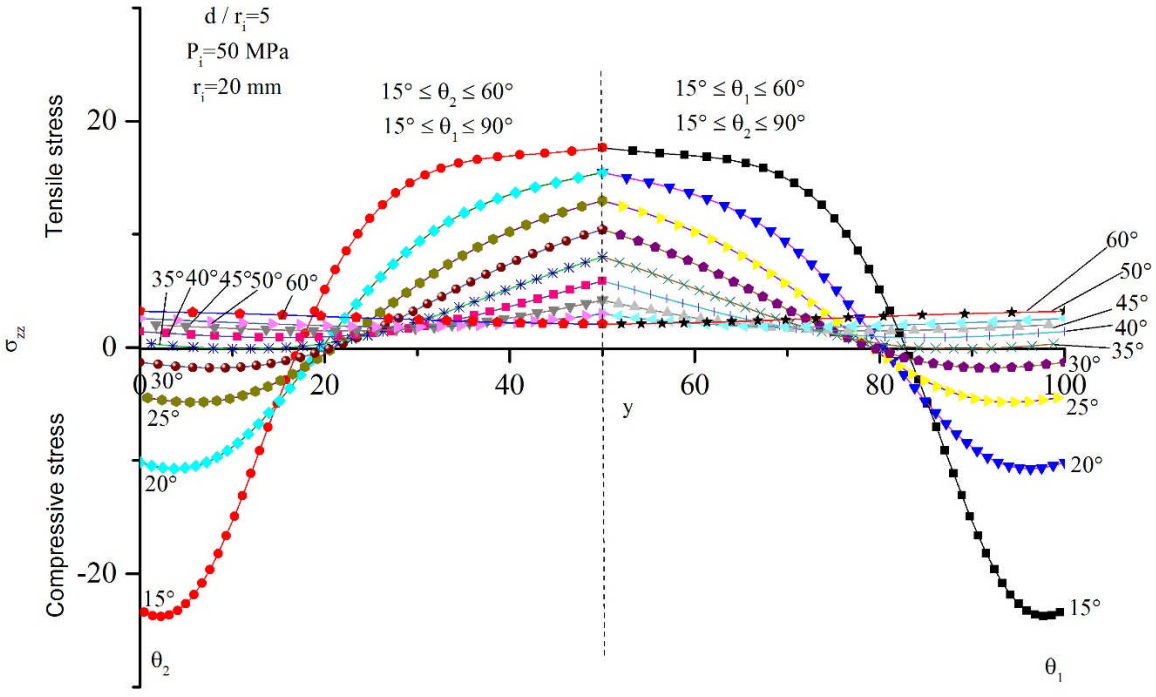

(c)

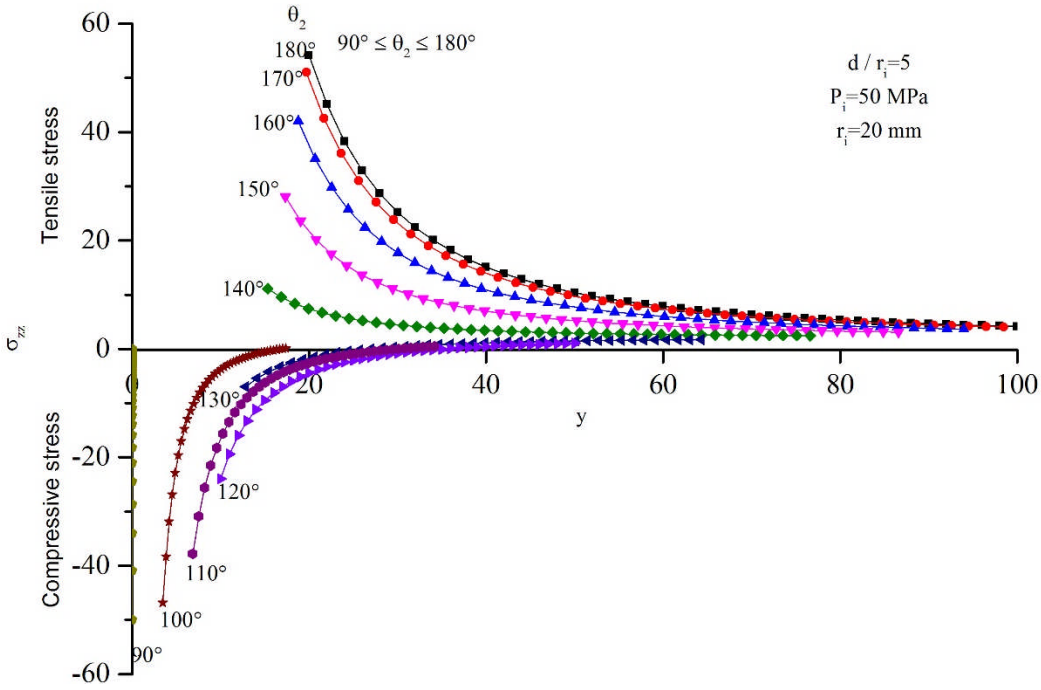

Figure A 4.4 Principle stress along Z-axis in Cartesian coordinate system. **a** Stress distributed in the middle part of two symmetrical holes when $0^\circ \le \theta_1 \le 12^\circ$,$0^\circ \le \theta_2 \le 78^\circ$ (the right part) and $0^\circ \le \theta_2 \le 12^\circ$,$0^\circ \le \theta_1 \le 78^\circ$ (the left part); **b** Stress distributed in the middle part of two symmetrical holes when $15^\circ \le \theta_1 \le 60^\circ$, $15^\circ \le \theta_2 \le 90^\circ$((the right part), $15^\circ \le \theta_2 \le 60^\circ$, $15^\circ \le \theta_1 \le 90^\circ$, (the left part); **c** Stress distributed in the edge of hole 2 where $90^\circ \le \theta_2 \le 180^\circ$. Assuming $p_{(t)}$=50 MPa, r_i=20 mm and d/r_i=5. Note that positive stress is tensile and negative stress is compressive.

Stress equation at any point along hole spacing line is

$$\begin{aligned}\sigma_{yy} &= \frac{r_i^2 p_{(t)}}{d^2 - r_i^2}\left(\cos^2_{\theta_1} - \frac{d^2}{r_1^2}\cos^2_{\theta_1} + \sin^2_{\theta_1} + \frac{d^2}{r_1^2}\sin^2_{\theta_1} + \cos^2_{\theta_2} - \frac{d^2}{r_2^2}\cos^2_{\theta_2} + \sin^2_{\theta_2} + \frac{d^2}{r_2^2}\sin^2_{\theta_2} \right) \\ &= \frac{r_i^2 p_{(t)}}{d^2 - r_i^2}\left[2 + \frac{d^2}{r_1^2}\left(\sin^2_{\theta_1} - \cos^2_{\theta_1} \right) + \frac{d^2}{r_2^2}\left(\sin^2_{\theta_2} - \cos^2_{\theta_2} \right) \right] \\ &= \frac{r_i^2 p_{(t)}}{d^2 - r_i^2}\left[2 + d^2\left(\frac{2\sin^2_{\theta_1} - 1}{r_1^2} + \frac{2\sin^2_{\theta_2} - 1}{r_2^2} \right)\right]\end{aligned} \qquad \text{(A - 7)}$$

Figure A 4.5 presents the distribution of principle stress along Y-axis in Cartesian coordinate system. Similarly to the stresses along Z-axis, the stress along the spacing line is not equally distributed. The compressive stress dominates in the area A and stresses acting on the element on the middle line in this area are the same (See Figure A 4.3a, the right part), i.e. $\frac{-6 r_i^2 p_{(t)}}{d^2 - r_i^2}$

when $\theta_1 = \theta_2, and\ r_1 = r_2 = \frac{d}{2}$. It also can be seen that the compressive stress concentration appears around the hole edge and the largest compressive stress is 49.5 MPa on the middle edge which is quite close to the assumed internal pressure 50 MPA.

(a)

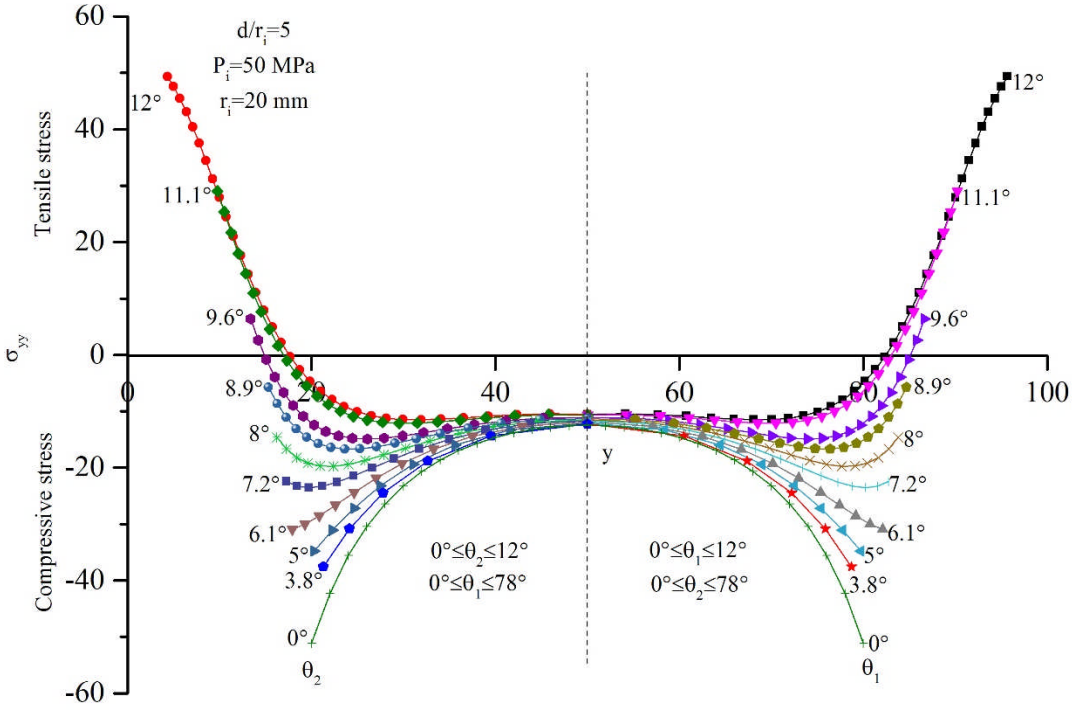

(b)

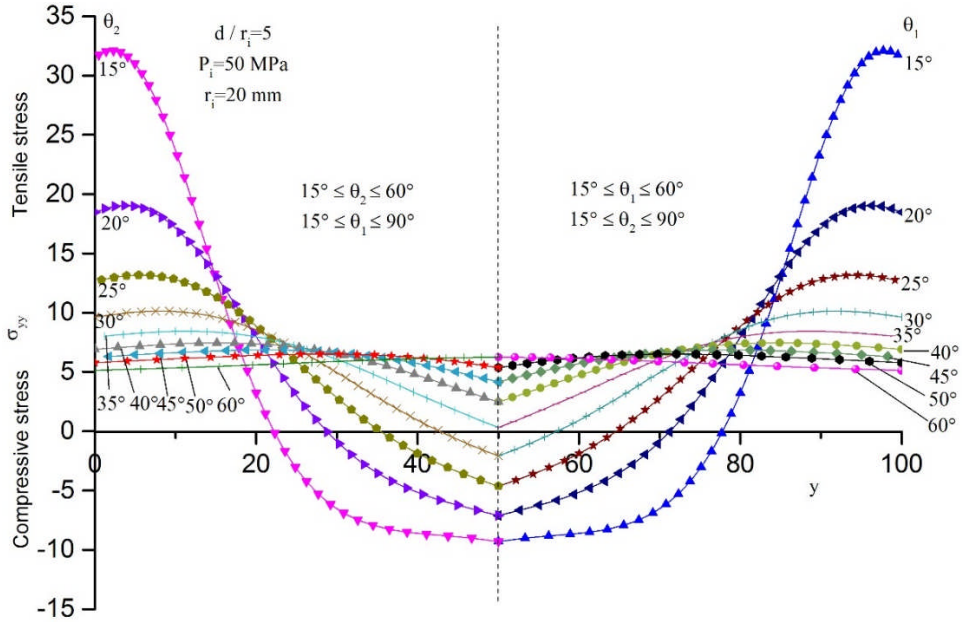

(c)

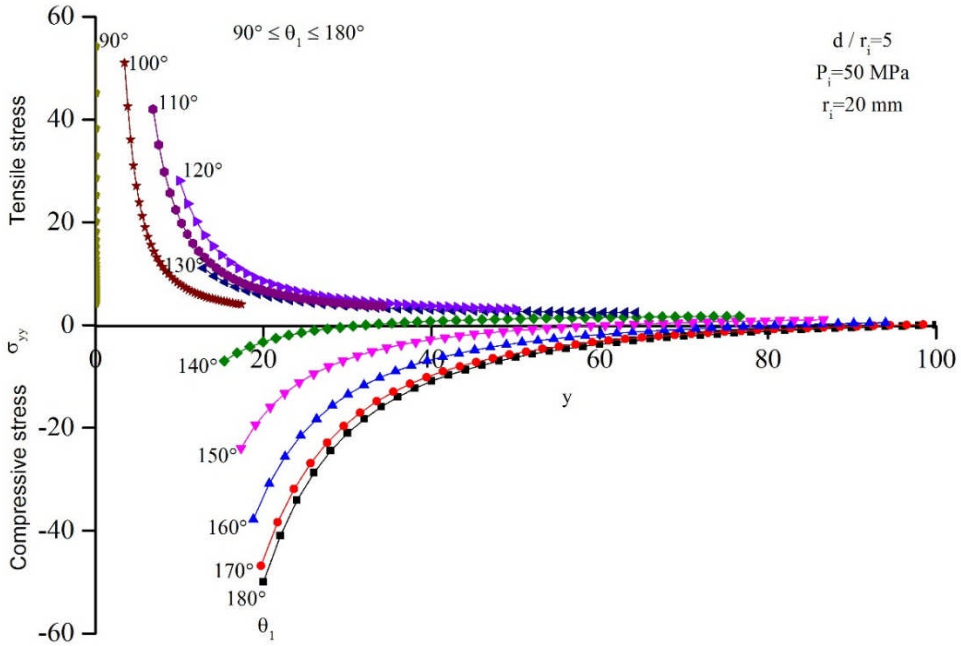

Figure A 4.5 Principle stress along Y-axis (spacing of two cylinders) in Cartesian coordinate system. **a** Stress distributed in the middle part of two symmetrical holes when $0^{\circ} \le \theta_1 \le 12^{\circ}, 0^{\circ} \le \theta_2 \le 78^{\circ}$ (the right part) and $0^{\circ} \le \theta_2 \le 12^{\circ}, 0^{\circ} \le \theta_1 \le 78^{\circ}$ (the left part); **b** Stress distributed in the middle part of two symmetrical holes when $15^{\circ} \le \theta_1 \le 60^{\circ}$, $15^{\circ} \le \theta_2 \le 90^{\circ}$ ((the right part), $15^{\circ} \le \theta_2 \le 60^{\circ}$, $15^{\circ} \le \theta_1 \le 90^{\circ}$, (the left part); **c** Stress distributed in the edge of hole 2 where $90^{\circ} \le \theta_2 \le 180^{\circ}$. Assuming $p_{(t)}$=50 MPa, r_i=20 mm and d/r_i=5. Note that positive stress is tensile where negative stress is compressive.

List of References

Aitkenhead, N., Barclay, W.J., Brandon, A., Chadwick, R.A., Chisholm, J.I., Cooper, A.H., and Johnson, E.W., 2002. The Pennines and adjacent areas (Fourth edition): British Geological Survey, p. 8-14.

Ameen, M.S., 1995. Fractography: fracture topography as a tool in fracture mechanics and stress analysis. An introduction: Geological Society Special Publication, no. 92, p. 1-10.

Amir Kazemi, A.D., Srinivas Murthy, N., and Govinda Raju, N., 1989. Stress intensity factor determination of radially cracked circular ring subjected to tension using photoelastic technique: Engineering Fracture Mechanics, v.32, no. 3, p. 403-408.

Antonio, B., and Yu, H., 2015. Stress field near the tip of a crack in a poroelastic transversely anisotropic saturated rock: Engineering Fracture Mechanics, v.141, p. 1-18.

Antonio, B., 2000. The initiation of secondary cracks in compression: Engineering Fracture Mechanics, v.66, p. 187-219.

Arthurton, R.S., Johnson. E.W., and Mundy, D.J.C., 1988. Geology of the contry around Settle: Memoir of the British Geological Survey, Sheet 60 (English and Wales).

Baecher, G.B., Lanney, N.A., and Einstein, H.H., 1977. Statistical description of rock properties and sampling: Proceeding of the 18th U.S. Symposium on Rock Mechanics, Colorado, p. 5C1.1 – 5C1.8.

Bahaaddini, M., Sharrock, G., and Hebblewhite, B.K., 2013. Numerical investigation of the effect of joint geometrical parameters on the

mechanical properties of a non-persistent jointed rock mass under uniaxial compression: Computers and Geotechnics, v.49, p. 206-225.

Bahaaddini, M., Hagan, P., Mitra, R., and Hebblewhite, B.K., 2016. Numerical study of the mechanical behaviour of nonpersistent jointed rock masses: International Journal of Geomechanics, v.16, no. 1, p. 1-10.

Barker, L.M., 1977. A simplified method for measuring plane strain fracture toughness: Engineering Fracture Mechanics, v.9, p. 361-369.

Barker, L.M., 1983. Compliance calibration of a family of short rod and short bar fracture toughness specimens: Engineering Fracture Mechanics, v.17, no. 4, p. 289-312.

Barla, B., and Innaurato, N., 1973. Indirect tensile testing of anisotropic rocks: Rock Mechanics and Rock Engineering, v. 5, p. 215-230.

Barnett, D.M., and Asaro, R.J., 1972. The fracture mechanics of slit-like cracks in anisotropic elastic media: Journal of the Mechanics and Physics of Solids, v. 20, no. 6, p. 353-366.

Barla, G, and Innaurato, N., 1973. Indirect tensile testing of anisotropic rocks: Rock Mechanics and Rock Engineering, v. 5, p. 215-230.

Barton, N., 1973. Review of a new shear-strength criterion for rock joints: Engineering Geology, v.7, p. 287-332.

Barton, N., 1975. Suggested methods for the description of rock masses, joints and discontinuities, ISRM Working Party.

Barton, N., 1976. The shear strength of rock and rock joints: International Journal of Rock Mechanics and Mining Sciences, v.13, p. 255-279.

Barton, N., 1990. Scale effects or sampling bias? : Proceeding of the International Workshop Scale Effects in Rock Masses, Balkema Publishers, Rotterdam, p. 31-55.

Barton, N., and Quadros, E., 2015. Anisotropy is everywhere, to see, to measure and to model: Rock Mechanics and Rock Engineering, v.48, p. 1323-1339.

Bearman, R.A., 1999. The use of the point load test for the rapid estimation of Mode I fracture toughness: International Journal of Rock Mechanics and Mining Sciences, v.36, p. 257-263.

Bharani, N., and Kaiser, P.K., 2013. Strength degradation of non-persistently jointed rock mass: International Journal of Rock Mechanics and Mining Sciences, v.62, p. 28-33.

Bieniawski, Z.T., 1989. Engineering Rock Mass Classifications. Wiley, New York.

Bogy, D.B., 1972. The plane solution for anisotropic elastic wedges under normal and shear traction: Journal of Applied Mechanics, v. 39, p. 1103-1109.

Bowie, O.L., and Freese, C.E., 1972. Central crack in plane orthotropic rectangular sheet: International Journal of Fracture Mechanics, v. 8, 49-58.

Brace, W.F., 1964. Brittle fracture of rocks: State of Stress in the Earth's Crust. Judd, W.R. (ed.), Elsevier, New York, p. 111-174.

Bradley, W.B., and Kobayashi, A.S., 1971. Fracture dynamics-a photoelastic investigation: Engineering Fracture Mechanics, v.3, p. 317-332.

Brideau, M.A., Sturzenegger, M., Stead, D., Jaboyedoff, M., Lawrence, M., Roberts, N., Ward, B., Millard, T., and Clague, J., 2012. Stability analysis of the 2007 Chehalis lake landslide based on long-range terrestrial photogrammetry and airborne LiDAR data: Landslides, v.9, p. 75-91.

Bridges, M.C., 1976. Presentation of fracture data for rock mechanics: Proceeding of 2nd Australian – New Zealand Conference on Geomechanics, p. 144-148.

Brzovic, A., and Villaescusa, E., 2007. Rock mass characterization and assessment of block-forming geological discontinuities during caving of primary copper ore at the EI Teniente mine, Chile: International Journal of Rock Mechanics and Mining Sciences, v. 44, p. 565-583.

Cai, M., Kaiser, P.K., Uno, H., Tasaka, Y., and Minami, M., 2004. Estimation of rock mass deformation modulus and strength of jointed hard rock masses using the GSI system: International Journal of Rock Mechanics and Mining Sciences, v.41, p. 3-19.

Carloni, C., Piva, A., and Viola, E., 2003. An alternative complex variable formation for an inclined crack in an orthotropic medium: Engineering Fracture Mechanics, v.70, p. 2033-2058.

Chakrabarty, J., 1987. Theory of Plasticity, McGraw-Hill, New York.

Chang, C., and Jo, Y., 2015. Heterogeneous in situ stress magnitudes due to the presence of weak natural discontinuities in granitic rocks: Tectonophysics, v. 664, p. 83-97.

Chen, C.S., Pan, E., and Amadei, B., 1998. Fracture mechanics analysis of cracked discs of anisotropic rock using the boundary element method: International Journal of Rock Mechanics and Mining Sciences, v.35, no. 2, p. 3-19.

Chen, C.S., and Hsu, S.C., 2001. Measurement of indirect tensile strength of anisotropic rocks by the ring test: Rock Mechanics and Rock Engineering, v. 34, no. 4, p. 293-321.

Chen, J.F., 1990. The development of the cracked-chevron-notched Brazilian disc methods for rock fracture toughness measurement: Proceedings of the 1990 SEM Spring Conference on Experimental Mechanics, Albuquerque, USA, P. 18-23.

Chen, Y.Z., 1993. New Fredholm integral equation for multiple crack problem in plane elasticity and antiplane elasticity: International Journal of Fracutre, v.64, p. 63-77.

Chen, Y.Z., 1995. A survey of new integral equations in plane elasticity crack problem: Engineering Fracture Mechanics, v.51, no. 1, p. 97-134.

Chong, K.P., and Kurupu, M.D., 1984. New specimen for fracture toughness determination for rock and other materials, v. 26, p. R59-R62.

Chong, K.P., and Kuruppu, M.D., 1987. Fracture roughness determination of layered materials, v.28, no. 1, p. 43-54.

Cidgem, K., and Levent, T., 2011. Investigation of proper specimen geometry for mode I fracture toughness testing with flattened Brazilian disc method, v.169, p. 61-75.

Collins, B.D., and Stock G.M., 2016. Rockfall triggering by cyclic thermal stressing of exfoliation fractures: Nature Geoscience, v. 9, p. 395-401.

Cravero, M., and Iabichino, G., 2004. Analysis of the flexural failure of an overhanging rock slab: International Journal of Rock Mechanics and Mining Sciences, v. 41, no. 3, p. 605-610.

Cruden, D.M., 1977. Describing the size of discontinuities: International Journal of Rock Mechanics and Mining Sciences, v. 144, p. 133-137.

Cundall, P.A., 1971. A computer model for simulating progressive large scale movements in blocky rock systems: Proceedings of the Symposium on International Society for Rock Mechanics, Nancy, France, v. 1, p. 1-8.

Dai, F., Wei, M.D., Xu, N.W., Zhao, T., and Xu, Y., 2015. Numerical investigation of the progressive fracture mechanisms of four ISRM-suggested specimens for determining the mode I fracture toughness of rocks: Computers and Geotechnics, v.69, p. 424-441.

Dan, D.Q., and Konietzky, H., Herbst, M., 2013. Brazilian tensile strength tests on some anisotropic rocks: International Journal of Rock Mechanics and Mining Sciences, v. 58, p. 1-7.

Deere, D.U., 1968. Geological considerations. In Rock Mechanics in Engineering Practice (eds., K.G.Stagg and O.C.Zienkiewicz), New York: Wiley.

Deparis, J., Johgmans, D., Garambois, S., Levy, C., Baillet, L., and Meric O., 2011. Geophysical detection and structural characterization of discontinuities in rock slopes: Rockfall Engineering, p. 1-38.

Dershowitz, W.S., and Einstein, H.H., 1988. Characterizing rock joint geometry with joint system models, v.21, p. 21-51.

Einstein, H.H., Veneziano, D., Baecher, G.B., and Oreilly, K.J., 1983. The effect of discontinuity persistence on rock slope stability: International Journal of Rock Mechanics and Mining Sciences, v. 20, no. 5, p. 227-236.

Elmouttie, M.K., Poropat, G.V., 2012. A method to estimate in situ block size distribution: Rock Mechanics and Rock Engineering, v. 45, p. 401-407.

Erarslan, N., and Williams, D.J., 2012. Experimental, numerical and analytical studies on tensile strength of rocks: International Journal of Rock Mechanics and Mining Sciences, v. 49, p. 21-30.

Feng, Q., Sjogren, P., Stephansson, O., and Jing, L., 2001. Measuring fracture orientation at exposed rock faces by using a non-reflector total station, v.59, p. 133-146.

Fischer, M.P., Elsworth, D., Alley, R.B., and Engelder, T., 1996. Finite element analysis of the modified ring test for determining mode I fracture toughness, v.33, no. 1, p. 1-15.

Fowell, R.J., and Xu, C., 1993. The cracked chevron notched Brazilian disc test-geometrical considerations for practical rock fracture toughness measurement: International Journal of Rock Mechanics and Mining Sciences, v.30, no. 7, p. 821-524.

Fowell, R.J., and Xu, C., 1994. The use of the cracked Brazilian disc geometry for rock fracture investigations: International Journal of Rock Mechanics and Mining Sciences, v.31, no. 6, p. 571-579.

Gehle, C., and Kutter, H.K., 2003. Breakage and shear behaviour of intermittent rock joints: International Journal of Rock Mechanics and Mining Sciences, v.30, no.40, p. 687-700.

Ghazvinian, A., Nikudel, M.R., and Sarfarazi, V., 2007. Effect of rock bridge continuity and area on shear behaviour of joints: 11th Congress of the International Society for Rock Mechanics, p. 247-250.

Ghazvinian, A., Sarfarzai, V., and Schubert, W., 2012. A study of the failure mechanism of planar non-persistenct open joints using PFC2D: Rock Mechanics and Rock Engineering, v.45, p. 677-693.

Ghazvinian, A., Nikudel, M.R., and Sarfarazi. V., 2007. Effect of rock bridge continuity and area on shear behaviour of joints: In: 11th congress of the international society for rock mechanics, Lisbon, Portugal.

Gholamreza, K., Rafiei, B., and Abdilor, Y., 2015. An experimental investigation of the Brazilian tensile strength and failure patterns of laminated sandstones: Rock Mechanics and Rock Engineering, v. 48, p. 843-852.

Goodman, R.E., 1993. Engineering Geology: Rock in Engineering Construction. Wiley, New York, p. 385.

Goodman, R.E., and Shi, G., 1985. Block theory and its application to rock engineering, Prentice-Hall, New Jersey.

Grandjean, G., and Gourry, J.C., 1996. GPR data processing for 3D fracture mapping in a marble quarry: Journal of Applied Geophysics, v. 36, p.19-30.

Griffith, A.A., 1920. The phenomena of rupture and flow in solids: Philosophical transactions of the royal society of London, p.163-198.

Gutierrez, M., and Youn, D.J., 2015. Effects of fracture distribution and length scale on the equivalent continuum elastic compliance of fractured rock masses: Journal of Rock Mechanics and Geotechnical Engineering, v.7, p. 626-637.

Halakatevakis, N., and Sofianos, A.I., 2010. Strength of a blocky rock mass based on an extended plane of weakness theory: International Journal of Rock Mechanics and Mining Sciences, v. 47, p.568-582.

Hashiba, K., and Fukui, K., 2014. Effect of water on the deformation and failure of rock in uniaxial tension: Rock Mechanics Rock Engineering , v.47, p. 1-11.

Hawkes. I., Mellor. M., and Gariepy, S., 1973. Deformation of rocks under uniaxial tension: International Journal of Rock Mechanics and Mining Sciences, v. 10, p. 493-507.

He, Z., Kotbousov, A., Fanviulli, A., and Berlo, F., 2015. An experimental method for evaluating mode II stress intensity factor near crack tip field: International Journal of Fracture, v. 197, no. 1, p. 119-126.

Hencher, S.R., 2004. Weathering and erosion processes in rock – implications for geotechnical engineering: Proceedings symposium on Hong Kong soils and rocks, London, United Kingdom.

Hencher, S.R., 2012. Practical Engineering Geology, Spon Press, Oxon, 438p.

Hencher, S.R., 2014. Characterizing discontinuities in naturally fractured outcrop analogues and rock core: the need to consider fracture development over geological time: The Geological Society of London, Special Publications, advances in the study of fractured reservoirs, v. 374, p.113-123.

Hencher, S.R., 2015a. Characterizing discontinuities in naturally fractured outcrop analogues and rock core: the need to consider fracture development over geological time: Geological Society of London, Special Publications, advances in the study of fractures reservoirs, v. 374, p. 113-123.

Hencher, S.R., and Knipe, R., 2007. Development of rock joints with time and consequences for engineering: Proceeding of the 11th congress of the international society of rock mechanics, Lisbon, Portugal.

Hencher, S.R., and Richards, L.R., 2014. Assessing the shear strength of rock discontinuities at laboratory and field scales: Rock Mechanics and Rock Mechanics, v.48, p. 883-905.

Hencher, S.R., 2015. Practical rock mechanics. Taylor and Francis Group, London, p. 356.

Hobbs, D.W., 1965. An assessment of a technique for determining the tensile strength of rock: British Journal of Applied Physics, v. 16, p. 259-268.

Hoek, E., 1964. Fracture of anisotropic rock: Journal of the South African Institute of Mining and Metallurgy, v. 64, p. 501-518.

Hoek, E., 2007. Practical Rock Engineering. PHD file, 2007edition, Hoek's Corner website.

Hoek, E., and Brown, E.T., 1997. Practical estimates of rock mass strength: International Journal of Rock Mechanics and Mining Sciences, v. 34, no. 8, p. 1165-1186.

Hoek, E., and Martin, C.D., 2014. Fracture initiation and propagation in intact rock-A review, v.6, p. 287-300.

Hoening, A., 1982. Near tip behaviour of a crack in plane anisotropic elastic body: Engineering Fracture Mechanics, v. 16, p. 393-403.

Huang, J., Chen G., Zhao, Y., and Wang R., 1990. An experimental study of the strain field development prior to failure of a marble plate under compression: Tectonophysics, v. 175, no. 1-3, p. 269-284.

Hudson, J.A., and Priest, S.D., 1979. Discontinuities and rock mass geometry: International Journal of Rock Mechanics and Mining Sciences, v. 16, p. 339-362.

Ingraffea, A.R., and Heuze, F.E., 1980. Finite element models for rock fracture mechanics: International Journal for Numerical and Analytical Methods in Geomechanics, v. 4, no. 1, p. 25-43.

Iqbal, M.J., and Mohanty, B., 2006. Experimental calibration of stress intensity factors of the ISRM suggested cracked-notched Brazilian disc specimen used for determination of mode-I fracture toughness:

International Journal of Rock Mechanics and Mining Sciences, v. 43, p. 1270-1276.

Irwin, G., 1957. Analysis of stresses and strains near the end of a crack traversing a plate: Journal of Applied Mechanics, v. 24, p. 361-364.

ISRM, 1978a. Suggested methods for the quantitative description of discontinuities in rock masses: International Journal of Rock Mechanics and Mining Sciences, v.15, p. 319-368.

ISRM, 1978b. Suggested methods for determining tensile strength of rock materials: International Journal of Rock Mechanics and Mining Sciences, v.15, p. 99-103.

Jennings, J.E., 1970. A mathematical theory for the calculation of the stability of slopes in open cast mines: Planning Open Pit Mines, Proceedings of the Symposium on the Theoretical Background to the Planning of Open Pit Mines with Special Reference to Slope Stability, Johannesburg, p. 87-102.

Jiang, M.J., Jiang, T., Crosta, G.B., Shi, Z.M., Chen, H., and Zhang, N., 2015. Modelling failure of jointed rock slope with two main joint sets using a novel DEM bond contact model: Engineering Geology, v. 193, p. 79-96.

Jimenze-Rodriguez, R., and Sitar, N., 2006. Inference of discontinuity trace length distributions using statistical graphical models: International Journal of Rock Mechanics and Mining Sciences, v. 43, p. 877-893.

Johansson, F., 2016. Influence of scale and matedness on the peak shear strength of fresh unweathered rock joints, v. 82, p. 36-47.

Ke, C.C., Chen, C.S., and Tu, C.H., 2008. Determination of fracture toughness of anisotropic rocks by boundary element method, v. 41, no. 4, p. 509-538.

Kevin, J.O., 1980. The effect of joint plane persistence on rock slope reliability: Massachusetts Institute of Technology, Unpublished PhD thesis.

Khan, A.S., and Irani, F.K., 1987. An experimental study of stress wave transmission at a metallic-rock interface and dynamic tensile failure of sandstone, limestone and granite: Mechanics of Materials, v.6, p. 285-292.

Kim, B.H., Cai, M., and Kaiser, P.K., 2007a. Rock mass strength with non-persistent joints: 1st Canada – U.S. Rock Mechanics Symposium, Vancouver, Canada.

Kim, B.H., Cai, M., Kaiser, P.K., and Yang, H.S., 2007b. Estimation of block sizes for rock masses with non-persistent joints: Rock Mechanics and Rock Engineering, vo. 40, no. 2, p. 169-192.

Kim, B.H., Kaiser, P.K., and Grasselli, G., 2007c. Influence of persistence on behaviour of fractured rock masses, The Geological Society of London, Special Publications, rock physics and geomechanics in the study of reservoirs and repositories, v. 284, p.161-173.

King, W.B.R., 1934. The Lower Palaeozoic rocks of Austwick and Horton-in-Ribblesdale, Yorkshire: Quarterly Journal of Engineering Geology and Hydrogeology, p. 7-31.

Kittitep, F., and Numchok, K., 2010. Influence of loading rate on deformability and compressive strength of three Thai sandstones: Geotechnical and Geology Engineering, v. 28, p. 707-715.

Kulatilake, P.H.S.W., and Wu, T.H., 1984. Estimation of mean trace length of discontinuities: Rock Mechanics and Rock Engineering, v. 17, p. 215-232.

Kumar, A., 2008. The effect of stress rate and temperature on the strength of basalt and granite: Geophysics, v. 33, no. 3, p. 501-510.

Kuo, M.G., and Bogy, D.B., 1974. Plane solutions for the displacements and traction-displacement problem for anisotropic elastic wedges: Journal of Applied Mechanics, v. 41, p. 197-203.

Kuruppu, M.D., Obara, Y., Ayatollahi, M.R., Chong, K.P., and Funstsu, T., 2014. ISRM-suggested method for determining the mode I static fracture toughness using semi-circular bend specimen: Rock Mechanics and Rock Engineering, v. 47, p. 267-274.

Kwansniewski, M., 2009. Testing and modelling of the anisotropy of tensile strength of rocks: Proceeding of the international conference on rock joints and jointed rock masses Arizona, United State.

Lajtai, E.Z., 1969a. Shear strength of weakness planes in rock: International Journal of Rock Mechanics and Mining Sciences, v. 6, p. 499-515.

Lajtai, E.Z., 1969b. Strength of discontinuous rocks in direct shear: Geotechnique, v. 19, no. 2, p. 218-233.

Latham, J.P., Meulen, J.V., and Dupray, S., 2006. Prediction of in-situ block size distributions with reference to armourstone for breakwaters: Engineering Geology, v. 86, p. 19-36.

Levent, T., and Keles, C., 2012. Effects of geometric factors on mode I fracture toughness for modified ring tests: International Journal of Rock Mechanics and Mining Sciences, v. 51, p. 149-161.

Li, D., and Wong, L.N.Y., 2013. The Brazilian disc test for rock mechanics applications: review and new insights: Rock Mechanics and Rock Engineering, v. 46, no. 2, p. 269-287.

Liao, J.J., Yang, M. T., and Hsieh, H.Y., 1997. Direct tensile behaviour of transversely isotropic rock: International Journal of Rock Mechanics and Mining Sciences, v. 34, no. 5, p. 837-849

Li, H.B., Li, J.C., Bo, L., Li, J.R., Li, S.Q., and Xia, X., 2013. Direct tension test for rock material under different strain rates at quasi-static loads: Rock Mechanics and Rock Engineering, v.46, p. 1247-1254.

Li, X., Zuo, Y., Zhuang, X., and Zhu, H., 2014. Estimation of fracture trace length distributions using probability weighted moments and L-moments: Engineering Geology, v. 168, p. 69-85.

Liao, J.J., Yang, M.T., and Hsieh, H.Y., 1997. Direct tensile behaviour of a transversely isotropic rock: International Journal of Rock Mechanics and Mining Sciences, v.34, no.5, p. 837-849.

Lim, I.L., Johnston, I.W., Choi, S.K., and Boland, J.N., 1994. Fracture testing of a soft rock with semi-circular specimens under three-point bending. Part 1-mode I: International Journal of Rock Mechanics and Mining Sciences, v. 31, no. 3, p. 185-197.

Liu, H.W., 1983. On the fundamental basis of fracture mechanics: Engineering Fracture Mechanics, v. 17. No. 5, p. 425-438.

Liu, J.F., Chen, L., Wang, C., Man, K., Wang, L., Wang, J., and Su, R., 2014. Characterizing the mechanical tensile behaviour of Beishan granite with different experimental methods: International Journal of Rock Mechanics and Mining Sciences, v.69, p.50-58.

Longoni, L., Arosio, D., Scaioni, M., Papini, M., Zanzi, L., Roncella, R., and Brambilla, D., 2012. Surface and subsurface non-invasive investigations to improve the characterization of a fractured rock mass: Journal of Geophysics and Engineering, v. 9, p. 461-472.

Lu, P., and Latham, J.P., 1999. Developments in the assessment of in-situ block size distributions of rock masses: Rock Mechanics and Rock Engineering, v. 32, no. 1, p. 29-49.

Luong, M.P., 1988. Direct tensile and direct shear strengths of Fontainebleau sandstone: Key Questions in Rock Mechanics, Balkema, Rotterdam.

Lyman, G.J., 2003. Rock fracture mean trace length estimation and confidence interval calculation using maximum likelihood methods: International Journal of Rock Mechanics and Mining Sciences, v. 40, p. 825-832.

Maerz, H.H., 1996. Image sampling techniques and requirements for automated image analysis of rock fragmentation: Proceedings of the FRAGBLAST 5 Workshop on Measurement of Blast Fragmentation, Montreal, Quebec, Canada, Aug. p. 115-120.

Manouchehr, S., Lohrasb, F., Ahmad, F., Sareh, G., Abolfazl, M., and Ashar, R., 2015. Shear strength of discontinuities in sedimentary rock masses based on direct shear tests: International Journal of Rock Mechanics and Mining Sciences, v. 75, p. 119-131.

Mattew, J.L., and Malte, V., 2012. Automated mapping of rock discontinuities in 3D lidar and photogrammetry models: International Journal of Rock Mechanics and Mining Sciences, v. 54, p. 150-158.

Mauldon, M., 1994. Intersection Probabilities of impersistent joints: International Journal of Rock Mechanics and Mining Sciences, v. 31, no. 2, p. 107-115.

Mauldon, M., 1998. Estimating mean fracture trace length and density from observations in convex windows: Rock Mechanics and Rock Engineering, v. 31, no. 4, p. 201-216.

Mauldon, M., Dunne, W.M., Rohrbaugh Jr, M.B., 2001. Circular scanlines and circular windows: new tools for characterizing the geometry of fracture traces: Journal of Structural Geology, v. 23, p. 247-258.

McClintock, F.A., and Walsh, J.B., 1962. Friction on Griffith cracks in rock under pressure: Proceedings of the 4th U.S. National Congress on Applied Mechanics, New York, v. 2, p. 15-21.

Mendelson, A., 1968. Plasticity: theory and application, The Macmillan Company, New York.

Mier, J.G.M., and Shi, C., 2002. Stability issues in uniaxial tensile tests on brittle disordered materials: International Journal of Solids and Structures, v. 39, p. 3359-3372.

Moleuar, A.A.A, Scarpas, A. Liu, X., and Erkerns S.M.J.G., 2002. Semi-circular bending test: simple but useful: Journal of the Association of Asphalt Paving Technologists, v. 71, 794-815.

Mughieda, O., 1997. Failure mechanisms and strength of non-persistent rock joints: Unpublished PhD thesis, University of Illinois.

Munz, D., Bubsey, R.T., and Srawley, J.E., 1980. Compliance and stress intensity coefficients for short bar specimens with chevron notches: International Journal of Fracture, v. 14, no, 4, p. 359-374.

Murakami, Y., 1976. A simple procedure for the accurate determination of stress intensity factors by finite element method: Engineering Fracture Mechanics, v. 8, p. 643-655.

Murrell, S.A.F., 1958. The strength of coal under tri-axial compression: Walton WH, editor. Mechanical properties of non-metallic brittle materials. London, p. 123-145.

Muskhelishvili, N.I., 1977. Some basic problems of the mathematical theory of elasticity, Spring Science, p. 681.

Nejati, M., Paluszny, A., and Zimmerman, R.W., 2015. A disk-shaped domain integral method for the computation of stress intensity factors using tetrahedral meshes: International Journal of Solids and Structures, v. 69-70, p. 230-251.

Obara, Y., Sasaki, K., and Yoshinaga, T., 2007. Estimation of fracture roughness of rocks under vapour pressure by semi-circular bend (SCB) test: Journal of the Mining and Materials Processing Institute of Japan, v. 123, p. 145-151.

Okubo, S., and Fukui, K., 1996. Complete stress-strain curves for various rock types in uniaxial tension. International Journal of Rock Mechanics and Mining Sciences, v.33, no,6, p. 549-556.

Ord, A., Cheung, L.C., Hobbs, B.E., and Blanc, D.L., 1991. Automatic mapping of rock exposures for geotechnical purposes: The 2nd Australian Conference on Computer Applications in the Mineral Industry, The University of Wollongong, N.S.W., July.

Ouchterlony, F., 1988. Suggested methods for determining the fracture toughness of rock: International Journal of Rock Mechanics and Mining Sciences, v.25, no. 2, p. 76-96.

Pahl, P.J., 1981. Estimating the mean length of discontinuity traces: International Journal of Rock Mechanics and Mining Sciences, v. 18, no. 3 p. 221-228.

Palleske, C., Diederichs, M.S., Hutchinson, D.J., and Elimo, D., 2014. Block size distributions as a rock mass classification tool: 48th U.S. Rock Mechanics/Geomechanics Symposium, Minneapolis, Minnesota.

Palmstrom, A., 2005. Measurements and correlations between block size and rock quality designation (RQD): International Journal of Rock Mechanics and Mining Sciences, v. 20, p. 362-377.

Panek, L.A., 1981. Design and operation of caving and sublevel stoping mines. Society for Mining Metallurgy, p. 843.

Pariseau, W.G., Puri, S., and Schmelter, S.C., 2008. A new model for effects of impersistent joint sets on rock slope stability: International Journal of Rock Mechanics and Mining Sciences, v. 45, p. 122-131.

Park, H.J., 2005. A new approach for persistence in probabilistic rock slope stability analysis, v. 9, no. 3, p. 287-293.

Park, H.J., and West, T.R., 2002. Sampling bias of discontinuity orientation caused by linear sampling technique: Engineering Geology, v. 66, p. 99-110.

Paronuzzi, P., and Serafini, W., 2009. Stress state analysis of a collapsed overhanging rock slab: A case study: Engineering Geology, v. 108, p. 65-75.

Patton, F.D., 1966. Multiple modes of shear failure in rock: Proceedings of the First International Congress on Rock Mechanics, Lisbon, p. 509-513.

Pell, P.J.N., 1993. Uniaxial strength testing. In: Comprehensive rock engineering, v. 3, Pergamon Press, p.67-85.

Pell, P.J.N., Bienawski, Z.T., Hencher, S.R., and Pells, S., 2015. RQD: time to rest in peace: Géotechnique (in press).

Pollard, D.D., and Aydin, A., 1998. Progress in understanding jointing over the past century: Geological Society of America Bulletin, v. 100, p. 1181-1204.

Potyondy, D.O., and Cundall, P.A., 2004. A bonded-particle model for rock: International Journal of Rock Mechanics and Mining Sciences, v. 41, p. 1329-1364.

Priest, S.D., and Hudson, J.A., 1981. Estimation of discontinuity spacing and trace length using scanline surveys: International Journal of Rock Mechanics and Mining Sciences, v. 18, p. 183-197.

Prudencio, M., and Van Sint Jan, M., 2007. Strength and failure modes of rock mass models with non-persistent joints: International Journal of Rock Mechanics and Mining Sciences, v. 44, p. 890-902.

Rao, Q., Sun, Z., Stephansson, O., Li, C. and Stillborg, B., 2003. Shear fracture (Mode II) of brittle rock: International Journal of Rock Mechanics and Mining Sciences, v. 40, p. 355-375.

Rathod, H.T., 1979. A study of asymmetrically loaded Griffith crack in plane anisotropic elastic body: Engineering Fracture Mechanics, v. 11, p. 87-93.

Roberts, G., 2000. Highwall joint mapping in 3-D at the Moura mine using SIROJOINT: Bowen Basin Symposium, Coal and Mining the New Millennium, Rockhampton.

Robertson, A.M., 1970. The interpretation of geological factors for use in slope theory: Planning Open Pit Mines. Van Rensburg, P.W.J. (Ed.). Cape Town, South Africa: Balkema.

Rogers, S.F., Kennard, D.K., Dershowitz, W.S., and Van As, A., Characterising the in situ fragmentation of a fractured rock mass using a discrete fracture network approach: 1st Canada – US. Rock Mechanics Symposium.

Rosser, N.J., Petley, D.N., Lim, M., Dunning, S.A., and Allison, R.J., 2005. Terrestrial laser scanning for monitoring the process of hard rock coastal cliff erosion: Quarterly Journal of Engineering Geology and Hydrogeology, v. 38, no. 4, p. 363-375.

Sabri, M., Ghazvinian, A., and Nejati, H.R., 2016. Effect of particle size heterogeneity on fracture toughness and failure mechanism of rocks: International Journal of Rock Mechanics and Mining Sciences, v. 81, p. 79-85.

Saiang, D., Malmgren, L., and Nodlund, E., 2005. Laboratory tests on shotcrete-rock joints in direct shear, tension and compression: Rock Mechanics and Rock Engineering, v.38, no,4, p. 275-297.

Sainsbury, B., Pierce, M., and Mas Ivars, D., 2008. Simulation of rock mass strength anisotropy and scale effects using a ubiquitous joint rock mass method: Continuum and District Element Numerical Modelling in Geo-Engineering.

Sangha, C.M., and Dhir, R.K., 1972. Influence of time on the strength deformation and fracture properties of a lower Devonian sandstone: International Journal of Rock Mechanics and Mining Sciences, v. 9, p. 343-354.

Savin, G.N., 1961. Stress concentration around holes. New York: Pergamon.

Sen. Z., and Eissa, E.A., 1992. Rock quality charts for log-normally distributed block sizes: International Journal of Rock Mechanics and Mining Sciences, v.29, no. 1, p. 1-12.

Shang, J., Hu, J., and Zhou, K., 2013. Numerical tests on heterogeneous effect in damage and acoustic emission characteristic of rocks under uniaxial loading: Journal of Central South University (Science and Technology), v.6, p. 2470-2475.

Shen, B., and Stephansson, O., 1994. Modification of the G-criterion for crack propagation subjected to compression: Engineering Fracture Mechanics, v. 47, no. 2, p. 177-189.

Sheshde, E.A., and Cheshomi, A., 2015. New method for estimating unconfined compressive strength (UCS) using small rock samples: Journal of Petroleum Science and Engineering, v. 133, p. 367-375.

Sih, G.C., Paris, P.C., and Irwin, G.R., 1965. On cracks in rectilinearly anisotropic bodies: International Journal of Fracture, v.1, no.3, p.189-203.

Singh, B., and Sinha, U.N., 2000. Testing of rock joints.

Smedley, P.L., Neumann, I., and Brown, S., 2005 The Permo-Triassic sandstone aquifer of shropshire. Baseline Report Series: 20, British Geology Survey.

Sun, C.T. and Jin, Z., 2011. Fracture Mechanics, 1st

Sun, Z., and Ouchterlony, F., 1986. Fracture toughness of Stripa granite cores: International Journal of Rock Mechanics and Mining Sciences, v. 23, no. 6, p. 317-324.

Swan, G., 1980. Fracture stress scale effects for rocks in bending: International Journal of Rock Mechanics and Mining Sciences, v. 17, p. 317-324.

Slob, S., 2010. Automated rock mass characterisation using 3-D terrestrial laser scanning: Unpublished PhD thesis, The University of Twente, p.301.

Song, J.J., and Lee, C.I., 2001. Estimation of joint length distribution using window sampling: International Journal of Rock Mechanics and Mining Sciences, v. 38, p . 519-528.

Soper, N.J., and Dunning, F.W., 2005, Structure and sequence of the Ingleton Group, basement to the central Pennines of northern England: Proceedings of the Yorkshire Geological Society, v.55, p. 241-261.

Sopon, W., Chaowarin, W., and Kittitep, F., 2015. Effects of loading rate and temperature on tensile strength an deformation of rock salt: International Journal of Rock Mechanics and Mining Sciences, v. 73, p. 10-14.

Stevenson, I.P., and Gaunt, G.D., 1971. Geology of the country around Chapel-en-le-Frith. Memoir of the Geological Survey of Great Britain, English and Wales, Sheet 99.

Stimpson, B., 1978. Failure of slopes containing discontinuous planar joints: Proceedings of the 19th US Symposium on Rock Mechanics, Stateline, Nevada, p. 296-302.

Sturzenegger, M., and Stead, D., 2009a. Quantifying discontinuity orientation and persistence on high mountain rock slopes and large landslides using terrestrial remote sensing techniques: Natural Hazards and Earth System Sciences, v. 9, p. 267-287.

Sturzenegger, M., and Stead, D., 2009b. Close-range terrestrial digital photogrammetry and terrestrial laser scanning for discontinuity characterization on rock cuts: Engineering Geology, v. 106, no. 3-4, p. 163-182.

Sturzenegger, M., Stead, D., and Elmo, D., 2011. Terrestrial remote sensing-based estimation of mean trace length, trace intensity and block size/shape: Engineering Geology, v. 119, no. 3-4, p. 96-111.

Tating, F., Hack, R., and Jetten, V., 2015. Weathering effects on discontinuity properties in sandstone in a tropical environment: case study at Kota Kinabalu, Sabah Malaysia: Bulletin of Engineering Geology and the Environment, v.74, p.427–441.

Theotokogloug, E.N., 1990. Integral equation solution of the cracked finite elastic disc: Engineering Fracture Mechanics, v. 36, no. 4, p. 611-618.

Thiercelin, M., 1987. Fracture toughness under confining pressure using the modified ring test: The 28th U.S. Symposium on Rock Mechanics, Tucson, p. 149-156.

Thiercelin, M., 1989. Fracture toughness and hydraulic fracturing: International Journal of Rock Mechanics and Mining Sciences, v. 26, p. 177-183.

Thiercelin, M., and Roegiers, J.C., 1986. Toughness determination with the modified ring test: The 27th U.S. Symposium on Rock Mechanics, Tuscaloosa, Alabama, p. 616-622.

Thuro, K., Plinniinger, R.J., Zah, S., and Schutz, S., 2001. Scale effects in rock strength properties. Part 1: Unconfined compressive test and Brazilian test: Rock Mechanics-a Challenge for Society, Sarkka & Eloranta.

Ting, T.C.T, and Chou, S.C., 1981. Edge singularities in anisotropic composites: International Journal of Solids and Structures, v. 17, no. 11, p. 1057-1068.

Tuckey, Z., and Stead, D., 2016. Improvements to field and remote sensing methods for mapping discontinuity persistence and intact rock bridges in rock slopes: Engineering Geology, v. 208, p. 136-153.

Tuckey, Z., Stead, D., Sturzenegger, M., Elmo, D., and Terbrugge, P., 2012. Towards a methodology for characterizing intact rock bridges in large open pits: In: 46th US Rock Mechanics/Geomechanics Symposium held in Chicago, IL, USA, 24-27, June 2012.

Tupholme, G.E., 1974. A study of cracks in orthotropic crystals using dislocation layers: Journal of Engineering Mathematics, v. 8, no. 1, p. 57-69.

Turichshev, A., and Hadjigeorgiou, J., 2014. Experimental and numerical investigations into the strength of intact veined rock: Rock Mechanics and Rock Engineering, v.48, p. 1897-1912.

Turkingdton, A.V., and Paradise, T.R., 2005. Sandstone weathering: a century of research and innovation: Geomorphology, v.67, p.229–253.

Tweed, J., and Das, S.C., 1972. The stress intensity factors of a radial crack in a finite elastic disc: International Journal of Engineering Science, v. 10, p. 323-335.

Umili, G., Ferrero, A., and Einstein, H.H., 2013. A new method for automatic discontinuity traces sampling on rock mass 3D model: Computers and Geosciences, v. 51, p. 182-192.

Viviana, B.S., Luc, S., Frederic-Victor, D., and Marc, E., 2015. DEM analysis of rock bridges and the contribution to rock slope stability in the case

of translational sliding failures: International Journal of Rock Mechanics and Mining Sciences, v. 80, p. 67-78.

Wang, W., 2009. Rock Mass Mechanics (English edition). Central South University Press, Changsha, China.

Wang, H., Latham, J.P., and Poole, A.B., 1991. Predications of block size distribution for quarrying: Quarterly Journal of Engineering Geology, v. 24, p. 91-99.

Wang, L.G., Yamashita, S., Sugimoto, F., Pan, C., and Tan, G., 2003. A methodology for predicting the in situ size and shape distribution of rock blocks: Rock Mechanics and Rock Engineering, v. 36, no. 2, p. 121-142.

Wang, Q.Z., Jia, X.M., Kou, S.Q., Zhang, Z.X., and Lindqvist, P.A., 2003. More accurate stress intensity factor derived by finite element analysis for the ISRM suggested rock fracture toughness specimen-CCNBD: International Journal of Rock Mechanics and Mining Sciences, v. 40, p. 233-241.

Wang, Q.Z., and Xian, X.F., 1990. A method for calculating stress intensity factors of chevron-notched three-point bend bound bars: International Journal of Fracture, v. 45, p. R37-R41.

Wasantha, P.L.P., Ranjith, P.G., Xu, T., Zhao, J., and Yan, Y.L., 2014. A new parameter to describe the persistency of non-persistent joints: Engineering Geology, v.181, p. 71-77.

Waters, C.N., Aitkenhead, N., Jones, N.S., and Chisholm, J.I., 1996. Late Carboniferous stratigraphy and sedimentology of the Bradford area, and its implications for the regional geology of northern England:

Proceeding of the Yorkshire Geological Society, v. 51(Part 2), p. 87-101.

Whittaker, B.N., Singh, R.N., and Sun, G., 1992. Rock fracture mechanics principles, design and applications, developments in geotechnical engineering. Elsevier, Amsterdam.

Willenberg, H., Simon, L., Eberhardt, E., Evans, K.F., Spillmann, T., Heincke, B., Maurer, H., and Green, A.G., 2008. Internal structure and deformation of an unstable crystalline rock mass above Randa (Switzerland): Part I – Internal structure from integrated geological and geophysical investigations: Engineering Geology, v. 101, p. 1-14.

Wuerker, R.G., 1955. Measuring the tensile strength of rock: Mining Engineering, v. 7, no. 2, p. 157-168

Xu, C., and Fowell, R.J., 1994. Stress intensity factor evaluation for cracked chevron notched Brazilian disc specimens: International Journal of Rock Mechanics and Mining Sciences, v. 31, no. 2, p. 157-162.

Yarema, S.Y., 1979. Analysis of cracked disk specimens: Engineering Fracture Mechanics, v. 12, p. 365-375.

Yarema, S.Y., and Krestin, G.S., 1966. Determination of the modulus of cohesion of brittle materials by compressive tests on disc specimens containing cracks: Soviet Materials Science, v. 2, no. 1. p. 7-10.

Yoshitake, I., Rajabipour, F., Mimura, Y., and Scanlon, A., 2014. A prediction method of tensile young's modulus of concrete at early age: Advances in Civil Engineering, v.2012, p. 1-10.

Zhang, H.Q., Zhao, Z.Y., Tang, C.A., and Song, L, 2006. Numerical study of shear behaviour of intermittent rock joints with different geometrical

parameters: International Journal of Rock Mechanics and Mining Sciences, v. 43, p. 802-816.

Zhang, L., and Einstein, H.H., 2000. Estimating the intensity of rock discontinuities: International Journal of Rock Mechanics and Mining Sciences, v. 37, p. 819-837.

Zhang, L., and Einstein, H.H., 2000. The planar shape of rock joints: Rock Mechanics and Rock Engineering, v. 43, no. 1, p. 55-68.

Zhang, L., Einstein, H.H., and Dershowitz, W.S., 2002. Stereological relationship between trace length and size distribution of elliptical discontinuities: Geotechnique, v. 52, no. 6, p. 419-433.

Zhang, Q., Zhu, H., Zhang, L., and Ding, X., 2011. Study of scale effect on intact rock strength using particle flow modelling: International Journal of Rock Mechanics and Mining Sciences, v. 48, p. 1320-1328.

Zhang, Z.X., 2002. An empirical relation between mode I fracture toughness and the tensile strength of rock: International Journal of Rock Mechanics and Mining Sciences, v. 39, p. 401-406.

Zhao, G., and Yang, S., 2015. Analytical solutions for rock stress around square tunnels using complex variable theory: International Journal of Rock Mechanics and Mining Sciences, v.80, p. 302-307.

Zhou, H., Yang, Y., Zhang, C., and Hu, D., 2015. Experimental investigations on loading-rate dependency of compressive and tensile mechanical behaviour of hard rocks: European Journal of Environmental and Civil Engineering, v. 19, sup. 1, p. s70-s82.